INTERNATIONAL DOCTORAL SCHOOL OF THE USC

Noa
Varela Domínguez

PhD Thesis

Active control of thermal conductivity in mesophases and complex oxides

Santiago de Compostela, 2025

Doctoral Programme in Materials Science

ESCOLA DE DOUTORAMENTO
INTERNACIONAL DA USC

DOCTORAL THESIS

ACTIVE CONTROL OF THERMAL CONDUCTIVITY IN MESOPHASES AND COMPLEX OXIDES

Author

Noa Varela Domínguez

Supervisors: José Francisco Rivadulla Fernández

María del Carmen Giménez López

Tutor: José Francisco Rivadulla Fernández

PHD PROGRAMME IN MATERIALS SCIENCE

SANTIAGO DE COMPOSTELA

The doctoral candidate declares no conflicts of interest related to her thesis.

ACKNOWLEDGEMENTS

Con la presentación de esta tesis termina una de las etapas más emocionantes y felices de mi vida. El camino no siempre fue fácil, y a menudo estuvo plagado de inseguridades, frustraciones y decepciones. Sin embargo, al escribir este manuscrito y repasar el trabajo de estos casi cinco años, siento que valió la pena. Solo alguien que ha pasado por lo mismo puede entender la satisfacción que se siente al ver que todo tu trabajo se materializa en una publicación o en una tesis doctoral. No siempre se cumple, pero, en mi caso, puedo decir que todo esfuerzo tiene su recompensa.

Sin embargo, este no es un éxito individual, sino colectivo. A lo largo de esta etapa he tenido la suerte de coincidir con muchas personas –dentro y fuera del laboratorio– que, de una forma u otra, me han acompañado en el camino. Este es mi pequeño tributo a todas ellas. Espero no olvidarme de nadie.

Para empezar, quiero dar las gracias a mis directores de tesis, Fran y María, por su guía y apoyo durante estos años.

Fran, gracias por ser el director de tesis que todo el mundo desearía tener. Siempre estuviste ahí, con la puerta del despacho abierta para resolver cualquier duda, calmar miedos o explicarme –por enésima vez– lo que fuese que me traía de cabeza, sin importar lo ocupado que estuvieses. Gracias por confiar en mí, por valorarme y por valorar mis ideas, incluso cuando aún estaban a medio formar. Gracias por acompañarme con paciencia, entusiasmo (a veces, un poco ansioso, pero hasta eso tiene su encanto) y una energía contagiosa, que permitieron que mantuviese siempre la motivación y que esta tesis llegase a buen puerto. Espero haber estado a la altura. Un día te escuché decir que una de las cosas que más valorabas de J. B. Goodenough era su humanidad: su cercanía, su paciencia, comprensión y el respeto que mostraba hacia sus estudiantes. Quizás no eres consciente, pero tú eres el Goodenough que está marcando muchas generaciones.

María, muchas gracias por haber confiado en mí desde el principio y darme la oportunidad de empezar esta tesis con un contrato laboral, mientras esperaba la resolución de las becas. Te agradezco sinceramente la ayuda que me prestaste en la preparación de las distintas convocatorias y solicitudes, y el tiempo que me has dedicado siempre que lo necesité. Gracias por tu apoyo en los momentos importantes y por guiarme en este camino.

Gracias también a todos los demás que me han acompañado en esta aventura científica. En especial, a Carlos López (el Bueno), que me acogió cuando llegué al laboratorio y me enseñó, con admirable paciencia, todo lo que necesitaba saber: desde rellenar una hoja de pedido o solicitar vacaciones, hasta soldar, hacer litografía o medir en el 3ω. Este camino fue mucho más sencillo gracias a ti.

Una mención muy especial para mi grupo TEAM ONE (Yolanda, Eugenia y Marcelo), mi familia del P0L2, que me adoptó cuando me convertí en la única estudiante de doctorado del grupo. Gracias por ser uno de mis grandes apoyos, tanto dentro como fuera del CiQUS. La investigación es mucho más fácil rodeada de amigos, y vosotros tenéis gran culpa de que termine esta etapa un maravilloso recuerdo. Porque, al final, no hay problema lo suficientemente grande que no se resuelva con una tarde de cañas en la Taberna.

También quiero darles las gracias a todos mis compañeros de CmCLab, que hicieron del P0L4 el mejor ambiente de trabajo imaginable. Víctor Álvarez, que, aunque me queje, es el mejor compañero de trabajo que se puede tener. Javi, mi compi celeste, que me pone al día de las previsiones futbolísticas. Rafa, una persona simplemente indescriptible. Gracias por las risas, los chistes, las cervezas y relativizar la importancia de cualquier obstáculo. Víctor Leborán, el experto en Labview, Matlab y prácticamente cualquier cosa que uno pueda necesitar. Gracias por ayudarme a programar, por las orejas en Carnavales, las frambuesas en verano y, sobre todo, por rendirte en los debates políticos. Marcel, gracias por resolverme todas las dudas, y por leerte con paciencia párrafos enteros de este manuscrito para evitarme más de una cafrada. Y las últimas incorporaciones del grupo: Diogo y Martín. Aunque hayáis inclinado la balanza hacia el lado de los físicos, no os guardo rencor. Gracias por las risas, por vuestra buena energía y por todo lo que está por venir.

No me olvido tampoco de todos los demás que han hecho que el día a día fuera mucho más ameno: mis compañeros de despacho, de congresos o de cañas. Alvarito, Garoé, Lucía, Lidia, Manuel, Samuel, Jan, Elías: gracias por vuestra compañía y por todos los buenos momentos compartidos.

Tampoco quiero dejar pasar la oportunidad de dar las gracias a todos los coautores de las publicaciones (presentes y futuras) que dan lugar a esta tesis: Alejandro López, Gustavo Rama, Carlos Vázquez, Arturo López, Enrique Carbó, César Magén, Araceli Gutiérrez, Eric Langenberg y José Santiso. Vuestra contribución ha sido fundamental para que este proyecto saliera adelante. Además, quiero darle las gracias al profesor Chang-Beom Eom por darme la oportunidad de realizar una estancia en su laboratorio, y por hacer posible una experiencia inolvidable en Madison.

Y, ahora, dejando un poco de lado la parte científica, quiero darles las gracias a mis amigas de siempre, las niñas: Marta, Laura, Sara Pardavila, Sara Martínez, Sara D'orgambide, Paula, Alicia, Marina. Las que me han visto crecer y han confiado siempre en mí. Las se alegran de mis logros casi como si fuesen suyos. Gracias por estar siempre ahí.

Por supuesto, gracias a las personas sin las cuales no estaría hoy escribiendo estas líneas: mis padres. Gracias por creer siempre en mí, por animarme en todas mis aventuras y darme todas las oportunidades que necesité. Gracias por quererme y cuidarme incondicionalmente y, en definitiva, por convertirme en la persona que soy hoy. Espero que os sintáis, al menos, un poco orgullosos. Gracias también a mi hermana, Alba, mi otro yo. La persona más diferente y, a la vez, más parecida a mí. Quizás en el fondo lo de la astrología no sea tan engaño… (no).

Por último, pero no menos importante, gracias a Pablo. Por acompañarme, aun sin entender. Por animarme y motivarme para desarrollar los mejores superconductores (era así?). Gracias por distraerme cuando más lo necesitaba, y no dudar nunca de mí. Gracias por alegrarme la vida y hacer del mundo un sitio más bonito.

Sin todos vosotros esta experiencia no habría sido lo mismo. A estas alturas, creo que esta tesis ya no es solo mía: es nuestra.

Gracias.

LIST OF PUBLICATIONS

The following publications, which are a product of this thesis, are partially reproduced in this manuscript:

Chapter 3:

"Light-induced bi-directional switching of thermal conductivity in azobenzene-doped liquid crystal mesophases" *Journal of Materials Chemistry C*, **2023**, 11, 4588-4594. https://doi.org/10.1039/D3TC00099K

Noa Varela-Domínguez[1], Carlos López-Bueno[1], Alejandro López-Moreno[1,2], Marcel S. Claro[1], Gustavo Rama[1], Víctor Leborán[1], María del Carmen Giménez-López[1], and Francisco Rivadulla*[1]

> [1]CiQUS, Centro Singular de Investigación en Química Biolóxica e Materiais Moleculares, 15782-Santiago de Compostela, Spain
>
> [2]Present address: IMDEA Nanociencia, 28049-Madrid, Spain.

Editorial: The Royal Society of Chemistry ISSN: 2050-7534

Personal contribution: synthesis and structural characterization of azobenzene derivatives, thermal conductivity measurements, analysis and discussion of results.

5-Year Impact Factor: 5.6. Q1 in Applied Physics. This article was featured on the inside front cover (https://doi.org/10.1039/D3TC90076B).

Chapter 4:

"Exploring Topochemical Oxidation Reactions for Reversible Tuning of Thermal Conductivity in Perovskite Fe Oxides" *Chemistry of Materials*, **2024**, 36, 10249-10258. https://doi.org/10.1021/acs.chemmater.4c02023

Noa Varela-Domínguez[1], Marcel S. Claro[1], Enrique Carbó-Argibay[2], César Magén[3] and Francisco Rivadulla*[1]

> [1]CiQUS, Centro Singular de Investigación en Química Biolóxica e Materiais Moleculares, 15782-Santiago de Compostela, Spain
>
> [2]International Iberian Nanotechnology Laboratory (INL), 4715-330 Braga, Portugal.
>
> [3]Instituto de Nanociencia y Nanomateriales de Aragón (INMA), CSIC-Universidad de Zaragoza, 50009-Zaragoza, Spain.

Editorial: American Chemical Society ISSN: 1520-5002

Personal contribution: deposition of thin films and structural characterization by X-ray diffraction and reciprocal space mapping, topotactic oxidations, thermal conductivity measurements, analysis and discussion of results.

5-Year Impact Factor: 8.1. Q1 in Materials Science.

Chapter 5:

"Electric-Field Control of the Local Thermal Conductivity in Charge Transfer Oxides" *Advanced Materials*, **2025**, 37, 2413045. https://doi.org/10.1002/adma.202413045

Noa Varela-Domínguez[1], Marcel S. Claro[1], Carlos Vázquez-Vázquez[2], Manuel Arturo López-Quintela[2] and Francisco Rivadulla*[1]

[1]CiQUS, Centro Singular de Investigación en Química Biolóxica e Materiais Moleculares, 15782-Santiago de Compostela, Spain

[2]iMATUS, Instituto de Materiales, 15782-Santiago de Compostela, Spain.

Editorial: Wiley-VCH ISSN: 1521-4095

Personal contribution: deposition of thin films and structural characterization by X-ray diffraction, AFM experiments, thermal conductivity measurements, analysis and discussion of results.

5-Year Impact Factor: 28.9. Q1 (D1) in Condensed Matter Physics.

LIST OF ABBREVIATIONS

^{1}H-NMR	Proton nuclear magnetic resonance
8CB	4-octyl-4’-cyanobiphenyl
AC	Alternating current
AFM	Atomic force microscopy
BHF	Buffered hydrofluoric acid
BM	Brownmillerite
C-AFM	Conductive atomic force microscopy
CCD	Charge-coupled device
CFO	$CaFeO_x$
Cr	Crystal
DART	Dual AC Resonance Tracking
DC	Direct current
DMF	N,N-dimethylformamide
DSC	Differential scanning calorimetry
DSO	$DyScO_3$
DW	Dipole wave
EDS	Energy dispersive X-ray spectroscopy
E_F	Fermi level
FDTR	Frequency domain thermoreflectance
FFT	Fast Fourier transform
FWHM	Full width at half maximum
HAADF	High-angle annular dark field
IL	Isotropic liquid
KPFM	Kelvin probe force microscopy
LAO	$LaAlO_3$
LC	Liquid crystal
L-PFM	Lateral piezoresponse force microscopy
LSAT	$(LaAlO_3)_{0.3}(Sr_2AlTaO_6)_{0.7}$

LSCO	$La_{0.6}Sr_{0.4}CoO_{3-x}$
LSMO	$La_{0.7}Sr_{0.3}MnO_3$
MBE	Molecular beam epitaxy
Nd:YAG	Neodymium-doped yttrium aluminum garnet
N-LC	Nematic liquid crystal
PCM	Phase-change material
PFM	Piezoresponse force microscopy
PGEC	Phonon glass electron crystal
PLD	Pulsed laser deposition
PnCs	Phononic crystals
POM	Polarized optical microscopy
PPMS	Physical property measurement system
PTO	$PbTiO_3$
PV	Perovskite
PZT	$PbZr_xTi_{1-x}O_3$
RF	Radiofrequency
RH	Relative humidity
RSM	Reciprocal space mapping
RTA	Relaxation time approximation
SC	Supercrystal
SCO	$SrCoO_{3-x}$
SFO	$SrFeO_x$
SI	International system of units
SKPM	Scanning Kelvin probe microscopy
SL	Superlattice
Sm-LC	Smectic liquid crystal
SMO	$SrMnO_3$
STEM	Scanning transmission electron microscopy
STO	$SrTiO_3$
TBC	Thermal boundary conductance
TEM	Transmission electron microscopy
u.c.	Unit cell
UV	Ultraviolet light

V	Vortex
Vis	Visible light
V-PFM	Vertical piezoresponse force microscopy
XPS	X-ray photoelectron spectroscopy
XRD	X-ray diffraction
XRR	X-ray reflectivity
YSZ	Yttria-stabilized zirconia, Y_2O_3:ZrO_2

TABLE OF CONTENTS

SUMMARY

Thermal energy plays a critical role in a wide range of technologies. For instance, in applications such as refrigeration and thermal insulation, materials with ultra-low thermal conductivity are essential to prevent unwanted heat transfer. Conversely, in microelectronics, materials with high thermal conductivity are required to effectively dissipate the excess heat generated during performance, thereby preventing device failure. Yet, despite its central importance, thermal conductivity has traditionally been considered a passive material property –primarily governed by intrinsic factors such as composition, crystal structure, or defect concentration. This static perspective contrasts with the growing demand for dynamic thermal management systems, in which heat flow can be actively and reversibly modulated depending on specific operational requirements.

Achieving such active control over thermal transport would unlock new functionalities in diverse applications, including switchable thermal insulation or reconfigurable thermal logic devices. However, because all materials conduct heat to some extent –and because heat, unlike electric charge or magnetization, lacks a natural external control field–, the precise and reversible modulation of thermal conductivity remains a significant scientific and technological challenge. Within this context, the main goal of this thesis is to contribute to the development of thermal switches: materials whose thermal conductivity can be precisely and reversibly tuned on demand by applying an external stimulus. In doing so, this work embraces the paradigm of treating heat as an actively controllable property, rather than a passive consequence of material identity.

To address this goal, this thesis explores four complementary strategies, each based on different material platforms and physical mechanisms. These include: i) light-induced structural transitions in soft mesophases; ii) topotactic redox transformations in complex oxide thin films; iii) electric-field driven control of oxygen stoichiometry in charge-transfer oxides; and iv) the engineering of polar architectures in epitaxial ferroelectric superlattices. These approaches offer diverse capabilities in terms of switching contrast, reversibility, type of stimulus, spatial resolution, and long-term stability, contributing to a growing toolbox for the design of adaptive thermal materials.

The first strategy, explored in Chapter 3, focuses on azobenzene-based mesophases, which undergo light-induced *trans-cis* isomerization upon UV/Vis illumination. This reversible structural transformation alters the molecular packing and intermolecular interactions, thereby influencing thermal transport. By systematically varying the alkyl chain length of the azobenzene derivatives, we achieved reversible changes in thermal conductivity during UV/Vis irradiation cycles of up to ≈35%. Furthermore, by embedding small amounts of these photoactive molecules into non-photoresponsive commercial liquid crystal matrices, we demonstrated that their photoisomerization can reversibly modulate the thermal conductivity of the host system. In particular, these composite materials allowed for a bi-directional change in thermal conductivity, with fast switching speeds, high stability, and excellent cyclability, establishing light as an effective, contactless stimulus for the dynamic control of heat flow in soft matter.

The second research line, presented in Chapter 4, explores the use of topotactic redox phase transitions to modulate heat transport. Specifically, we studied the reversible conversion between brownmillerite $(Ca,Sr)FeO_{2.5}$ and perovskite $(Ca,Sr)FeO_3$ structures, which involves the insertion and extraction of oxide ions into the crystal lattice. We evaluated several oxidation routes –including liquid phase, gas phase and solid-state oxidation using a solid electrolyte– and found that the reversibility of this redox process is strongly dependent on the oxidation mechanism. Aqueous chemical oxidation leads to the irreversible degradation of the crystalline structure due to the inherent instability of charge-transfer oxides in liquid environments. Gas-phase oxidation offers improved structural tunability, but the progressive accumulation of defects eventually leads to irreversibility issues after several cycles. In contrast, electrochemical oxidation using a YSZ solid electrolyte enables fully reversible O^{2-} insertion/extraction, resulting in stable and repeatable switching of the thermal conductivity by nearly a factor of two. These findings highlight the importance of ionic control in achieving robust, non-volatile thermal states in correlated oxides.

The third strategy (described in Chapter 5) focuses on the electric-field control of oxygen vacancies in charge-transfer oxide thin films. By applying localized electric fields with a voltage-biased atomic force microscopy tip, we induced the accumulation of oxygen vacancies in particular regions of the material, leading to spatially localized reductions in thermal conductivity without altering the surface morphology or structure. These modified states were persistent under ambient conditions and could be erased via thermal annealing, enabling rewritable and non-volatile thermal patterning. The ability to write, erase, and reprogram thermal states with micrometer precision using an electric field introduces a powerful new paradigm for active thermal management, with implications for thermal memory and logic applications. This method combines spatial control, reversibility, and stability, offering a viable route for non-destructive modulation of heat flow in nanoscale devices.

Finally, in Chapter 6 we investigate the control of thermal transport through the manipulation of polar architectures in ferroelectric $PbTiO_3/SrTiO_3$ (PTO/STO) superlattices. By tuning epitaxial strain and superlattice periodicity, we stabilized a rich variety of polar configurations, including conventional a_1/a_2 stripe domains, flux-closure patterns, and more complex polar textures such as dipole waves and polar supercrystals. Thermal conductivity measurements showed that these superlattices consistently exhibit lower thermal conductivities than similar systems of comparable interface densities. This behavior is attributed to enhanced phonon scattering arising from continuous polarization rotation, lateral strain gradients, and nanoscale dipolar inhomogeneities intrinsic to polarization textures. Moreover, the 3D organization of polarization into supercrystals induces a further reduction in thermal transport, reinforcing the role of polar topology as a tunable phonon-scattering mechanism. Importantly, since many of these polar architectures are thermally unstable, they also provide a platform for temperature-dependent, reversible switching of thermal conductivity in ferroelectric systems.

In conclusion, the results presented in this thesis demonstrate that active modulation of thermal conductivity can be achieved through a wide range of mechanisms, each offering unique advantages depending on the desired application. By integrating concepts from photochemistry, soft-matter physics, solid-state chemistry, and ferroelectric topology, this thesis lays the foundation for the development of adaptive, programmable, and multifunctional thermal materials –key components for the next generation of intelligent thermal technologies.

1. INTRODUCTION

> *“All sorts of things can happen when you’re open to new ideas and playing around with things.”*
>
> Stephanie Kwolek, American chemist who invented Kevlar.

Ohm’s Law, one of the fundamental principles of physics, states that all materials present an inherent resistance to the flow of electric current. This resistance leads to Joule heating, an unavoidable phenomenon where part of the energy in an electric current is irreversibly converted into heat. While this effect has long influenced the design of electronic systems – from early incandescent bulbs to modern microprocessors–, the rapid advancement of electronics has made the efficient dissipation of heat an increasingly critical challenge.

Historically, thermal management in electronics was addressed through passive solutions such as heat sinks and cooling systems, which simply dissipate excess heat. However, with the continuous miniaturization of electronic components and the growing demand for higher processing powers, these conventional approaches are reaching their physical and practical limits. As devices shrink to the nanoscale, power densities increase, leading to higher heat generation per unit volume. Simultaneously, the reduced size of the components limits the available surface area for heat dissipation, making effective heat removal increasingly difficult. This accumulation of heat negatively impacts device efficiency, accelerates material degradation, and significantly increases the risk of electronic failure. In nanoscale and high-power applications, where billions of transistors switch at extreme speeds, heat is no longer just a byproduct: it has become a fundamental constraint on technological progress (*1*).

Yet, the challenge of thermal management extends beyond electronics. Different applications require different thermal transport behaviors: in high-power electronic devices, efficient heat dissipation is essential, necessitating materials with high thermal conductivity (κ); conversely, applications such as thermal insulation, refrigeration, or thermoelectric applications (where maintaining a temperature gradient is crucial) rely on materials with ultra-low thermal conductivity (*2*).

Traditionally, materials have been engineered to exhibit either high or low thermal conductivity depending on their intended use. However, the ability to dynamically modulate thermal transport (i.e., switching between high and low thermal conductivity states on demand), would revolutionize adaptive thermal management and energy-efficient electronics. Just as semiconductors revolutionized electronics by enabling tunable electrical properties, another breakthrough lies in materials where thermal transport can be externally controlled.

Still, achieving precise manipulation of heat is significantly more complex than controlling electricity. Unlike electrical current, which selectively flows through conductors and can be blocked by insulators, all materials conduct heat to some extent, making accurate control extremely difficult. Moreover, the study of thermal transport presents both theoretical and experimental challenges (*3*):

Theoretical challenges:

- Heat is transported by different energy carriers (phonons, electrons, etc.), each behaving differently across materials, even if we restrict our analysis to solids.
- Modeling many-body interactions among these carriers is extremely complex.
- Interfacial thermal resistance is difficult to simulate and predict accurately, particularly when different types of solids are involved (metal/dielectric oxide/semiconductor). This complicates predictions of heat flow at materials boundaries.
- At the nanoscale, heat transport shifts from diffusive to ballistic, making traditional models inadequate for describing heat conduction as the size of the system is reduced.

Experimental challenges:

- Since all materials transport heat, isolating and characterizing heat flow mechanisms is inherently challenging.
- Measuring thermal conductivity in non-ideal sample geometries introduces significant uncertainties.
- As devices shrink, current experimental techniques struggle to measure heat transport with high precision.

This thesis aims to contribute to this field by exploring the active control of thermal conductivity in mesophases and thin films of complex oxides. By means of an external stimulus, such as light or electric fields, we intend to redefine heat conduction as a controllable property, rather than a passive limitation.

In this chapter, we will first describe the fundamental mechanisms of heat transfer across different states of matter. Next, we will review key advancements in thermal management, from conventional strategies for controlling thermal conductivity to the latest developments in thermal switching materials: materials engineered to dynamically modulate heat transport. Lastly, this chapter concludes with the objectives of this thesis, providing a roadmap for the research presented in this book.

1.1. MECHANISMS OF HEAT TRANSFER

When a system in thermodynamic equilibrium experiences a gradient of a given property –such as matter, energy, etc.– a flux of that magnitude will arise to restore the original equilibrium state. In the case of a material that presents a temperature gradient, an energy flux (in the form of heat) will flow from the hotter region towards the cooler one. For small temperature gradients, the heat flux is proportional to the temperature gradient, a relationship described by Fourier's law of heat conduction:

$$\overrightarrow{J_Q} = \frac{\partial Q}{A \partial t} = -\kappa \, \frac{\partial T}{\partial x} \qquad \textit{(Eq. 1.1)}$$

where $\overrightarrow{J_Q}$ is the flux, representing the amount of heat (∂Q) transferred though an area A during a time interval ∂t, κ is the thermal conductivity (with SI units of J m^{-1} K^{-1} s^{-1}) and $\partial T/\partial x$ is the temperature gradient. This equation establishes the phenomenological foundation of heat conduction, and the starting point for the experimental determination of the thermal conductivity (*4*).

A microscopical expression for thermal conductivity can be easily derived if we apply the conditions of *Eq. 1.1* to the simplest possible system, i.e., an ideal gas under a small, unidirectional thermal gradient, as shown in **Figure 1.1**.

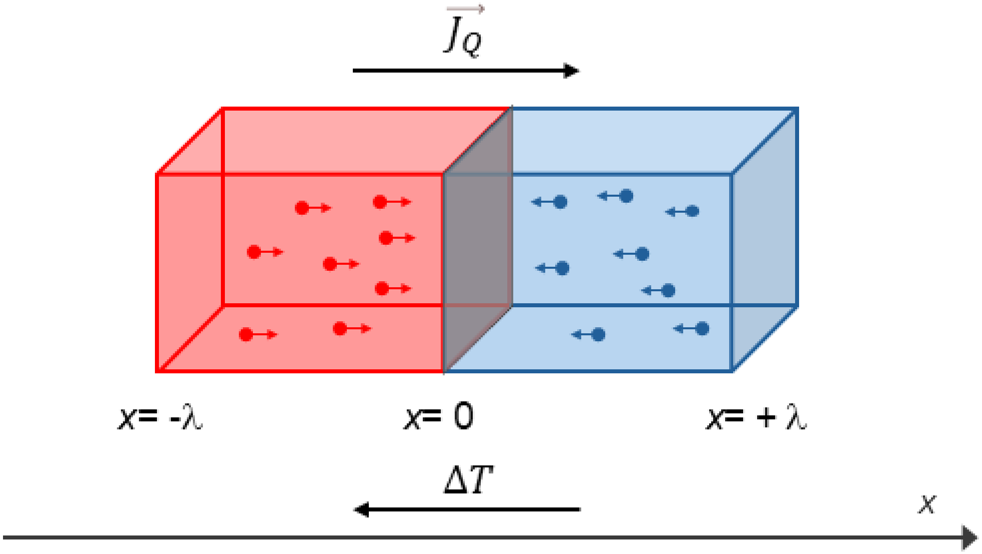

Figure 1.1. Schematic representation of heat flux in an ideal gas, where molecules transfer energy from the hotter region (*x*= -λ) to the cooler region (*x*= +λ) through molecular motion. The net flux ($\overrightarrow{J_Q}$) corresponds to the difference between the energy transported by molecules moving in opposite directions. Only the 1D transport along the *x*-dimension is considered in this example.

In gases, heat is primarily transferred through elastic collisions between molecules, and their ability to conduct heat depends on the energy (E) carried by the individual molecules and the efficiency of energy transfer, determined by the molecular speed (v) and mean free path (λ). The presence of the thermal gradient will establish a net flux of molecules moving from the hotter region to the cooler side. Intuitively (and through dimensional analysis), the heat flux can be expressed as the product of the energy density and the average speed at which heat is transported along the system: $J = v \cdot \frac{E}{V}$. In this way, the magnitude of the net flux may be simply calculated as the difference of the heat flux contributions from molecules moving in the negative x-direction (J_{-x}) and positive x-direction (J_{+x}) (*5*):

$$J_{-x} \propto \frac{v}{V} E(-dx) \qquad \text{(Eq. 1.2)}$$

$$J_{+x} \propto \frac{v}{V} E(+dx) \qquad \text{(Eq. 1.3)}$$

The net heat flux can be then expressed as:

$$\overrightarrow{J_Q} = J_{-x} - J_{+x} \propto \frac{v}{V}\frac{\partial E}{\partial x} dx = -\frac{1}{3} C_v v \lambda \frac{\partial T}{\partial x} \qquad \text{(Eq 1.4)}$$

where the relationship between the mean squared displacement (*dx*) and the mean free path (λ), with a $^1/_3$ correction to account for 3D transport, has been introduced. Note that, in this expression, C_v corresponds to the volumetric heat capacity of an ideal gas.

By comparing this equation with Fourier's law (*Eq. 1.1*), we identify a microscopic expression for thermal conductivity (*6*):

$$\kappa = \frac{1}{3} C_v v \lambda \qquad \text{(Eq. 1.5)}$$

Although this formula is derived from the kinetic theory of gases, its fundamental principles extend to all materials. Regardless of the energy carriers involved (electrons, phonons, etc.), thermal conductivity depends on three main parameters: the amount of energy stored in the excitations responsible for heat transport (i.e., the heat capacity), their propagation speed, and their mean free path before scattering. The challenge is to develop methods to control any of these parameters by an external field, if we aim to modulate thermal transport in different materials.

In the following sections, we will describe the mechanisms of heat conduction in solids (which are the primary system under study in this thesis) and liquids.

1.1.1. Solids

In solids, heat is primarily transferred by two types of energy carriers: electrons and phonons (i.e., lattice atomic vibrations). While other excitations such as magnons may also contribute to thermal transport in certain materials, their role will not be addressed in this thesis.

The total thermal conductivity of a solid (κ_s) can therefore be expressed as the sum of the electronic (κ_e) and lattice (κ_l) contributions, with their relative importance depending on the material's electronic structure and bonding:

$$\kappa_s = \kappa_e + \kappa_l \qquad \text{(Eq. 1.6)}$$

In metals and electrically conductive solids, electrons –which are free to move throughout the material– dominate thermal transport. These electrons carry both electrical charge and thermal energy, and their contribution to thermal conductivity (κ_e) may be approximately calculated from the electrical conductivity (σ) via the Wiedemann-Franz law:

$$\kappa_e = \sigma \cdot L \cdot T \qquad \text{(Eq. 1.7)}$$

where T is the absolute temperature and L is the Lorenz number, which is ≈ $2.44 \cdot 10^{-8}$ $\Omega \cdot W/K^2$ for pure metals. In semiconductors, however, the Lorenz number may vary slightly with carrier concentration (*3*).

To illustrate the leading role of electrons in these materials, consider bulk Au, which presents an experimental electrical resistivity of $2.271 \cdot 10^{-8}$ $\Omega \cdot m$ at 300 K (*7*). Using *Eq. 1.7*, this corresponds to an electronic thermal conductivity of about 322 W/mK. This value closely matches the experimentally reported total thermal conductivity of gold, κ_s= 318 W/mK (*8*). The small discrepancy between the κ_e and κ_s values (resulting in a total thermal conductivity slightly smaller than κ_e), can be attributed to experimental uncertainties or slight deviations in the assumed Lorenz number. Nevertheless, the comparison confirms that in metals, electrons are the dominant contributors to heat transport, and $\kappa_s \approx \kappa_e$.

In contrast, the situation is markedly different in dielectric materials (such as those studied in this thesis) or semiconductors with low carrier concentration, where electrons play negligible role in thermal transport. For instance, strontium titanate ($SrTiO_3$), a prototypical dielectric, has an electrical conductivity of roughly 10^{-4} $\Omega^{-1}m^{-1}$ at 300 K (*9*). Applying the Wiedemann-Franz law, the electronic contribution to its thermal conductivity is of the order of ≈$7 \cdot 10^{-10}$ W/mK, completely insignificant compared to its total thermal conductivity of κ_s= 11 W/mK at the same temperature (*10*). This discrepancy is far too large to be explained by variations in the Lorenz number alone. For perspective, any material with an electrical conductivity lower than ≈$3.5 \cdot 10^3$ $\Omega^{-1}m^{-1}$ would present an electronic contribution to thermal conductivity below the thermal conductivity of air (≈0.026 W/mK at 298 K and 1 atm (*11*)).

Instead, in dielectric materials heat is predominantly carried by phonons, which are quantized collective excitations of the atomic lattice vibrations. Although they are not particles in the traditional sense (they are commonly referred to as “quasiparticles”, as they only propagate in the medium where they are defined), phonons behave like discrete energy carriers and can transport thermal energy across a material when a temperature gradient is present. Consequently, both the thermodynamic and transport properties of insulating solids (e.g., heat capacity, thermal conductivity) are governed by the phonon spectrum and their interactions.

In 1912, Peter Debye proposed a model (*12*) that describes the atomic lattice as a system of coupled atoms capable of supporting collective vibrational modes. In this model, phonons span over a continuous distribution of frequencies up to a maximum limit known as the Debye frequency (ω_D), corresponding to the highest vibrational mode allowed in the crystal. This upper limit is imposed by the fact that a crystal composed of N atoms can only support $3N$ vibrational modes, corresponding to three degrees of freedom per atom (one longitudinal and two transverse modes) (*6*).

In practice, Debye’s model provides a good approximation for the behavior of acoustic phonons (modes in which neighboring atoms oscillate in phase with one another), which are the primary contributors to thermal conductivity in non-metallic solids as they typically exhibit higher group velocities and longer mean free paths than optical phonons (corresponding to out-of-phase atomic oscillations). Therefore, Debye’s model is often used when deriving microscopic expressions for lattice thermal conductivity. However, it is important to note that, while optical phonons (normally) do not propagate heat efficiently, they can still influence thermal conductivity by interacting with acoustic phonons, introducing additional scattering channels that reduce the overall heat-carrying capacity of the system (*5*, *13*).

To describe phonon-mediated thermal transport at the microscopic level, Klemens (*14*) introduced the relaxation time approximation (RTA), which assumes that, following a scattering event, any non-equilibrium phonon distribution relaxes exponentially back to equilibrium Bose-Einstein distribution, with a characteristic time $\tau(\omega)$ known as relaxation time. Physically, this means that after each scattering event, a phonon "forgets" its prior history and relaxes towards equilibrium over a time scale τ.

Under the RTA –considering the mean free path of phonons as $\lambda(\omega)= v_g(\omega)\cdot\tau(\omega)$–, the phonon contribution to the thermal conductivity (refer to *Eq. 1.5*) can be expressed as:

$$k_L = \frac{1}{3}\int C(\omega)v_g^2(\omega)\tau(\omega)d\omega \qquad \textit{(Eq 1.8)}$$

where $C(\omega)$ is the mode specific heat, $v_g(\omega)$ is the group velocity (assumed constant in Debye's model, v), and $\tau(\omega)$ is the relaxation time. Note that this expression is integrated over the entire phonon spectrum (*3*).

Substituting the corresponding expressions from Debye's model for the specific heat, a final expression for thermal conductivity is obtained:

$$\kappa_L = \frac{1}{2v\pi^2}\int_0^{\omega_D}\tau(\omega)\frac{\hbar^2\omega^4}{k_B T^2}\frac{e^{\frac{\hbar\omega}{k_B T}}}{\left(e^{\frac{\hbar\omega}{k_B T}}-1\right)^2}d\omega \qquad \textit{(Eq. 1.9)}$$

This expression, known as the Debye approximation for lattice thermal conductivity, incorporates the influence of material-specific phonon transport properties through the frequency-dependent phonon relaxation time, $\tau(\omega)$. Note that this simplified model considers the phonon velocity as a constat, independent of the phonon frequency.

In this approximation, the total phonon relaxation time is governed by the combined effects of different scattering mechanisms, which are treated as independent of each other. In this case, according to Matthiessen's rule, the net relaxation time $\tau_q(\omega)$ is given by the reciprocal sum of the individual scattering contributions:

$$\tau_q^{-1}(\omega) = \sum\tau_i^{-1}(\omega) \qquad \textit{(Eq. 1.10)}$$

where i runs over all possible scattering processes. The most common scattering mechanisms in dielectric materials are briefly described next.

Phonon-phonon scattering. Even in perfectly ordered crystal, phonons scatter with each other due to the anharmonicity of the lattice potential, which is quantified by the Grüneisen parameter (γ) (*13*). The dominant interactions are three-phonon processes, which can be classified as Normal (N) and Umklapp (U) processes. N-processes conserve both energy and momentum and serve to redistribute energy across the phonon spectrum without directly affecting heat flow; for this reason, they will no longer be considered in this thesis. In contrast, U-processes involve a net loss of crystal momentum and contribute to thermal resistance. In these interactions, two phonons with wavevectors q_1 and q_2 merge into a new third phonon, presenting a wavevector (q_3) that lies outside the first Brillouin zone and is folded back by the reciprocal lattice vector K (*15*):

$$q_1 + q_2 = q_3 + K \qquad \textit{(Eq. 1.11)}$$

Note that, in this equation, an N-process is described if *K*=0.

Although an exact analytical model for the scattering rate of the U-processes is challenging, it is often described by the following expression (*16*):

$$\tau_U^{-1}(\omega, T) = A_U \omega^2 T e^{\frac{-\Theta_D}{\alpha T}} \qquad A_U = \frac{\hbar \gamma^2}{\bar{M} v^2 \Theta_D} \qquad \text{(Eq.1.12)}$$

where A_U is a material-specific constant (determined by Debye's temperature, Θ_D, the Grüneisen parameter, and the average atomic mass per atom, among others), and α is an empirical fitting parameter that typically lies between 2 and 3 (*17*).

Phonon-boundary scattering. This scattering mechanism occurs when a traveling phonon interacts with a material surface, interface, or grain boundary. It becomes especially important at low temperatures or in nanostructured systems, as phonon wavelengths grow longer and their mean free paths exceed the characteristic dimensions of the material. Unlike phonon-phonon interactions, boundary scattering is purely geometric and does not depend on temperature or frequency. The relaxation time is typically given by the Casimir limit (*18*):

$$\tau_B^{-1} = \frac{v}{L} \qquad \text{(Eq. 1.13)}$$

where v is the phonon group velocity and L is the effective characteristic length of the structure (e.g., gain size, film thickness). Since boundary scattering is independent of phonon frequency and temperature, it dominates when intrinsic scattering mechanisms are weak (*16*).

Point-defect scattering. This type of scattering arises from local disruptions in the crystal lattice caused by substitutional impurities, isotropic disorder, or vacancies. These defects act as elastic scattering centers, and their impact is especially pronounced at high phonon frequencies. In general, the relaxation time for point defect scattering depends on both mass fluctuations and local strain field variations, as first described by Klemens (*19*). However, in this thesis we adopt a simplified version where only mass fluctuations are considered, valid in the Rayleigh scattering regime –when the phonon wavelength is much larger than the size of the defect:

$$\tau_D^{-1}(\omega) = A_D \omega^4 \qquad A_D = \frac{\delta^3}{4\pi v^3} \sum_i x_i \left(1 - \frac{m_i}{\bar{M}}\right)^2 \qquad \text{(Eq. 1.14)}$$

where A_D is a constant related to the average volume per atom (δ^3), concentration of defects (χ_i), and mass variance between host and impurity atoms. The strong ω^4 dependence implies that point defects effectively scatter high-energy phonons, significantly reducing thermal conductivity in materials with substantial atomic-scale disorder or mass contrast (*16*, *17*).

By combining all these contributions, *Eq. 1.10* can be rewritten as:

$$\tau_q^{-1}(\omega) = \tau_U^{-1} + \tau_B^{-1} + \tau_D^{-1} = A_U \omega^2 T e^{\frac{-\Theta_D}{\alpha T}} + \frac{v}{L} + A_D \omega^4 \qquad \text{(Eq. 1.15)}$$

which may be also inserted in Debye's approximation for lattice thermal conductivity (*Eq. 1.9*) to capture the temperature-dependent behavior arising from the different scattering processes.

These scattering mechanisms usually prevail in different thermal regimes, thereby shaping the overall thermal transport behavior of dielectric materials. At high temperatures (T >> Θ_D), Umklapp processes are the primary source of phonon scattering. Conversely, at low temperatures, phonon-phonon interactions are weak, allowing phonons to travel longer distances until they are scattered by physical boundaries, making boundary scattering the dominant mechanism in this region. In the intermediate temperature range, point-defect scattering often plays a leading role, as phonons possess the energy to strongly interact with mass or structural inhomogeneities.

To quantitatively illustrate the impact of each scattering mechanism on thermal transport, we will now simulate the temperature-dependent lattice thermal conductivity of different $PbTiO_3$ films using Debye's model (*Eq. 1.9*). The material-specific parameters required for this analysis were either calculated or obtained from literature, and are listed in **Table 1.1**:

Table 1.1. Parameters used to determine phonon relaxation times in $PbTiO_3$.

Parameter	Value	Reference
Θ_D (K)	464	(*20*)
γ	1.42	(*21*)
v (m/s)	3685	(*20*)
$\overline{M}$(kg)	$1.007 \cdot 10^{-25}$	*Calculated*
δ^3 (m^3)	$1.26 \cdot 10^{-29}$	*Calculated*

Since Umklapp scattering is an intrinsic process determined by material's crystal structure and bonding, we first estimate its contribution. Using *Eq. 1.12* and the values in **Table 1.1**, the Umklapp relaxation time can be expressed as $\tau_U^{-1} = 3.35 \cdot 10^{-19}\ \omega^2 T e^{\frac{-232}{T}}$ s^{-1} (with α=2). On the other hand, boundary scattering depends on the effective length of the material (*Eq. 1.13*); for a $PbTiO_3$ film with a thickness of 1 μm, boundary relaxation time is $\tau_B^{-1} = 3.68 \cdot 10^9$ s^{-1}. Finally, to account for point-defect scattering, we assume a $PbTiO_3$ film with 5% of randomly distributed oxygen vacancies, which are a common type of defect in perovskites (*22*, *23*). Given that in the case of vacancies the mass of the impurity is m_i=0 (*Eq. 1.14*), the point-defect relaxation time is $\tau_D^{-1} = 1.00 \cdot 10^{-42}\ \omega^4$ s^{-1}.

These relaxation times are then inserted into *Eq. 1.9* to simulate the thermal conductivity of $PbTiO_3$. The results are presented in **Figure 1.2**a (black curve), showing the expected trend for a bulk dielectric. At low temperatures, κ rises rapidly due to the activation of low-energy phonons (following the increase of C_v) which continues until thermal conductivity reaches a maximum. Beyond this point, Umklapp processes become significant, and κ begins to decrease approximately as 1/T, in agreement with experimental trends for most insulating crystals (*10*).

To evaluate the impact of reducing the effective sample size on thermal transport, **Figure 1.2**a also includes the simulation of a 25 nm thick $PbTiO_3$ film with the same 5% concentration of oxygen vacancies (orange curve, $\tau_B^{-1} = 1.47 \cdot 10^{11}$ s^{-1}). The substantial increase in boundary scattering severely limits phonon transport, resulting in a significant reduction in thermal conductivity, of the order of 60% at 300 K. Moreover, the characteristic drop in thermal conductivity at high temperatures is now suppressed, remaining relatively constant. The origin of this behavior is clarified in **Figure 1.2**c, which plots the spectral contribution to thermal conductivity (integrand of *Eq. 1.9*) at 100 K for both film thicknesses. In the thinner film, the thermal conductivity is considerably reduced due to the enhanced boundary scattering of low-frequency phonons (<30 THz), whose long wavelengths are now limited by the sample thickness.

On the other hand, in **Figure 1.2**b we assess the effect of increasing defect concentration in thin films. To do so, we included the simulation of a 25 nm $PbTiO_3$ film which, in addition to the 5% of oxygen vacancies, presents and additional 5% of Pb vacancies (green curve), a common issue in $PbTiO_3$ films due to the volatility of lead during deposition –which may leave either as Pb^{2+} or PbO (*24*, *25*). In this case, the defect scattering relaxation time doubles ($\tau_D^{-1} = 2.00 \cdot 10^{-42}\, \omega^4$ s^{-1}), leading to a ≈50% reduction in thermal conductivity. This reduction is primarily attributed to enhanced scattering of high-frequency phonons (>20 THz), as predicted by *Eq. 1.14* and confirmed by the corresponding spectral contributions at 100 K (**Figure 1.2**d).

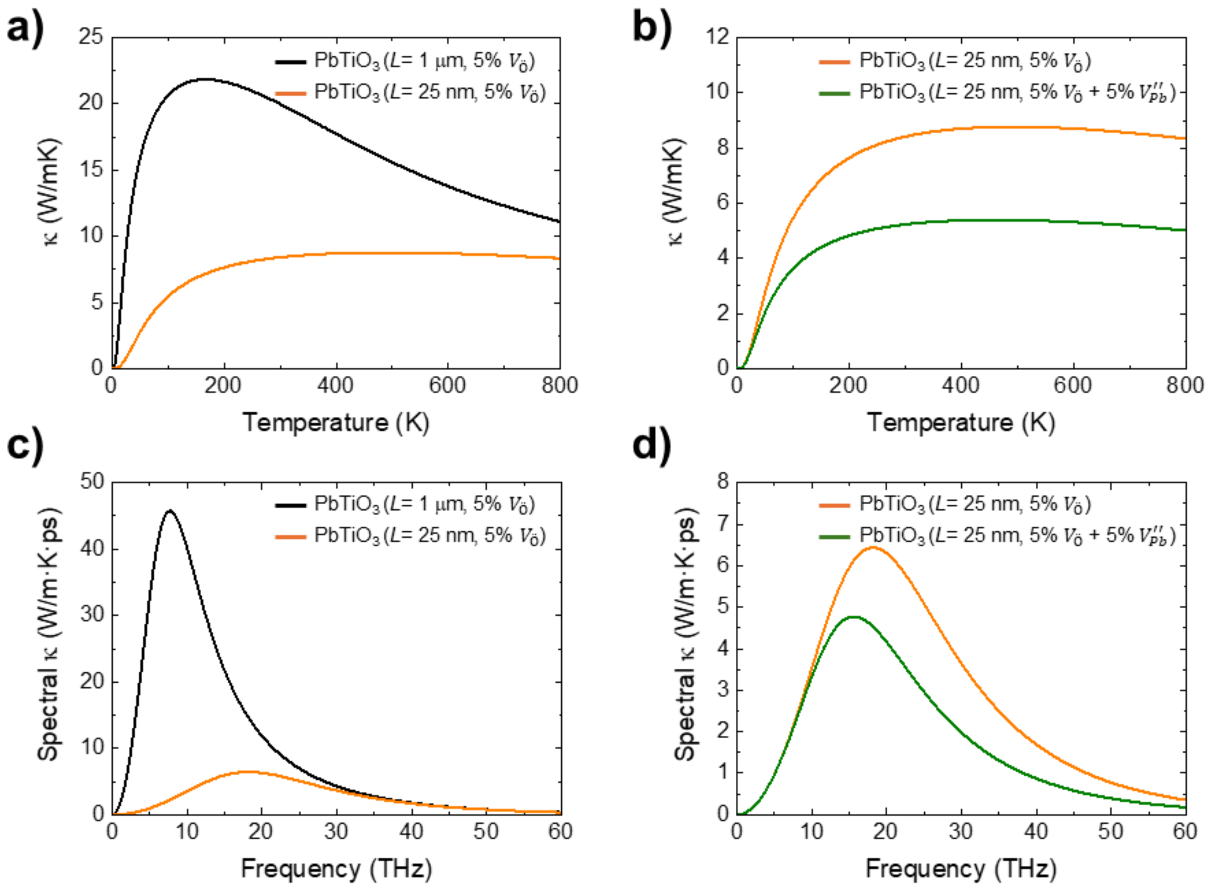

Figure 1.2. Simulations of Debye's model for the lattice thermal conductivity of $PbTiO_3$ films with different thicknesses and defect concentrations. a) Temperature-dependent thermal conductivity of $PbTiO_3$ films containing 5% of oxygen vacancies and thicknesses of 1 μm (black curve) and 25 nm (orange curve). b) Thermal conductivity of 25 nm thick films with different defect concentrations: 5% of oxygen vacancies (orange curve) and an additional 5% of Pb vacancies (green curve). c) Spectral thermal conductivity at 100 K for the thin films in (a), illustrating the suppression of low-frequency phonons due to boundary scattering. d) Spectral thermal conductivity at 100 K for the thin films in (b), showing enhanced scattering of high-frequency phonons due to increased point-defect concentration.

These simulations underscore the critical role of phonon scattering mechanisms in the thermal conductivity of dielectric thin films. Therefore, they will provide valuable insights when designing strategies for the active control of heat transport in these materials, with the aim of developing thermal switches.

Finally, it is worth noting that the significant reduction in thermal conductivity when increasing the concentration of defects (**Figure 1.2**b) proves a key advantage of thermal conductivity measurements: their extreme sensitivity to point defects. As demonstrated in ref. (*25*), standard structural characterization techniques such as X-ray diffraction or atomic force microscopy (AFM) often fail to detect low concentrations of point defects, especially when they are randomly distributed. However, thermal conductivity is strongly affected by such defects, as they act as highly effective phonon scatterers. As a result, thermal conductivity measurements can also serve as a powerful, indirect probe of crystalline order, effectively functioning as a complementary structural characterization technique.

1.1.2. Liquids

Although this thesis primarily focuses on investigating and controlling heat transport in crystalline dielectric solids –specifically oxide thin films, as discussed in Chapters 4 to 6–, Chapter 3 addresses the active modulation of thermal conductivity in soft-mesophases driven by different solid to isotropic liquid or liquid crystal to isotropic liquid phase transitions. For this reason, it is also important to briefly describe the mechanisms governing heat transport in liquid media.

In contrast to solids and gases, for which well-established theoretical frameworks exist, a comprehensive theory of heat transport in liquids has not yet been developed. This theoretical gap arises from the intrinsic complexity of liquids, which exhibit features in between ordered and disordered systems. On the one hand, interatomic interactions in liquids are too strong to allow treatment as non-interacting particles, as in the case of ideal gases. On the other hand, the absence of long-range translational symmetry and the presence of large, thermally driven structural fluctuations make it impossible to apply the harmonic approximations and periodic boundary conditions that enable the prediction of heat conduction in crystalline solids. As a result, liquids occupy a complex intermediate regime –behaving as strongly interacting yet disordered systems–, which complicates the development of a unified description of their thermal transport properties. Moreover, interactions in liquids tend to be highly system-specific, meaning that they strongly depend on the liquid under consideration (ionic, polar, non-polar, etc.) (*26*).

One of the earliest and most influential theoretical approaches to this problem was proposed by Frenkel in the early 20th century (*27*). Frenkel recognized the dual nature of liquids: they behave like disordered solids on short time scales, but flow like viscous fluids on longer time scales. He introduced the concept of a characteristic relaxation time, τ, which represents the average time between two successive local rearrangements ("jumps") of atoms or molecules within the liquid. These rearrangements involve particles escaping from their transient cages formed by their neighbors, as illustrated in **Figure 1.3**.

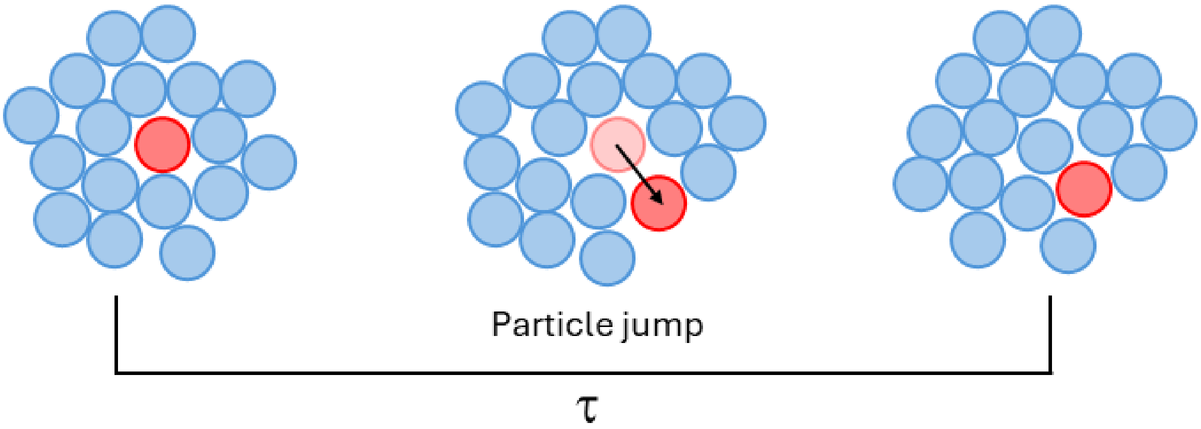

Figure 1.3. Schematic representation of particle dynamics in a liquid. On short time scales, particles vibrate around quasi-equilibrium positions; on longer time scales, they undergo diffusive rearrangements, characterized by an average relaxation time τ.

According to Frenkel's theory, when the observation time is shorter than τ, atoms vibrate around quasi-equilibrium positions, allowing the propagation of vibrational (phonon-like) modes like in solids. Under these conditions, the liquid can support one longitudinal and two transverse shear modes. However, for timescales longer than τ, particle rearrangements prevent the persistence of shear elasticity, and the liquid behaves as a viscous fluid, capable of only sustaining longitudinal modes. This transition introduces the so-called Frenkel frequency (ω_F), which is defined as (*28*):

$$\omega > \omega_F = \frac{2\pi}{\tau} \qquad \textit{(Eq. 1.16)}$$

Only vibrational modes with higher frequencies than ω_F can propagate elastically. Below this threshold, shear modes are suppressed, and energy transfer occurs primarily through diffusive motion rather than coherent vibrations.

This framework allows liquids to be partially described using concepts from solid-state physics. The thermal conductivity in Frenkel's picture is thus governed by both vibrational (phonon-like) and diffusive mechanisms and can be again described by *Eq. 1.5*. However, due to the lack of long-range order, vibrational modes in liquids cannot propagate over long distances. As a result, their mean free paths are typically of the order of a few intermolecular distances, which accounts for the generally low thermal conductivity of liquids –usually between 0.1-1 W/mK (*29*, *30*). In polar liquids like water, where H-bonds form 3D networks of connected molecules, Frenkel's picture also allows to develop an intuitive understanding of its relatively large thermal conductivity, which is around ≈0.6 W/mK at room temperature.

Frenkel's theory provides a qualitative insight into the temperature-dependent thermal conductivity of liquids, which typically shows a weak variation with temperature compared to solids. At low temperatures, where the relaxation time is longer, vibrational contributions to heat transport can be significant. As temperature increases, structural rearrangements become more frequent (i.e., τ decreases), reducing the phonon-like contribution and favoring a purely diffusive transport. However, because liquids are already structurally disordered, this transition results in a modest variation in thermal conductivity, far less pronounced than in crystalline solids, where Umklapp scattering leads to a strong decrease in $\kappa(T)$ at high temperatures (see **Figure 1.2**a).

Nevertheless, Frenkel's model is largely phenomenological and lacks predictive power. In recent years, more rigorous theoretical treatments based on equilibrium molecular dynamics and statistical mechanics have emerged (*31–33*). These approaches allow for a more detailed, system-specific analysis of the interplay between microscopic structure and macroscopic energy transport, especially in complex or molecular liquids.

Despite its limitations, Frenkel's theory continues to serve as a powerful conceptual tool, offering an intuitive picture of the dual vibrational-diffusive nature of heat transport in liquids, bridging the gap between solid and fluid transport theories.

1.2. TRADITIONAL METHODS TO CONTROL THERMAL CONDUCTIVITY

As demonstrated throughout this chapter, regardless of the physical state of the system under study or the specific mechanisms governing heat conduction, *Eq. 1.5* provides a general framework for describing thermal conductivity. According to this expression, thermal conductivity is determined by three key parameters: the heat capacity, the mean free path of the energy carriers, and their propagation speed. Consequently, any strategy aimed at modulating heat transport must ultimately influence one or more of these parameters. Indeed, various strategies have been developed to this end, some of which are briefly reviewed in this section.

Among these, the most common –and probably the most accessible– approach for tuning thermal conductivity in crystalline solids relies on modifying the phonon mean free path by introducing additional phonon scattering mechanisms, such as point defect or boundary scattering.

Historically, the introduction of point defects into bulk crystals was one of the earliest methods explored for reducing thermal conductivity. For instance, in the 1960s, Walker *et al.* (*17*) investigated the thermal conductivity of KCl crystals containing controlled amounts of KI, NaCl or $CaCl_2$. These substitutional impurities disrupted the lattice periodicity, significantly reducing the thermal conductivity. Similarly, Slack and collaborators (*34*) synthesized CdTe crystals doped with 1 mol% of Mn, Fe or ZnTe, thus promoting point-defect phonon scattering, as illustrated in **Figure 1.4**a. Additionally, in the cases of Mn and Fe doping, magnetic scattering also contributed to thermal resistance, although this mechanism is beyond the scope of this thesis.

In a related approach, Asen-Palmer *et al.* (*35*) demonstrated that the thermal conductivity of Ge crystals can be tuned by systematically varying their isotopic composition (**Figure 1.4**b). Increasing isotopic purity reduces mass variance and therefore phonon scattering, resulting in higher thermal conductivity; conversely, introducing isotropic disorder enhances scattering and reduces the mean free path (*Eq. 1.14*).

More recently, the introduction of atomic-scale impurities has become a central strategy for tailoring thermal conductivity in thermoelectric materials, where achieving a high thermoelectric figure of merit requires simultaneously maximizing electrical conductivity while minimizing thermal conductivity. One of the most effective strategies in this context is alloying

(*36*), which serves a dual purpose: p-type or n-type dopants are introduced to enhance carrier concentration and, consequently, electrical conductivity, while the mass and bond disorder generated increase phonon scattering, particularly for high frequency modes. A classic example is the Si-Ge alloy system, where the disordered lattice effectively suppresses phonon transport without significantly compromising electronic properties due to the similar band structures of Si and Ge (*37*).

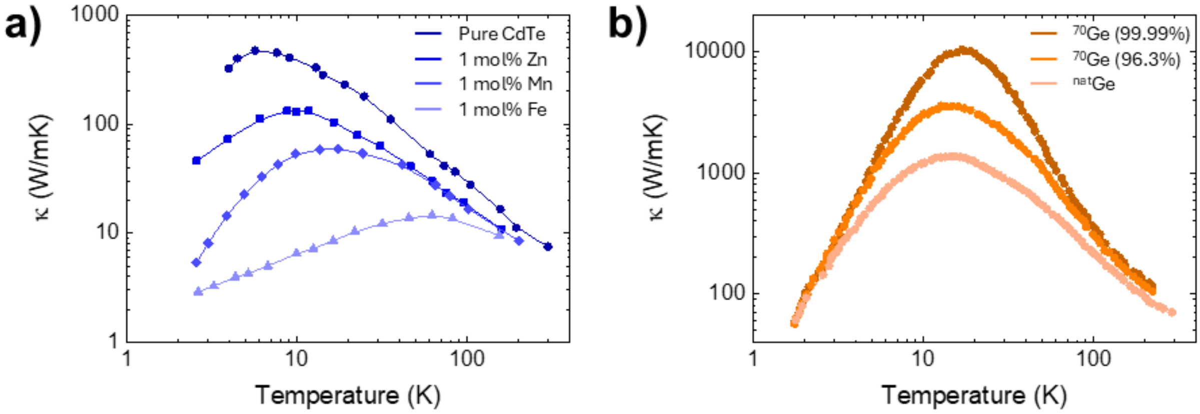

Figure 1.4. a) Temperature-dependent thermal conductivity of CdTe crystals doped with ≈1 mol% of Zn, Mn and Fe, compared to pure CdTe. Data extracted from Slack *et al.* (*34*). b) Temperature-dependent thermal conductivity of Ge crystals with varying isotopic compositions, including a sample with the naturally occurring mixture of five isotopes (^{nat}Ge). Data from Asen-Palmer *et al.*(*35*).

However, as previously demonstrated in **Figure 1.2**d, atomic-scale defects primarily scatter high-frequency (short-wavelength) phonons, while low- and mid-frequency phonons, which carry a substantial portion of heat in many materials, are less affected and continue to contribute to thermal transport. To address this limitation, the concept of "nanoparticles-in-alloy" was developed. In this approach, nanometer-sized precipitates or inclusions are embedded within the alloy matrix to act as additional boundary scattering centers, targeting mid- and long-wavelength phonons. This multiscale scattering approach enables a more complete suppression of phonon transport across the frequency spectrum (*38*, *39*).

Vacancies represent another effective class of point defects for disrupting phonon transport. In the particular case of oxides, oxygen vacancies are among the most prevalent and energetically favorable type of defects. These vacancies can form spontaneously during growth –specially under reducing atmospheres or oxygen-deficient conditions– or can be deliberately introduced through post-annealing treatment or electrochemical methods. For example, Luckyanova and coworkers (*40*) demonstrated that the thermal conductivity of $Pr_{0.1}Ce_{0.9}O_{2-x}$ thin films can be substantially reduced –by as much as 50%– by varying the oxygen partial pressure during post-growth annealing in a pulsed lased deposition (PLD) chamber. Similar reductions in thermal conductivity induced by oxygen vacancy engineering have been reported in other complex oxides (*41*, *42*), further confirming the effectiveness of this approach for thermal transport control.

Beyond oxygen non-stoichiometry, cation vacancies also play a significant role in governing the thermal conductivity of complex oxides (*43*). A particularly illustrative case is the study by Bugallo *et al.* (*44*), who systematically investigated the influence of Pb^{2+} and Ti^{4+} vacancies in $PbTiO_3$ thin films by employing a spread geometry during molecular beam epitaxy

(MBE) growth, which introduced a gradient in cation stoichiometry –from Ti-deficient (≈25%) samples to Pb-deficient (≈20%) films, as well as a compositionally stoichiometric reference.

Surprisingly, the stoichiometric $PbTiO_3$ film in this work, which was expected to contain the fewest point-defects, exhibited the lowest thermal conductivity. This counterintuitive result was attributed to the dominance of boundary scattering (see *Eq. 1.13*), arising from a dense network of ferroelectric domain walls. In contrast, the non-stoichiometric films exhibited stronger point-defect scattering, yet their thermal conductivities remained higher than that of the stoichiometric film. These results underscore a key insight: distinct scattering mechanisms can compete depending on the structural characteristics of the material. In non-stoichiometric $PbTiO_3$ films, point-defect scattering dominates due to lattice disruption from cation vacancies, while in stoichiometric films, domain-wall boundary scattering becomes the prevailing mechanism.

The importance of domain-wall scattering in ferroelectric thin films has been further supported by other studies (*45–47*), confirming its dominance when defect concentrations are low. In particular, Langenberg *et al.* (*48*) demonstrated that the periodicity and orientation of ferroelectric domain walls in $PbTiO_3$ thin films can be tuned by epitaxial strain, enabling thermal conductivity modulations of up to 60%. These results underscore the potential of ferroelectric domain walls as effective phonon-scattering centers, paving the way for the development of thermal switches based on ferroelectric materials, as they may be manipulated by external electric fields (*49*).

A similar boundary-scattering mechanism is observed in polycrystalline materials, where grain boundaries act as structural discontinuities that scatter phonons. These boundaries, formed at the interfaces between differently oriented crystalline domains, disrupt phonon propagation due to elastic mismatch, misorientation, and local structural disorder. As a result, grain boundary scattering can significantly reduce thermal conductivity, especially when the grain size is reduced to the nanoscale, where boundary density is high and phonons are more frequently scattered (*50*, *51*).

Building on the concept of interface-induced scattering, another widely employed strategy to control thermal conductivity is the introduction of artificial interfaces, such as those found in multilayer structures. Among these, superlattices –periodic stacks of alternating thin layers of two or more materials (**Figure 1.5**a)– have attracted particular attention due to their tunable thermal transport properties, especially when the thickness of each individual layer (denoted as L) is of the order of the phonon mean free path. These structures introduce a dense network of interfaces that strongly interact with heat-carrying phonons. Interestingly, the efficiency of heat transport in such systems depends on whether phonons propagate as waves or behave more like classical particles.

To conceptualize this dual behavior, it is instructive to draw an analogy with X-ray diffraction. When X-rays pass through a well-ordered crystal, they are scattered by the periodic arrangement of atoms. If the wavelength of the incoming X-rays and the interplanar spacing satisfy Bragg's law, the scattered waves interfere constructively, producing sharp diffraction peaks. However, if the atomic structure is disordered or the spacing between planes is too large relative to the wavelength, this interference is lost, and the X-ray signal becomes diffuse.

A similar phenomenon arises in phonon transport through superlattices. When the layer period thickness L exceeds the phonon coherence length –the characteristic distance over which phonons maintain phase coherence–, phonons lose their phases between successive layers. In this incoherent regime, phonons behave like classical particles, scattering diffusely at each interface without retaining memory of their prior trajectory. This is analogous to X-rays interacting with amorphous materials, where no long-range interference occurs. In this case, the superlattice effectively behaves as a composite material where each interface acts as a scattering center, and the phonon mean free path becomes limited by the layer thickness due to enhanced boundary scattering (*Eq. 1.13*). This regime results is a notable reduction in thermal conductivity compared to the bulk, with further reductions observed as the period thickness is decreased, as widely reported in literature (*52–55*).

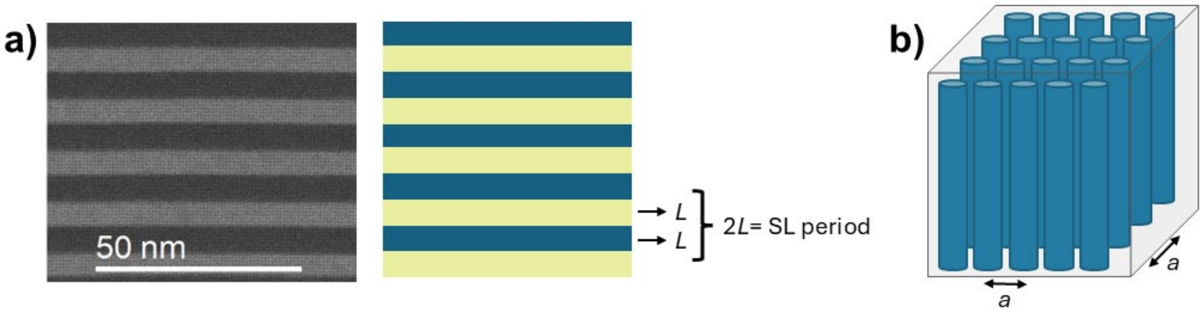

Figure 1.5. a) Transmission electron microscopy (TEM) image of a superlattice synthesized in this thesis (discussed in Chapter 6), composed of 5 repetitions of a bilayer with individual layer thickness *L*, resulting in a total period of 2*L*. The right panel shows a schematic representation of the corresponding multilayer structure. b) Schematic representation of a two-dimensional phononic crystal, consisting of a periodic array of cylindrical inclusions with lattice parameter *a*, designed to modulate phonon propagation through wave interference effects.

In contrast, when *L* is smaller than the phonon coherence length and the interfaces are atomically smooth, phonons can maintain phase coherence across multiple layers. In this coherent regime, the superlattice behaves as a homogeneous, periodic material, where the interfaces function as Bragg reflectors, modifying the phonon dispersion relation through effects like zone folding and the formation of phonon minibands. These changes alter the group velocity and density of states and can, in some cases, enhance thermal conductivity by facilitating the propagation of long-wavelength phonons (*56*, *57*). A notable example of this behavior was reported by Luckyanova *et al.* (*58*), who demonstrated that the thermal conductivity of GaAs/AlAs superlattices increased with the number of interfaces, a signature of coherent phonon transport. Similar effects have been reported in oxide superlattices as well (*59*).

Ultimately, the nature of phonon transport (coherent or incoherent) depends on the interplay between layer thickness, coherence length, interface quality, and phonon wavelength; by tuning these parameters, one can induce a transition between the coherent and incoherent transport regimes. Interestingly, this transition gives rise to a minimum at *L*, marking the boundary between the two regimes (*60*, *61*).

Beyond superlattices, coherent phonon transport has also been demonstrated in other highly periodic structures such as phononic crystals (PnCs). These materials consist of periodic arrays of inclusions with different elastic constants (**Figure 1.5**b) which induce phonon bandgaps, i.e. frequency ranges where phonon propagation is forbidden due to destructive interference (*62*, *63*). Furthermore, even outside the bandgap, the periodic modulation of elastic properties leads to a flattening of the phonon dispersion curves, resulting in a reduction of phonon group velocities which further suppress heat transport. As a result, phononic crystals have emerged as promising candidates for the design of ultra-low thermal conductivity materials (*64*, *65*).

In addition to structural periodicity, another effective strategy for modulating phonon dispersion and reducing thermal conductivity is the introduction of localized vibrational modes, commonly known as “rattling”. This mechanism is characteristic of materials with loosely bound heavy atoms confined within oversized atomic cages or lattice sites. These “rattler” atoms are weakly coupled to the surrounding lattice and therefore vibrate with large amplitude and low restoring forces, giving rise to localized, low-frequency optical phonon modes that can strongly interact with heat-carrying acoustic phonons. This interaction flattens the acoustic phonon branches and reduces the group velocity, also introducing resonant scattering across a broad frequency range (*66*, *67*). Importantly, this effect selectively targets phonons while preserving electronic transport, giving rise to the phonon-glass electron-crystal (PGEC) behavior –thermal transport resembling that of disordered (glassy) materials, coexisting with crystalline-like electrical conduction. This decoupling of thermal and electronic transport makes rattling an especially attractive mechanism for improving thermoelectric performance (*68*).

A paradigmatic example is provided by Christesen *et al.* (*69*)*,* who investigated the type-I clathrate $Ba_8Ga_{16}Ge_{30}$ using inelastic neutron scattering. In this system, Ba atoms are trapped inside oversized cages formed by the Ga/Ge network, and exhibit low-frequency, localized vibration. Their experiments revealed that phonon lifetimes remained significantly longer than expected, confirming that these rattlers, rather than inducing strong scattering, primarily reduce thermal conductivity by flattening the acoustic phonon branches and lowering their group velocities. These findings underscore the importance of rattling as a dispersion-engineering mechanism and highlight its role in achieving PGEC behavior in thermoelectric clathrates.

Finally, while most strategies focus on modulating phonon mean free path or group velocity, the heat capacity can also influence thermal conductivity, as indicated in *Eq. 1.5*. However, tuning the heat capacity of a material –particularly in crystalline solids– is considerably difficult, since it is primarily dictated by atomic mass and bonding strength, which are not easily altered without fundamentally changing the material. In contrast, liquids and amorphous solids, due to their lack of long-range order, offer greater flexibility in tailoring the heat capacity. Intermolecular interactions such as hydrogen bonding, van der Waals forces, or ionic coordination can introduce new vibrational modes or shift the population of existing ones, thereby influencing how much thermal energy the system can store per unit temperature. For example, López-Bueno *et al.* (*70*) showed that adding small concentrations of short-chain alcohols to water enhances the hydrogen bonding network and increases thermal conductivity.

In summary, this section has reviewed a variety of strategies for tuning thermal conductivity by targeting the three key parameters identified in *Eq. 1.5*: heat capacity, phonon mean free path, and group velocity. These methods –summarized in **Table 1.2**– have enabled significant advances in the design of materials with tailored thermal transport properties. However, it is important to emphasize that all the strategies discussed so far produce passive changes in thermal conductivity: once the structural or chemical modification is introduced, the thermal properties of the material are permanently altered and cannot be reversed.

Table 1.2. Summary of the strategies reviewed in this section for controlling thermal conductivity, classified according to the parameter in *Eq. 1.5* being affected: phonon mean free path (λ), group velocity (*v*), or heat capacity (C_v).

Parameter	Strategy
λ	-**Introduction of defects** (impurities, isotopes, alloying, vacancies). -**Addition of interfaces** (ferroelectric domain walls, gran boundaries, superlattices in incoherent transport regime).
v	-**Modification of phonon spectrum** (superlattices and phononic crystals in coherent transport regime, rattling).
C_v	-**Modification of intermolecular forces** (in liquids).

In the next section, we will explore an emerging class of approaches aimed at achieving active modulation of thermal conductivity, a key step toward the realization of thermal switching technologies.

1.3. ACTIVE CONTROL OF THERMAL CONDUCTIVITY

Among the most promising and ambitious strategies for dynamically controlling heat flow is the development of thermal switches: materials or devices capable of actively modulating thermal conductivity between two or more different states in response to external stimuli such as light, temperature, electric fields, etc. (**Figure 1.6**). In contrast to passive thermal management approaches, thermal switches offer reversible, on-demand control over thermal transport properties, opening new possibilities for adaptive heat regulation in advanced technologies.

To be viable for practical implementation, a thermal switch must satisfy several essential requirements (*71*):

- A high ON/OFF ratio, ensuring a pronounced contrast between its high- and low-conductivity states.
- Full reversibility, allowing the system to return to its original state without degradation.
- Fast response time, typically of the order of seconds or less.
- High endurance and cycling stability, enabling repeated operation without mechanical fatigue, functional loss, or chemical degradation.
- Environmental robustness, ensuring stable functionality under a broad range of conditions (e.g., ambient atmosphere, vacuum, variable humidity, etc.).

Meeting all these criteria is challenging, particularly in the case of solid dielectric materials, as phonons present broad spectral distributions and, lacking both charge and magnetic moment, exhibit only weak interactions with external fields.

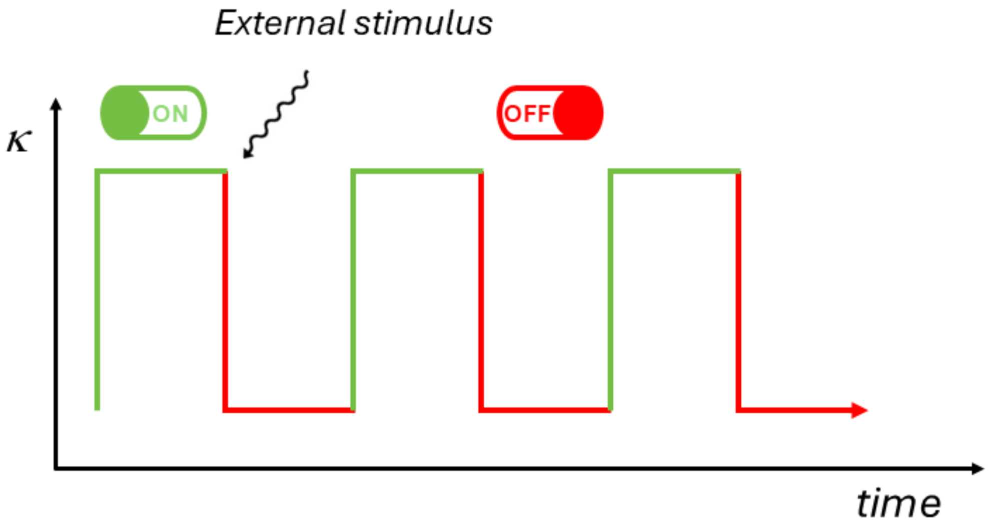

Figure 1.6. Schematic representation of a thermal switch operating under external control. The thermal conductivity (κ) alternates between a high-conductivity "ON" state (green) and a low-conductivity "OFF" state (red) in response to an external stimulus (e.g., electric field, light, mechanical strain, etc.). The process is reversible and repeatable over time, enabling dynamic modulation of heat transport.

Despite these difficulties, several strategies have been explored in recent years to achieve active control of thermal conductivity. Among them, one of the earliest and most extensively studied approaches involves the use of phase-change materials (PCMs), which exhibit reversible phase transitions between different structural or electronic states in response to external stimuli (*72*). These transitions are usually accompanied by the absorption/release of latent heat and abrupt changes in materials properties, such as thermal conductivity, making them promising candidates for thermal switching applications. A canonical example is VO_2, which undergoes a thermally induced metal-to-insulator transition at approximately 340 K. This phase transition leads to modifications in both electronic and lattice structures, leading to a pronounced change in thermal conductivity with an ON/OFF ratio of ≈2.5 (*73*).

Similar thermally-activated behavior has been observed in liquid systems. For instance, López-Bueno *et al.* (*74*) demonstrated that imidazole-based ionic liquids can undergo reversible transitions to either crystalline or glassy states by tuning the relative contribution of Coulomb and hydrogen bonding interactions, resulting in thermal conductivity changes of the order of ≈35% (**Figure 1.7**a). Likewise, Zeng and colleagues (*75*) explored liquid-solid transitions in liquid suspensions such as graphite-in-hexadecane, reporting thermal conductivity reductions of up to 66% during melting/freezing cycles (**Figure 1.7**b), depending on particle concentration.

However, while these examples demonstrate the feasibility of dynamic thermal control through phase transitions, they also reveal an inherent limitation: the modulation of thermal conductivity is confined to a narrow temperature range, in the vicinity of the phase transition, as illustrated by the shaded regions in **Figure 1.7**. This restricted operating window poses a major constraint for applications requiring broader or ambient-condition functionality. For this reason, research efforts have increasingly focused on non-thermal stimuli alternatives.

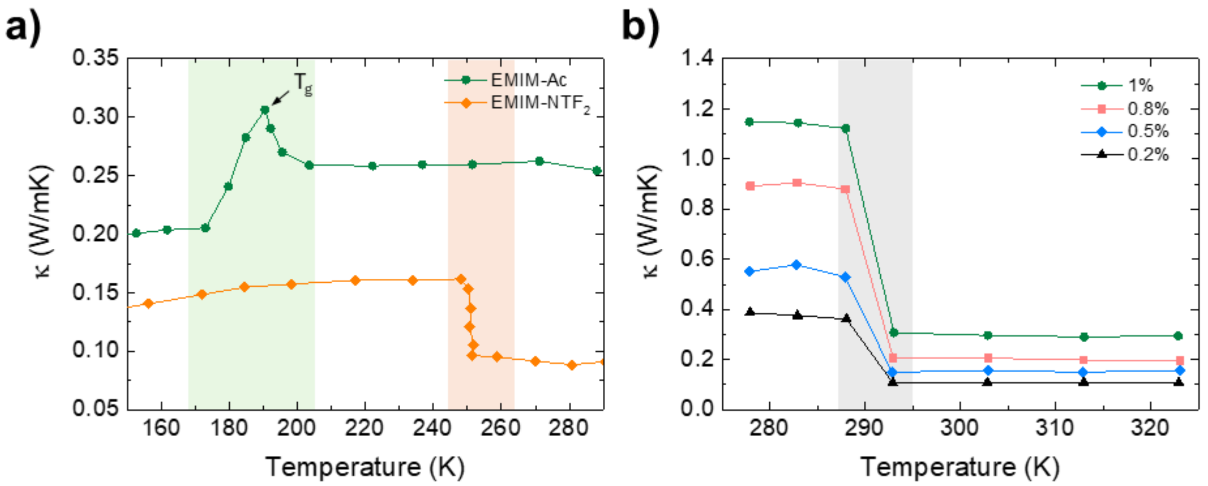

Figure 1.7. a) Temperature-dependent thermal conductivity of 1-ethyl-3-methylimidazolium acetate (EMIM-Ac, green) and 1-ethyl-3-methylimidazolium bis(trifluoromethylsulfonyl)imide (EMIM-NTF$_2$, orange) ionic liquids across the solid/glass-to-liquid transition. Data obtained from López-Bueno *et al.* (*74*). b) Temperature-dependent thermal conductivity across the liquid-solid transition of liquid suspensions with different graphite volume fractions. Data extracted from Zheng *et al.* (*75*). In these systems, the phase transition results in a pronounced change in thermal conductivity, but this modulation is restricted to a narrow temperature window, indicated by the colored shaded areas.

One particularly promising direction involves the use of interfacial engineering, where changes in interfacial coupling between adjacent nanostructures are exploited to dynamically control heat flow. In a notable study, Yang and coworkers (*76*) demonstrated that the thermal conductivity of boron nanoribbons can be reversibly modulated by controlling the wetting state at their interfaces. When an ethanol/water mixture was applied, it effectively welded the ribbons together, enhancing van der Waals interactions and allowing phonons to efficiently transmit across the interfaces, resulting in a high thermal conductivity ON state. Conversely, replacing the solvent with isopropyl alcohol left residual deposits upon evaporation that acted as spacers, decoupling the ribbons and suppressing phonon transport across the interfaces, thereby producing a low thermal conductivity OFF state.

This concept of controlling interfacial coupling introduces a powerful paradigm: by modifying the physical contact or mechanical interaction between structural units –without changing their intrinsic composition– one can dynamically reconfigure the thermal transport pathways in a material system. This principle naturally extends to mechanical stimuli, such as pressure and strain, which offer an additional degree of control over phonon dynamics.

An interesting example is provided by bulk MoS$_2$, a layered transition-metal dichalcogenide characterized by weak van der Waals interactions between adjacent layers, just like the previously discussed boron nanoribbons. Owing to this structural characteristic, MoS$_2$ exhibits exceptional tunability of cross-plane thermal conductivity under mechanical strain. Using a diamond anvil cell, researchers have demonstrated that the application of mild compressive stress can increase the out-of-plane thermal conductivity from 3.5 to about 25 W/mK –nearly a sevenfold enhancement (*77*). This dramatic change is attributed to both strain-enhanced interlayer coupling and significant modifications in the phonon band structure.

Comparable effects have been predicted and experimentally observed in highly porous materials (*78*, *79*), such as graphene-based composite foams. These systems not only exhibit substantial increases in thermal conductivity under mechanical compressions (ON/OFF ratio ≈8) but also allow for the stabilization of multiple intermediate states, enabling continuous and wide-range tuning of heat transport. However, despite these promising attributes, pressure-induced switching mechanisms present practical drawbacks: the requirement for mechanical actuation, often via complex setups, complicates integration into scalable, energy-efficient thermal devices.

Mechanical strain has also been explored as a route to modulate thermal conductivity in ferroelectric materials, as it determines the periodicity and configuration of ferroelectric domain walls (*80*). However, dynamic control of thermal transport via strain remains elusive in practice, as most strain in thin films is imposed statically by the substrate, hindering real-time tunability (*45*, *48*). Instead, the most effective strategy to actively modulate thermal conductivity in these systems exploits the electric-field control of ferroelastic domain walls, which can be reconfigured without mechanical deformation.

For example, Ihlefeld *et al.* (*81*) demonstrated electric-field induced modulation of thermal conductivity in polycrystalline $PbZr_xTi_{1-x}O_3$ (PZT) bilayers. By applying 10 V, they increased the density of domain walls, which act as phonon scattering centers, leading to an instantaneous reduction in thermal conductivity at room temperature. This switching occurred on a sub-second scale (<300 ms), indicating potential for fast thermal regulation. However, partial irreversibility was observed, with the thermal conductivity remaining ≈2.7% below its original value after the field was removed. Additionally, the ON/OFF ratio achieved was modest, of the order of 1.15.

Interestingly, when the same research group applied the same methodology to strain-released PZT membranes (*82*), a different response was observed: the application of an electric field reduced the domain wall density, leading to an increase in thermal conductivity. This contrasting behavior was attributed to the absence of mechanical clamping by the substrate, which allowed domains to increase in size and thereby reduce phonon scattering at domain walls. Nonetheless, the ON/OFF ratio remained similar, within experimental uncertainty.

In the case of antiferroelectric materials –where adjacent dipoles are aligned in antiparallel configurations, resulting in no net macroscopic polarization–, the response to electric-fields is more complex and is still under active investigation. Aryana and collaborators (*83*) reported that applying an electric field to $PbZrO_3$ induces an antiferroelectric-to-ferroelectric phase transition, which is accompanied by the formation of ferroelectric domains. These structural features act as additional phonon scattering centers, leading to a reduction in thermal conductivity.

In contrast, Liu and coworkers (*84*) observed the opposite trend in the same material: the application of an electric field resulted in a notable increase in thermal conductivity. This enhancement was attributed to a significant reduction in the unit cell volume during the antiferroelectric-ferroelectric phase transition, which altered the phonon-phonon scattering phase space thereby increasing phonon lifetimes and mean free paths. Their findings suggest that phonon-boundary scattering by ferroelectric domain walls plays a negligible role in governing thermal conductivity, which is primarily determined by volume-dependent phonon interactions. Using this mechanism, an ON/OFF ratio of ≈2.2 was achieved, nearly twice the one reported by Aryana under similar conditions. The origin of these different behaviors in $PbZrO_3$ thin films remains unclear, but likely arises from differences in microstructure, defect chemistry or strain state. However, these contrasting results underscore the complex interplay between microstructure, defect chemistry, and strain state in determining the thermal response of ferroic materials. Additionally, they highlight another important issue that will be discussed during this thesis: the extreme difficulty of obtaining reliable and accurate thermal conductivity measurements in nanostructures.

Yet, while ferroelectric and antiferroelectric systems offer fast response times and solid-state integration, their relatively limited ON/OFF ratios and dependence on crystallographic domain reconfiguration constrain the magnitude and range of achievable thermal modulation. In search of greater tunability and more chemically versatile platforms, researchers have increasingly turned to electrochemical methods as an alternative strategy to dynamically reconfigure heat transport in functional materials.

In electrochemically tunable systems, an external voltage is used to drive the insertion/extraction of mobile ions (such as H^+, Li^+, or O^{2-}) into a host lattice. This process leads to reversible changes in crystal structure, defect concentration, and unit cell volume, all of which significantly impact phonon dispersion and scattering mechanisms. Crucially, since this approach does not depend on intrinsic ferroic order or domain structure, it can be implemented across a wider variety of materials.

For instance, Cho and collaborators (*85*) demonstrated electrochemical modulation of thermal conductivity in $LiCoO_2$, a prototypical cathode material in lithium-ion batteries. Using liquid-electrolyte gating, they showed that the thermal conductivity of $LiCoO_2$ films could be reversibly tuned by controlling the lithium content: delithiation to $Li_{0.6}CoO_2$ reduced thermal conductivity from approximately 5.4 to 3.7 W/mK, yielding an ON/OFF ratio of ≈1.5. This reduction was attributed to enhanced phonon scattering associated with lithium vacancy formation and possible structural rearrangements.

Building on this concept, Sood *et al.* (*86*) extended this approach to two-dimensional layered materials, demonstrating an electrochemical thermal transistor based on lithium intercalation in MoS_2 thin films. The authors reported that Li^+ insertion induced stacking disorder, c-axis strain, and the emergence of low-frequency rattling modes, all of which significantly increase phonon scattering. This process enabled reversible modulation of thermal conductance by nearly an order of magnitude (ON/OFF ratio ≈10), which is among the highest reported values for solid-state systems. However, the full switching cycle required approximately 14 minutes to complete, which is too slow for most practical applications. Moreover, the use of liquid electrolytes increases integration challenges, including issues such as electrolyte leakage.

To address these limitations, researchers have explored solid-state electrochemical platforms as a more robust and scalable alternative, particularly through the reversible manipulation of oxygen vacancy concentrations. For example, Bian *et al.* (*87*) presented solid-state electrochemical thermal transistors based on $SrCo_{1-x}Fe_xO_y$ compounds, where thermal conductivity can be modulated by electrochemically driven oxygen stoichiometry changes without involving volatile liquid electrolytes or mechanical actuation. In the oxidized ON-state (y= 3), the materials adopt the perovskite structure and exhibit relatively high thermal conductivities, with values reaching ≈3.8 W/mK for $SrCoO_3$ (x= 0), including both lattice and electronic contributions. Upon reduction to the OFF-state (y= 2), the films transition to either defect perovskite or infinite layer structures, depending on x composition. These phases are more disordered and electrically insulating (κ_e= 0), thus presenting significantly lower thermal conductivities (≈1–1.2 W/mK) due to increased phonon scattering and loss of electronic transport channels.

The results demonstrate that the thermal conductivity of these oxides is strongly correlated with oxygen stoichiometry-induced structural phase transformations, leading to an ON/OFF ratio ≈4. However, the methodology presents some practical limitations, such as the requirement for elevated temperatures (≈280 °C) to ensure sufficient oxygen mobility. Moreover, the authors did not report detailed information regarding switching speed or long-term cyclability, both of which are essential for real-world thermal management applications.

Altogether, the wide array of strategies reviewed in this section illustrates the substantial progress made toward the realization of active thermal switches. Each approach offers unique advantages in terms of switching speed, thermal contrast, structural compatibility, or operational temperature range. However, no single method reported to date simultaneously fulfills all the critical requirements for practical implementation. As a result, despite the rapid advances and technological promise, the development of an ideal thermal switch remains an open challenge. Continued interdisciplinary research –combining materials design, nanoscale engineering, and device integration– is essential to overcome these limitations and unlock the full potential of active thermal management in next-generation electronic, thermoelectric, and energy systems

1.4. OBJECTIVES

As discussed in the previous sections, the general objective of this thesis is to contribute to the development of a thermal switch by synthesizing and characterizing materials capable of reversibly accessing distinct thermal conductivity states, with large thermal contrast among them, in response to external stimuli. To achieve this, four different strategies have been explored throughout this thesis, each targeting heat transport modulation through different physical mechanisms and material systems. These strategies, detailed in Chapters 3 to 6, encompass distinct experimental approaches and are guided by specific objectives, summarized below:

Chapter 3: Light-induced thermal conductivity switching in mesophases.

- Synthesize and characterize photoresponsive mesophases based on azobenzene derivatives with varying alkyl chain lengths, capable of undergoing reversible *trans-cis* isomerization upon UV/Vis illumination.
- Evaluate the effect of light-induced isomerization on the thermal conductivity of these mesophases.
- Optimize the molecular composition and mesoscale morphology to enhance the ON/OFF thermal conductivity ratio and switching speed upon illumination.
- Investigate the potential of azobenzene derivatives as photoactive dopants for enabling light-triggered, reversible thermal modulation in non-photoresponsive host materials.

Chapter 4: Topotactic oxidations for thermal modulation in oxides.

- Investigate the reversibility of brownmillerite-to-perovskite topotactic transformations in negative charge-transfer oxides, using conventional structural characterization techniques such as X-ray diffraction or transmission electron microscopy.
- Compare different oxidation pathways for O^{2-} insertion –liquid phase, gas phase and solid-state electrochemical oxidation– and evaluate their efficiency, structural defects and suitability for reversible phase switching.
- Measure the thermal conductivity of the different phases, employing it as a complementary probe of phase evolution and transformation reversibility.
- Correlate the changes in thermal transport with structural and compositional evolution across the different oxidation pathways.
- Evaluate the viability of using these topotactic transformations as a functional mechanism for thermal switching applications.

Chapter 5: Electric-field driven thermal tuning in charge-transfer oxides.

- Investigate the use of localized electric fields, applied via a voltage-biased atomic force microscopy tip, to induce controlled accumulation of oxygen vacancies in charge-transfer oxides.
- Evaluate the impact of vacancy accumulation on the local thermal conductivity of the material.
- Optimize the chemical composition of the oxides to enable the formation of stable, non-volatile thermal states with a high ON/OFF thermal conductivity ratio, and develop protocols for both vacancy writing and erasure.
- Acquire high-resolution thermal conductivity maps of electrically modified regions using frequency domain thermoreflectance (FDTR), to evaluate the spatial precision and thermal contrast achievable at the nanoscale.
- Examine the potential of this approach for the implementation of reconfigurable thermal circuits or thermal memory elements.

Chapter 6: Thermal transport in superlattices: effect of polar structures.

- Synthesize epitaxial $PbTiO_3/SrTiO_3$ superlattices with varying periodicities, total thickness and epitaxial strain to promote the formation of emergent polar structures, such as vortices and skyrmions.
- Characterize the formation, spatial arrangement, and evolution of these polar structures with temperature using different structural characterization techniques.
- Measure the thermal conductivity of the superlattices and evaluate the influence of the type, density and configuration of polar structures on phonon transport.
- Modulate the polar structures with temperature, exploring temperature-driven phase transitions as a means to reversibly control thermal conductivity.

2. METHODOLOGY

> *“Most innovative things are not obvious to other people at the time. You have to believe in yourself. If you’ve got a good idea, follow it even though others tell you it’s not.”*
>
> ---
>
> Frances Arnold, Nobel Prize in Chemistry (2018) for the directed evolution of enzymes.

The ultimate goal of this thesis is to study the suitability of different materials to work as thermal switches: materials whose thermal conductivity can be controlled by the application of an external stimulus. To achieve this, we investigated strategies for tuning thermal transport in soft-mesophases of azobenzene derivatives (Chapter 3), complex oxide thin films (Chapters 4 and 5) and oxide superlattices (Chapter 6).

In this chapter, we provide a concise description of the synthetic procedures employed for the preparation of the samples used in these studies. Given the different nature of the materials, the methodology includes tasks typical of traditional chemical synthesis as well as the use of advanced physical vapor deposition techniques. Additionally, we offer an overview of the fundamental principles behind the main experimental techniques utilized in this work. Lastly, given their relevance for the discussion of the results, we describe the two methods used for measuring thermal conductivity: the 3ω method and frequency domain thermoreflectance (FDTR).

2.1. SYNTHETIC PROCEDURES

2.1.1. Synthesis of azobenzene derivatives

In Chapter 3, we report the light-induced modulation of thermal conductivity in a series of 4,4’-dialkyloxy-3-methylazobenzene derivatives, with alkyl chain lengths, -OR= $-OC_nH_{2n+1}$, n= 3, 5, 6, 8, 10 and 14. The synthesis of these azobenzene derivatives was carried out following a multi-step process, based on a previously established route (*88*, *89*).

The process begins with the formation of the precursor 4,4’-dihydroxy-3-methylazobenzene (**Figure 2.1**a). This step involves the generation of the diazonium ion, an electrophilic intermediate, which undergoes an electrophilic aromatic substitution with *o*-cresol. The coupling reaction is driven by the electron-donating hydroxyl group on the *o*-cresol, which increases its nucleophilicity, leading to efficient product formation.

To synthesize the dialkyloxy derivatives, 4,4’-dihydroxy-3-methylazobenzene is then reacted with alkyl bromides of varying chain lengths, under basic conditions. Potassium carbonate acts as a base, deprotonating the hydroxyl groups to form phenoxide ions, which then undergo nucleophilic substitution with the alkyl bromides via an S_N2 mechanism, resulting in the ether bonds that define the dialkyloxy structure (**Figure 2.1**b). A catalytic amount of potassium iodide is added to enhance the reaction rate by temporarily forming more reactive alkyl iodide intermediates, thereby increasing the overall efficiency of the etherification process.

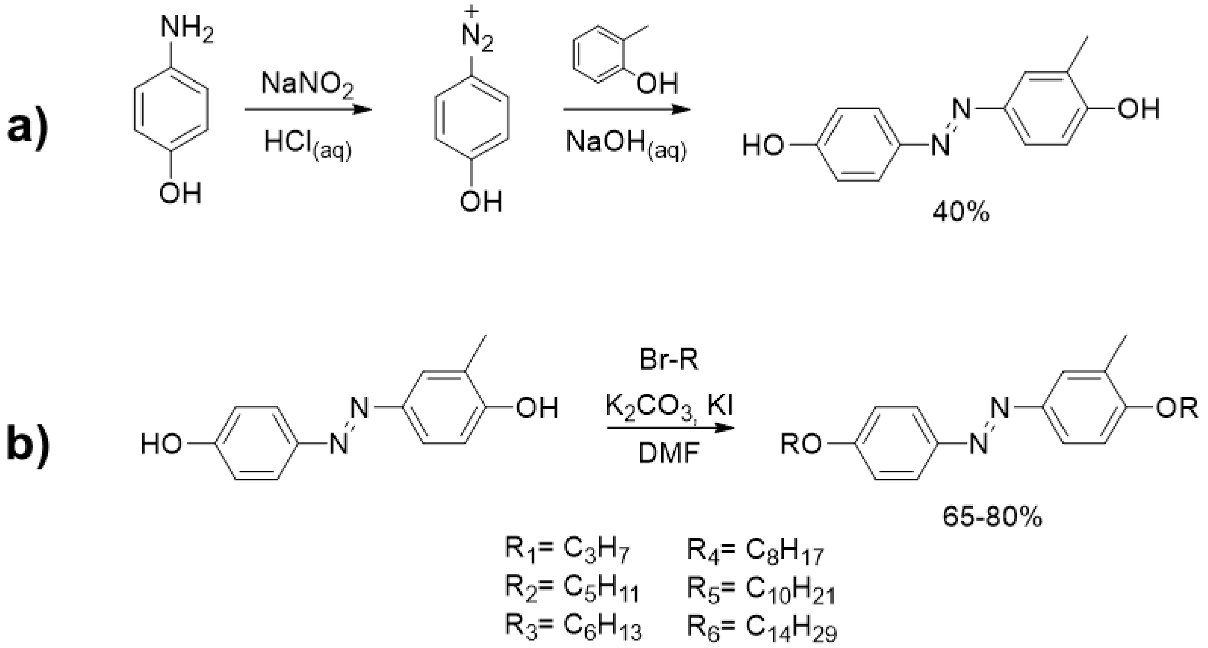

Figure 2.1. Synthesis of 4,4’-dialkyloxy-3-methylazobenzene derivatives. The first step of the reaction consists of the synthesis of the unsubstituted azobenzene core (a), followed by its alkylation with alkyl bromides of different chain lengths (b).

The complete experimental procedure followed for the synthesis and purification of each compound, along with the structural characterization through ^{1}H-NMR, are provided in the Annex I to the thesis.

2.1.2. Deposition of oxide thin films

In Chapters 4 and 5 we explore the modulation of thermal conductivity in epitaxial thin films of perovskite oxides ($CaFeO_3$, $SrFeO_3$, $La_{0.6}Sr_{0.4}CoO_3$, $La_{0.7}Sr_{0.3}MnO_3$) which were grown by pulsed laser deposition (PLD). On the other hand, in Chapter 6 we describe the measurement and tuning of thermal conductivity in epitaxial $PbTiO_3/SrTiO_3$ superlattices. This last study has been done in collaboration with Prof. Chang-Beom Eom from University of Wisconsin-Madison, using samples prepared by magneton sputtering during a 3-month research stay that I performed at his laboratory.

Both PLD and sputtering are physical vapor deposition techniques where atoms or clusters of a material are evaporated from a target, being then subsequently deposited onto the desired substrate. However, they differ in several aspects, including the method used for evaporating the starting material. Next, we provide a brief description of each of these techniques, highlighting their main strengths and weaknesses in the context of our project.

2.1.2.1. Pulsed laser deposition

Pulsed laser deposition is one of the simplest and most versatile physical vapor deposition techniques, contributing to its widespread use and applicability. The process is conducted inside a vacuum chamber containing a solid target (normally with the stoichiometric composition of the desired film,) and a substrate (in our case, a single-crystal oxide), as depicted in **Figure 2.2** (*90*).

A pulsed laser beam is focused onto the target; at sufficiently high energy densities, each laser pulse ablates a small portion of the target material, creating a highly directed plasma plume (see **Figure 2.2**a) that transfers the material into the substrate. The temperature of the substrate can be controlled in most systems, typically between 600 ºC and 1000 ºC at least, thus allowing the incoming atoms to rearrange and adapt to the crystalline structure of the substrate, promoting epitaxial growth (*91*). However, since the plasma plume trajectory is highly concentrated, it can lead to uneven deposition over large areas, making conventional PLD unsuitable for thin film growth over large substrates. To mitigate this problem, substrates of maximum 5 x 5 mm^2 are used in our experiments, and both the target and substrate are simultaneously rotated during deposition to ensure the uniform ablation of the target surface and uniform growth on the substrate (*92*).

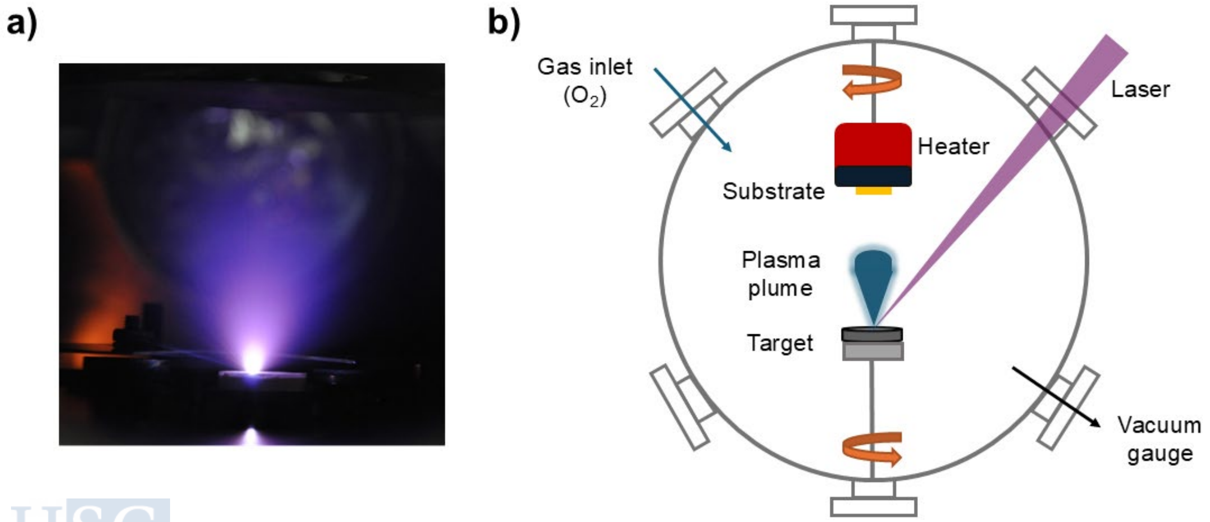

Figure 2.2. a) Photograph of the PLD system used in this work during deposition. The image was captured when the laser beam hits the ceramic target, creating a high-energy plasma plume. b) Schematic representation of the PLD chamber used in this thesis.

In PLD, a background gas is often employed to facilitate film formation. Reactive gases such as molecular oxygen (for the deposition of oxides) or ammonia/nitrous oxide (for nitrides) can actively participate in the chemistry of the film, enabling multication thin film growth. In these cases, the target provides the desired stoichiometry of the cations in the final structure, while the stoichiometry of the anion (O^{2-}, N^{3-}, etc.) is determined by the partial pressure of the reactive gas. In addition to participating in the structure of the resulting film, these gases also reduce the kinetic energies of the ablated species, thus improving film quality (*91*).

There are several features that make PLD particularly attractive for the deposition of complex materials, including the aforementioned possibility of using reactive gases during growth, the wide range of background pressures admitted (from ultra-high vacuum to 1 Torr) and its compatibility with chemically complex targets. However, among all of them, the most significant advantage offered by PLD is its ability to realize stoichiometric transfer from multication targets to the substrate. This arises from the nonequilibrium nature of the ablation process when high laser energy densities are absorbed by a small volume of material. For example, at low laser fluences (i.e., energy delivered per area) the laser simply heats the target, and material is ejected due to the thermal evaporation of target species, which is in turn determined by the vapor pressures of their constituents. Conversely, at high laser fluences – when the ablation threshold of the target species is surpassed–, energy absorption by the ejected species leads to plasma formation at the target surface. By precisely selecting the ablation wavelength and absorbing target material, this localized energy absorption vaporizes the target without being limited by the constituents' vapor pressures, ensuring stoichiometric transfer to the substrate (*91*).

Despite these advantages, it is important to note that producing high-quality films with PLD requires the careful optimization of several parameters, such as laser wavelength, pulse frequency, laser fluence, growth atmosphere and pressure, substrate type, target composition and surface quality, and target-to-substrate distance. This flexibility, while beneficial, poses a significant challenge as each material demands rigorous optimization of these parameters, especially when the growth conditions were not previously reported in literature (*90*).

In this thesis, we deposited several transition-metal oxoperovskites using PLD, thus requiring the addition of molecular oxygen into the vacuum chamber during growth. The ceramic targets used contained the desired stoichiometric proportion of the cations in the final structure and were fabricated in our laboratory. The oxygen content in the perovskite was controlled through the oxygen partial pressure inside the chamber. For all depositions, we used a frequency-quadrupled Nd:YAG laser with a wavelength of 266 nm and a maximum pulse energy of 100 mJ. All the samples discussed in Chapters 4 and 5 were synthesized with a laser repetition rate of 5 Hz and target-to-substrate vertical distance of approximately ≈8 cm. To ensure uniform ablation, the target was rotated at 91°/s with a horizontal raster of 47°/s. Simultaneously, the substrate rotated at 51°/s to promote homogeneous film deposition.

The remaining experimental conditions used for the thin film growth of each material (substrate temperature, laser fluence, oxygen partial pressure, etc.) were ex-situ optimized by X-ray diffraction and X-ray reflectivity, and the resulting values are provided in a dedicated section within the corresponding chapters.

2.1.2.2. Magnetron sputtering

The basic sputtering process relies on the production of a plasma through the electrical discharge and electrostatic acceleration of ions (usually Ar^+) towards the target material to be deposited, which acts as the cathode, inside a vacuum chamber. This bombardment process results in the transfer of momentum to the target atoms, which are ejected from the surface in the form of plasma and condensed on the substrate (anode), resulting in film formation. However, even though this process has been widely used to successfully deposit several materials, its applicability is limited by the low deposition rates and low ionization efficiency in the plasma. To address these challenges, magnetron sputtering was developed (*93*, *94*).

In magnetron sputtering, magnets are placed behind the cathode, as depicted in **Figure 2.3**a, generating a magnetic field that confines the secondary electrons from the plasma close to the target surface, while ions are hardly affected due to their higher atomic mass. Trapping electrons in this way prologues their residence time within the plasma, increasing the collisions between electrons and background gas and improving the ionization efficiency. This, in turn, leads to an increased ion bombardment of the target, giving higher sputtering and deposition rates, and large deposition areas. As a result, magnetron sputtering offers superior scalability compared to other physical vapor deposition techniques (such as PLD or molecular beam epitaxy), making it the preferred choice for industrial-scale applications (*93*, *95*).

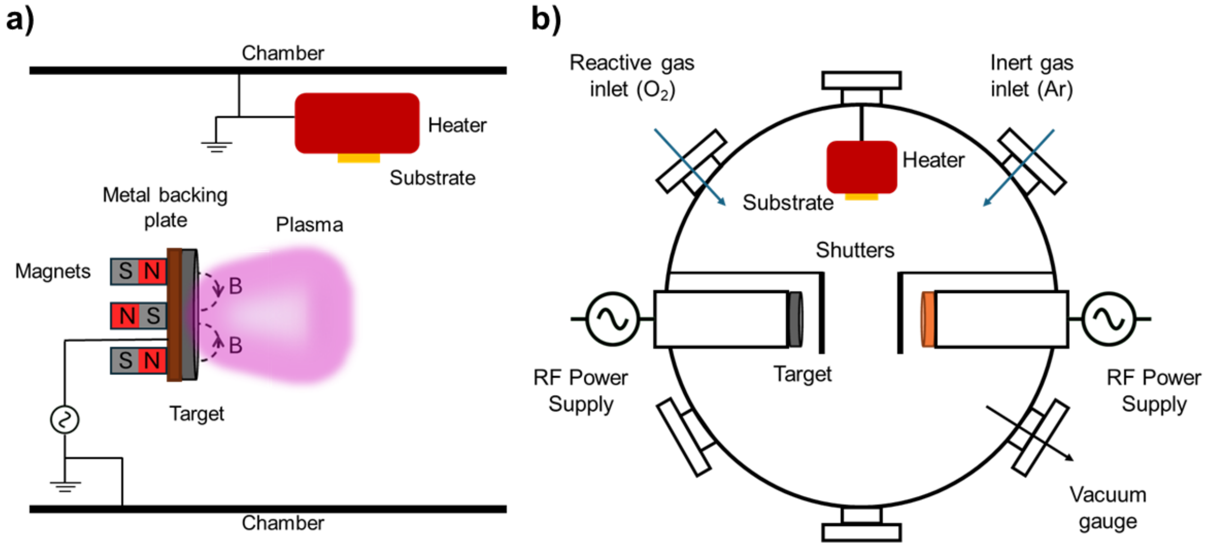

Figure 2.3. a) Diagram illustrating the sputtering guns employed in magnetron sputtering. b) Schematic representation of an RF magnetron sputtering chamber in off-axis configuration, based on the one used in this thesis.

This technique allows for the deposition of a wide range of materials, from metals to ceramics, by simply adjusting the target composition and the power supply generating the electric field. For conductive materials like metals, a DC bias is sufficient to ionize the background gas and accelerate ions toward the target for effective sputtering. However, this method is unsuitable for non-conductive materials since the continuous bombardment of insulating targets with positive ions leads to surface charging, creating a repulsive force that precludes the sputtering process. To overcome this, a radiofrequency (RF) power source is employed instead, which alternates the polarity of the cathode thus ensuring the effective sputtering of non-conductive materials.

Unlike PLD, magnetron sputtering does not provide stoichiometric transfer from the target to the substrate. Therefore, adjustments must be made to achieve the desired composition, especially when dealing with volatile elements or complex materials. For instance, when depositing materials containing volatile elements like Pb, it is necessary to use targets with an excess of these elements to compensate for their tendency to evaporate from the film during deposition. Similarly, when depositing oxides, O_2 must be injected into the sputtering chamber as reactive gas to fight the tendency of oxides to be oxygen deficient. The correct Ar:O_2 ratio depends on the material to be deposited and typically requires optimization, which is done by controlling the flow rates of both gases with mass flow controllers, ensuring precise regulation of the deposition atmosphere (*94*).

In this thesis, RF magnetron sputtering was used to synthesize superlattices of $PbTiO_3/SrTiO_3$, using ceramic targets of stoichiometric $SrTiO_3$ and $Pb_{1.2}TiO_3$ –with 20% excess of Pb–, and injecting O_2 as reactive gas with an Ar:O_2 ratio of 85%:15% (total pressure of 200 mTorr). The growth conditions used for the deposition of the different superlattices are detailed in Chapter 6, along with the optimized growth parameters of each material.

For the sequential growth of $SrTiO_3$ and $PbTiO_3$, two sputtering guns were simultaneously introduced in the sputtering chamber, using shutters to avoid cross-contamination of the targets. As illustrated in **Figure 2.3**b, these two guns are placed forming a 90 º angle with respect to the substrate, in an off-axis sputtering configuration initially proposed by Prof. Chang-Beom Eom (*96*). This configuration avoids re-sputtering, which occurs when high-energy atoms or ions re-emit from the deposited material due to ion bombardment, damaging the thin film. By positioning the guns at a 90 º angle, only thermalized atoms (those with lower energy and uniform distribution) reach the substrate surface, significantly improving thin film quality.

2.2. EXPERIMENTAL TECHNIQUES

2.2.1. X-ray techniques

Several X-ray based techniques have been used for the structural characterization of the samples used in this thesis, as they provide valuable information about their thickness, crystalline quality, orientation and epitaxial relation with the substrate in the case of thin films and superlattices.

All the experiments described in this thesis have been conducted with a high-resolution Malvern Panalytical Empyrean diffractometer, using Cu K-α radiation (wavelength of 1.5406 Å). This diffractometer allows the independent adjustment of four different angles, as depicted in **Figure 2.4**, whose configuration would depend on the type of measurement to be performed.

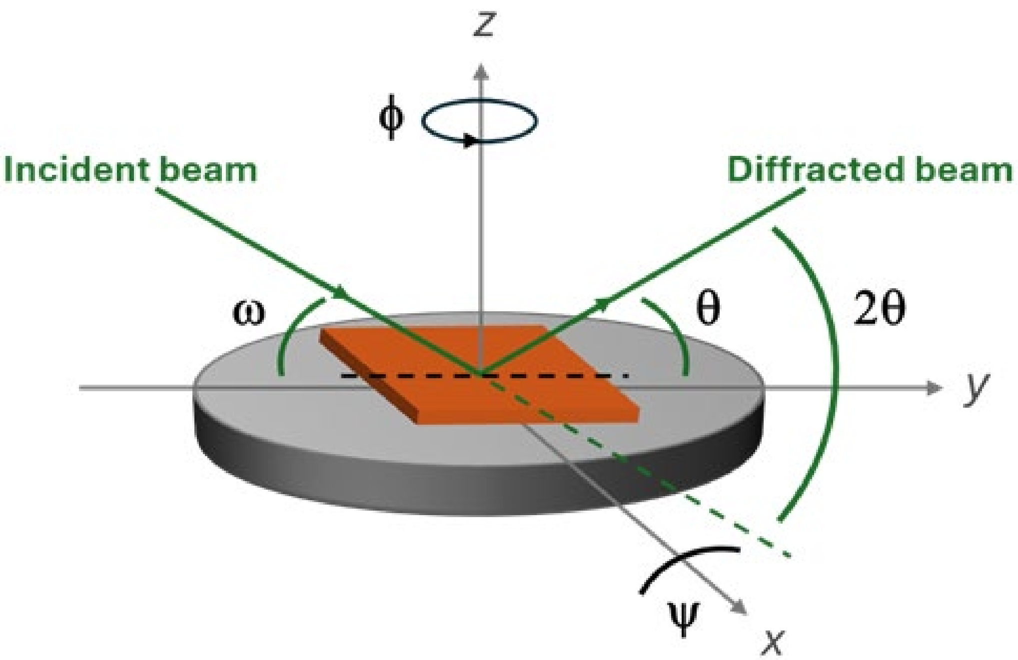

Figure 2.4. Schematic illustration of the four adjustable angles in the diffractometer used in this thesis: ω represents the angle between the incident X-ray beam and the sample surface, θ is the scattering angle between the sample surface and the detector, ϕ corresponds to the in-plane sample rotation, and ψ refers to the polar angle, indicating the tilt of the sample relative to the incident beam. Additionally, the x, y and z axes are shown, representing the horizontal and vertical displacements of the sample, which can be independently adjusted for precise positioning. In this scheme, ω and θ have the same values, corresponding to a symmetric reflection; however, this condition is not necessary.

2.2.1.1. X-ray reflectivity

X-ray reflectivity (XRR) is a structural characterization technique widely used to determine the thickness, roughness and density of thin films and multilayers. In this thesis, XRR has been primarily employed for ex-situ optimization of the growth rate of the materials deposited by PLD and sputtering, as well as for precise thickness determination of the resulting thin films and superlattices.

This technique is based on the reflection and scattering of the X-ray beams at low incident angles. To perform the XRR measurements, the diffractometer is configured in a symmetric ω/2θ geometry (as depicted in **Figure 2.4**), with the X-ray beam directed at grazing incidence angles (typically ranging from near zero to 2-3 º) (*97*).

Below a critical incidence angle (θ_c), which depends on the refraction index contrast between the thin film and substrate, the X-rays undergo total external reflection, meaning that they do not penetrate the material. As the angle increases beyond θ_c, the incident X-rays start penetrating the film, experiencing multiple reflections at the interfaces of the film. When the wavelength, the angle of incidence and the film thickness have some given relationship, there are some reinforcing interferences that lead to an increase in the intensity at particular angles. The result is the appearance of characteristic oscillations in the reflectivity curve, such as those observed in **Figure 2.5**a. These oscillations, known as Kiessig fringes or Kiessig oscillations, are the result of constructive and destructive interferences of the reflected X-rays, and provide valuable information about the film thickness (t). In particular, the periodicity of these fringes is inversely proportional to the thickness of the film, as defined by:

$$\theta_m^2 = \theta_c^2 + \left(\frac{\lambda}{2t}\right)^2 \cdot m^2 \qquad \textit{(Eq. 2.1)}$$

where m is the order of the oscillation, λ is the wavelength of the X-rays and t is the thickness of the layer (*98*).

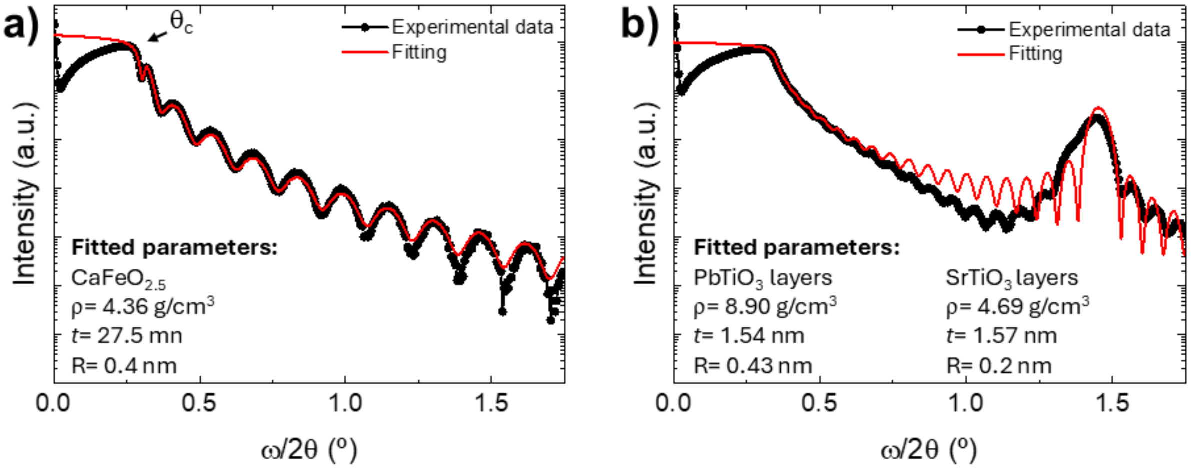

Figure 2.5. a) XRR curve of a $CaFeO_{2.5}$ thin film deposited on (001) $SrTiO_3$. The fitting of the experimental data (red curve) provides a film thickness of 27.5 nm, density of 4.36 g/cm^3 and surface roughness of 0.4 nm. b) XRR curve of a $SrTiO_3/PbTiO_3$ superlattice deposited on (110) $DyScO_3$, consisting of 20 repetitions with a nominal periodicity of 3.12 nm (corresponding to 1.56 nm per layer), and total thickness of 62.4 nm. The refined fit yields a superlattice periodicity of 3.11 nm, with total thickness of 62.20 nm.

In the case of multilayers (which will be studied in Chapter 6), constructive interferences from multiple reflections at the different interfaces will also take place. If these interfaces are equally separated (i.e., in the case of a superlattice), a series of additional maxima appears in the reflectivity curve, as observed in **Figure 2.5**b, corresponding to its periodicity. In such cases, the superlattice period can be determined using a variation of *Eq. 2.1*, where the thickness of the layer is replaced by the superlattice period.

Furthermore, XRR also provides valuable insights into surface and interface roughness (R). A gradual decrease in reflectivity intensity indicates increasing roughness, as surface irregularities cause enhanced diffuse scattering and reduced fringe visibility. Additionally, the amplitude of the Kiessig fringes depends on the density difference between the film and the substrate; a higher contrast results in more pronounced fringes, improving the accuracy of thickness determination.

All these structural parameters –thickness, roughness, and film density– can be obtained by fitting the experimental XRR curves to mathematical models. In this thesis, data fitting was performed using the AMASS software (Advanced Material Analysis and Simulation Software).

Figure 2.5a presents the experimental XRR curve of a $CaFeO_{2.5}$ thin film deposited on (001) $SrTiO_3$ (STO), along with the corresponding fit. The refined parameters indicate a film thickness of 27.5 nm, density of 4.36 g/cm^3, and surface roughness of 0.4 nm. Similarly, **Figure 2.5**b shows the XRR curve of a $SrTiO_3/PbTiO_3$ superlattice deposited on (110) $DyScO_3$ (DSO), formed by 20 repetitions of 3.12 nm periodicity (corresponding to 1.56 nm per layer). The best-fit model yields a refined superlattice periodicity of 3.11 nm, with individual layer thicknesses of 1.54 and 1.57 nm for $PbTiO_3$ and $SrTiO_3$, respectively.

Lastly, it is important to note that, unlike diffraction techniques (which are discussed in the next section), XRR does not depend on the crystallinity of the samples. As a result, this technique can be also used for thickness determination in amorphous films, making it a versatile technique for thin film characterization.

2.2.1.2. X-ray diffraction

X-ray diffraction (XRD) is one of the most essential structural characterization techniques for studying thin films, primarily for two key reasons: it enables precise structural analysis at the atomic scale, and it is non-destructive, ensuring that the sample remains intact during measurement.

X-ray diffraction occurs when the electromagnetic radiation interacts with a periodic crystal structure where the spacing between atomic planes (d_{hkl}) is of the order of the X-ray wavelength. When the incident X-ray beam satisfies Bragg's law *(Eq. 2.2)*, constructive and destructive interferences result in characteristic diffraction peaks:

$$n\lambda = 2d_{hkl} sin\theta \qquad \text{(Eq. 2.2)}$$

where n is an integer (the diffraction order), λ is the wavelength of the X-rays, d_{hkl} is the interplanar spacing for a given Miller index (*hkl*) and θ is the incidence angle (*98*).

In this thesis, XRD has been extensively employed to analyze the structural properties of thin films and multilayers, using different types of scanning modes and diffractometer configurations, each providing distinct information. The different types of scans are described next.

ω/2θ scans. In these experiments, the diffractometer is placed in a symmetrical configuration, with the incident (ω) and diffracted (θ) beams forming equal angles with the sample surface (such as in the scheme of **Figure 2.4**). The diffraction pattern is collected by simultaneously varying the incidence angle of the incoming X-ray by ω and the scattering angle by 2θ while measuring the scattered intensity as a function of the latter. Despite this continuous variation of both angles during measurement, the ω = θ condition is always maintained. For this reason, this type of scan is also denoted as θ/2θ scan.

In this configuration, only those lattice planes that are oriented parallel to the sample surface contribute to Bragg reflection, thus providing information about the out-of-plane lattice parameter (c), exclusively. The out-of-plane lattice parameter for cubic (or pseudo-cubic) unit cells can be determined using a combination of Bragg's law *(Eq. 2.2)* and interplanar spacing formula (*98*):

$$c = \frac{\lambda\sqrt{h^2+k^2+l^2}}{2\sin\theta} \qquad \text{(Eq. 2.3)}$$

Figure 2.6a presents the XRD pattern of a $La_{0.7}Sr_{0.3}MnO_3$ thin film grown on (001) STO, centered around the (002) reflection of the substrate. The diffraction peak appears at 47.02 °, which corresponds to an out-of-plane lattice parameter of 3.862(5) Å, according to *Eq. 2.3*.

Notably, a set of oscillations appears around the film's (002) diffraction peak, as observed in the figure. These oscillations, denoted as Laue oscillations or Laue fringes, arise from the constructive interference between the diffracted beams coming from the atomic planes of the film. Since these oscillations only occur when these interfaces are atomically abrupt, their presence indicates high-crystalline quality (*97*).

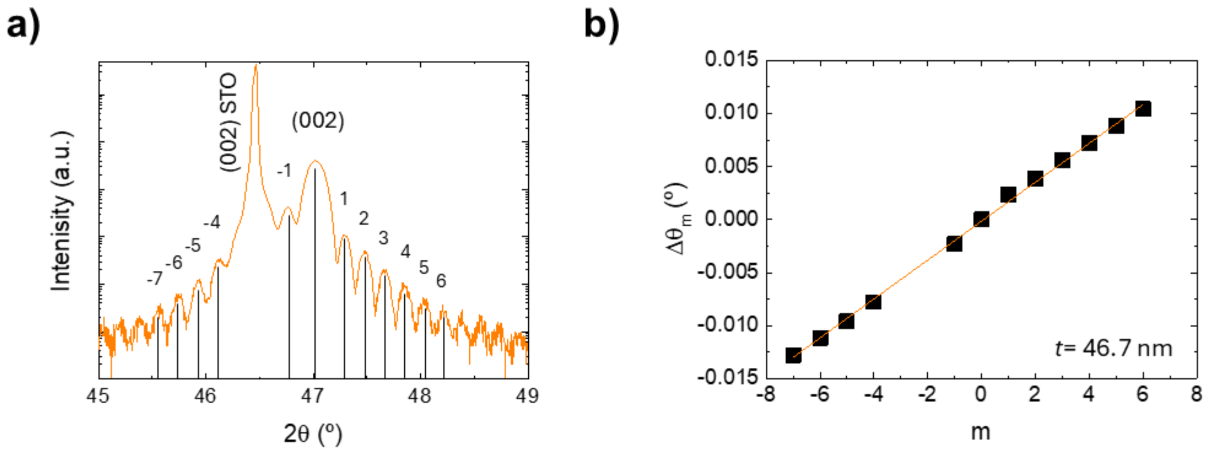

Figure 2.6. a) XRD $\omega/2\theta$ scan of a $La_{0.7}Sr_{0.3}MnO_3$ thin film (deposited on (001) STO) around the (002) reflection, with the order of each Laue fringe (*m*) indicated. b) The linear fitting of the Laue oscillations to *Eq. 2.4* allows the determination of the film thickness, providing a value of 46.7 nm in this case.

Their origin is similar to the Kiessig fringes discussed before, as both are interference effects due to finite-thickness of the films. Thus, the angular separation between Laue fringes can be used to estimate the film thickness, according to:

$$t = \frac{\lambda\, m}{\Delta\theta_m\, 2\cos\theta} \qquad \text{(Eq. 2.4)}$$

where *m* is the index of the Laue oscillation, θ is the diffraction peak and $\Delta\theta_m$ is the angular separation between the Laue fringe of order *m* and the diffraction peak.

Figure 2.6b shows the linear fitting of Laue oscillations to *Eq. 2.4*, yielding a film thickness of 46.7 nm. However, it is important to note that this method can slightly underestimate the actual film thickness, as it relies on constructive interference from only perfectly parallel atomic planes. This contrasts with XRR measurements, in which the whole film is considered, as the interference pattern is governed by differences in the refraction index of the different materials. For comparison, the same sample measured via XRR provides a thickness of 48.3 nm.

In a particular case of superlattices, $\omega/2\theta$ scans exhibit additional satellite peaks around the primary diffraction peak, corresponding to the X-ray reflection on the different interfaces that result in constructive interferences at certain angles. **Figure 2.7**a shows the XRD pattern of a $PbTiO_3/SrTiO_3$ superlattice deposited on (001) STO, consisting of 15 repetitions with a nominal periodicity of 11.7 nm (5.85 nm thickness in each layer). The superlattice (002) diffraction peak appears at 45.35 °, with several satellites (denoted as $SL_{\pm m}$) surrounding it.

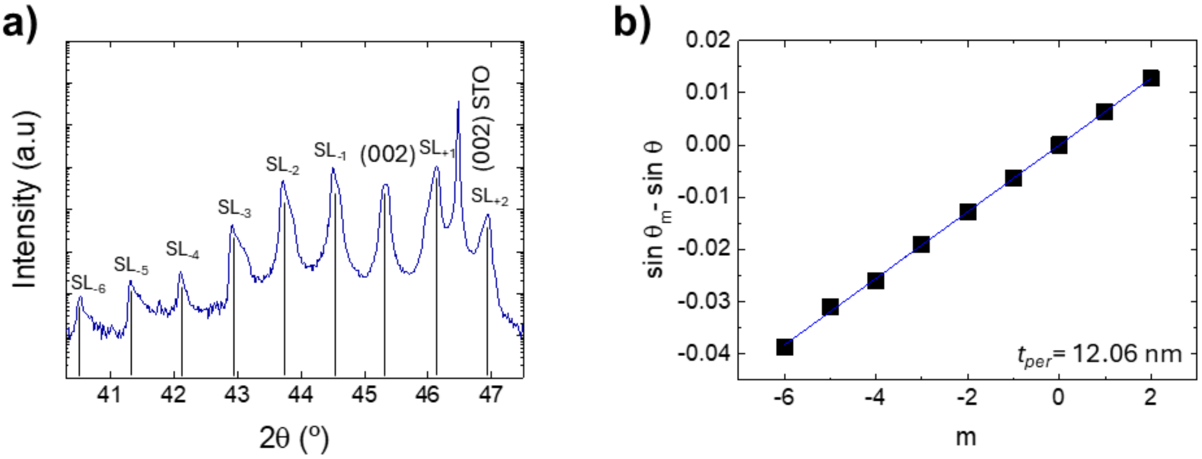

Figure 2.7. a) XRD ω/2θ scan of a $PbTiO_3/SrTiO_3$ superlattice (15 repetitions, 11.70 nm periodicity) deposited on (001) STO. The order of each satellite peak is indicated in the image. By linearly fitting the position of the satellite peaks to *Eq. 2.5* (b) we can determine the superlattice periodicity, which in this case is 12.06 nm.

Using a variation of Bragg's law *(Eq. 2.2)*, the angular distance between the satellite peaks can be converted to thickness, which in this case turns out to be the superlattice period (t_{per}):

$$t_{per} = \frac{\lambda\, m}{2\,(\sin\theta_m - \sin\theta)} \qquad \textit{(Eq. 2.5)}$$

where *m* is the order of the satellite peak (positioned at θ_m), and θ refers to the main diffraction peak of the superlattice.

Figure 2.7b presents the linear fitting of the satellite peak position to *Eq. 2.5*, yielding a superlattice periodicity of 12.06 nm, which closely matches the intended value of 11.70 nm.

ω scans, also denoted as rocking curves, consists of a ω scan around a fixed 2θ value, usually at or near a diffraction peak. As a result, both ω and θ are decoupled in these experiments. Since the scan direction is approximately parallel to the atomic planes, this type of measurement is highly sensitive to material quality, including defects, texture, and preferred orientation, among other factors (*97*).

A key parameter in these measurements is the full width at half maximum (FWHM) of the diffraction peak. A narrow FWHM indicates high crystallinity (large crystal domains) with minimal defects. In contrast, a broader peak generally suggests increased disorder, which may result from mosaicity, dislocations, or strain relaxation within the film.

For instance, **Figure 2.8** presents the rocking curves around the (002) diffraction peak of $PbTiO_3$ thin films grown by sputtering under identical conditions on two different substrates: (001) STO (a) and (110) DSO (b). As observed in the figure, the film deposited on STO exhibits a sharp and intense diffraction peak, with an FWHM of approximately 0.03 °, indicating excellent crystalline quality. In contrast, the film deposited on DSO shows a much broader and less intense peak, with an FWHM of 1.25 °, that may be attributed to significant mosaicity, higher defect density, and reduced crystalline order.

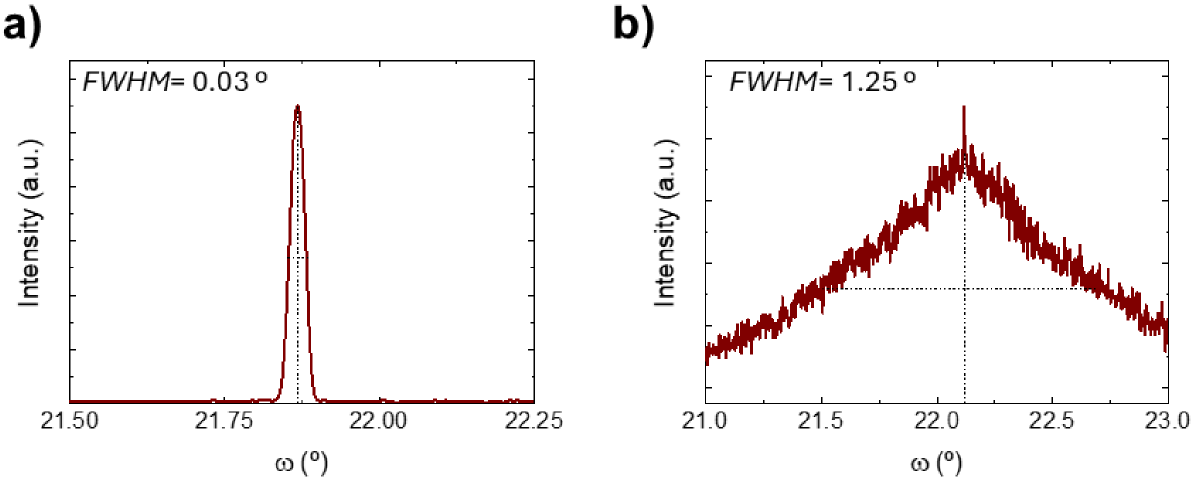

Figure 2.8. Rocking curves from the (002) diffraction peak of $PbTiO_3$ thin films deposited on (001) STO (a) and (110) DSO (b) substrates. The full width at half maximum (FWHM) of the diffraction peak is 0.03° for the film grown on STO, indicating high crystalline quality with minimal defects. In contrast, the film deposited on DSO exhibits a significantly broader peak with an FWHM of 1.25°, suggesting increased disorder in the film.

Reciprocal space mapping (RSM). This technique provides detailed information about the structural properties of thin films, as it captures the full scattering distribution of an asymmetric reflection in a two-dimensional graph. Unlike conventional ω/2θ scans, which only provide information about the out-of-plane lattice parameters, RSM allows for a comprehensive analysis of both in-plane and out-of-plane lattice parameters, as well as the epitaxial relationship between film and substrate.

This type of measurement is performed by recording a series of 2θ scans at different ω values, maintaining the remaining instrumental parameters constant. These angular coordinates are then converted into reciprocal space vectors, allowing the reciprocal space map to be plotted in terms of diffraction intensities as a function of two reciprocal lattice components: Q_x, which is parallel to the sample surface; and Q_z, which is perpendicular to the surface (*97*). Their mathematical expressions are given by:

$$Q_x = \frac{4\pi}{\lambda} sin\theta \sin(\theta - \omega) \qquad \text{(Eq. 2.6)}$$

$$Q_z = \frac{4\pi}{\lambda} sin\theta \cos(\theta - \omega) \qquad \text{(Eq. 2.7)}$$

From the position of the (Q_x,Q_z) coordinates of the peaks in reciprocal space map, the corresponding lattice parameters of a cubic (or pseudo-cubic) unit cell can be determined using the following expressions:

$$a = \frac{2\pi\sqrt{h^2+k^2}}{Q_x} \qquad \text{(Eq. 2.8)}$$

$$c = \frac{2\pi l}{Q_z} \qquad \text{(Eq. 2.9)}$$

For this reason, RSM provides direct insight into the epitaxial relationship between film and substrate: if the film is epitaxially grown on the substrate, they will present matching Q_x

coordinates; however, if the film undergoes relaxation, its Q_x value will differ from that of the substrate.

Figure 2.9 presents two reciprocal space maps of a $CaFeO_{2.5}$ (CFO) thin film (≈120 nm) grown on two different substrates: a) (001) STO and b) (001) $LaAlO_3$ (LAO). As observed, the CFO film grown on STO retains the same Q_x lattice vector than the substrate, meaning that they present matching in-plane lattice parameters. However, the CFO film deposited on LAO exhibits a significantly larger Q_x lattice vector, indicating partial relaxation with a reduced in-plane lattice parameter compared to the substrate.

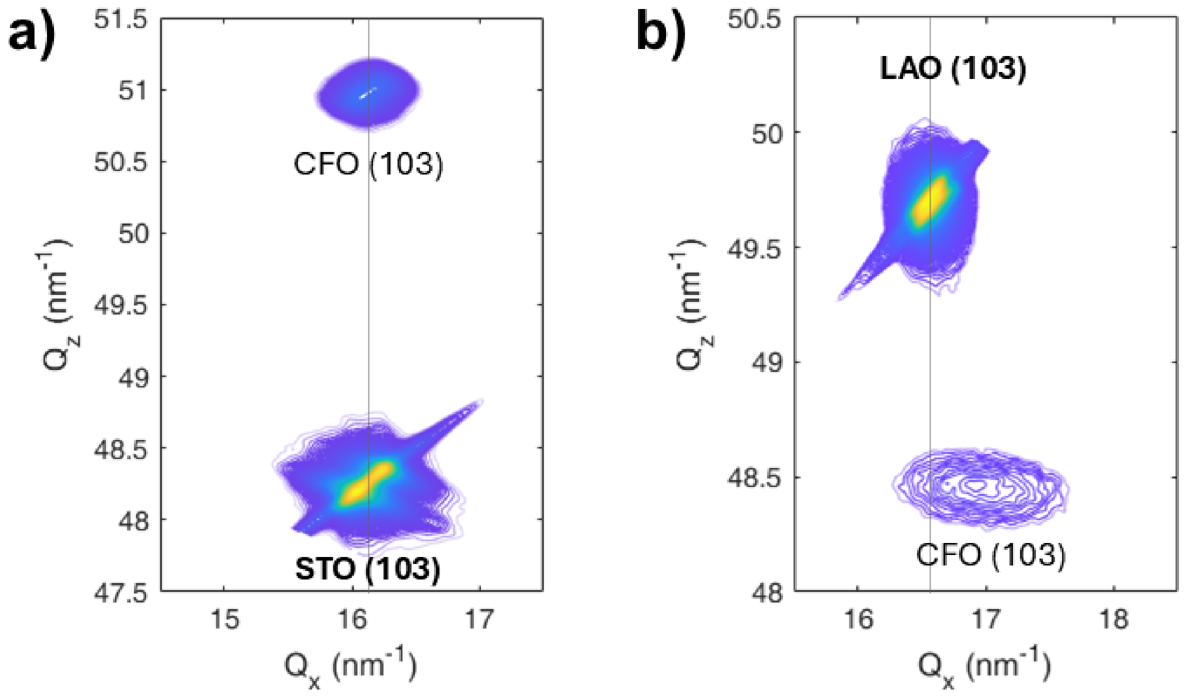

Figure 2.9. Reciprocal space maps around the (103) substrate reflection of $CaFeO_{2.5}$ thin films (≈120 nm) deposited on (001) STO (a) and LAO (b). The film on STO growths fully strained to the substrate, adopting its in-plane lattice parameter. However, the film deposited on LAO shows partial relaxation, as indicated by the different Q_x lattice vector.

This distinct behavior of CFO thin films arises from the different epitaxial strain imposed by STO and LAO substrates, which can be quantified using the following equation:

$$s\ (\%) = \frac{a_s - a_f}{a_f} \cdot 100 \qquad \textit{(Eq. 2.10)}$$

where a_s refers to the in-plane lattice parameter of the substrate (3.905 Å for STO and 3.821 Å for LAO substrates, both purchased from CrysTec GmbH), and a_f to the pseudo-cubic lattice parameter of the film in the bulk from (*98*).

$CaFeO_{2.5}$ presents a bulk lattice parameter of a_f= 3.898 Å (*99*), resulting in mild tensile strain when deposited on STO (s= +0.18%) and severe compressive strain when grown on LAO (s= -1.97%), leading to the epitaxial relaxation of the thin film in the latter, as observed in **Figure 2.9**b.

Beyond thin film analysis, RSM is also a valuable tool for analyzing superlattices, as it captures multiples satellite peaks in reciprocal space, similar to conventional ω/2θ scans. These satellite peaks provide direct information about the periodicity of the superlattice (t_{per}), which can be determined using a combination of *Eqs. 2.5-2.7*, with the following expression:

$$Q_{z,m} - Q_{z,0} = \frac{m\,2\pi}{t_{per}} \qquad \text{(Eq. 2.11)}$$

where $Q_{z,0}$ refers to the position of the main superlattice peak, and $Q_{z,m}$ refers to the position of the satellite peak of order m.

Figure 2.10 shows the reciprocal space map of a $PbTiO_3/SrTiO_3$ superlattice deposited on (001) STO, consisting of 5 repetitions with a nominal periodicity of 11.7 nm. The map was recorded around the symmetric STO (002) reflection, and apart from the Bragg diffractions of STO and the superlattice, multiple satellite peaks are visible. By fitting their positions to the equation above, we can determine the superlattice periodicity, resulting in 12.37 nm in this case (**Figure 2.10**b), very close to the intended periodicity of 11.7 nm, thus confirming the periodic structure of the multilayer.

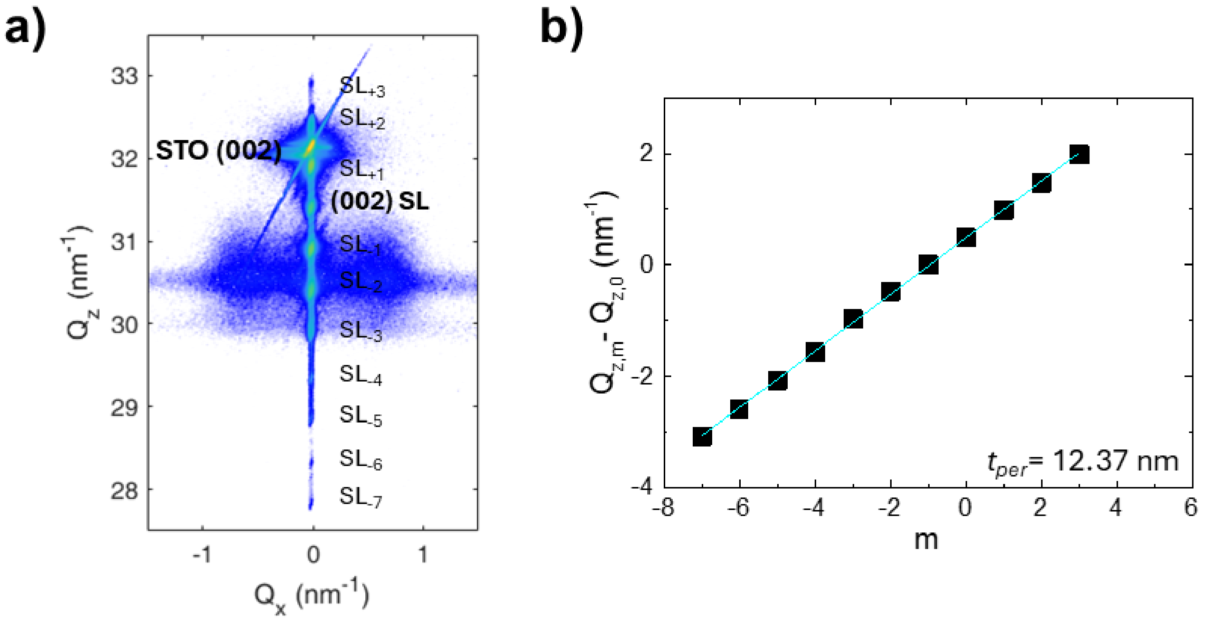

Figure 2.10. a) Reciprocal space map around the (002) peak of STO of a $PbTiO_3/SrTiO_3$ superlattice consisting of 5 repetitions with a nominal periodicity of 11.7 nm. The order of the satellite peaks is indicated next to them, and their position is fitted to extract the periodicity of the superlattice (b), providing a value of 12.37 nm in this case.

2.2.2. Atomic force microscopy

Atomic force microscopy (AFM) is a high-resolution imaging technique used to analyze surfaces at the nanoscale. It was developed in 1986 by Binnig, Quate and Gerber (*100*) as an extension of the scanning tunneling microscope (STM), which was limited to conductive materials. AFM, however, provides atomic-scale information on both conductive and isolating materials, making it a versatile tool in nanotechnology and materials science.

AFM operates by scanning the surface of the sample with a sharp probe, a cantilever with a nanometer-scale tip. As the tip interacts with the sample, either attractive or repulsive forces arise between them, causing the cantilever to deflect. This deflection can be quantified by monitoring a laser beam that is reflected off the backside of the cantilever onto a position-sensitive photodetector, as illustrated in **Figure 2.11**. Any variations in surface morphology affect the cantilever movement, thus being detected by the photodiode.

The sample is placed on a piezoelectric scanner, enabling precise, repetitive scanning of the surface. Meanwhile, the photodetector establishes a feedback loop to control the scanner's vertical movement as the cantilever moves across the sample. The recorded cantilever deflections are converted into a height profile, providing detailed topographical information of the sample surface. For instance, **Figure 2.11** presents a topography image of a (001) $SrTiO_3$ substrate after thermal annealing in air (1000 ºC for 1 hour), revealing surface terraces (*101*).

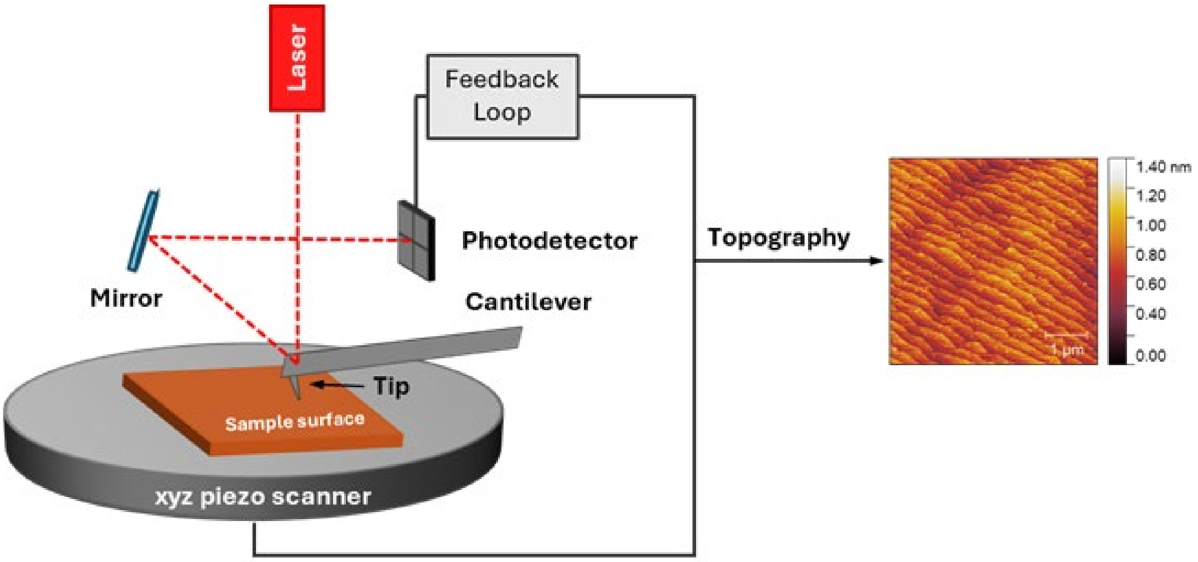

Figure 2.11. Schematic description of the atomic force microscopy setup. The AFM cantilever is bent upon scanning the sample surface, which results in a deflection in the laser beam that is detected by the photodiode. The processed signal is then translated into topographic information, such as the one shown on the right side, corresponding to a $SrTiO_3$ substrate with visible terraces on the surface.

A key component of AFM is the cantilever, which serves as the sensor to measure forces due to tip-sample interactions. To achieve high vertical and lateral resolution at extremely low forces (as low as 0.1 nN), cantilevers must have low spring constants. However, to minimize the impact of environmental vibrations (which typically occur around 100 Hz), a high resonant frequency (ranging from 10 to 100 kHz) is also desirable. Most modern AFM cantilevers are microfabricated from silicon or silicon nitride using advanced photolithographic techniques. Typical lateral dimensions are on the order of 100 µm, with thicknesses of ≈1 µm (*102*).

AFM imaging can be performed in three basic modes: static or contact mode, dynamic or non-contact mode and tapping or force modulation mode (*101*).

i) Contact mode. In this scanning mode, the AFM tip is brought into direct contact with the sample surface, and the atoms at the end of the tip experience repulsive forces due to electrostatic interactions. As the tip scans the surface, these forces cause the cantilever to deflect, and this deflection is measured by the photodetector. A feedback loop maintains this deflection at a constant value (known as setpoint) by adjusting the scanner height, allowing the AFM to reconstruct surface topography with extremely high resolution, reaching vertical values below 0.1 nm and lateral resolutions around 0.2 nm.

However, while scanning in contact mode, the cantilever applies substantial shear forces, potentially damaging the sample and/or the tip apex. For this reason, particularly delicate materials (such as biomolecules, soft polymers, or adsorbed layers) should be avoided. Furthermore, AFM tips on soft cantilevers are susceptible to lateral forces and stick to surface contamination layers that are present on most surfaces in ambient air, resulting in image distortions.

Despite these limitations, various advanced AFM techniques have been developed based on contact mode, as they require a constant tip-sample contact to measure additional surface properties, such as conductivity, resistance, capacitance, piezoresponse or thermal behavior.

ii) Non-contact mode. In this mode, the AFM tip remains a few nanometers above the sample surface, avoiding direct contact. Because the tip-sample distance is greater than in contact mode, repulsive forces are minimized, and instead, attractive van der Waals forces (arising from dipole-dipole interactions) become predominant. However, since these forces are extremely weak, direct measurement of cantilever deflection is impractical. For this reason, non-contact AFM detects phase shifts or changes in vibration amplitudes induced by the tip-sample interaction as the cantilever oscillates near its resonant frequency. By monitoring these changes, the AFM system reconstructs the surface topography.

This mode is particularly useful for imaging soft biological samples or fragile materials, as it prevents damage and extends the lifespan of the AFM tip. However, due to the weak force interactions, maintaining stable tip-sample interactions can be challenging, and resolution is generally lower compared to contact mode.

iii) Tapping mode. This is a hybrid between contact and non-contact modes. In this approach, the cantilever oscillates near its resonant frequency, similar to non-contact mode, but it periodically taps the surface, making brief, intermittent contact. The system detects changes in the oscillation amplitude of the cantilever as a function of tip-sample interaction forces, allowing the reconstruction of sample topography.

Unlike true non-contact mode, which operates exclusively in the attractive force regime, tapping mode enters the repulsive force regime at the lower turning point of oscillation, where the tip momentarily touches the surface. The oscillation amplitude is used as the topography feedback signal, ensuring that the movement of the z scanner compensates for amplitude variations. Additionally, phase shift detection provides insights into the mechanical properties of the sample.

Over the years, AFM has experienced great evolution to meet specific scientific demands, leading to the development of various electrical, magnetic and mechanical modes, among others. However, all these specialized AFM techniques are based on the three scanning modes previously described.

In this thesis, a Park Systems NX10 AFM was used for topographic imaging and roughness determination, employing both non-contact and tapping modes. Additionally, various electrical modes were used for studying the electrical properties of materials. All these advanced modes are briefly described next (*101*).

2.2.2.1. Conductive AFM

Conductive AFM (C-AFM) is a widely used technique for investigating the electrical properties of various materials, such as nanoparticles, carbon nanotubes, 2D materials or thin films. In this method, the sample surface is scanned in contact mode while a DC bias voltage is applied between the tip and the sample, and the resulting current is measured. Consequently, conductive cantilevers are used. In our experiments, we used cantilevers coated with 5 nm of Cr and 25 nm of Pt, with a tip radius of less than 25 nm.

To ensure consistent imaging and electrical contact, the feedback system maintains a constant cantilever deflection during scanning, thereby controlling the tip-sample force which was set to 30 nN in our measurements. A current-to-voltage preamplifier is employed to convert and amplify the detected current signal; given that the measured electric current can range from picoamperes to milliamperes, selecting an appropriate amplifier based on the sample's conductivity is crucial for obtaining accurate and reliable measurements.

In this thesis, C-AFM was not used to study the electrical properties of the samples, but rather as a tool to apply localized electric fields with the biased AFM tip. We scanned the surface of several oxoperovskite thin films while applying voltages ranging from -5 V to -10 V, to promote the localized accumulation of oxygen vacancies in these regions (see Chapter 5 for a detailed description of the method). The resulting charge distribution modifications were analyzed using Kelvin probe force microscopy.

2.2.2.2. Kelvin probe force microscopy

Kelvin probe force microscopy (KPFM), also known as scanning Kelvin probe microscopy (SKPM), is a non-contact AFM technique that allows the determination of surface potential and work function of conductive and semiconductive materials with nanoscale resolution. This method provides crucial insights into charge distribution, making it widely applicable in materials science.

KPFM operates by applying an AC bias (with frequency ω) between a conductive AFM tip and the sample surface, while simultaneously maintaining a fixed DC bias (V_{DC}). As the tip scans the surface in non-contact mode, electrostatic forces arise due to differences in work function between the tip and the sample. These differences lead to the formation of a contact potential difference (V_{CPD}), which induces an oscillating electrostatic force acting on the tip. The fundamental principle of KPFM is to identify the V_{DC} value that cancels out the electrostatic force caused by V_{CPD}; when V_{DC} exactly matches V_{CPD} but in the opposite direction, the electrostatic force is nullified. The required DC voltage at each point corresponds to the local surface potential, thus allowing for the generation of a high-resolution potential map (*103*).

As a result, this technique provides quantitative measurements of the local surface potential distribution. However, determining the absolute surface potential can be challenging, as it requires precise knowledge of the tip's work function. In this thesis, we focus on a semi-quantitative analysis, comparing relative surface potentials between different regions of the sample surface or analyzing temporal variations in surface potential.

For example, **Figure 2.12** presents KPFM potential maps of a $La_{0.6}Sr_{0.4}CoO_3$ thin film after surface modification with a voltage-biased AFM tip (C-AFM mode) at -8 V and -10 V. The application of the electric field induces a local accumulation of oxygen vacancies, which produces a significant increase in surface potential, of approximately 0.50 V (**Figure 2.12**a). The KPFM potential map was also recorded in the same area after one week (**Figure 2.12**b), showing a clear decrease in surface potential, which is now of the order of 0.3 V now. Finally, as shown in **Figure 2.12**c, the increase in surface potential can be eliminated by performing a thermal annealing in air at 300 ºC, restoring the initial surface potential state.

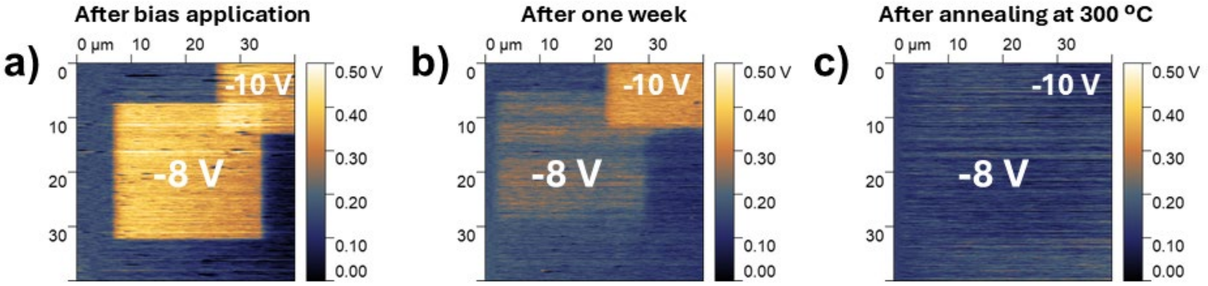

Figure 2.12. KPFM potential map of a $La_{0.6}Sr_{0.4}CoO_3$ thin film deposited on STO, after scanning an area of 25 x 25 μm^2 with -8 V (and with -10 V in the upper part of the image) using the C-AFM mode (a). The application of the tip bias results in a localized increase in the surface potential of the scanned area. KPFM measurements were performed in the same area after one week, keeping the sample under ambient conditions (b), displaying a considerable decrease in surface potential. Surface potential can be reversed to the original value by thermally annealing the sample in air at 300 ºC (c).

As discussed in the next chapters, KPFM was used to map the local and transient accumulation of surface charge in the films used in this thesis.

2.2.2.3. Piezoresponse force microscopy

Piezoresponse force microscopy (PFM) is a specialized AFM technique designed to investigate the nanoscale electromechanical properties of materials exhibiting ferroelectricity and piezoelectricity. In this thesis, PFM is employed in Chapter 6 for the characterization of ferroelectric domains and polar vortices in $SrTiO_3/PbTiO_3$ superlattices.

PFM is based on the coupling between electrical and mechanical responses in piezoelectric materials. It operates by applying an alternating voltage (AC bias) to a conductive AFM tip while in contact mode with the sample surface. This electric field generates a mechanical deformation in the material due to the inverse piezoelectric effect, where an applied electric field induces a strain response. The resulting surface displacement (piezoresponse) is detected through cantilever deflection or torsion, which is measured using the optical beam deflection system of the AFM.

PFM can probe both out-of-plane and in-plane polarization components. The vertical deflection of the cantilever corresponds to out-of-plane piezoresponse, revealing the polarization direction beneath the tip, a technique known as vertical PFM (V-PFM). Conversely, lateral deflection (torsion) of the cantilever provides information about in-plane polarization components, referred to as lateral PFM (L-PFM). When both V-PFM and L-PFM signals are properly calibrated, the full electromechanical response vector can be determined, a method known as vector PFM, which provides a comprehensive mapping of polarization behavior in ferroelectric materials.

Furthermore, beyond passive imaging, PFM can be also used to manipulate ferroelectric domains. By applying a direct current (DC) bias in addition to the AC voltage, it is possible to induce local domain switching, enabling the study of hysteresis loops, coercive fields, and domain stability. When the applied electric field exceeds the local coercive field, it triggers ferroelectric polarization reversal, allowing researchers to "write" single domains, domain arrays, or complex domain patterns without altering the sample’s topography (*104*, *105*).

Unlike the previous AFM modes, which were applied using the Park Systems NX10 AFM, PFM experiments were conducted during a one-week research stay at the Autonomous University of Barcelona (under the supervision of Prof. Jordi Sort and Dr. Eric Langenberg) and an Asylum MFP-3D AFM was used. This AFM supports both vertical and lateral PFM and allows for the application of AC/DC voltages up to ±150 V. The findings from these experiments are presented in Chapter 6.

2.2.3. Differential scanning calorimetry

Differential scanning calorimetry (DSC) measures the heat exchanged during a phase transition and other conformational changes in the sample. In this method, a sample (placed in an aluminum pan) and a reference (an empty aluminum pan) are positioned in separate holders inside a common furnace block, as depicted in **Figure 2.13**a. Thermocouples located beneath each platform measure the temperatures of the sample and the reference, while an additional thermocouple at the base monitors the overall system temperature. The furnace is programmed to follow a controlled temperature ramp, either heating or cooling at a constant rate (10 K/min in our experiments).

Under normal conditions, the sample and reference maintain the same temperature. However, when the sample undergoes a thermal event –such as a phase transition– its temperature temporarily deviates from that of the reference. During an endothermic transition (e.g., melting), the sample absorbs heat, causing its temperature to lag behind, as additional energy is required to overcome intermolecular forces. Conversely, in an exothermic transition (e.g., crystallization), the sample releases heat, leading to a temporary temperature increase relative to the reference. The DSC continuously adjusts the heat input needed to keep the same temperature at the sample and reference cells, and the resulting energy change is recorded as a function of temperature or time (*106*, *107*).

Each phase transition produces a characteristic feature on the DSC curve. In our system, endothermic transitions appear as downward peaks, and exothermic transitions are displayed as upward peaks. The area under these peaks corresponds to the enthalpy change (ΔH) associated with the transition, thus allowing for quantitative thermal analysis when appropriate baseline corrections and calibrations with reference materials are performed.

Figure 2.13b presents a DSC scan of 4,4'-dioctyloxy-3-methylazobenzene, where multiple phase transitions can be identified. During heating, three endothermic events are observed, corresponding to a crystal-to-crystal transition (Cr-Cr), a crystal-to-liquid crystal transition (Cr-LC), and the melting of the liquid crystal into an isotropic liquid (LC-IL). The reverse exothermic transitions occur during cooling, though at significantly lower temperatures, particularly in the case of the Cr-Cr transformation.

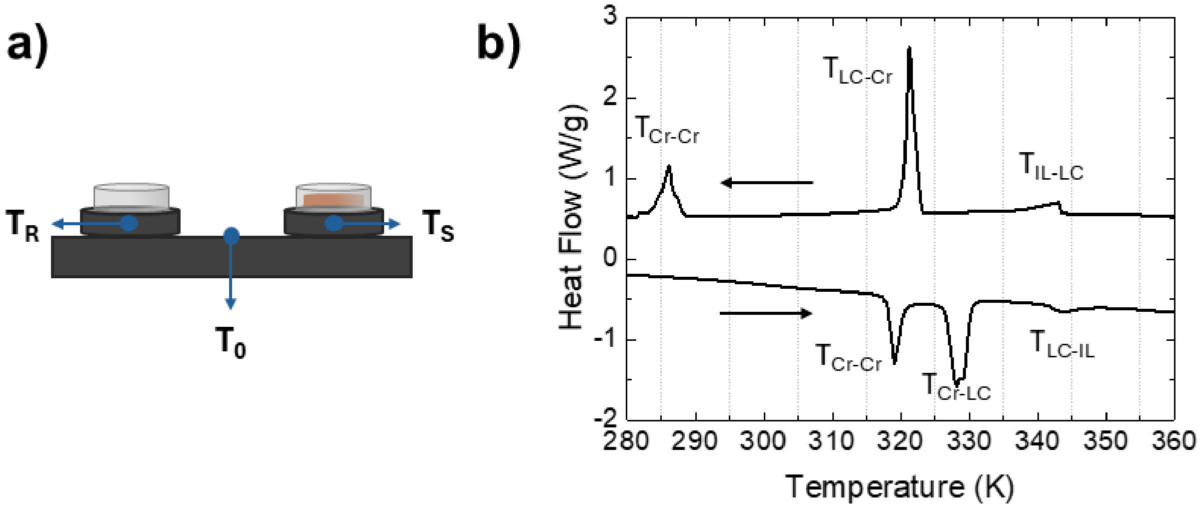

Figure 2.13. a) Schematic representation of the experimental setup used in differential scanning calorimetry. Thermocouples (blue circles) are positioned beneath each cell to measure the temperatures of the reference (T_R) and the sample (T_S). An additional thermocouple at the base monitors the setpoint temperature (T_0). b) DSC scan of 4,4'-dioctyloxy-3-methylazobenzene, showing multiple endothermic and exothermic peaks corresponding to different phase transitions. The identified transformations are labelled, with Cr, LC and IL corresponding to crystal, liquid crystal and isotropic liquid, respectively.

In this work, DSC was extensively used to characterize the azobenzene derivatives synthesized in Chapter 3, allowing for the identification of different phases at varying temperatures and their respective thermal stability. This information was then correlated with changes observed in thermal conductivity. The experiments were conducted using a TA Instruments Q200 DSC, equipped with a refrigerated cooling system RSC90, which enables measurements in the temperature range of -90 to 550 ºC.

2.2.4. Polarized optical microscopy

As previously discussed, DSC is widely used for characterizing phase transitions. However, identifying the exact nature of these transitions can be sometimes challenging, particularly when distinguishing between the formation of different types of liquid crystals and an isotropic liquid. To address this limitation, DSC experiments are often complemented with additional techniques that provide further insight into phase identification. One of the most common methods for investigating liquid crystal formation is polarized optical microscopy (POM), as it enables the detection of materials with anisotropic optical properties, a key characteristic of liquid crystals.

The fundamental principle of POM is based on the interaction of polarized light with birefringent materials, which have different refractive indices depending on the direction of light propagation. A typical POM setup consists of a polarizer, which ensures that only light oscillating in a specific direction reaches the sample, and an analyzer (a second polarizer), positioned perpendicular to the first one to selectively transmit altered light. When linearly polarized light passes through an isotropic material, such as a conventional liquid, its polarization state remains unchanged. As a result, under crossed polarizers no light reaches the detector, and the material appears black under the microscope. In contrast, when light interacts with an anisotropic material, such as a liquid crystal, it splits into two perpendicular components that travel at different speeds, introducing a phase difference. This interference generates characteristic contrast and colors, revealing details about the sample's internal structure (*108*).

This capability makes POM particularly valuable for detecting phase transitions in liquid crystals, which exhibit unique optical properties due to their intermediate state between solids and liquids. For instance, in the isotropic phase at high temperatures, liquid crystals behave like ordinary fluids and do not exhibit birefringence, appearing dark under crossed polarizers (**Figure 2.14**c). In contrast, the nematic liquid crystal phase, which has long-range orientational order but no positional order (i.e., rotational symmetry breaking), displays bright textures due to variations in molecular alignment (**Figure 2.14**b). Meanwhile, smectic phases, which present both orientational and some degree of positional order (i.e., rotational and translational symmetry breaking in one direction), produce even more distinct optical textures depending on the specific sub-phase (**Figure 2.14**a).

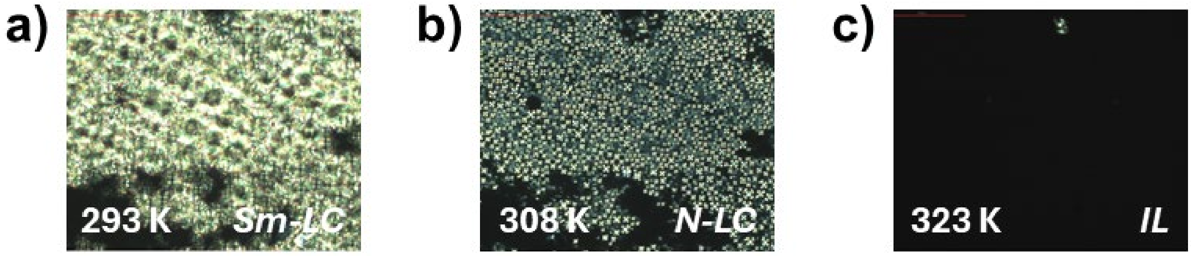

Figure 2.14. Polarized optical microscopy images of 4-octyl-4'-cyanobiphenyl, recorded under crossed polarizers. This compound forms a smectic liquid crystal at room temperature (a), which transitions into a nematic liquid crystal (b) before melting into the isotropic liquid phase (c).

In this thesis, POM images were acquired using a Leica DM2700 M microscope, equipped with a Linkam stage and a LNP96-S liquid nitrogen pump, enabling precise temperature control. This technique was employed to identify different liquid crystalline phases and investigate their phase transitions as a function of temperature, complementing DSC measurements for a more comprehensive phase characterization.

2.2.5. Thermal conductivity measurements

Two different techniques were employed in this thesis for measuring thermal conductivity: the 3ω method was used to investigate the thermal conductivity of azobenzene derivatives (Chapter 3), while frequency domain thermoreflectance (FDTR) was used to determine the thermal conductivity of thin films and superlattices (Chapters 4-6). Both techniques are described in detail in the following sections.

2.2.5.1. The 3ω method

To measure the temperature-dependent thermal conductivity of the azobenzene derivatives synthesized in this thesis, we employed a variation of the 3ω method developed in our research group, using a home-made setup inserted in a liquid nitrogen cryostat (*30*). The original 3ω method, introduced by D. G. Cahill (*109–111*), was specifically designed for measuring the thermal conductivity of solids and thin films. However, our adaptation extends its applicability to liquids and mesophases, thus allowing us to monitor the thermal conductivity of azobenzene derivatives across all their different phases, including crystalline powders, liquid crystals and isotropic liquids.

This technique employs a metallic strip that acts both as a heater and a thermometer. In the original 3ω method, the metallic strip is directly deposited on the surface of the material under study. When an alternating current (AC) at frequency ω is applied to the metallic strip, Joule heating generates periodic temperature oscillations at 2ω ($\Delta T_{2\omega}$). Since the resistance of the heater depends on temperature (*dR/dT*), the voltage drop along the heater exhibits a small signal at the third harmonic of the current frequency ($V_{3\omega}$), given by:

$$V_{3\omega} = \frac{I_0}{2}\left(\frac{dR}{dT}\right)\Delta T_{2\omega} \qquad \textit{(Eq. 2.12)}$$

where I_0 is the amplitude of the AC current.

The magnitude $\Delta T_{2\omega}$ is related to the thermal diffusivity (*D*) of the material and can be obtained by solving the heat equation, as demonstrated in ref. (*30*). For a sufficiently narrow metallic strip (width << length), the average temperature increase in the sensor is given by:

$$\Delta T \simeq \frac{P}{\pi l \kappa}\left[\frac{1}{2} ln\left(\frac{D}{b^2}\right) - \frac{1}{2}\ln(2\omega) + \eta - \frac{i\pi}{4}\right] \qquad \textit{(Eq. 2.13)}$$

where *P* is the effective dissipated power, *b* is the half-width of the strip, *η* is a constant related to the sample's diffusivity and κ is the thermal conductivity. By combining this expression with *Eq. 2.12*, we obtain:

$$\frac{V_{3\omega}}{V_{1\omega}} = \frac{I_0^2}{4\pi l \kappa}\left(\frac{dR}{dT}\right)\left[\frac{1}{2} ln\left(\frac{D}{b^2}\right) - \frac{1}{2}\ln(2\omega) + \eta - \frac{i\pi}{4}\right] \qquad \textit{(Eq. 2.14)}$$

As a result, the thermal conductivity can be determined from the slope (*m*) of the $V_{3\omega}/V_{1\omega}$ *vs* ln (2ω) curve:

$$\kappa = \frac{I_0^2}{8\pi l m}\left(\frac{dR}{dT}\right) \qquad \textit{(Eq. 2.15)}$$

For measuring the liquids, we first deposited a Pt sensor (consisting of a 10 nm Cr adhesion layer followed by 100 nm of Pt, with dimensions of 1 mm in length and 10 µm in width) via optical lithography and lift-off onto a low-thermal conductivity glass substrate, as depicted in **Figure 2.15**a. Then, the liquid is placed on top of the sensor, so that the Pt heater/sensor is placed at the interface between the two materials: the sample and the glass substrate. Consequently, the measured $V_{3\omega}$ signal contains contributions from both materials, and the apparent thermal conductivity is given by:

$$\kappa_{apparent} = \kappa_{substrate} + \kappa_{sample} \qquad \textit{(Eq. 2.16)}$$

Since the thermal conductivity of the glass substrate ($\kappa_{substrate}$) can be determined through independent measurements, the thermal conductivity of the sample (κ_{sample}) can be obtained from a single $V_{3\omega}$ (ω) measurement by simple subtraction.

In our experimental setup, the AC current to the Pt resistor was applied using a Keithley 5221 AC current source, and the $V_{3\omega}$ signal was measured using a Stanford Research Systems SR830 lock-in amplifier. Since the lock-in amplifier detects both the $V_{1\omega}$ and $V_{3\omega}$ components, and the $V_{1\omega}/V_{3\omega}$ ratio typically ranges from 10^3 to 10^6, the 1ω voltage must be suppressed prior to lock-in detection to improve the signal-to-noise ratio. To achieve this, our group previously developed a circuit (shown in **Figure 2.15**b) that eliminates the $V_{1\omega}$ component by using a potentiometer in series with the Pt strip and three differential amplifiers. The resistance of the potentiometer is independent of temperature and thus does not contain a 3ω component, enabling the subtraction of $V_{1\omega}$ from both resistances using differential amplifiers.

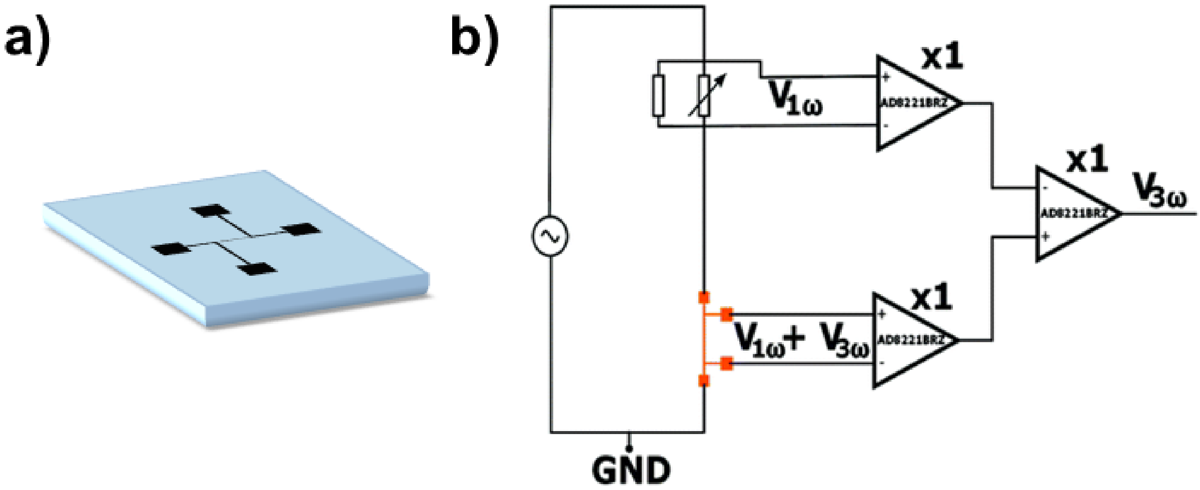

Figure 2.15. a) Schematic representation of the Pt strip used in this technique, deposited on top of a low thermal conductivity glass substrate. b) Scheme of the circuit developed in our group to eliminate the $V_{1\omega}$ component, using a variable resistor in series with the Pt strip and three differential amplifiers. Reproduced with permission from ref. (*30*). Copyright (2018) The Royal Society of Chemistry.

To ensure accurate measurements, we first calibrated the temperature-dependent resistance of the Pt strip (*dR/dT*) and determined the thermal conductivity of the glass substrate (**Figure 2.16**a) over a temperature range between 280 and 380 K, with a ramp rate of 1 K/min.

For the measurement of the azobenzene derivatives, a small amount of the sample (≈100 µg) was melted on top of the Pt sensor, as shown **Figure 2.16**b, and thermal conductivity measurements were conducted following the same procedure as for the glass substrate, within the same temperature range.

As observed in **Figure 2.16**c, the addition of the sample results in a decrease in the $V_{3\omega}/V_{1\omega}$ *vs* ln (2ω) slope, consistent with a higher apparent thermal conductivity. By subtracting the glass substrate's thermal conductivity from the apparent thermal conductivity at each temperature, we obtained the temperature-dependent thermal conductivity of the sample.

For optimizing the data acquisition speed during temperature-dependent thermal conductivity measurements (ramping heating and cooling runs), we extracted the slope of *Eq. 2.14* (*m*) using only two selected frequencies (76 Hz and 362 Hz), which significantly reduced measurement time. However, the linearity of the $V_{3\omega}/ V_{1\omega}$ *vs* ln (2ω) relationship was verified over a broader frequency range, from 56 to 2120 Hz (as shown in **Figure 2.16**c), before applying this optimization.

This verification was conducted at intermediate temperatures for all the measurements reported in this thesis, ensuring reliability in the determination of temperature-dependent thermal conductivity.

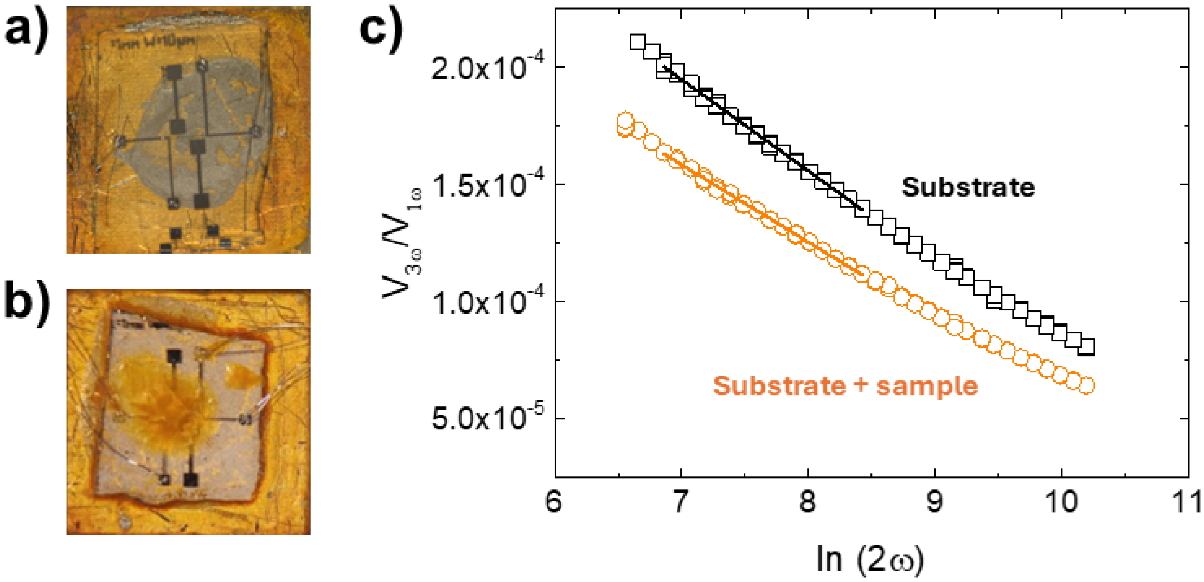

Figure 2.16. a) Optical microscopy photograph of the Pt resistor used to measure thermal conductivity. b) Optical microscopy photograph of the same setup shown in (a) with a small amount of the sample melted on top of the sensor. c) Comparison of the $V_{3\omega}/V_{1\omega}$ of a Pt metallic strip deposited on a cover glass substrate (black squares) and after melting a small amount of 4,4'-dihexyloxy-3-methylazobenzene on top (orange circles), along with their corresponding linear fitting between 76 and 362 Hz. Both measurements were carried out at 295 K.

The typical uncertainty for this method is ≈10%, with the primary source of error coming from the measurement of the sample (and not the substrate). However, several factors must be carefully considered when using this technique. First, there must be a significant thermal conductivity contrast between the sample and the substrate to effectively detect variations in heat transport. Moreover, the power dissipated through the Pt strip is a critical parameter: if the applied power is too low, the sensitivity to the sample's thermal conductivity may be insufficient, while high powers can introduce artifacts into the measurements, many of them related to evaporation of the liquids. To mitigate power-related issues, all samples were measured at two different powers (2 mW and 3 mW) to confirm the consistency and accuracy of the results.

2.2.5.2. Frequency domain thermoreflectance

Frequency domain thermoreflectance (FDTR) is a non-contact optical technique developed by Schmidt *et al.* (*112*) for measuring the thermal conductivity of a wide range of solid materials, including both organic and inorganic substances, in either bulk or thin film form. This technique can also be adapted for measuring liquids, but this requires a modified experimental setup (*113*) that will not be discussed in this thesis.

Compared to the 3ω method, FDTR offers several advantages: i) it requires minimal sample preparation, as only a thin transducer layer must be deposited on top of the sample; ii) it does not require electrical contacts; iii) it is suitable for measuring electrically conductive materials; iv) it is particularly indicated for thin films and other nanostructures. FDTR has also some drawbacks: i) it requires a smooth sample surface; ii) the material under study must not absorb the radiation of the lasers (only the transducer); iii) the experimental setup is more complex and expensive. Furthermore, extracting thermal parameters from FDTR measurements relies on intricate thermal modeling, requiring careful consideration of interface effects and heat transport mechanisms to ensure accurate data interpretation.

Figure 2.17 shows a simplified scheme of our experimental FDTR setup. Two laser beams, a pump (λ= 405 nm) and a probe (λ= 532 nm), are focused at the same point on the surface of the sample. The sample is first coated with a metallic layer, which acts as a transducer. In our experiments, we have deposited a thin layer of Au, with a thickness between 60-100 nm. At the wavelength of the pump, Au shows an almost complete absorbance, thus transforming the energy of the laser into heat.

Moreover, the pump laser is intensity-modulated over a frequency range of 20 kHz to 50 MHz, which induces the periodic heating of the sample surface. Then, a continuous probe laser detects these temperature variations by measuring changes in surface reflectivity (ΔR), a phenomenon known as thermoreflectance effect. Note that at the wavelength of the probe, Au reflects most of the energy of the incoming laser.

For small temperature variations (<10 K), the change in reflectivity is proportional to the change in surface temperature (ΔT), and can be expressed as (*114*):

$$\Delta T = \left(\frac{dR}{dT}\right)^{-1} \Delta R = \beta^{-1} \Delta R \qquad \textit{(Eq. 2.17)}$$

where *dR/dT* is the thermoreflectance coefficient.

To ensure precise optical alignment, a beam splitter and dichroic mirrors are used to direct and separate the optical paths of the pump and probe lasers. A microscope objective lens focuses both beams onto the same point of the sample surface, while a photodetector captures the reflected probe signal. To improve the signal-to-noise ratio at low modulation frequencies and compensate for phase-shift offsets introduced by beam paths and electronic components, a portion of the modulated pump beam is split off and sent to a reference photodetector identical to the primary one. This setup ensures an accurate determination of the phase of the pump as it reaches the sample.

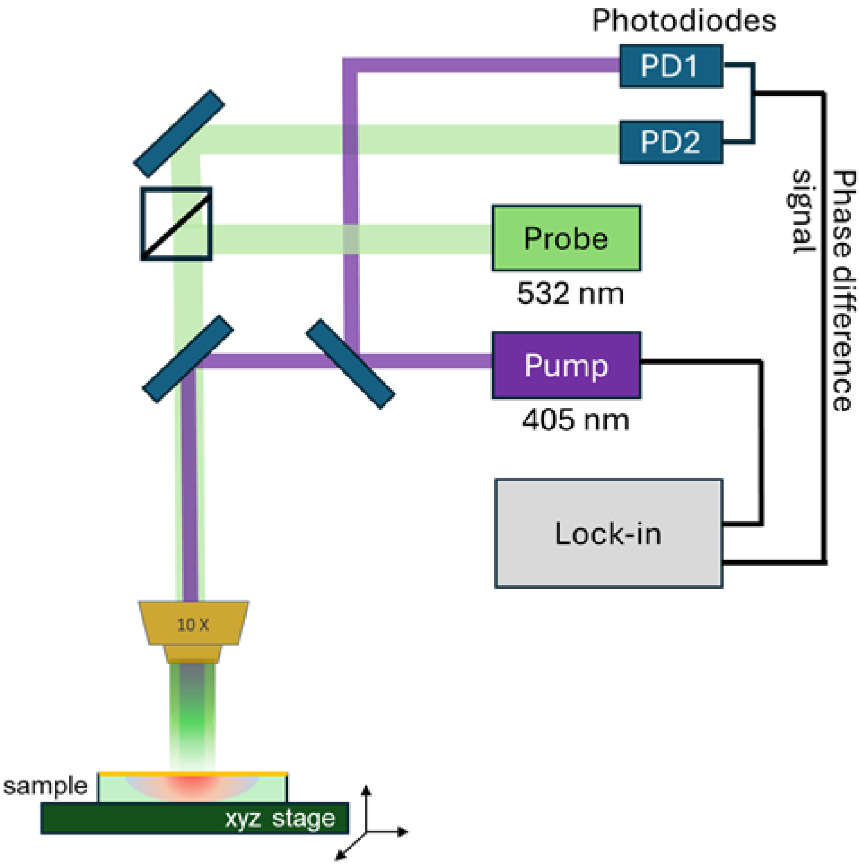

Figure 2.17. Simplified scheme of the FDTR experimental setup used in this thesis. A frequency-modulated pump laser is absorbed by the Au transducer, generating a periodic thermal wave in the sample. The resulting temperature variations are detected by a probe laser through thermoreflectance effect. The phase lag between both lasers is analyzed and fitted into a thermal diffusion model, enabling precise determination of the material's thermal conductivity.

A lock-in amplifier extracts the amplitude and phase of the temperature response, which are analyzed as a function of the pump modulation frequency. The phase lag between the thermal wave (probe) and the modulated heating signal (reference of the pump) contains information about the material's thermal properties.

Our experimental setup enables FDTR measurements using two different pump spot sizes, with Gaussian $1/e^2$ radii of ≈3.8 and ≈10.5 μm. The spot size is measured by fitting the spatial derivative of the pump signal to a Gaussian profile in both x and y directions (**Figure 2.18**), with a typical repeatability of ±0.05 μm. Moreover, to ensure accurate sample alignment, the sample height is carefully adjusted with a piezoelectric stage until the image on a CCD camera is in sharp focus, ensuring that the sample plane coincides with the measured spot profiles (*115*).

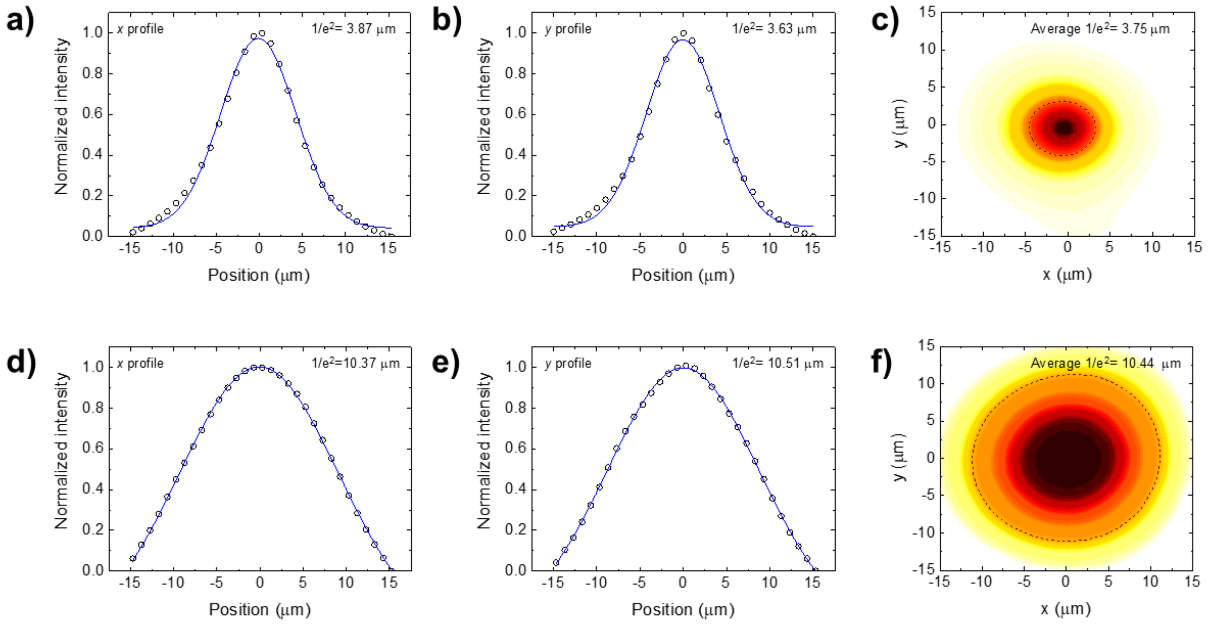

Figure 2.18. Gaussian fitting of the pump spot size in both *x* and *y* directions, along with the corresponding 2D intensity map, for the two spot sizes available in our FDTR experimental setup. a,b) Gaussian fits for the smaller spot size, yielding 1/e² radii of 3.87 µm (*x*) and 3.63 µm (*y*), with an average 1/e² radius of 3.75 µm. c) Corresponding 2D intensity map, where the average spot radius is marked with a dashed line. d,e) Gaussian fits for the larger spot size, with 1/e² radii of 10.37 µm (*x*) and 10.51 µm (*y*), resulting in an average 1/e² radius of 10.44 µm. f) Corresponding 2D intensity map, with the average spot radius also indicated by a dashed line.

After the measurement, the experimental data of the pump-probe phase difference is fitted to an analytical solution of the heat diffusion equation in a multilayer system, as described in refs. (*112*, *116*). In this model, the heat capacity, thermal conductivity and thickness of each layer (Au transducer, thin film and substrate) must be considered, as well as the thermal boundary conductance (TBC) between the different layers (**Figure 2.19**b).

In our case, the heat capacity of the substrates used in this thesis was determined from previous experiments in a PPMS from Quantum Design, and the thermal conductivity was obtained from ref. (*10*). The heat capacity of the films was either obtained from literature or estimated from ab initio calculations (performed by Dr. Marcel S. Claro), and sample thickness was measured by X-ray reflectivity. In the case of the Au transducer, we obtained the heat capacity from ref. (*117*). Moreover, we co-deposited Au on cover glass substrates, determined the thickness by XRR, measured the electrical conductivity (σ) and used the Wiedemann-Franz law (*Eq. 1.7*) to obtain its thermal conductivity:

To differentiate the influence of the thermal boundary conductances (TBCs) from the intrinsic thermal conductivity of the samples, we deposited the thin films on only half of the substrate, while the Au transducer covered both regions, as depicted in **Figure 2.19**a. This was achieved by masking part of the substrate during film deposition. The bare substrate region allowed us to independently determine the Au/substrate thermal boundary conductance, which was then used as an initial value for fitting the Au/film TBC (TBC1).

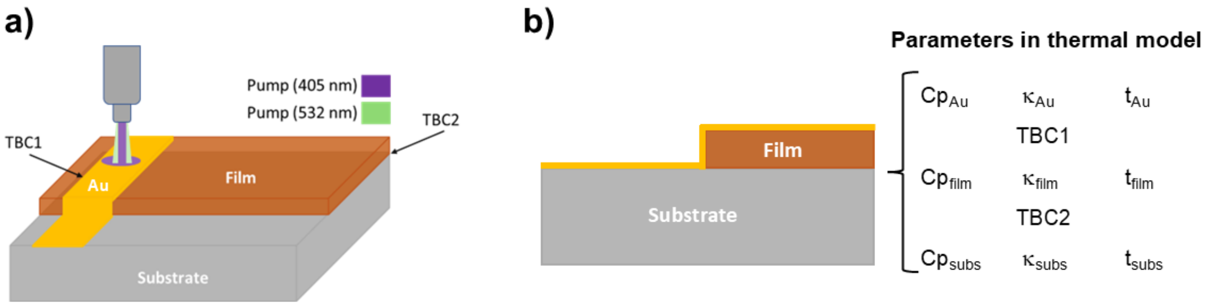

Figure 2.19. a,b) Schematic description of the thin films studied in this thesis. Half of the substrate was covered during film deposition, but Au transducer was deposited in both regions. As a result, we can simultaneously measure the thin film and substrate. The different parameters introduced in the thermal model for fitting the experimental data are highlighted in (b), where *Cp*, κ and *t* refer to the heat capacity, thermal conductivity and thickness of each layer, respectively.

The values of TBC1 (Au/film interface), TBC2 (film/substrate interface), and the film's thermal conductivity were determined by independently fitting the experimental data within the frequency range where their sensitivities are maximized. To quantify the influence of each parameter (α) on the phase signal (in radians), we define the sensitivity function as (*118*):

$$S(\alpha) = \frac{d\phi}{d\ln\alpha} \qquad \textit{(Eq. 2.18)}$$

For an accurate determination of the thermal conductivity of our films, the measurements should exhibit a high sensitivity to this parameter while presenting lower sensitivity to the other parameters in the model. **Figure 2.20** presents the sensitivity analysis to the thermal conductivity of a $CaFeO_{2.5}$ (≈15 nm thick) thin film deposited on STO, at different values of TBC1 and TBC2. As shown in the figure, the frequency range where the sensitivity to the thermal conductivity of the film is maximized is ≈10^6-10^7 Hz, in all cases. However, the extent of this sensitivity depends on the specific values of the TBCs, particularly in the case of TBC1.

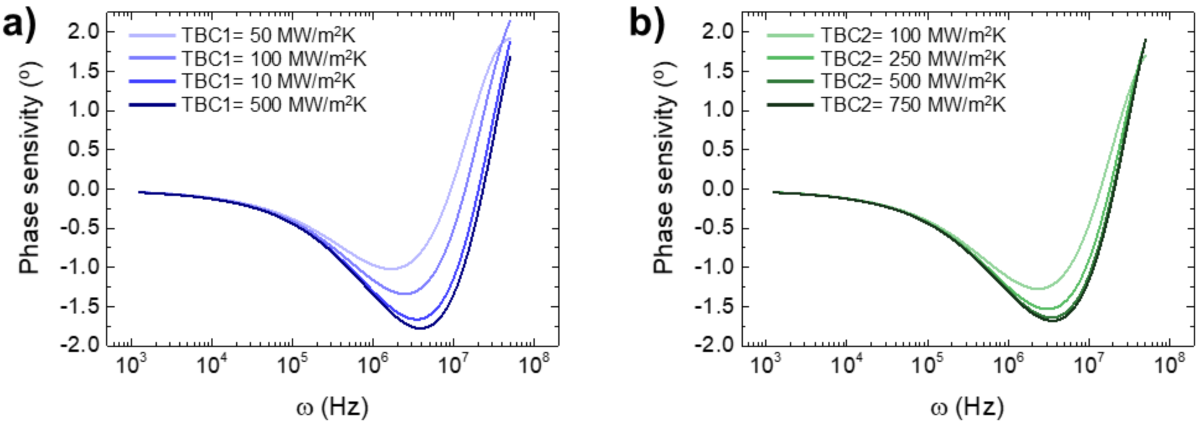

Figure 2.20. Phase sensitivity analysis to the thermal conductivity of a 15 nm thick $CaFeO_{2.5}$ thin film deposited on STO, maintaining all the parameters constant except for TBC1 (panel a, with TBC2 fixed at 250 MW/m^{2}K) and TBC2 (panel b, with TBC1 fixed at 10 MW/m^{2}K). As the values of TBC1 and TBC2 change, the sensitivity of our measurements to the thermal conductivity of the sample varies, either increasing or decreasing.

To effectively decouple the sensitivity of the different parameters, we conducted measurements in samples of different film thicknesses and employed the two pump spot sizes

(Gaussian spot sizes 1/e^2 radii ≈3.8 and 10.5 μm); a smaller spot size provides enhanced resolution and lower noise levels, whereas the larger spot size generally increases sensitivity to certain parameters such as film's through-plane thermal conductivity, due to the more one-dimensional nature of heat flow in this regime (*115*).

This approach allows us to identify distinct frequency ranges where each parameter contributes most significantly, as demonstrated in **Figure 2.21**, while maintaining an increased sensitivity to the sample's thermal conductivity compared to the TBCs. As a result, by fitting each parameter within its optimal frequency range, we obtained an accurate determination of the thermal conductivity of the film. Note that the sensitivity analysis shown in **Figure 2.21** is provided as an example, this procedure was systematically applied to all the samples studied in this thesis to ensure reliable and reproducible results.

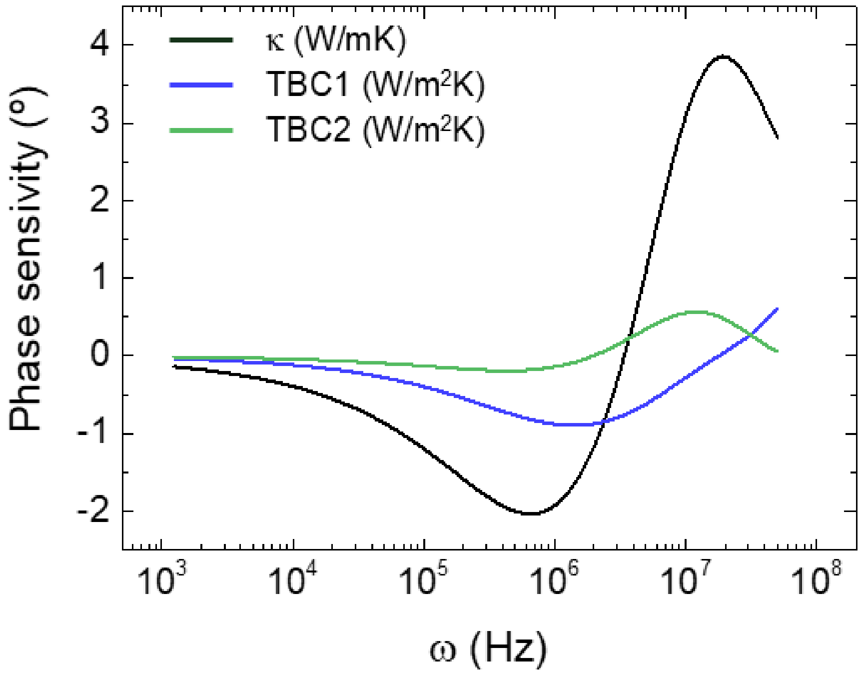

Figure 2.21. Sensitivity analysis of the thermal conductivity and thermal boundary conductances (TBC1 and TBC2) of a CaFeO$_{2.5}$ thin film (≈40 nm) deposited on a SrTiO$_3$ substrate, using the smaller spot size (1/e^2 radius of ≈3.8 mm). By combining different spot sizes and sample thickness, it is possible to decouple the maximum sensitivity region for each parameter, ensuring the accurate determination of the thermal conductivity of the film as well as the TBCs.

Figure 2.22 presents the experimental FDTR data of CaFeO$_{2.5}$ thin film (≈40 nm) deposited on SrTiO$_3$, along with the best-fit curve (grey line) for the thermal conductivity. To further validate the accuracy of our results, the figure also presents the effect of varying TBC1 (a) or TBC2 (b) by ±25% (blue/red dashed lines) on the thermal conductivity fitting. As observed, the resulting changes in the fitting are negligible, confirming the robustness of the thermal conductivity determination and validating our procedure. In this case, the different fits to the experimental data yielded a thermal conductivity of 2.5 ± 0.2 W/mK.

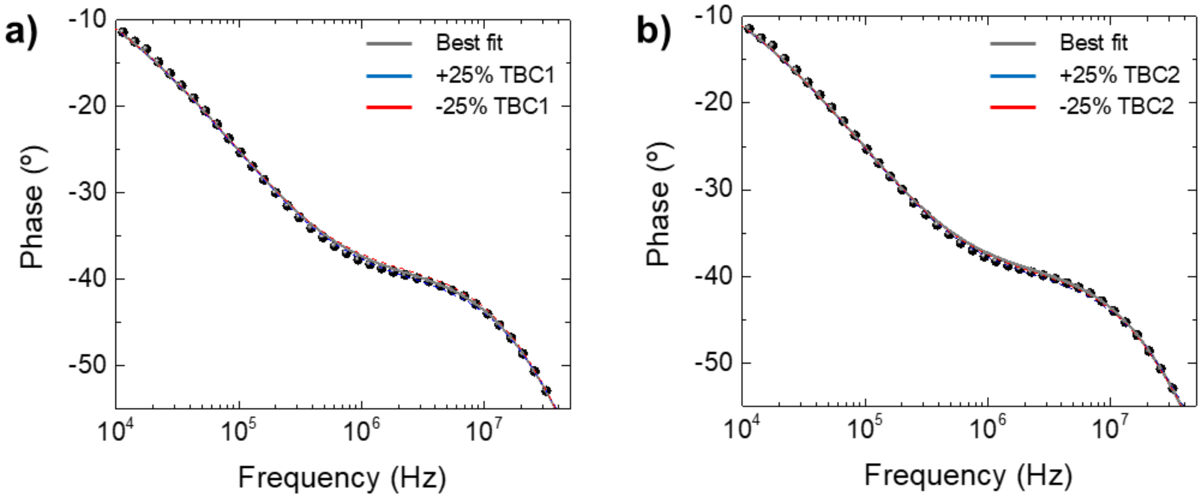

c)

Layer	Cp (MJ/Km³)	κ (W/mK)	Thickness (nm)	TBC (MW/m²K)
Au transducer	2.4	55	60	70
$CaFeO_{2.5}$ film	2	*fitting parameter*	40	100
$SrTiO_3$ substrate	2.6	9	$5·10^5$	

Figure 2.22. a,b) FDTR phase lag data for a $CaFeO_{2.5}$ thin film (≈40 nm) deposited on STO, along with the best-fit to the thermal conductivity (grey line). Blue/red dashed lines show the effect of varying TBC1 (a) and TBC2 (b) by ±25%, respectively. As observed, in both cases the change in thermal conductivity fitting is negligible, demonstrating the robustness of our method. c) Table containing the parameters used for fitting the curves in (a,b), where the thermal conductivity of the sample is the only free parameter.

The uncertainties in the thermal conductivity values obtained with this method typically range between 10% and 25%. These arise from various factors, including the accuracy of the fitting and uncertainties in key input parameters such as film thickness, heat capacity, and transducer layer thickness. To improve measurement reliability and minimize uncertainties, we conducted FDTR measurements at multiple spots sizes across the film, analyzed different sample areas, and investigated films of varying thicknesses.

Finally, apart from performing discrete measurements in our films (like those shown in **Figure 2.22**), our experimental setup includes an XYZ piezoelectric stage capable of precise displacement (±100 μm in each axis, with a step of 0.1 μm). This feature enables spatially resolved thermal conductivity measurements, allowing us to generate thermal conductivity maps and utilize FDTR as a microscopy imaging technique (*115*). The use of this piezo stage is key for the experiments discussed in Chapter 5.

Furthermore, our setup allows for temperature-dependent thermal conductivity measurements using an Instec thermal stage, which is integrated with a nitrogen pump and a temperature controller. This configuration enables measurements over a wide temperature range, from approximately 150 K to 773 K, as will be demonstrated in Chapter 6.

3. LIGHT-INDUCED THERMAL CONDUCTIVITY SWITCHING IN MESOPHASES

> *“I never am really satisfied that I understand anything; because, understand it well as I may, my comprehension can only be an infinitesimal fraction of all I want to understand about the many connections and relations which occur to me.”*
>
> ---
>
> Ada Lovelace, British mathematician. She is considered the mother of Computer Programming.

The results presented in this chapter are published in:

“Light-induced bi-directional switching of thermal conductivity in azobenzene-doped liquid crystal mesophases” *Journal of Materials Chemistry C*, **2023**, 11, 4588-4594. https://doi.org/10.1039/D3TC00099K

Noa Varela-Domínguez[1], Carlos López-Bueno[1], Alejandro López-Moreno[1,2], Marcel S. Claro[1], Gustavo Rama[1], Víctor Leborán[1], María del Carmen Giménez-López[1], and Francisco Rivadulla*[1]

[1]CiQUS, Centro Singular de Investigación en Química Biolóxica e Materiais Moleculares, 15782-Santiago de Compostela, Spain

[2]Present address: IMDEA Nanociencia, 28049-Madrid, Spain.

Editorial: The Royal Society of Chemistry   ISSN: 2050-7534

Personal contribution: synthesis and structural characterization of azobenzene derivatives, thermal conductivity measurements, analysis and discussion of results.

5-Year Impact Factor: 5.6. Q1 in Applied Physics. This article was featured on the inside front cover (https://doi.org/10.1039/D3TC90076B).

3.1. INTRODUCTION

Over the past decades, there has been intense research in the field of thermal regulation, particularly in the development of materials that function as thermal switches. However –as inferred from the introduction of this manuscript–, this research focused mostly on solids, such as ferroelectrics (*80*, *82*, *83*), multilayers (*58*, *59*, *119*) or oxides and chalcogenides with complex structures (*120–122*). In contrast, despite their widespread use in classical thermal dissipation, liquids (including pure liquids and additive-liquid mixtures) are practically unexplored for thermal switching, mainly because the mechanisms of heat transport are not as well understood.

An interesting approach that bridges the gap between solids and liquids is the use of materials belonging to the "soft-matter" classification, such as gels, colloids, polymers, or mesophases. These materials offer a unique combination of properties: they maintain a more efficient heat conduction than liquids, with mechanisms more assimilable to crystalline solids, while also providing the flexibility of liquids to conform to different volumes and surfaces. This adaptability is particularly advantageous in dynamic environments or irregular geometries, where rigid solids may struggle to keep effective thermal contact. Furthermore, soft-matter systems can respond to external stimuli like temperature, pressure, or electric fields, enabling a priori reversible and tunable thermal conductivity. This responsiveness makes them ideal candidates for the development of advanced, switchable thermal devices that require precise control over thermal transport.

Among soft-materials, polymers garnered considerable attention as potential thermal switches. For example, Ishibe *et al.* (*123*) demonstrated that block copolymers can be engineered to exhibit a reversible change in their thermal conductivity through order-order transitions. Similar studies have been conducted on polyethylene nanofibers (*124*, *125*), where phase transition results in significant morphological changes, leading to impressive ON/OFF ratios of up to ≈12. However, these systems only exhibit thermal switching within a narrow temperature window, limited to the phase transition, which restricts their practical applications.

On the other hand, Tomko *et al.* (*126*) developed bio-inspired polymeric materials capable of large, reversible changes in thermal conductivity by manipulating their network topology and hydration levels, as shown in **Figure 3.1**b. While this approach achieved high modulation ratios and fast switching times, it is less feasible in environments where precise control of moisture levels is difficult or impractical.

An innovative approach for controlling thermal transport involves the use of light to modulate the properties of photoactive molecules. Nobel Laureate Ben Feringa has pioneered the development of molecular switches and molecular machines (*127–130*). These molecules, containing photoactive functional groups, undergo changes in their structure or spatial organization when exposed to light of specific wavelengths, modulating properties such as chemical reactivity, electrical conductivity, or mechanical behavior. Shin *et al.* (*131*) extended this concept to thermal transport by using UV/Vis irradiation cycles to tune the thermal conductivity of azobenzene-based polymers, triggering a crystal-to-liquid transition that results in a remarkable 60% change in thermal conductivity (*132*).

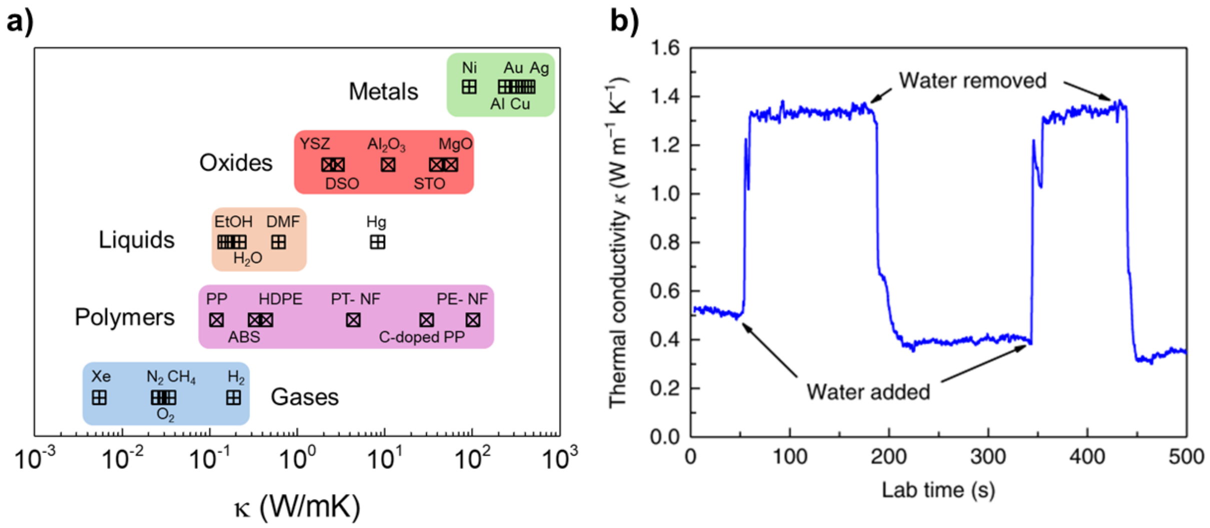

Figure 3.1. a) Thermal conductivity of different materials at room temperature. Data reproduced from references (*10, 29, 30, 133-138*). b) Thermal conductivity switching during hydration/dehydration cycles in the bio-polymers studied by Tomko and coworkers. Reproduced with permission from ref (*126*). Copyright (2018) Springer Nature.

The underlying mechanism of this method relies on the photochemical isomerization of the azobenzene group, which exists in two isomeric forms: the thermodynamically stable *trans* isomer, which has a rod-like shape, and the less stable *cis* isomer, characterized by a bent molecular structure. Upon irradiation at specific wavelengths within their absorption bands, azobenzene undergoes reversible isomerization between these two states (*139*), as schematized in **Figure 3.2**. The absorption spectra of the *trans* and *cis* isomers are defined by π-π* and *n*-π* electronic transitions, which are sensitive to substituents of the azobenzene molecule. When these absorption bands overlap, irradiation at the coinciding wavelength range promotes efficient *trans-cis-trans* isomerization cycles, leading to molecular reorientation (*140*, *141*). This dynamic behavior directly impacts the material's thermal properties during light exposure.

Although the method presented by Shin and coworkers (*131*) enables highly controllable and remote regulation of thermal conductivity, its effectiveness is sometimes compromised by incomplete reversibility in some polymeric azobenzenes, mainly due to the restricted orientational mobility of *trans* isomers at room temperature (*142*).

As we will demonstrate in this chapter, this limitation can be overcome by using molecular azobenzene derivatives (instead of polymeric azobenzenes) that self-assemble either into 3D crystals or liquid crystal mesophases close to room temperature. In principle, the thermal conductivity of these molecular mesophases could be directly modified by UV/Vis irradiation, while keeping the *trans-cis* isomerization completely reversible.

In the *trans*-configuration, the phenyl groups are nearly co-planar with the azo-group, and the molecules are relatively flat, which facilitates strong π-π interactions and molecular self-assembly. As a result, many of these molecules form crystals or mesophases (liquid crystals) at room temperature. On the other hand, in the *cis* configuration the molecule is bent, and the phenyl groups are not coplanar, which reduces π-π interaction, and results in a liquid-like isotropic arrangement.

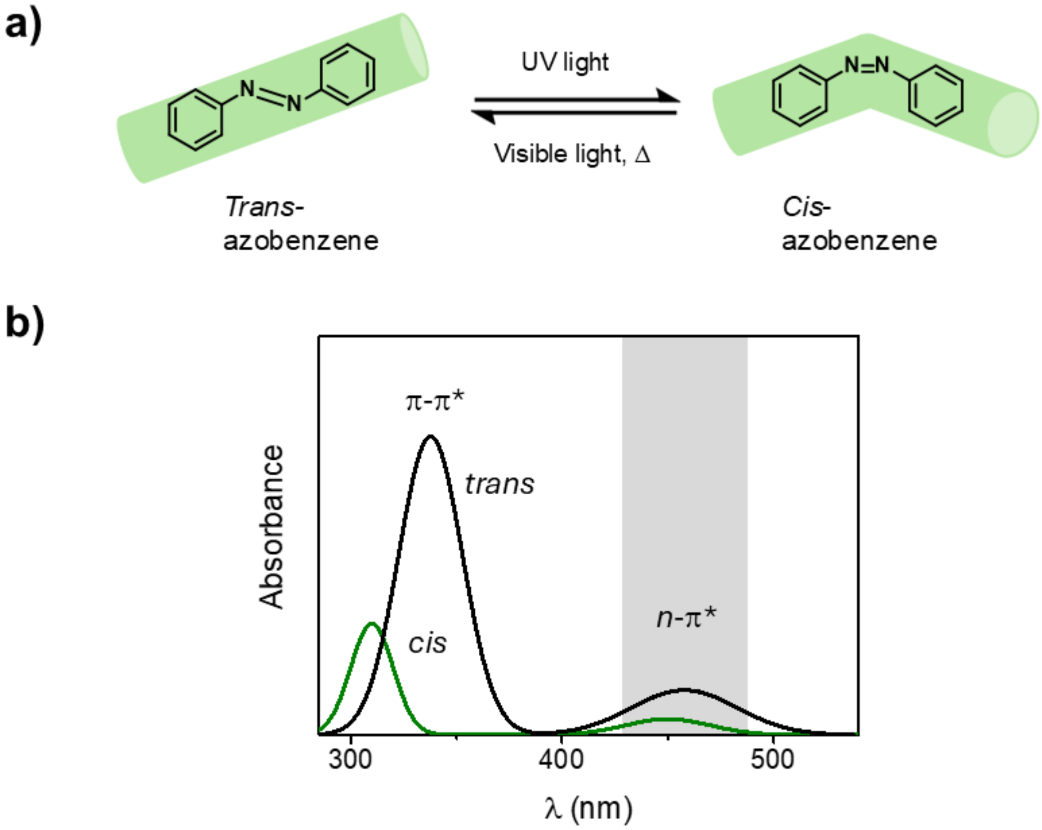

Figure 3.2. a) Schematic illustration of the reversible *trans*-*cis* isomerization of an azobenzene molecule. The transition is triggered by light of specific wavelengths: ultraviolet light induces the transformation from the *trans* to the *cis* isomer, while visible light or heat reverts the molecule back to the *trans* configuration. b) Representative absorption spectra of *trans* and *cis* isomers. Both isomers exhibit overlapping *n*-π* transition in the visible region, which can be exploited for reversible isomerization cycles. The absorption spectra of both isomers are sensitive to azobenzene substitutions.

The research group led by Yasuo Norikane made significant contributions to the synthesis of photosensitive molecular azobenzenes (*143*), providing insights into the structural requirements for achieving reversible light-induced crystal-to-liquid transitions close to room temperature. In particular, they investigated a series of rod-shaped dialkyloxy-azobenzene derivatives with methyl group substitution at different positions: at the 3-position (structures 2a-c, **Figure 3.3**), at both the 3- and 3'-positions (structures 3a,b) or omitted entirely (structures 1a,b).

Their experiments revealed that the asymmetry introduced by the methyl group in the 2a-c structures hinders the packing and weakens the intermolecular interactions during self-assembly, promoting a crystal-to-liquid phase transition at room temperature under UV/Vis excitations (*89*). In contrast, this behavior has not been observed in the totally symmetric structures (1a,b and 3a,b).

Interestingly, the variation in phase transition behavior among these derivatives cannot be fully explained by the molecular arrangements in the crystal lattice, as compounds 2b and 3b, for example, exhibit nearly identical crystal structures. However, studies identified a key difference in the melting point of the *cis* isomers: the *cis* isomer of 2b melts at -6 ºC, while the *cis* isomer of 3b has a significantly higher melting point of approximately 90 ºC, preventing photoinduced liquefaction at room temperature. These findings highlight how subtle structural modifications, such as the placement of a methyl group, can drastically alter thermal behavior.

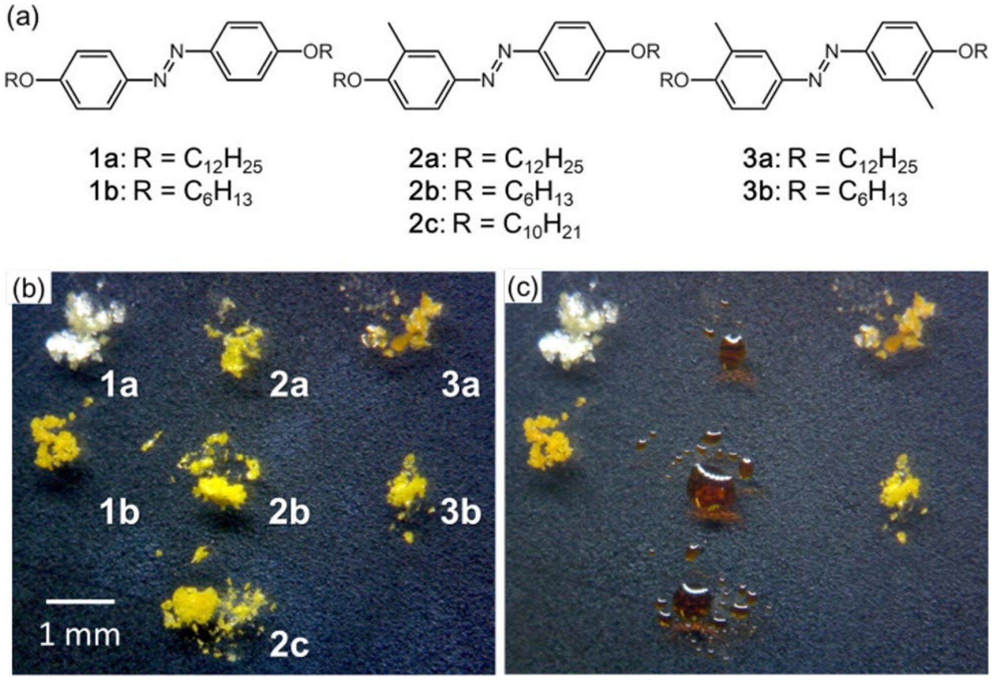

Figure 3.3. a) Chemical structures of the azobenzene derivatives studied by Norikane and coworkers. b) Photograph of the crystalline powders of the different azobenzene derivatives. c) Photograph of the same powders displayed in (b) after irradiation with UV (365 nm) light, at room temperature. Photoinduced liquefaction only takes place in the azobenzene derivatives with a methyl group in the 3-position (structures 2a-c). Reproduced with permission from ref. (*89*). Copyright (2014) American Chemical Society.

On the other hand, they also reported that, for structures with methyl group at the 3-position (structures 2a-c), compounds with alkyloxy chains of 7 to 12 carbon atoms exhibited liquid crystalline behavior close to room temperature, opening new possibilities for designing azobenzene-based materials with tunable phase transitions and liquid crystalline properties (*88*). Therefore, this family of asymmetric molecules could provide a good starting point in the search for photochromic molecular materials where reversible thermal conductivity states can be achieved under mild conditions.

In this chapter, we report the performance of these azobenzene derivatives as light-controlled thermal switches. Specifically, we examine the influence of the alkyl chain length on the thermal stability and thermal conductivity of the materials. In addition to studying the influence of temperature/light on the thermal conductivity of each azobenzene derivative, we also report the potential of these molecules to be used as photoactive dopants: by incorporating these molecules into host matrices, we achieved light-induced modulation of the thermal conductivity of the entire system. While this strategy has been widely used for tuning the morphology and physical properties of the host matrix (*144–147*), this is the first time that it is applied to the modulation of thermal conductivity.

3.2. RESULTS AND DISCUSSION

3.2.1. Structural characterization of the azobenzene derivatives

For this study, we synthesized a series of 4,4’-dialkyloxy-3-methylazobenzene derivatives with different alkyl chain lengths, -OR= $-OC_nH_{2n+1}$, n= 3, 5, 6, 8, 10 and 14 (**Figure 3.4**). The synthesis of these azobenzene derivatives was done using a multi-step process based on a previously established route (*88*, *89*), as described in Chapter 2 (section 2.1.1).

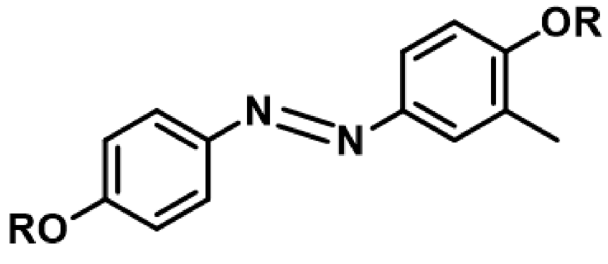

$R_1 = C_3H_7$ $R_4 = C_8H_{17}$
$R_2 = C_5H_{11}$ $R_5 = C_{10}H_{21}$
$R_3 = C_6H_{13}$ $R_6 = C_{14}H_{29}$

Figure 3.4. Chemical structure of the 4,4’-dialkyloxy-3-methylazobenzene derivatives synthesized in this work.

All the azobenzene derivatives were structurally characterized by ^{1}H-NMR spectroscopy (see Annex I), which confirmed the successful formation of the desired molecular structures. This technique also verified that the *trans* isomer is the thermodynamically stable structure for all derivatives, with one notable exception: for the azobenzene with n= 5, signals corresponding to the *cis* isomer were observed at room temperature, as shown in **Figure 3.5**a. Quantitative integration of these signals indicated that approximately 10% of the azobenzene exists in the *cis* form at room temperature. Upon increasing the temperature of the experiment, the signals corresponding to the *cis* isomer disappear, due to the thermal reconversion of the *cis* isomer back to the thermodynamically favored *trans* from, highlighting the temperature-dependent dynamics of the isomerization process.

Similarly, irradiating with UV-light the azobenzene derivatives leads to *trans*-*cis* photoisomerization, thus appearing the signals corresponding to the *cis*-isomer in the ^{1}H-NMR spectrum. This is exemplified in **Figure 3.5**b, where ^{1}H-NMR spectra of the azobenzene with n= 6 carbon atoms (in deuterated chloroform) before and after UV illumination, are shown. Irradiating with UV light the azobenzene solution inside NMR tube for 90 min results in a mixture of both *trans* and *cis* isomers. Longer illumination times would resul(*147*)the complete *trans*-*cis* isomerization (*148*).

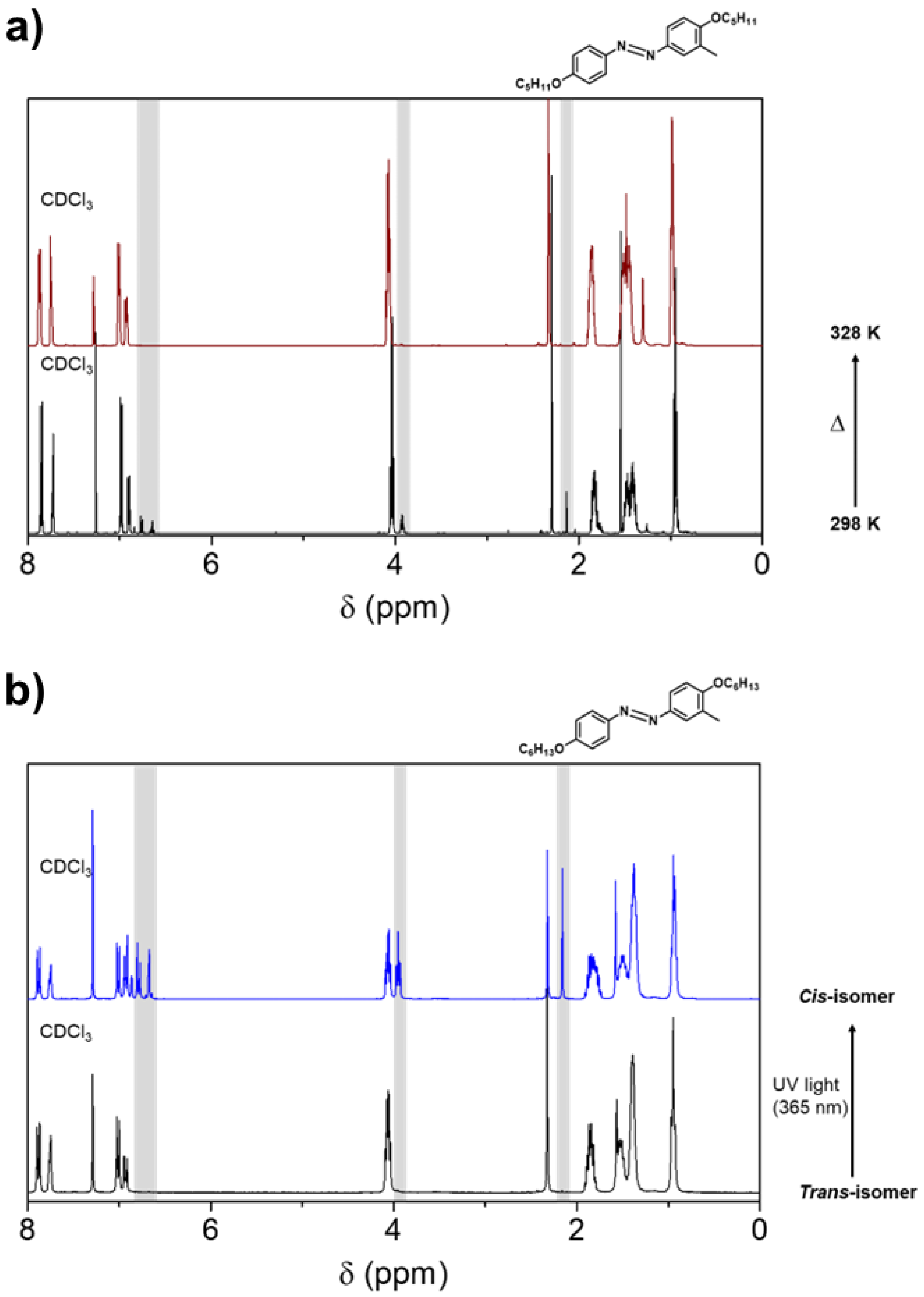

Figure 3.5. a) ^{1}H-NMR spectra of 4,4'-dipentoxy-3-methylazobenzene in CDCl$_3$, at room temperature (bottom panel) and at 328 K (top panel). Increasing temperature leads to *cis-trans* thermal reconversion, thus disappearing the signals from the *cis*-isomer (marked with a grey shadow). b) ^{1}H-NMR spectra of 4,4'-dihexyloxy-3-methylazobenzene in CDCl$_3$ at room temperature (bottom panel, no signals corresponding to the *cis* isomer are observed) and after irradiation with UV light for 90 min (top panel). After illumination, *trans-cis* photoisomerization occurs, appearing signals from the *cis* isomer (marked with a grey shadow).

In its dense pure form, strong intermolecular interactions cause these molecules to self-assemble into 3D crystalline structures or 3D/2D liquid crystal phases, below a certain temperature. The limits of the thermal stability of these phases for the different azobenzene derivatives were investigated by differential scanning calorimetry (DSC). To ensure the accuracy of the measurements, four consecutive heating/cooling cycles were performed for each sample, with a temperature ramp rate of 10 K/min. The resulting DSC scans are presented in **Figure 3.6**.

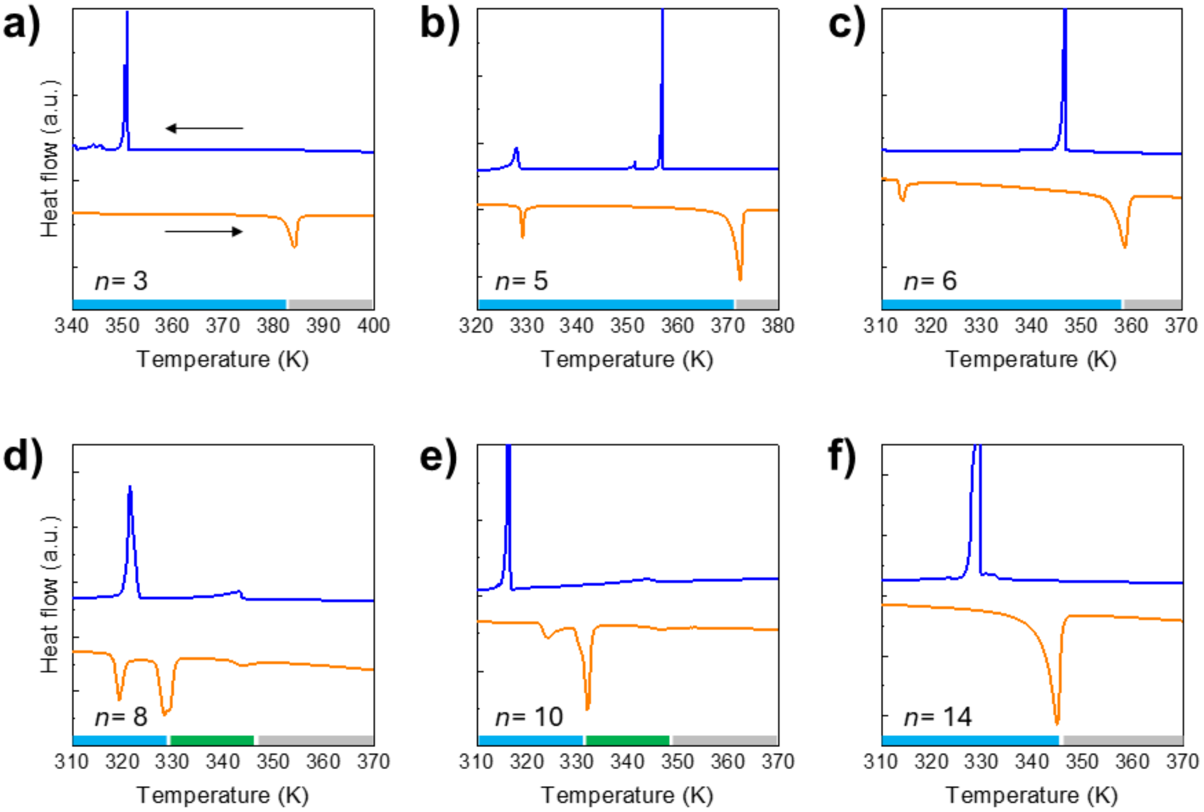

Figure 3.6. Differential scanning calorimetry scans of the azobenzene derivatives with alkyl chains of *n*= 3 (a), 5 (b), 6 (c), 8 (d), 10 (e) and 14 (f) carbon atoms. The scans were performed at a heating rate of 10 K/min, and results were recorded in “exothermic up” mode. Blue bars represent the temperature stability limits of crystalline phases, while green and grey bars correspond to intermediate nematic liquid crystal, and isotropic liquids, respectively. For molecules with *n*= 5, 6, 8 and 10, two distinct crystalline phases are observed, as evidenced by the initial endothermic peaks (310-330 K). In the case of *n*= 8 and 10, the presence of a nematic phase indicates a transitional alignment between the ordered crystalline structure and the disordered isotropic liquid. All scans were recorded after 4 heating/cooling cycles, to ensure reproducibility.

In agreement with the results by Norikane *et. al* (*88*), the thermal analysis revealed very distinct thermal behaviors with the length of the alkyl chains (-OC_nH_{2n+1}). For *n*= 3, 5, 6, and 14, the transition occurs directly from a crystalline solid phase (denoted by blue bars in **Figure 3.6**) to an isotropic liquid phase (denoted by grey bars in the same figure). However, for derivatives with *n*= 8 and 10, an intermediate phase (green bars) associated to a nematic liquid crystal that appears between the crystalline phase and the isotropic liquid, is observed. This nematic phase is characterized by long-range orientational order, where the molecules align preferentially along one spatial direction, while lacking positional order typical of a 3D crystal (*149*).

Additionally, molecules with *n*= 5, 6, 8 and 10 carbon atoms exhibit two distinct crystalline phases that are stable near room temperature. These crystal-to-crystal transitions are marked by the first endothermic peaks in the DSC scans, occurring between 310 and 330 K for these derivatives.

As said before, all phase transitions agree with previously reported data in literature, which ensures the purity of the molecules synthesized for this project (*88*).

The self-assembly into a nematic liquid crystal phase for the azobenzene derivatives with *n*= 8 and 10 carbon atoms in the alkyl chain was confirmed by polarized optical microscopy (POM). This technique is particularly useful for identifying liquid crystal phases because these materials have ordered fluid molecular arrangements that exhibit birefringence (*108*). By analyzing the observed textures and their behavior under varying conditions –such as temperature–, it is possible to confirm the presence of liquid crystalline phases, distinguishing between different types of mesophases –such as those depicted in **Figure 3.7**–, and study their transitions.

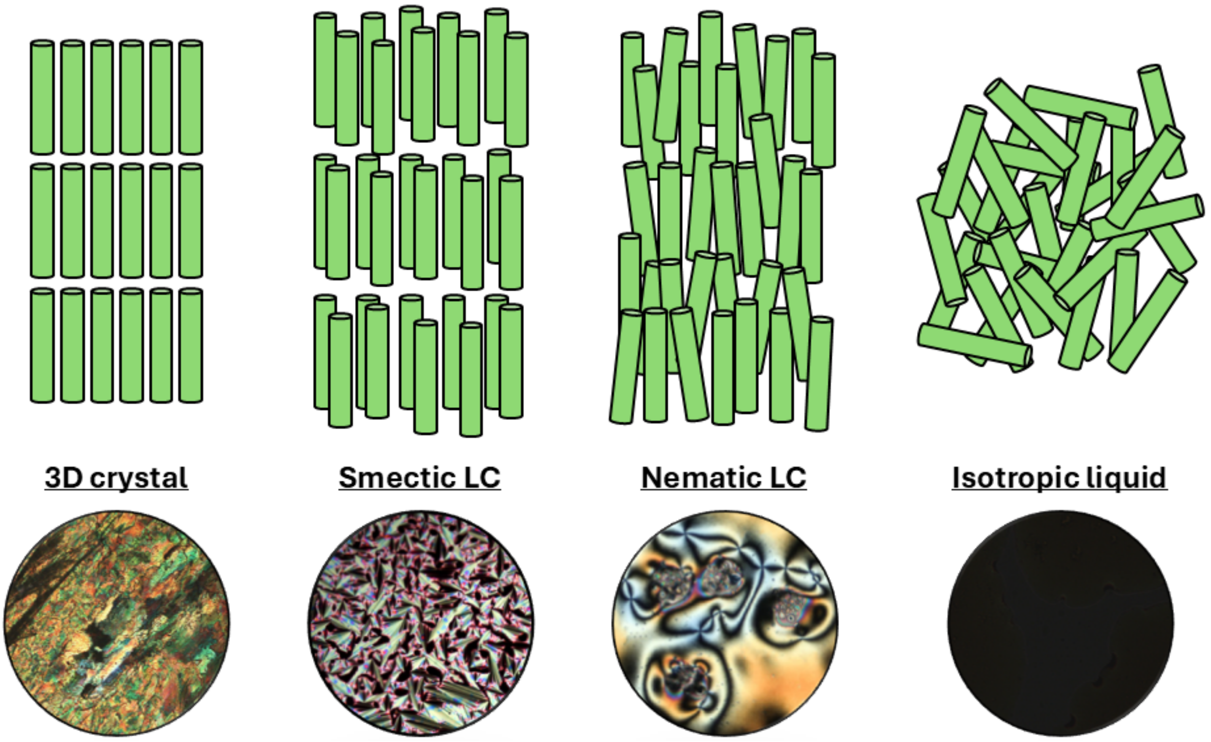

Figure 3.7. Schematic molecular organization in crystal, liquid crystal (smectic and nematic) phases and isotropic liquid of a material composed of elongated molecules, such as the azobenzene derivatives studied in this work. The corresponding POM images are shown below each scheme. In the smectic LC phase, the molecules are organized in layers, while in nematic liquid crystals the molecules exhibit only orientational ordering by staying nearly parallel to their neighbors. POM images of smectic and nematic LCs are reproduced with permission from ref. (*108*). Copyright (2018) IOP Publishing.

In our experiments, the polarized optical microscope was coupled to a Linkam thermal stage with a liquid nitrogen pump, allowing us to capture images at controlled temperatures. The samples were heated at 2 K/min from room temperature to their melting points. As observed in **Figure 3.8**, at room temperature, the azobenzene derivatives with *n*= 8 and 10 are in a crystalline state, displaying textures typical of solid anisotropic structures. Upon heating, these materials transition into the nematic liquid crystal phase, characterized by fluid textures and birefringent patterns in the POM images. Finally, at higher temperatures, the nematic phase melts into the isotropic liquid. In this phase, the sample becomes optically isotropic, and the POM image appears completely black, as there is no birefringence, and the crossed polarizers block all transmitted light. These phase transitions agree with those observed in the DSC scans shown in **Figure 3.6**d,e.

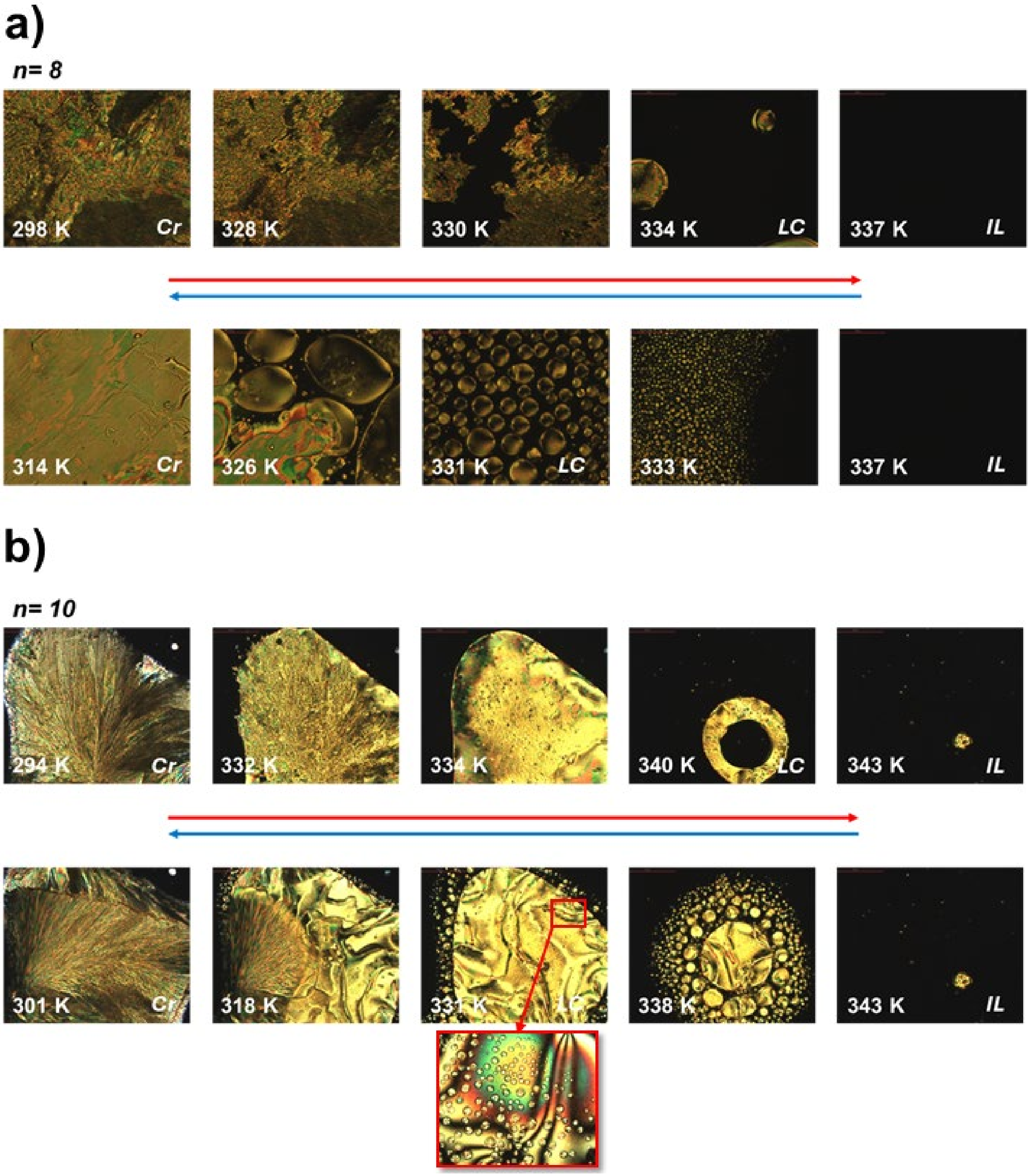

Figure 3.8. Polarized optical microscopy images of azobenzene derivatives with 8 (a) and 10 (b) carbon atoms in their alkyl chain, captured at different temperatures during heating (red arrows) and cooling (blue arrows). The stable phase at each temperature range is indicated, where Cr, LC and IL stand for crystal, liquid crystal, and isotropic liquid, respectively. The inset at 331 K (b) is a zoomed region of the LC, so that the birefringence characteristic of this phase can be easily appreciated.

All this information is summarized in **Figure 3.9**, where the thermal stability of each azobenzene derivative is specified.

Altogether, these experiments demonstrate that the number of carbon atoms in the alkyl chain determines the melting temperature of the different mesophases, having a minimum for *n*= 8 and *n*= 10. This is advantageous for applications where thermal transitions must occur near ambient conditions. Also, the light-induced transition between a nematic liquid crystal mesophase and an isotropic liquid may be studied with the purpose of thermal switching.

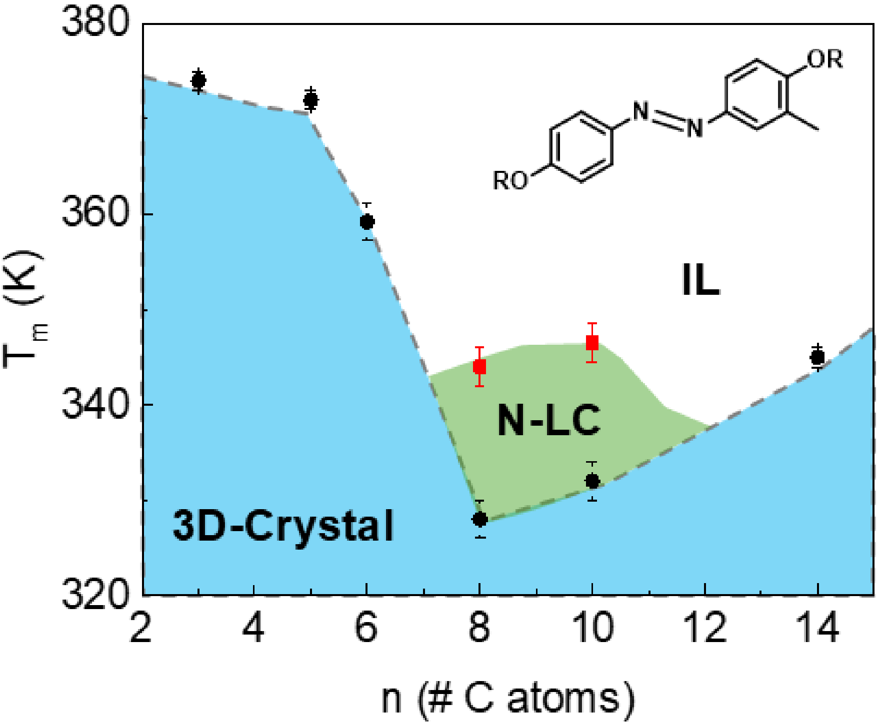

Figure 3.9. Phase diagram of the 4,4’-dialkyloxy-3-methylazobenzene derivatives with the number of carbon atoms in the alkyl chain; N-LC and IL refer to nematic liquid crystal and isotropic liquid, respectively.

After completing the structural and thermal characterization of the mesophases formed after self-assembly of the azobenzene derivatives, we investigated their ability to undergo photoisomerization under UV light, and its effect on the structure of the system. The *trans*-to-*cis* isomerization of 4,4’-dialkyloxy-3-methylazobenzene derivatives was followed, among other techniques, by UV-Vis absorption spectroscopy.

For this study, thin films of the azobenzene derivatives were prepared by spin-coating 20 μL of a solution of 3% of the different azo-derivatives on chloroform on Corning® borosilicate glass slides (11 x 22 mm). The absorption spectra of these films were recorded using a spectrophotometer coupled to a temperature controller, enabling measurements at different temperatures.

Figure 3.10a. illustrates the UV-Vis absorption spectra of a thin film of 4,4’-didecyloxy-3-methylazobenzene, recorded before and after UV illumination at room temperature. In the initial state the spectrum features a prominent absorption band near 360 nm, corresponding to the π-π* transition of the thermodynamically stable *trans* isomer. Upon exposure to UV light, a new absorption band appears at ≈450 nm, characteristic of the *cis* isomer, indicating successful isomerization (*89*). The decrease in intensity of the π-π* band further supports this transformation. Heating the sample to 333 K (**Figure 3.10**c, green line) results in the near-complete disappearance of the *cis* band, signifying thermal reconversion of the metastable *cis* isomer back to the *trans* configuration.

These UV-Vis absorption spectroscopy experiments have been performed for all the azobenzene derivatives studied in this work, demonstrating that a reversible *trans-cis* isomerization occurs in all cases under UV/Vis illumination.

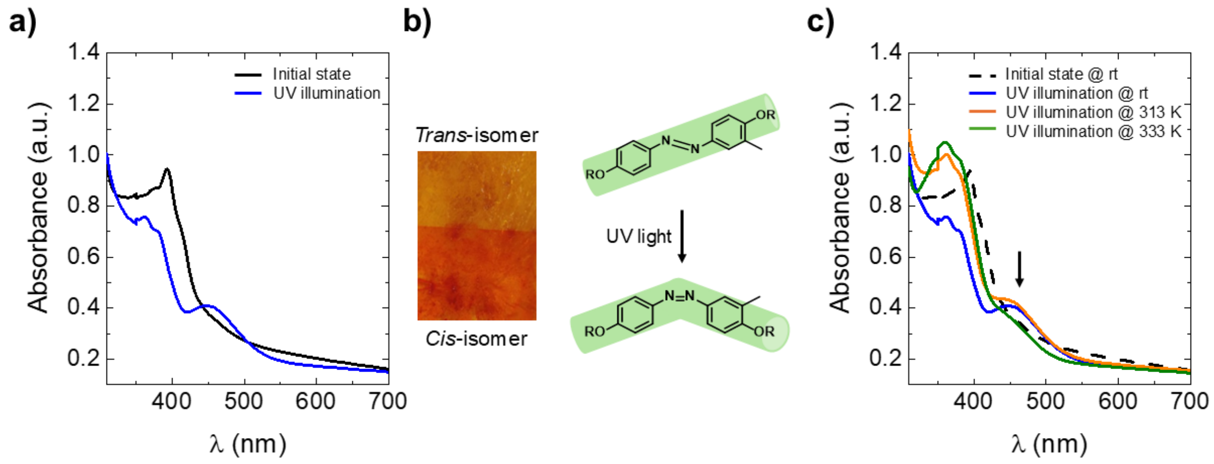

Figure 3.10. a) UV-Vis absorption spectra of a 4,4'-didecyloxy-3-methylazobenzene thin film as deposited (black line) and after 1 h illumination with UV light (365 nm, blue line). b) Optical microscopy photograph of a thin film whose upper half was covered during UV illumination; the *trans-cis* isomerization is accompanied by a notable change in color. c) UV-Vis absorption spectra of a 4,4'-didecyloxy-3-methylazobenzene thin film after UV illumination, and then heating at different temperatures, to study the effect of temperature in *cis-trans* reconversion.

The UV/Vis isomerization of the azobenzene derivatives was further investigated using polarized optical microscopy. In these experiments, the samples were maintained at a constant temperature while being irradiated with ultraviolet light (365 nm, ≈160 mW/cm^2). UV illumination triggers the *trans*-to-*cis* isomerization of the azobenzene derivatives, and in all cases, the *cis*-isomers exist as isotropic liquids at room temperature. As a result, polarized optical microscopy allows us to detect transition from an anisotropic phase (either a 3D crystal or a liquid crystal, depending on the temperature at which the UV irradiation is performed) into the *cis*- isotropic liquid.

Figure 3.11 shows POM images of 4,4'-didecyloxy-3-methylazobenzene during UV-illumination at two different temperatures: 313 K (panel a) and 338 K (panel b). At 313 K, UV light induces a transformation from the *trans*-crystalline solid to the *cis*-isotropic liquid.

On the other hand, irradiating the samples at 338 K promotes the transition from the *trans*-nematic liquid crystal to the *cis*-isotropic liquid. Notably, the improved molecular mobility within the liquid crystal mesophase significantly reduces the time required for the transition, from the nearly 20 minutes to convert the crystalline solid into the isotropic liquid, to only 26 s to go from the liquid crystal to the isotropic liquid.

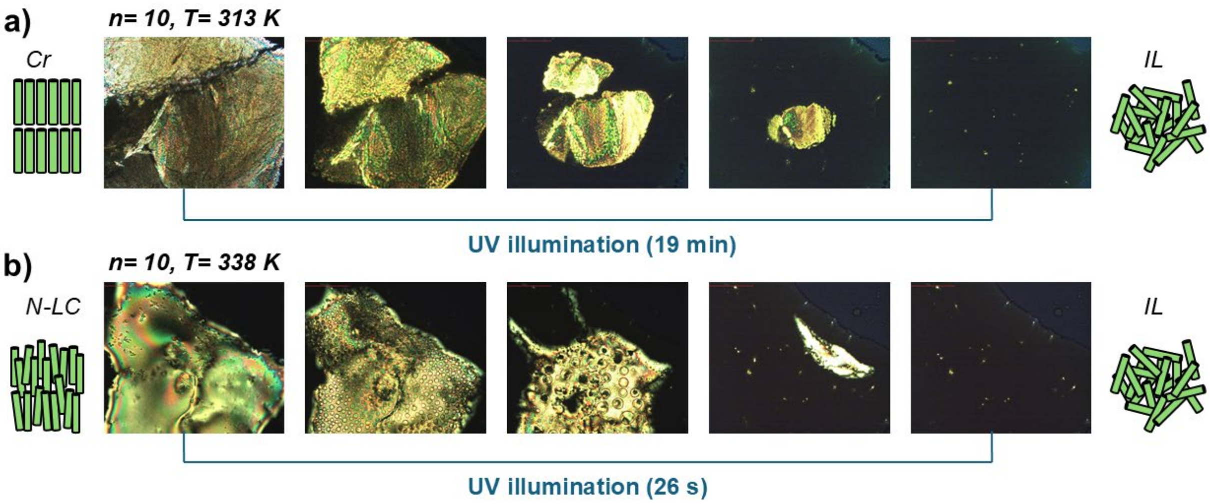

Figure 3.11. Polarized optical microscopy images of 4,4'-didecyloxy-3-methylazobenzene during UV illumination at 313 K for 19 min (a), showing the crystal to isotropic liquid transition (Cr to IL); and at 338 K for 26 s (b), inducing the nematic liquid crystal to isotropic liquid (N-LC to IL) transformation.

The different transformation paths are presented in **Figure 3.12**. As the temperature increases, the liquid crystal of the *trans*-isomer melts into the *trans*-isotropic liquid, while irradiating the liquid crystal with UV light transforms it into the *cis*-isotropic liquid. Additionally, it is possible to achieve a transformation between isotropic liquids through heating, since it drives the *cis*-*trans* thermal reconversion. These phase transformations present valuable strategies for designing thermal switches, as will be demonstrated next.

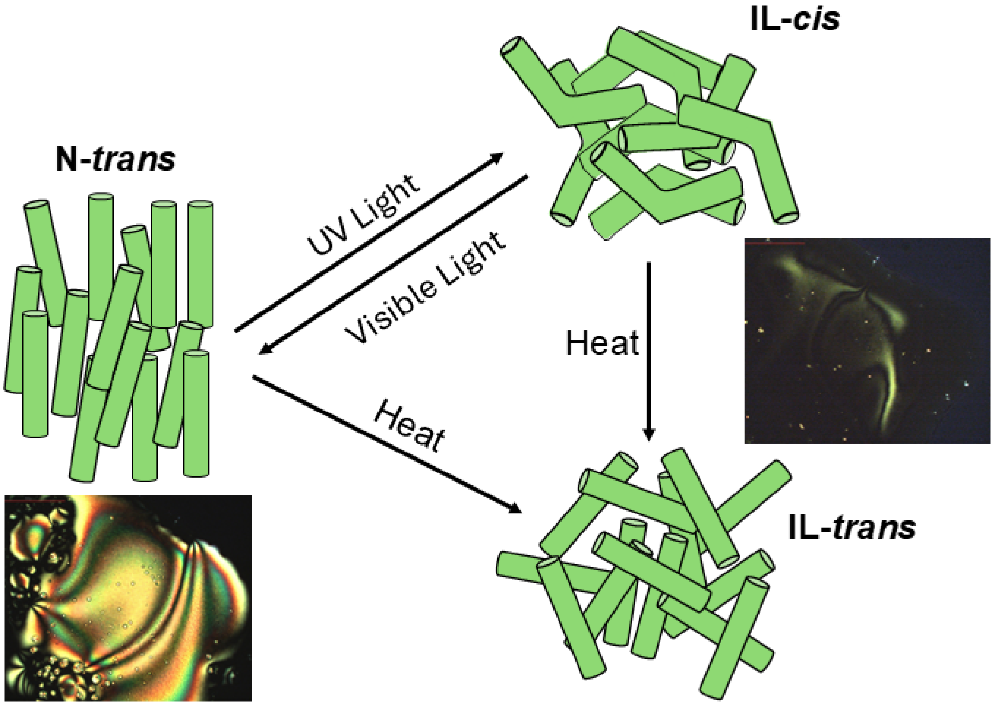

Figure 3.12. Scheme of the different phases, related to the two molecular isomers, achievable with temperature and UV/Vis light irradiation. The images were taken on a polarized optical microscope.

3.2.2. Thermal conductivity of azobenzene derivatives

In this section, we report the performance of these azobenzene derivatives as thermal switches, with special focus on optimizing thermal contrast and switching speed. Due to technical limitations of our experimental setup, these measurements will be limited to azobenzene derivatives with alkyl chain lengths of *n*= 6, 8, 10, and 14, excluding derivatives with *n*= 3 and 5 (melting points above 370 K).

Thermal conductivity measurements were performed by the 3ω method in a home-made setup (*30*) inserted in a liquid nitrogen cryostat. This technique involves the use of a metallic strip (in our case, platinum), that acts both as a sensor and heater, deposited by optical lithography on a low thermal conductivity glass (**Figures 2.15**a and **2.16**a). When an alternating current (AC) at a frequency ω is applied to the Pt strip, Joule heating generates periodic temperature oscillations at a frequency of 2ω. These, in turn, cause a change in the resistance of the platinum, producing a small voltage signal at the third harmonic of the current frequency (3ω), which is related to the thermal conductivity of the system.

For the measurements, we melted a small amount of the sample (≈ 100 μg) on top of the platinum resistance (**Figure 2.16**b). Measurements were registered continuously while the temperature was ramped up at a controlled rate of 1 K/min. For this, the slope of the 3ω voltage *vs* ln (2ω) was recorded at two frequencies, 76 and 362 Hz. To ensure the accuracy of the data, the linear relationship between the 3ω signal and ln (2ω) heating frequency was previously verified between 56 and 2120 Hz, approximately.

Figure 3.13 shows the temperature-dependent thermal conductivity (κ) of azobenzenes with alkyl chain lengths *n*= 6, 8, 10 and 14, accompanied by their corresponding differential scanning calorimetry scans for direct comparison. The transitions observed in κ correlate with the phase transitions detected via DSC. This demonstrates that thermal conductivity has very good sensitivity to small changes in the spatial/orientational arrangement of the molecules, that may be difficult to detect by macroscopic structural characterization techniques such as X-ray diffraction, for example.

In the crystalline state, the thermal conductivity remains very low (κ ≈0.2-0.3 W/mK), similar to amorphous polymers and molecular liquids (*150*) (see **Figure 3.1**a). Interestingly, these values are only slightly larger than those observed for the *trans*-isotropic liquid occurring at high temperatures, despite the lack of translational symmetry in the latter. In the azo-derivatives with *n*= 8 and 10, the pronounced drop in thermal conductivity at intermediate temperatures corresponds to the formation of the nematic liquid crystal. This phase exhibits lower thermal conductivity than the isotropic liquid, consistent with the planar alignment of the mesophase, as reported by different authors (*151*, *152*).

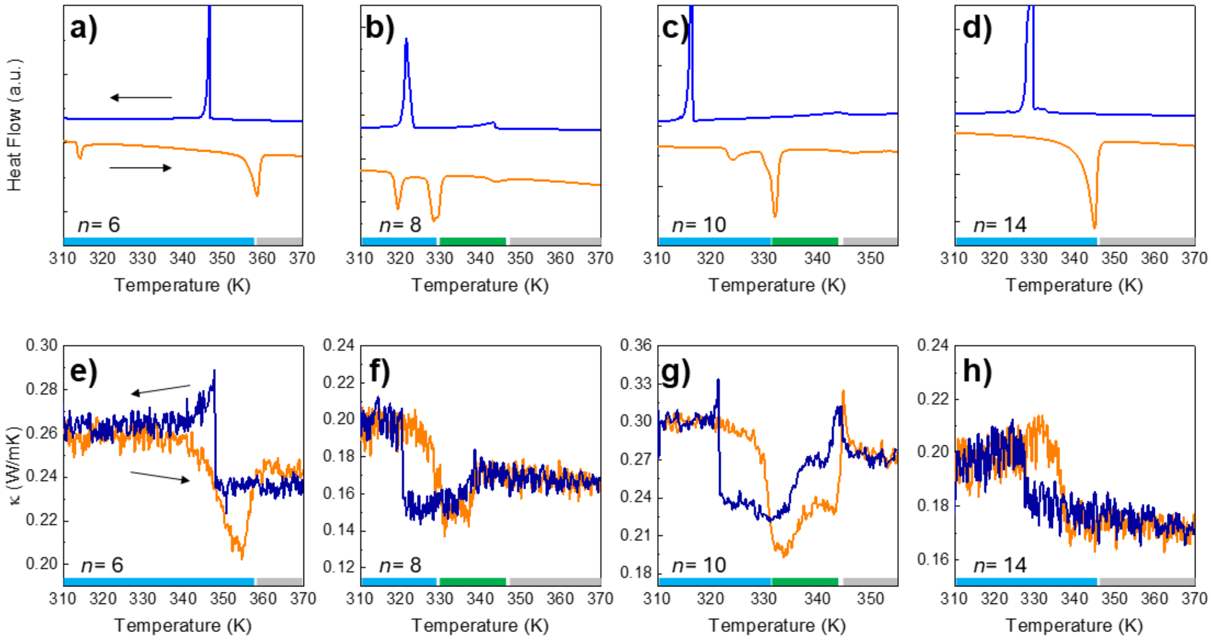

Figure 3.13. Differential scanning calorimetry (a-d) and thermal conductivity (e-h) measurements for the 4,4'-dialkyloxy-3-methylazobenzene derivatives with *n*= 6, 8, 10 and 14 carbon atoms in the alkyl chain. The peaks at the DSC, corresponding to transitions between a 3D crystal and IL (*n*= 6, 14) or between a 3D crystal and a N-LC (*n*= 8, 10), are reproduced in the thermal conductivity curves of the lower panel. The temperature range of stability of the different phases is indicated by the color bars at the bottom of each panel (blue, green and grey for the 3D crystal, liquid crystal, and isotropic liquid, respectively).

To study the evolution of the thermal conductivity after light-induced *trans-cis* isomerization, we used two LED lights (365 and 445 nm) incorporated inside the cryostat. Liquid nitrogen was used to minimize any possible self-heating of the LEDs during performance. In any case, to ensure that the observed changes in thermal conductivity were not caused by a phase transition because of sample heating, we carefully monitored the temperature rise during LED operation.

We calibrated the resistance-temperature ratio (*dR/dT*) of the platinum strip used for the 3ω measurements. We then measured the resistance of the Pt strip during UV illumination (≈160 mW/cm^2), under identical conditions to those applied to azobenzene samples, as shown in **Figure 3.14**. There is a change in resistance during illumination that corresponds to a maximum temperature rise of 2.5 K. Therefore, to avoid any possible influence of sample heating during illumination, we kept the samples much colder than 2.5 K from the phase transition temperature, so we can discard that any transition observed during illumination is due to the temperature. This careful control ensures accurate observation of the impact of UV/Vis-induced isomerization on the thermal properties of the azobenzene derivatives.

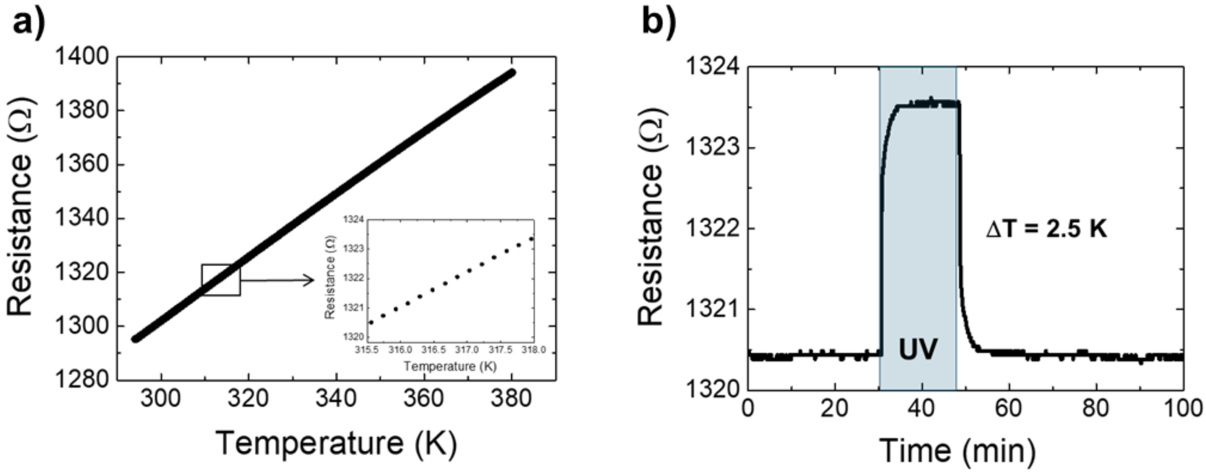

Figure 3.14. a) Calibration of the temperature-dependent resistance of the Pt sensor. b) Measurement of Pt resistance during ultraviolet illumination. Resistance calibration presented in (a) demonstrates that UV irradiation induces a maximum temperature rise of about 2.5 K. The inset shows a zoomed region of the resistance calibration.

Figure 3.15 shows the thermal conductivity measurements of azobenzenes with *n*= 6, 8, during UV/Vis illumination cycles. In these experiments, the thermal conductivity of the system was monitored at a fixed temperature of 300 K during UV/Vis irradiation, so both azo-derivatives are initially in the crystalline phase.

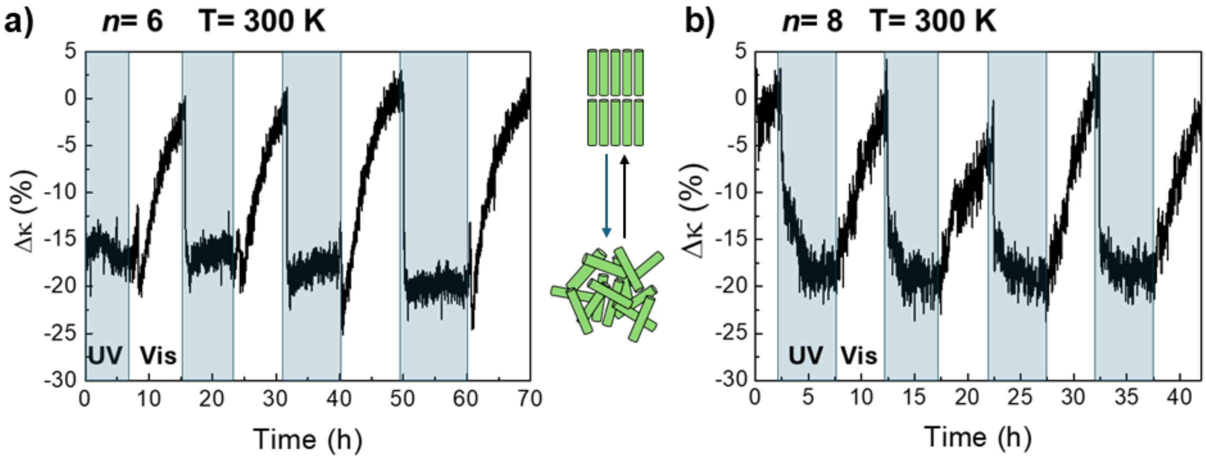

Figure 3.15. Relative variation of thermal conductivity during UV (365 nm) / Vis (445 nm) illumination cycles for the azobenzenes with *n*= 6 (a) and *n*= 8 (b) carbon atoms. In both cases, illumination cycles were performed at 300 K, implying *trans*-crystal to *cis*-isotropic liquid transitions.

As observed in the figure, illuminating the samples with UV light (365 nm) leads to a reduction in thermal conductivity, corresponding to the transition from the *trans*-crystalline phase to the *cis*-isotropic liquid. This phase change is stable during UV illumination, but irradiation with visible light (445 nm) recovers the original state. Subsequent UV illumination implies a new reduction in thermal conductivity, and this process can be repeated many times. Similar results have been found when, instead of performing UV/Vis irradiation cycles, we leave the system relax into the thermodynamically stable *trans* phase in the dark.

However, the thermal conductivity contrast is only of 15-20 %, too small for practical applications. And, in the case of the azobenzene with *n*= 14 (not shown), this thermal conductivity switch is even smaller (≈10%).

Higher thermal contrasts are found in the case of the azobenzene with *n*= 10, as observed in **Figure 3.16**. where maximum reductions of about 40% are achieved in thermal conductivity. Again, the illumination cycles were performed close to room temperature, which implies a *trans*-crystal to *cis*-isotropic liquid phase transition.

Very importantly, the reduction of ≈30-40% during UV illumination means that the thermal conductivity of the *cis*-isotropic liquid (≈0.2 W/mK) is considerably smaller than in the *trans*-IL, ≈0.27 W/mK, as reported in **Figure 3.13**g. We have measured a decrease of 2% in the density of the *cis*-IL compared to *trans*-IL, which seems too small to explain such a large change in κ (≈15-20%). This observation suggests that much less effective intermolecular interactions (π-π, most likely) are present among the bent molecules in the liquid (*132*). This observation confirms the usefulness of thermal conductivity to characterize the intermolecular interactions in complex molecular liquids.

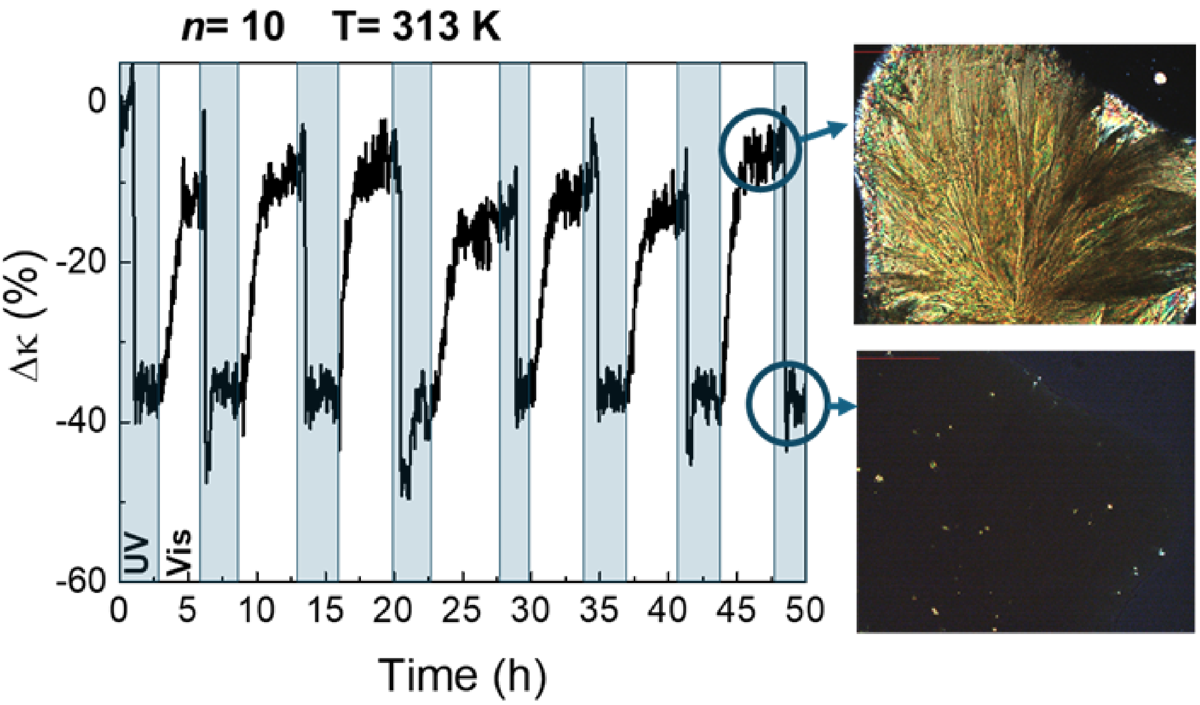

Figure 3.16. Relative variation of thermal conductivity for the azobenene with *n*= 10 during UV/Vis illumination cycles, at 313 K. The transition corresponds to the isothermal 3D crystal-to-isotropic liquid transformation, as shown in the POM images on the right.

Apart from a large thermal contrast between the different states, a good thermal switch should transform between these states as fast as possible, after application of an external stimulus. In this case, although the crystal-to-liquid transition occurs just within a few minutes, the full recovery of the initial state under Vis-light illumination requires several hours (**Figure 3.16**). This is due to the low mobility of the large azobenzene molecules at room temperature, which must diffuse through the liquid and reorganize to form back the *trans*-crystal. Note the DSC scan shown in **Figure 3.6**e: in the heating run, the 3D crystal melts at ≈330 K, but when cooling down the sample crystallization does not occur until ≈315 K. This, again, points towards a lower molecular mobility in the fluidic phase close to room temperature. This crystallization process is even more complicated in the case of molecules with larger alkyl chains.

The recovery to the higher-κ phase can be accelerated if the illumination cycles are performed in a phase where molecules exhibit higher mobilities, such as in the case of liquid crystal phases. As observed in **Figure 3.17**, illumination in the LC phase of the azobenzenes with *n*= 8 and 10 leads to faster switching rates, but at the expense of reducing the thermal contrast between the states (≈10-15%).

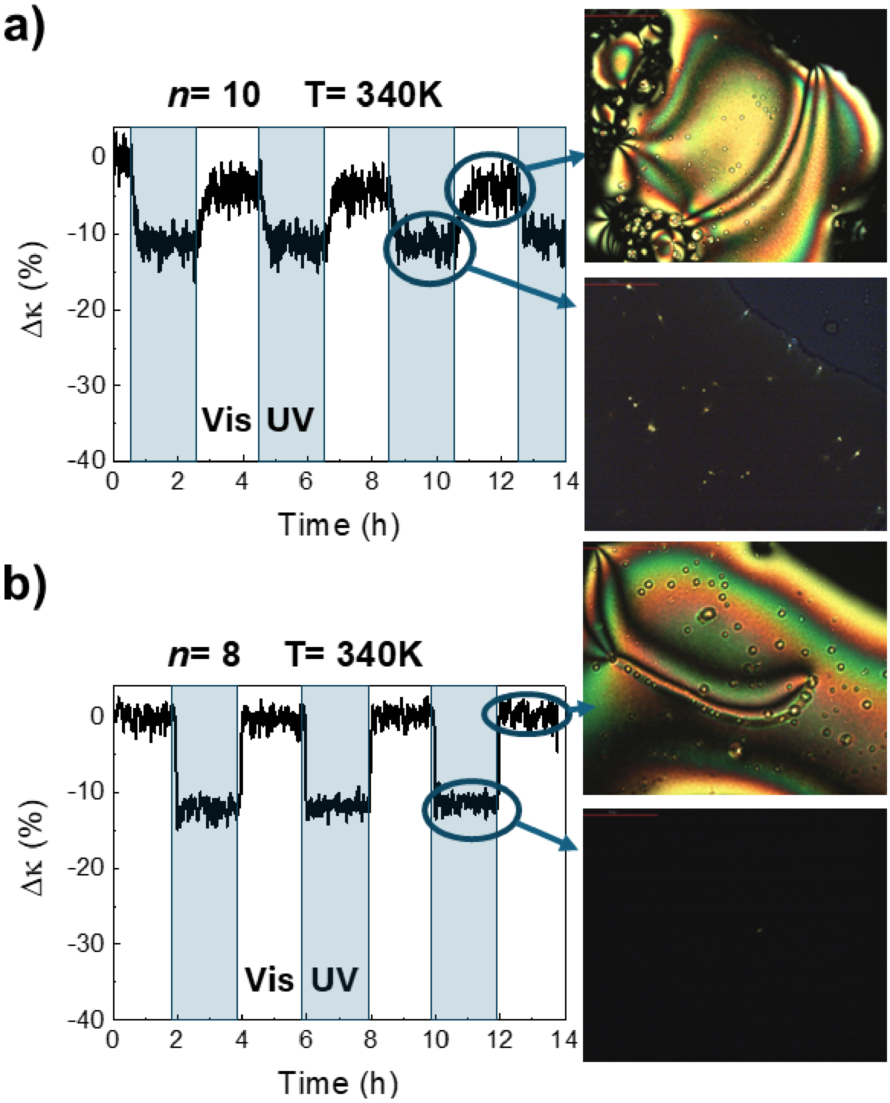

Figure 3.17. Relative variation of κ in *n*= 10 (a) and *n*= 8 (b), at 340 K, under UV/Vis irradiation. At these temperatures, light drives the transition from the nematic liquid crystal phase to the isotropic liquid, as shown in the POM images.

The speed of the switching process is shown in more detail in **Figure 3.18**. As observed in panel b, the recovery of the *trans*-ordered phase under Vis-light occurs much faster when the transition occurs between the IL and the LC than between the IL and the 3D crystal. The speed of the transition can be further accelerated by reducing the length of the alkyl chain.

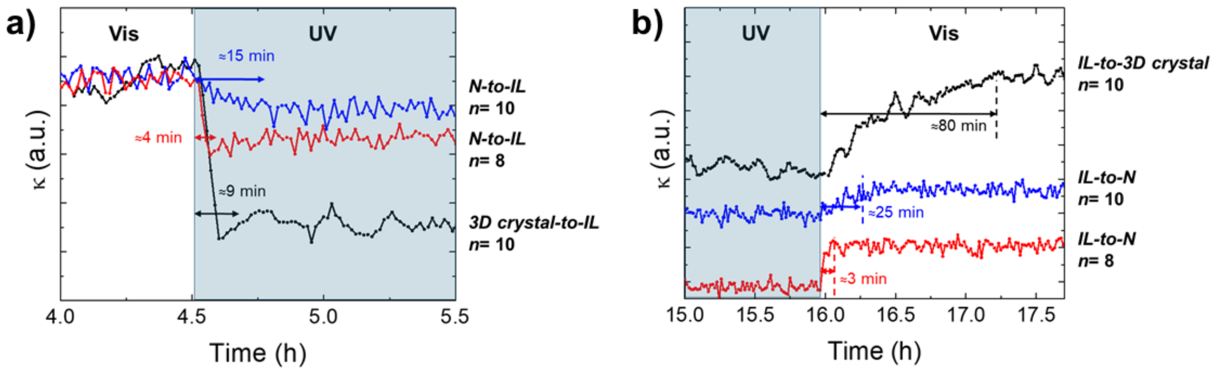

Figure 3.18. Time-dependence of thermal conductivity during UV (a) and Vis (b) illumination. These figures show the traces of the same transitions displayed in **Figs. 3.16** and **3.17**.

Therefore, the results presented so far demonstrate that:

- It is possible to observe light-induced reversible thermal conductivity switching in a wide temperature range around room temperature in self-assembled 4,4’-dialkyloxy-3-methylazobenzenes.
- The thermal contrast is maximized between the 3D crystal and the IL, but the transformation is very slow (in the range of hours).
- The speed of the switching increases (<5 min) when the thermal conductivity is switched between the LC and the IL, but the thermal contrast reduces.

After these observations, it seems that if we want to improve the kinetics of the thermal switching while maintaining a high thermal contrast, we must combine the high atomic order of the 3D crystal with the large molecular mobility of the LC mesophase.

For that reason, we explored the use of these 4,4’-dialkyloxy-3-methylazobenzenes as molecular machines to control the spatial arrangement of an achiral LC matrix with a high degree of molecular order. The hypothesis is that a small amount of the azobenzene molecule dispersed in the optically inactive LC could provoke a reversible order-disorder transition of the whole matrix under UV/Vis illumination. This, in turn, could produce a large, fast and reversible change of its thermal conductivity.

These experiments are explained in detail in the next section.

3.2.3. Azobenzene derivatives as photoactive dopants

Incorporating light-sensitive molecules into liquid crystal networks has been widely explored to induce macroscopic effects, such as bending, and translational or rotary motions through cooperative molecular interactions within the LC system (*144–147*). However, this approach has never been applied to the modulation of thermal conductivity in mesophases. To prove the viability of our hypothesis, we first searched for a LC that exhibits significant thermal contrast between its mesophases and the isotropic liquid, while maintaining chemical and structural compatibility with the 4,4’-dialkyloxy-3-methylazobenzene derivatives synthesized in this work.

We identified the commercial liquid crystal 4-octyl-4'-cyanobiphenyl (8CB) as a suitable candidate for our purpose. Its chemical structure (shown in **Figure 3.19**) supports compatibility with the azo-derivatives via π-π and lateral alkyl chain interactions. 8CB forms a smectic liquid crystal phase (Sm-LC) below 295 K, above this temperature it transforms into a nematic liquid crystal, before melting into the isotropic liquid at 315 K (*153*, *154*).

Marinelli *et al.*(*151*) studied the anisotropic thermal conductivity of this liquid crystal (**Figure 3.19**), finding higher thermal conductivities in samples homeotropically aligned (that is, LC molecules aligned parallel to heat flow) than with planar orientation (perpendicular to heat flow). However, they reported a large thermal contrast between the LC and IL phases in both cases, irrespective of molecular orientation.

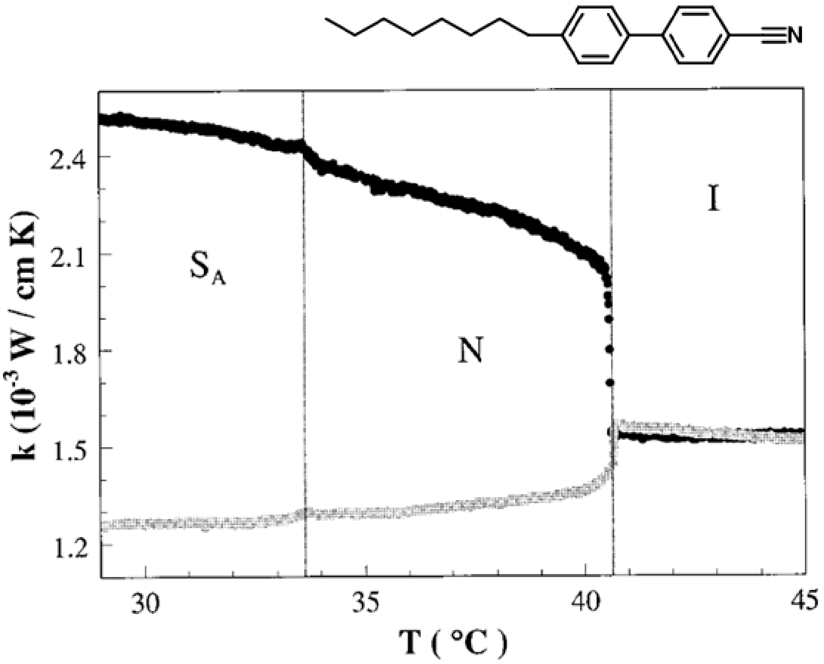

Figure 3.19. Temperature-dependent thermal conductivity of 8CB for planar (grey dots) and homeotropic (black dots) aligned samples. Reproduced with permission from ref. (*151*). Copyright (1996) The American Physical Society.

In **Figure 3.20**a we show the temperature-dependent thermal conductivity of 8CB measured in our setup. There is a reduction in thermal conductivity of ≈15-20% between the smectic liquid crystal phase and isotropic liquid, consistent with a LC phase with mixed orientations (homeotropic and coplanar, as reported by Marinelli *et al.* (*151*)). In addition to this, the nematic liquid crystal also shows lower thermal conductivity compared to the isotropic liquid, confirming the planar alignment of the LC molecules in the nematic phase (lower curve in **Figure 3.19**).

Although 8CB is not optically active, we measured its thermal conductivity during UV/Vis irradiation cycles, to fully discard any possible reorganizations in the mesophase. As we can see in **Figure 3.20**b, the thermal conductivity of the system remains unaffected during illumination cycles.

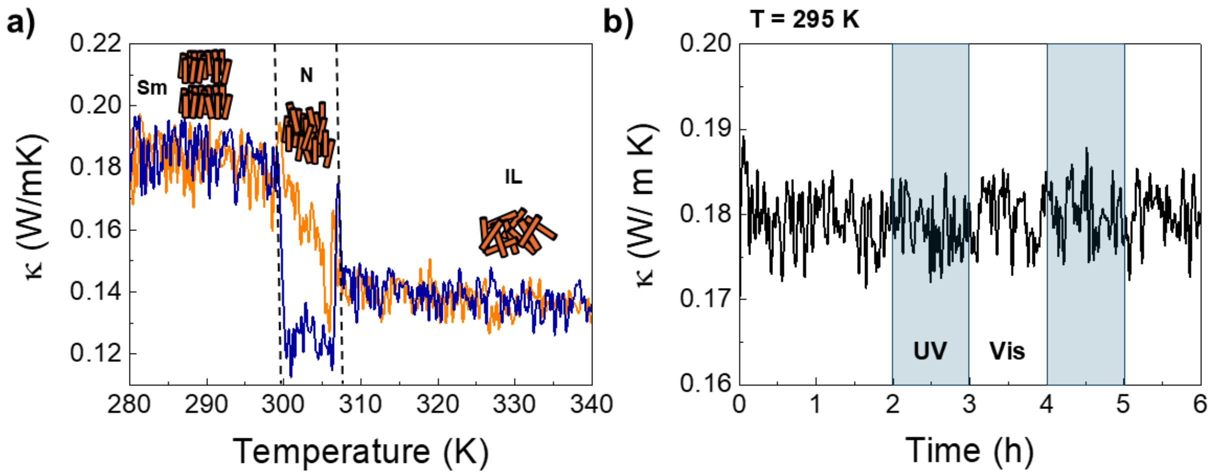

Figure 3.20. a) Temperature-dependent thermal conductivity of the liquid crystal 4-octyl-4'-cyanobiphenyl (8CB). b) Thermal conductivity of the same liquid crystal at a fixed temperature of 295 K, during UV/Vis irradiation cycles. 8CB does not absorb the light wavelengths used in this study (365 and 445 nm), so there is no change in its thermal conductivity during illumination.

The effect of UV/Vis illumination on the structure of pure 8CB liquid crystal was also studied with POM. As observed in **Figure 3.21**, the LC exhibits no observable changes during illumination, demonstrating that 8CB maintains its structural integrity under such conditions, and ruling out any potential thermal effects caused by light-induced heating.

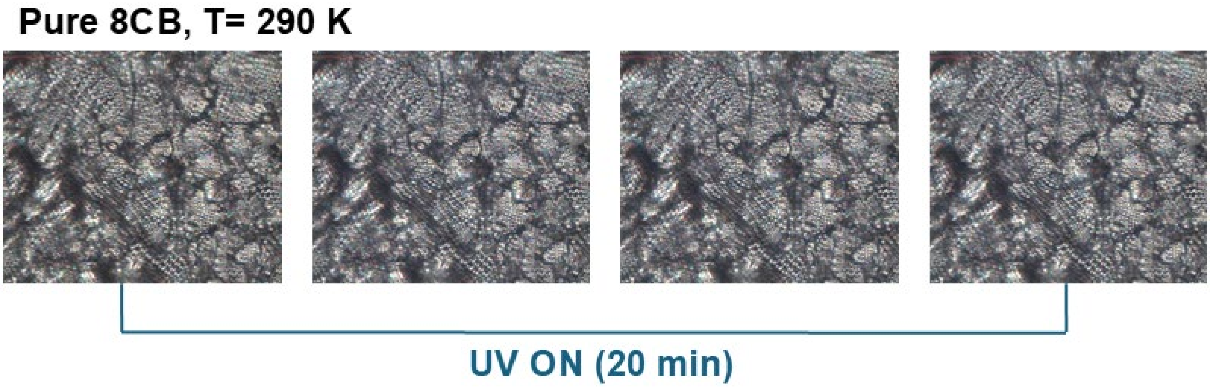

Figure 3.21. Polarized optical microscopy images of pure 4-octyl-4'-cyanobiphenyl (8CB) during UV illumination (20 min) at room temperature. The smectic liquid crystal phase is stable under ultraviolet illumination.

After confirming the suitability of the 8CB liquid crystal, we dispersed 4% (w/w) of the 4,4'-dihexyloxy-3-methylazobenzene (*n*= 6) in the 8CB commercial LC (from now on, we will refer to this mixture as 8CB:azobenzene). The concentration of azobenzene was chosen to be low enough to preserve the thermal behavior and stability of the host mesophase, yet sufficiently high to ensure that the effects of *trans*-*cis* isomerization could be observed across the entire system. **Figure 3.22** shows the comparison of the DSC scans of the pure 8CB liquid crystal, and the 8CB:azobenzene dispersion. As we can see, both scans are nearly identical, confirming that the incorporation of the azobenzene derivative does not disrupt the stability of the different phases of 8CB.

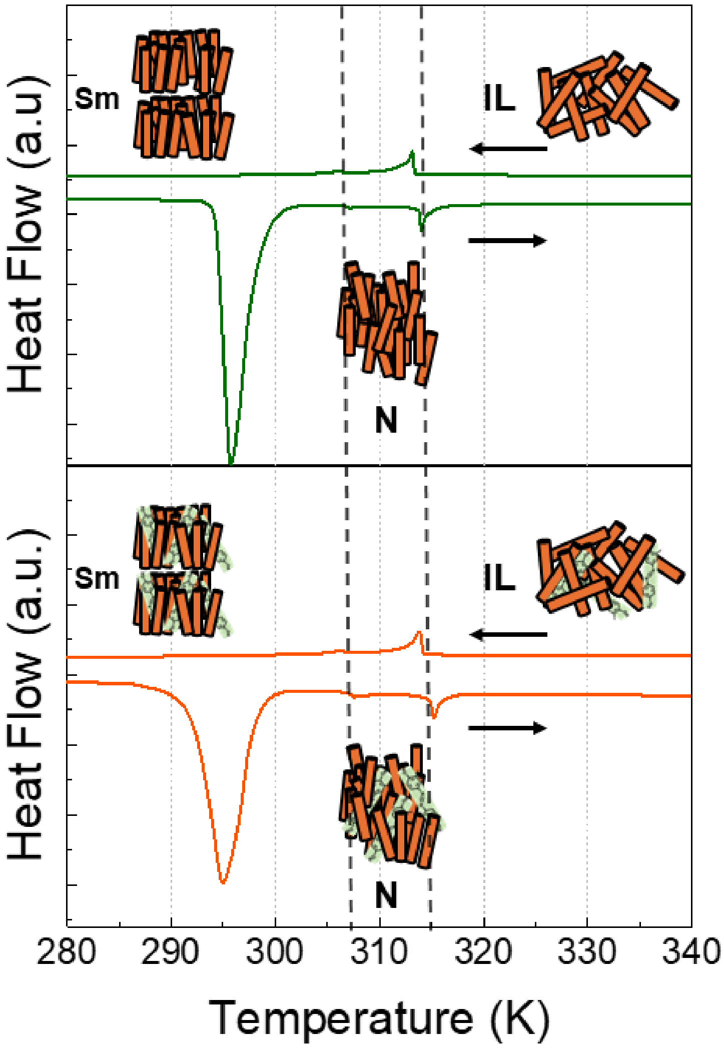

Figure 3.22. Differential scanning calorimetry scans of pure 4-octyl-4'-cyanobiphenyl liquid crystal (top panel), and the same liquid crystal doped with a 4% of 4,4'-dihexyloxy-3-methylazobenzene (bottom panel). The stability of the different phases and transition temperatures are not affected by the dispersion of the azo-derivative. The small discrepancies observed in transition temperatures between DSC measurements and thermal conductivity results (**Fig. 3.20**a) are due to the different scan rates employed during measurements: 10 K/min in DSC, and 1 K/min in thermal conductivity experiments.

The 8CB:azobenzene dispersion was irradiated at 290 K (in the smectic liquid crystal phase) with UV/Vis light while measuring the thermal conductivity. The results, shown in **Figure 3.23**a, demonstrate a reduction of ≈15% in κ, consistent with the transition between Sm-LC and IL. This confirms that the isomerization of the azobenzene into the *cis* isomer induces a cooperative molecular motion which destabilizes the bulk Sm-LC mesophase of 8CB. Note, also, that the time required for the full transformation is very short, of the order of 10 min.

On the other hand, irradiating the system at 300 K, within the nematic-LC region, transforms this phase into the IL, resulting in a ≈5% increase in thermal conductivity, which also occurs very fast (**Figure 3.23**b). Thus, the results presented in **Figure 3.23** demonstrate that the thermal conductivity of the LC system can be tuned by the UV-Vis photoisomerization of the azobenzene dopants. Moreover, fast and reversible bi-directional switching can be achieved by varying the order of the mesophase irradiated (**Figure 4.23**c).

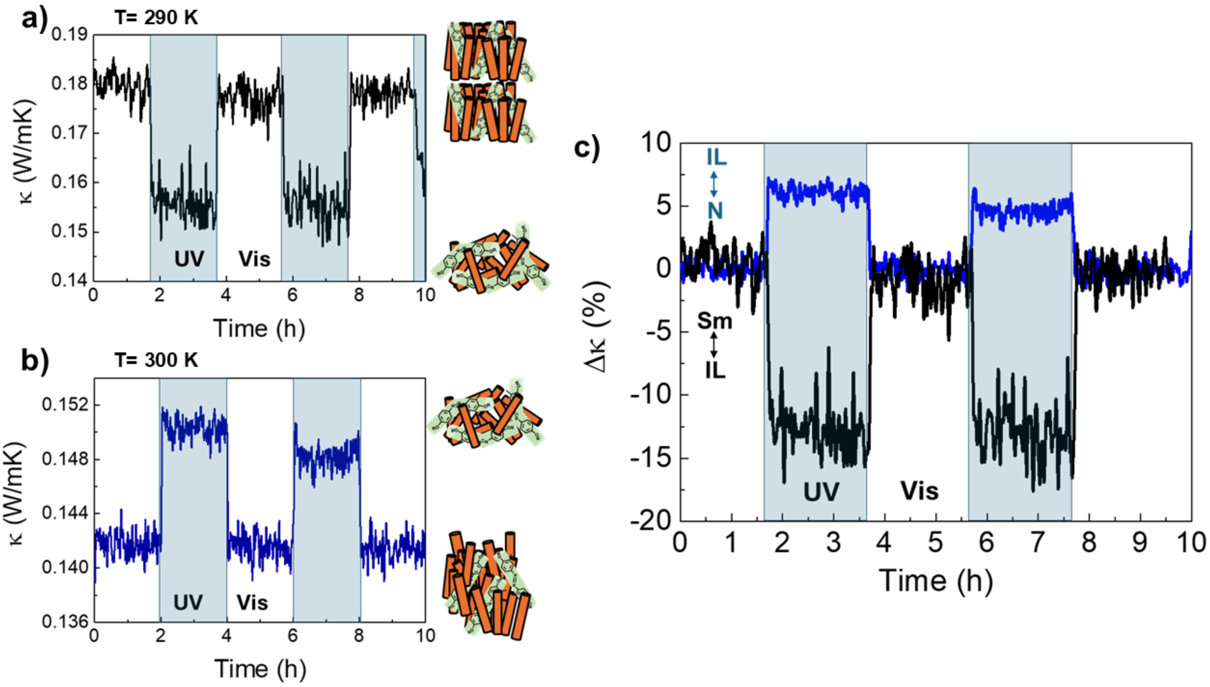

Figure 3.23. Room temperature light-triggered thermal conductivity switching of 8CB:azobenzene molecular system. Irradiating the Sm-LC phase (≈290 K) with UV light, transforms the system into the IL, reducing its thermal conductivity (a). On the other hand, irradiation on the N-LC phase (≈300 K) with UV light, transform the system in the IL too, but in this case increasing the thermal conductivity (b), in perfect agreement with the results shown in **Fig. 3.20**a. Bi-directional switching of the thermal conductivity is demonstrated in panel (c): either an increase or decrease of thermal conductivity can be achieved upon UV illumination of a partially ordered mesophase of 8CB:azobenzene system. Both changes are reversible upon illumination with visible light.

This is a very interesting result, because it opens a completely new possibility: doping achiral liquid crystals with photoactive molecules for designing thermal switches. Given the huge variety of liquid crystal mesophases reported in the scientific literature, we believe this may open a new and promising line of research for developing active thermal systems.

Finally, POM images (**Figure 3.24**) show that after UV illumination ceases, azobenzene molecules in the isotropic liquid recover their *trans* rod-like structure in the dark, and the whole system relaxes into the smectic-LC through an intermediate phase, most probably a N-LC.

The evolution of the thermal conductivity during the UV/dark cycles is shown in **Figure 3.25**. Although the intermediate phase cannot be univocally identified from POM, it does show the same thermal conductivity as the nematic phase in **Figure 3.20**a. Therefore, the most plausible situation is that the system relaxes in the dark very fast from the isotropic liquid to the nematic phase, and then slowly adapts the more ordered smectic liquid crystal phase, although this requires further research. In any case, given the different thermal conductivity among the three phases, three different thermal states can be achieved in a single UV light/darkness run in this composite molecular system.

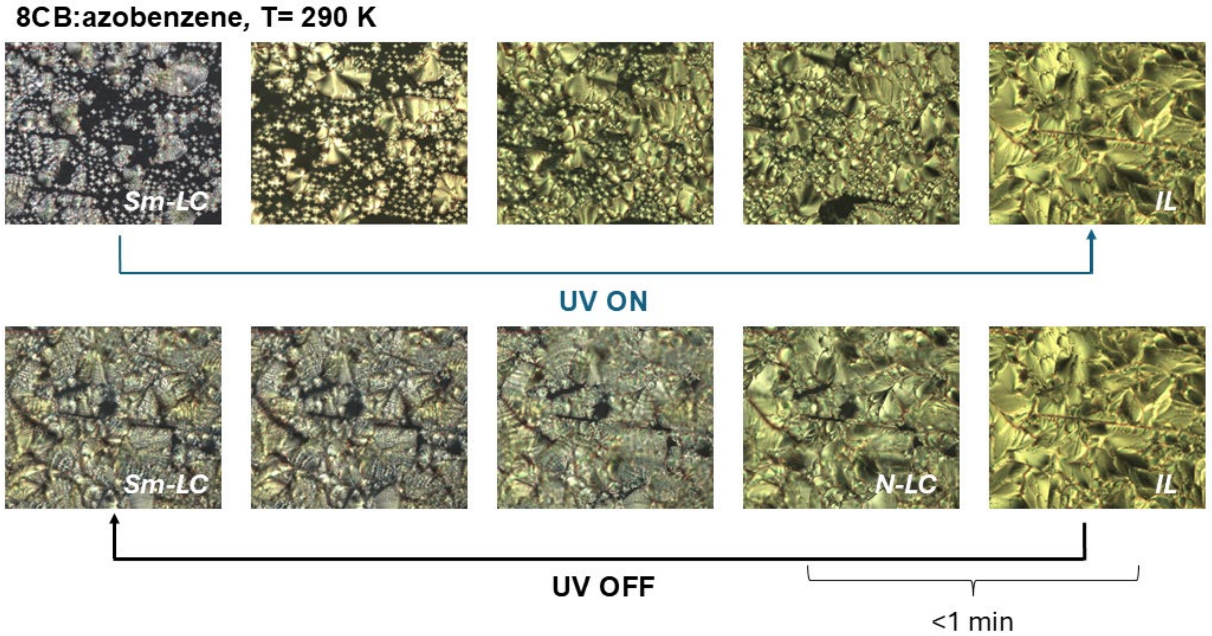

Figure 3.24. Polarized optical microscopy images of the 8CB:azobenzene system under UV illumination (total illumination time, 15 minutes) and then kept in the dark. After switching off the UV light, the system transits very rapidly (less than one minute) to an intermediate phase, before slowly relaxing back to the smectic liquid crystal phase.

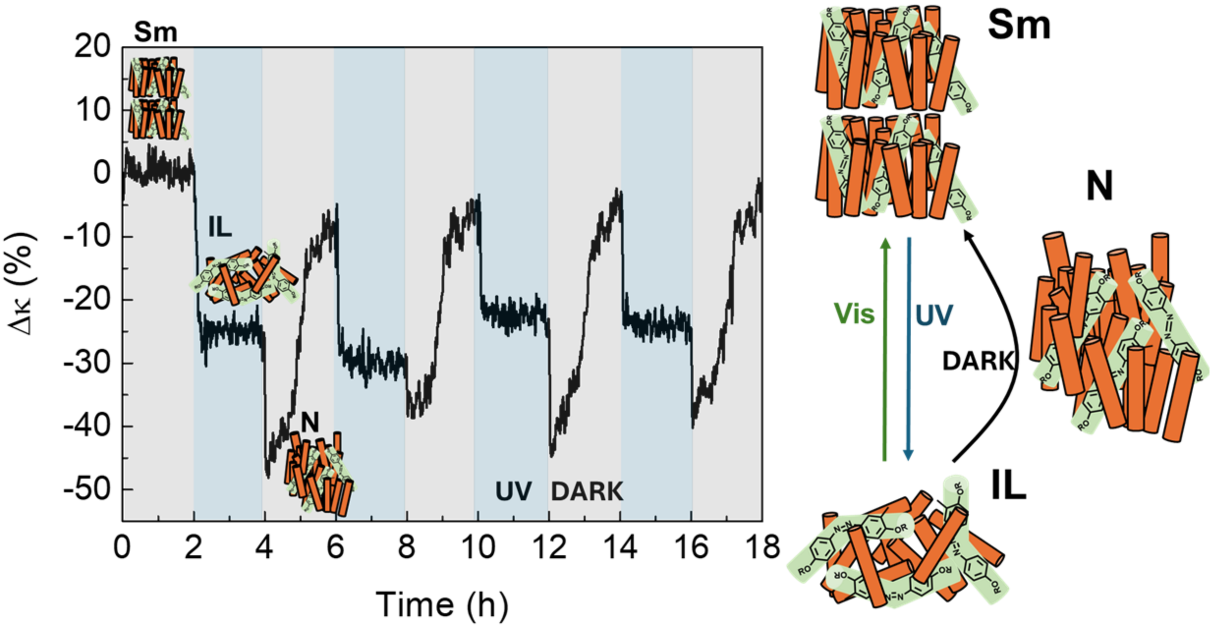

Figure 3.25. Thermal conductivity of 8CB:azobenzene molecular system during UV/darkness cycles, at 290 K. Three different thermal states can be identified in this case, associated with the different values of thermal conductivity for the Sm-LC, N-LC and IL presented in **Fig. 3.20**a.

3.3. CONCLUSIONS

In this chapter, we investigated the use of azobenzene derivatives to develop thermal switches. The main conclusions of our research are:

- Thermal conductivity is highly sensitive to small changes in molecular arrangements of self-assembled mesophases, which are sometimes difficult to observe using structural characterization techniques.
- We confirmed that self-assembled azobenzene derivatives can be switched between higher/lower thermal conductivity states under mild UV/Vis irradiation, around room temperature. However, the variations are modest.
- The kinetics of the transformation depends very much on the nature of the phase used: 3D crystal or nematic liquid crystal, and the length of the alkyl chain, which determines the molecular diffusivity.
- We verified the utility of these photoactive molecules as light-driven molecular machines, with the aim of reversibly altering the bulk order of conventional mesophases. The commercial liquid crystal 4-octyl-4'-cyanobiphenyl (8CB) was selected as a host matrix due to its chemical compatibility with azobenzene derivatives and its well-characterized thermal behavior. UV/Vis illumination experiments confirmed that the *trans-cis* isomerization of the azobenzene molecules had significant impact on the thermal properties of the whole system. Under UV/Vis light exposure, the system exhibited reversible changes in thermal conductivity.
- By irradiating different mesophases of doped-8CB, we induced a reversible bi-directional switch in the thermal conductivity of the system by UV/Vis irradiation.
- Finally, UV/darkness cycles at room temperature allowed us to access three-thermal states.

In summary, this chapter lays the foundation for using azobenzene derivatives to control thermal properties via light stimuli. Combining liquid crystals with photoresponsive molecules offers a promising strategy for developing functional materials that can respond to external stimuli, opening up new possibilities for applications in optothermal devices and advanced thermal management technologies. Given the vast variety of available liquid crystals and chemically compatible photoactive molecules, this method could pave the way for designing molecular materials with multiple, accessible, thermal states around room temperature.

4. TOPOTACTIC OXIDATIONS FOR THERMAL MODULATION IN OXIDES

> *"Reserve your right to think, for even to think wrongly is better than not to think at all."*
>
> ---
>
> Hypatia of Alexandria, first noted woman in mathematics, philosophy and astronomy.

The results presented in this chapter are published in:

"Exploring Topochemical Oxidation Reactions for Reversible Tuning of Thermal Conductivity in Perovskite Fe Oxides" *Chemistry of Materials*, **2024**, 36, 10249-10258. https://doi.org/10.1021/acs.chemmater.4c02023

Noa Varela-Domínguez[1], Marcel S. Claro[1], Enrique Carbó-Argibay[2], César Magén[3] and Francisco Rivadulla*[1]

[1]CiQUS, Centro Singular de Investigación en Química Biolóxica e Materiais Moleculares, 15782-Santiago de Compostela, Spain

[2]International Iberian Nanotechnology Laboratory (INL), 4715-330 Braga, Portugal.

[3]Instituto de Nanociencia y Nanomateriales de Aragón (INMA), CSIC-Universidad de Zaragoza, 50009-Zaragoza, Spain.

Editorial: American Chemical Society ISSN: 1520-5002

Personal contribution: deposition of thin films and structural characterization by X-ray diffraction and reciprocal space mapping, topotactic oxidations, thermal conductivity measurements, analysis and discussion of results.

5-Year Impact Factor: 8.1. Q1 in Materials Science.

4.1. INTRODUCTION

The development of X-ray and electron diffraction techniques in the early 20th century provided chemists with unprecedent insights into solid-state reactions. These advancements enabled detailed analysis of both reactants and products, laying the foundation for understanding transformations at the atomic level (*155*). To describe a specific class of solid-state reactions where the crystallographic relationship between the parent and product phases is preserved, the term "topotaxy" was introduced. Coined by Lotgering and Gorter (*156*), topotaxy was initially defined as "all chemical solid-state reactions which are correlated with crystal orientations in the initial product".

Over time, the definition of topotaxy evolved, leading to debate within the scientific community. Some researchers argued that topotaxy should strictly refer to cases where the lattice is nearly perfectly preserved, while others supported a broader interpretation, allowing for partial distortions or reorganization as long as the general framework of the crystal was retained (*157*).

Today, topotactic or topochemical reactions are generally understood as solid-state chemical transformations in which a crystalline lattice is modified by the selective insertion or removal of atoms, all while maintaining the structural integrity of the starting material (host). These processes are characterized by a high structural similarity between the host and the resulting product. The intercalating species involved in these transformations, usually known as "guests", can range from small ions (e.g., Li^+, Na^+, H^+, O^{2-}) to larger organic molecules or even polymers. In cases where ions are exchanged, the host material must simultaneously accommodate electron transfer to preserve the total charge balance, making these reactions a type of solid-state redox process (*158*).

A canonical example of topotactic reactions is the reversible insertion of Li^+ ions between the hexagonal CoO_2 planes of $Li_{1-x}CoO_2$ (*159*, *160*). This process is the basis for the operation of modern lithium-ion batteries, where Li^+ ions go in and out of the host structure during charging and discharging cycles, all while preserving the structural integrity of the system over thousands of cycles.

Although cationic exchange has historically dominated the study of topotactic reactions, the variable oxidation states of transition metals and the flexibility of the perovskite oxide lattice have opened the door to the reversible insertion/removal of oxide O^{2-} anions in these materials. This is especially relevant in late-transition-metal oxides, in which the strong covalency of the metal-oxygen bond reduces the enthalpy of oxygen vacancy formation (*161*).

In this chapter, we present the use of thermal conductivity to study the reversibility of topochemical oxidations between (Ca,Sr)FeO_x brownmillerite (BM) and perovskite (PV) phases (structures schematized in **Figure 4.1**). Thermal conductivity has a great sensitivity to the presence of defects within crystalline structures, which will provide useful information about the true reversibility of the topochemical process. On the other hand, the final goal is to determine the viability of using topochemical oxygen insertion to fabricate a thermal switch.

For this study, we have explored three different oxidation methods: liquid phase (NaOCl solutions), gas phase (O_2/O_3), and solid state (using Y_2O_3:ZrO_2) for the reversible insertion of O^{2-} ions into the brownmillerite lattice of these iron oxides.

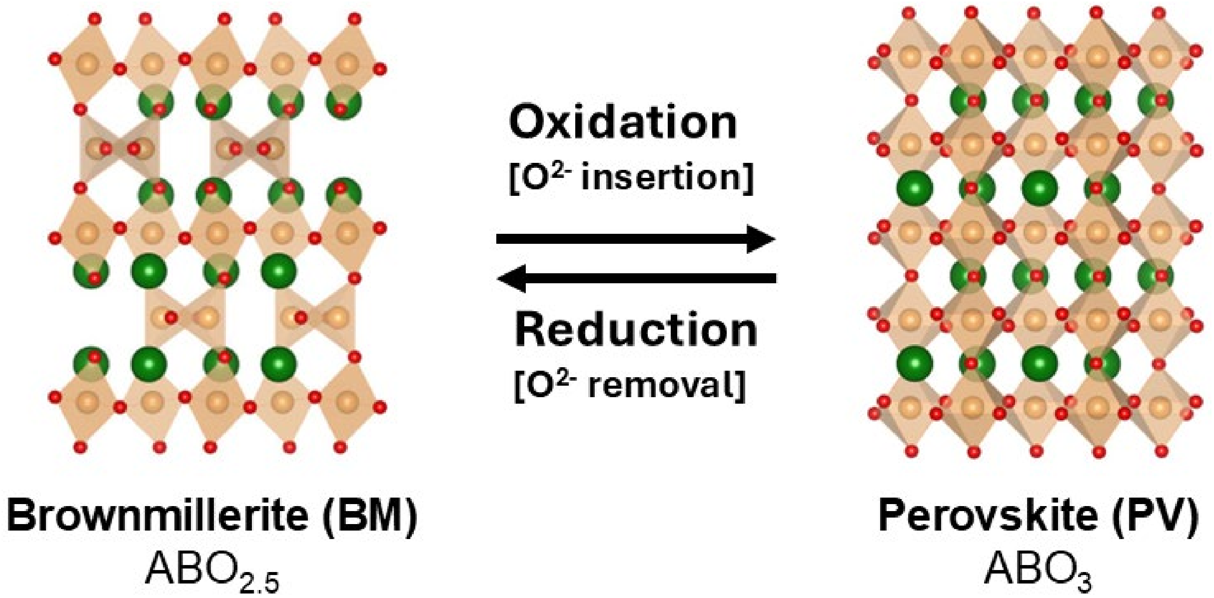

Figure 4.1. Schematic representation of the topotactic transformation between brownmillerite (BM, $ABO_{2.5}$) and perovskite (PV, ABO_3) phases. In the BM phase, approximately one-sixth of the oxide ions are removed, and subsequential ordering of the vacancies inside the crystalline lattice results in a layered structure, with alternating BO_6 octahedral and BO_4 tetrahedral sheets. Conversely, oxidation restores the PV structure, enabling reversible transitions between these phases. In these structures, A represents a divalent cation, such as Ca^{2+}, Sr^{2+}, Ba^{2+}; while B generally represents a transition metal capable of adopting the +3 and +4 oxidations states, such as $Fe^{3+/4+}$, $Mn^{3+/4+}$ or $Co^{3+/4+}$.

These perovskite-brownmillerite transformations have been widely used for the modification of the magnetic (*162*, *163*), electrical (*164*, *165*), optical (*166*, *167*), and electrochemical (*168*) properties of transition metal oxides.

In the last few years –since 2020–, several groups explored the potential of topotactic transformations to modulate the thermal conductivity of oxoperovskites: for example, ion-gel gating has been employed to tune the thermal conductivity of $La_{1-x}Sr_xCoO_{3-\delta}$ thin films, achieving large modulation ratios of up to ≈5 by topotactic insertion/removal of O^{2-} and H^+ ions (*121*, *122*). However, Lu *et al.* (*121*) reported the dissolution of part of the film, changing its thickness from 44 to 27 nm, after only two cycles of ion exchange with the ionic liquid 1-hexyl-3-methylimidazolium bis(trifluormethylsulfonyl)imide (HMIM-TFSI). This effect is due to the corrosion of the oxide by the ionic liquid under the electrochemical conditions used for ion insertion, and hence it cannot be avoided and poses a serious drawback for the applicability of the method.

Yang *et al.* (*120*) used a solid electrolyte (Y_2O_3:ZrO_2, YSZ) for the reversible O^{2-} insertion into $SrCoO_{3-\delta}$ under electrical bias, modulating thermal conductivity with an ON/OFF ratio of ≈4 (see **Figure 4.2**). This fully solid-state approach avoids the problems associated with liquid electrolytes, offering enhanced reliability and applicability. Even though the requirement for elevated operating temperatures (e.g., ≈280 ºC) could be a limitation for the practical implementation of this method for thermal regulation, it is probably the most promising strategy reported so far in this direction, as will be discussed next.

However, there is a growing concern about the existence of intrinsic irreversibility issues associated with reversible O^{2-} topochemical exchange in transition metal oxides (*169*–*173*). For instance, it is well known that after repeated cycling batteries suffer from poor performance (decrease in capacity), due to progressive loss of crystalline order and accumulation of lattice defects in the cathode (*174*). Similarly, as will be discussed in detail later in this work, this is common to many oxides after repeated O^{2-} ion intercalation. Therefore, while O^{2-} ion insertion has been historically considered a mild and reversible process in oxides, the results derived from our research suggest that this idea must be revised.

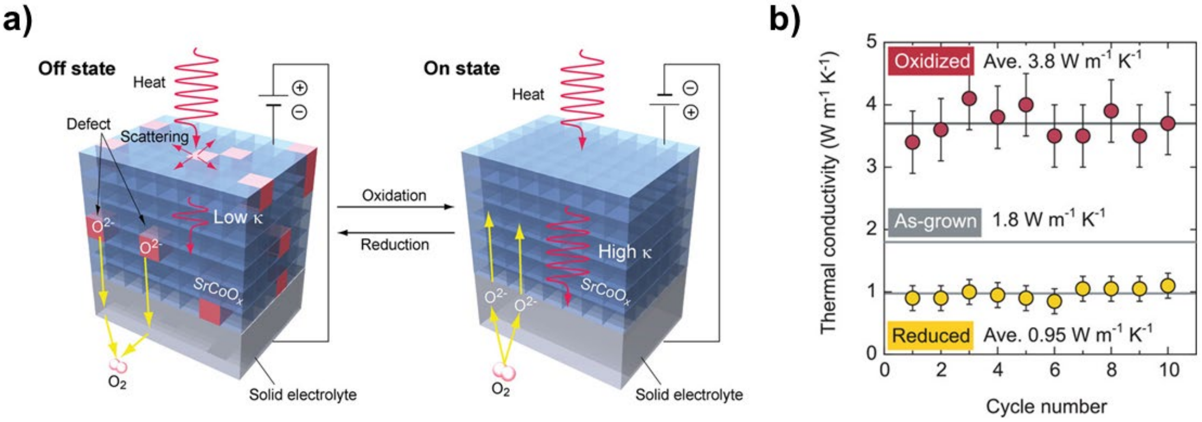

Figure 4.2. a) Schematic representation of the solid-state electrochemical thermal transistor reported by Yang *et al.* (*120*). In the off state (left), oxygen vacancies are generated in the $SrCoO_x$ layer, which act as defects and scatter the heat flow, thus reducing the thermal conductivity of the system. On the other hand, electrochemical oxidation of $SrCoO_x$ causes the oxygen vacancies to disappear (on state, right), increasing thermal conductivity. b) Change in the thermal conductivity of the reduced and oxidized phases upon redox cycles. Images reproduced with permission from ref. (*120*) (CC BY 4.0 license).

The clue about the origin of this irreversibility/instability can be obtained from the analysis of the electronic band structure of transition metal oxoperovskites –particularly at large oxidation states–, which is quite simple to rationalize from the coordination of the B-site metal ion (M) and the oxygen, as shown in **Figure 4.3**. The combination of Madelung and Crystal-Field energies results in the formation of bonding and antibonding MO molecular orbitals, whose symmetry reflects the different overlapping possibilities of the metal 3d and oxygen 2p orbitals. These MO_B and MO_{AB} states have a degree of cationic and oxygen character, which is given by the electronegativity difference between the metal cation and oxygen (i.e., by the covalence of the M-O bond).

On the other hand, with three oxygen (having each three 2p orbitals) per metal (with five 3d orbitals) in the perovskite AMO_3, some oxygen orbitals do not hybridize with cationic states. As a result, a set of non-bonding states of purely oxygen character is formed (O_{NB}). These states are referred to as ligand states, distinguishing them from the antibonding molecular orbitals MO_{AB} states that remain mostly cationic in character (*175*, *176*).

The increase in nuclear charge on moving along the first transition-metal period (from Sc to Zn) stabilizes the energy of the 3d states of the metal, so that the relative position of the MO_{AB}, MO_B and O_{NB} states determines the nature of the valence band and the gap, as well as many of the electronic properties of the solid. If U=E(MO_{AB})-E(MO_B) is lower/larger than Δ=E(MO_{AB})-E(O_{NB}) the system is termed a Mott-Hubbard/charge-transfer material (*177*, *178*).

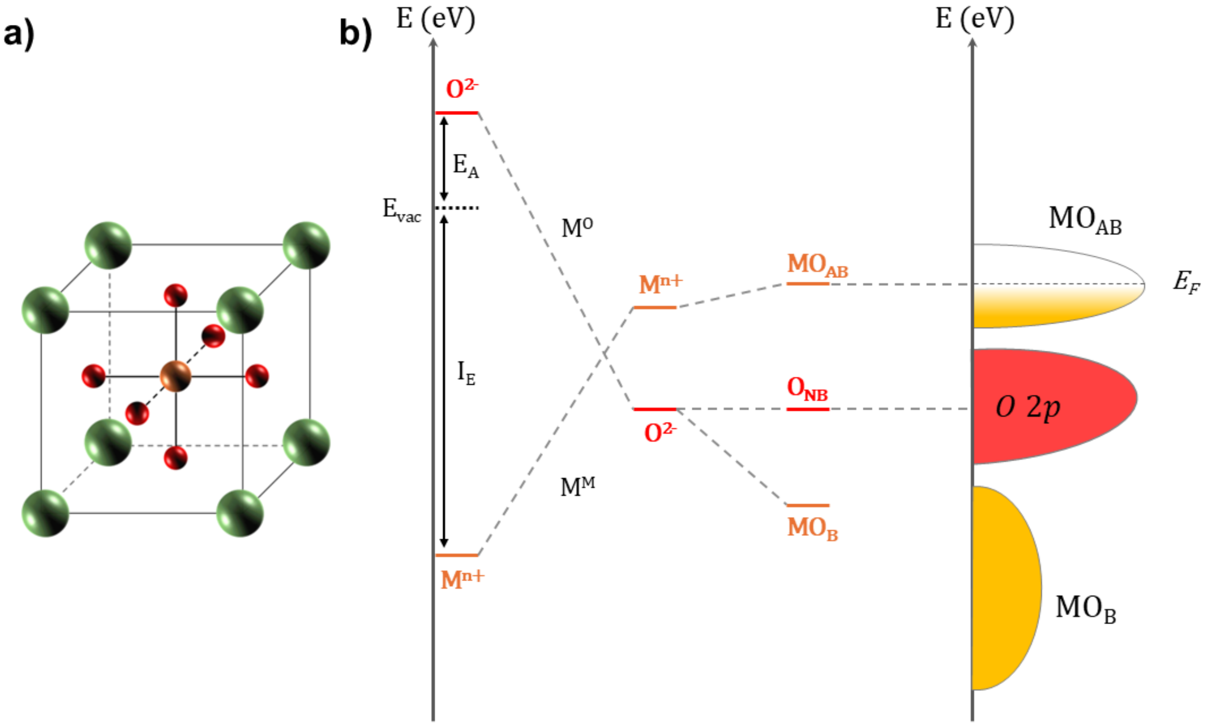

Figure 4.3. a) Crystal structure of the unit cell of the cubic perovskite. A-site ions (green) are in the vertices of the cube, while the B-site cation (orange) is placed at its center, octahedrally coordinated to the oxides (red). b) Schematic representation of the electronic band structure of perovskites, showing the electron affinity (E_A) of oxygen and the ionization energy (I_E) of the B-site metal (M). The Madelung site potentials are represented as M^O for oxygen and M^M for the metal. The bonding molecular orbitals with oxygen character are labeled as MO_B, while the antibonding molecular orbitals dominated by metal character are designated as MO_{AB}. O 2p denotes the oxygen non-bonding states (*177*).

Interestingly, when in the charge-transfer regime the oxidation state of the late-transition metal cation is large enough, there may be a charge-transfer energy less than zero ($\Delta< 0$); in this case, an spontaneous charge transfer occurs from the O^{2-} to the M^{n+} (an internal redox reaction), leading to the evolution of molecular oxygen and the stabilization of an oxygen deficient perovskite with general formula AMO_{3-x}. This situation occurs in $SrFeO_{3-x}$ and $SrCoO_{3-x}$ perovskites, for example, where a maximum oxidation state of $Fe^{3.7+}$ ($x \approx 0.15$) and $Co^{3.5+}$ ($x\approx 0.25$) is achieved (*164*, *179–183*). This electronic configuration is usually referred as Fe^{3+}-$\underline{L}$ or Co^{3+}-$\underline{L}$ to emphasize the hole residing in the oxygen band ($\underline{L}$ means ligand), rather than the usual Fe^{4+} or Co^{4+} configuration (*184–187*).

As a result of this electronic structure, negative charge-transfer oxides ($\Delta<0$) exhibit unique electronic and structural properties, like a substantial lowering of the enthalpy of oxygen vacancy formation. These characteristics, along with a non-negligible ionic conductivity at high temperatures, are critical for enabling the reversible deintercalation of O^{2-} ions.

The materials studied in this chapter, $CaFeO_{3-x}$ and $SrFeO_{3-x}$, are both oxygen deficient perovskites with negative charge-transfer energy. $SrFeO_{3-x}$ presents $\Delta\approx 0$ (*184*, *188*), and exhibits a small energy vacancy formation and high oxygen exchange rate and mobility (*161*, *189*, *190*). The replacement of Sr by Ca in $CaFeO_{3-x}$ reduces the Fe-O-Fe bond angle (*191*), resulting in more negative Δ. Moreover, in both compounds the BM and PV phases have been reported to exist and are stable under atmospheric conditions.

On the other hand, ab initio calculations performed in our group (by Dr. Marcel S. Claro) revealed that the thermal conductivity of PV $CaFeO_3$ is significantly higher than that of BM $CaFeO_{2.5}$ (**Figure 4.4**a), with thermal contrasts of up to 40% achievable in films thinner than 100 nm (**Figure 4.4**b). This thickness dependence highlights the potential for exploiting thermal conductivity as a tunable property in thin films, enabling precise monitoring of BM-PV transformations through oxygen insertion and removal.

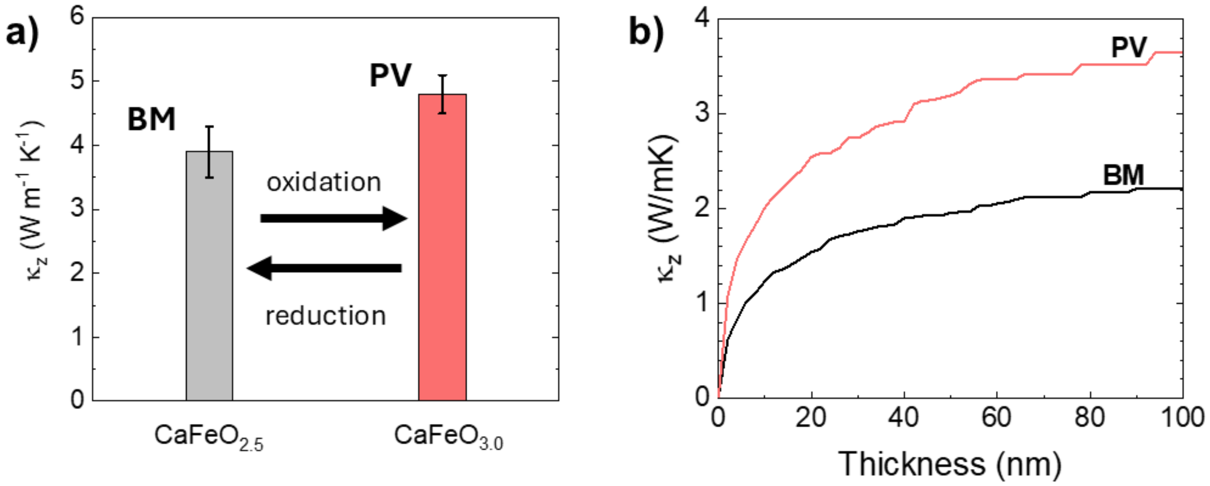

Figure 4.4. a) ab initio calculated bulk thermal conductivity along the c-axis of BM $CaFeO_{2.5}$ and PV $CaFeO_3$. The calculations predict an increase of thermal conductivity of 20% between bulk BM and PV phases. Due to the different dependence of κ with thickness (b), a larger thermal contrast of ≈40% can be observed in films under 100 nm. Data provided by Dr. Marcel S. Claro.

Therefore, crystalline thin films of $CaFeO_{3-x}$ and $SrFeO_{3-x}$ provide an excellent opportunity to compare the stability issues associated with repeated topochemical O^{2-} insertion/removal, using different oxidation mechanisms in two negative charge-transfer oxides.

4.2. RESULTS AND DISCUSSION

4.2.1. Fabrication of the thin films

For the experiments described in this chapter, we synthesized thin films of $CaFeO_x$ (CFO) and $SrFeO_x$ (SFO) on (001) $SrTiO_3$ (STO) substrates by pulsed lased deposition. The growth conditions were identical for both materials: 675 ºC, an oxygen partial pressure of 100 mTorr, and a laser fluence of approximately ≈1.5 J/cm^2. Different sets of films with thickness ranging from 15 to 45 nm were fabricated for this study.

Due to the aforementioned difference in the charge-transfer energy between CFO and SFO, these conditions favor distinct thermodynamic phases for each material: for CFO, the BM phase is thermodynamically stable, while oxygen-deficient PV is the stable phase for SFO, as shown in **Figure 4.5**a. The BM phase of SFO can be obtained by post-fabrication thermal annealing of the PV at 600 ºC, for 2 h, oxygen pressure of ≈10^{-6} Torr (**Figure 4.5**b).

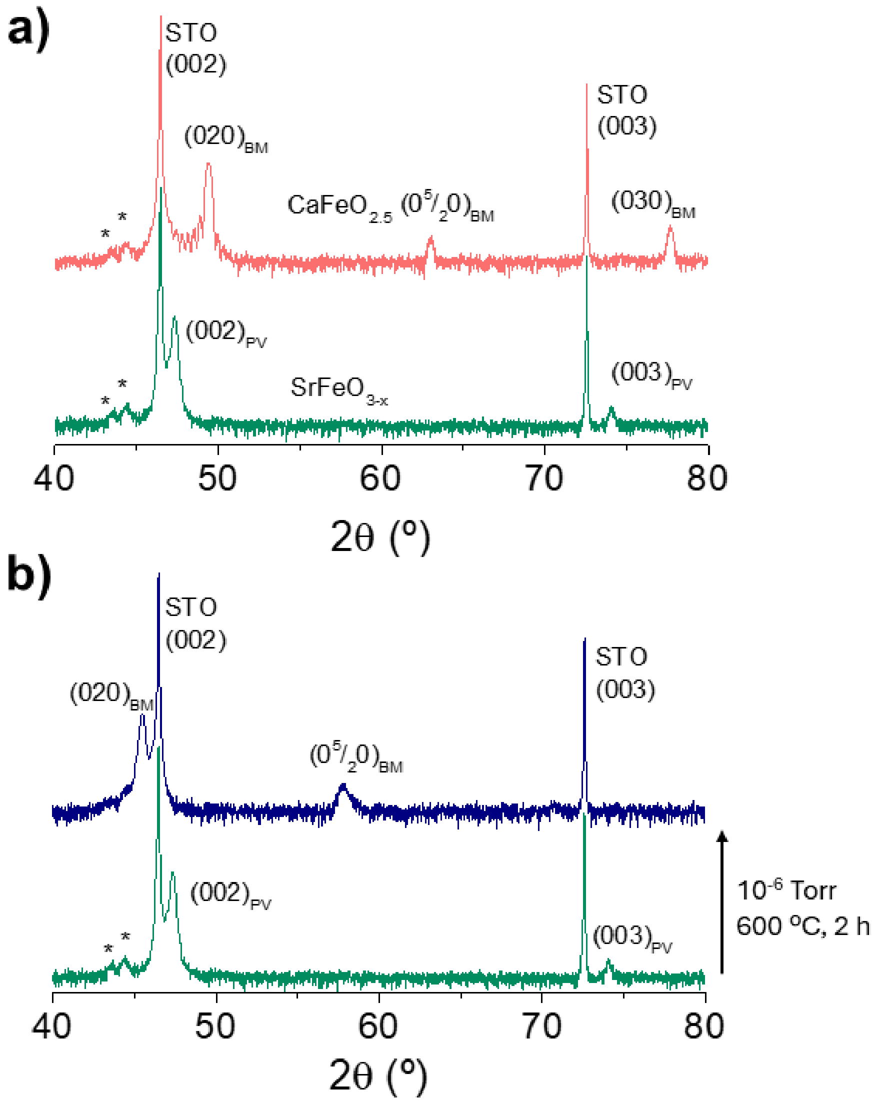

Figure 4.5. a) X-ray diffraction patterns of oxygen deficient PV-SFO and BM-CFO (≈40 nm), as deposited at 100 mTorr of oxygen. b) Reduction of the as-deposited SFO thin film to the BM phase, through thermal annealing under vacuum. The two peaks at ≈45 ° marked with an asterisk are reflections from the tungsten of the X-ray tube (not an impurity).

For the experiments with the solid electrolyte, we deposited thin films of CFO and SFO by PLD on (001) Y_2O_3-doped (9.5 mol%):ZrO_2 (YSZ) substrates, with an intermediate layer (≈10 nm) of 8 % Gd-doped CeO_2, at 650 ºC, 1 mTorr of oxygen, and laser fluence ≈1.5 J/cm^2. Under these conditions, the BM is the stable phase for both materials, as depicted in **Figure 4.6**. In these experiments, the YSZ substrate acts as an oxygen reservoir, enabling oxygen intercalation/deintercalation through the application of an electric field to the system. The intermediate CeO_2 layer is deposited to impede the formation of (Ca,Sr)ZrO_x, which would block oxygen migration across the YSZ/(Ca,Sr)FeO_x interface.

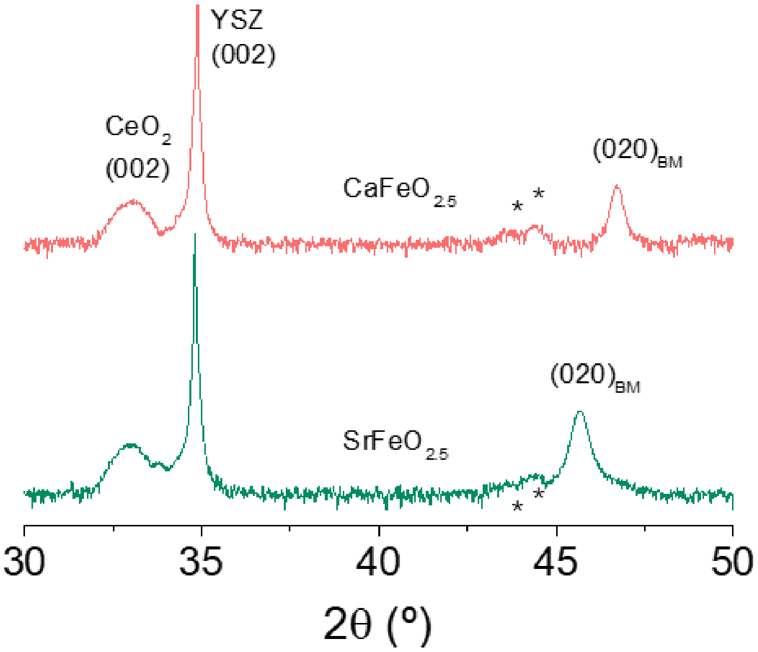

Figure 4.6. X-ray diffraction patterns of CFO and SFO thin films (≈140 nm) deposited at 1 mTorr of oxygen on (001) YSZ substrates, with an intermediate layer of Gd-doped CeO$_2$ (≈10 nm). The BM structure is the stable phase for both materials under these growth conditions. The two peaks at ≈45 ° marked with an asterisk are reflections from the tungsten of the X-ray tube.

4.2.2. Topotactic oxidations and effect on thermal conductivity

In this section, we report the effect of the oxidation pathway on the reversibility of the topotactic transformation between BM and PV phases in CFO and SFO thin films. We explored three different oxidation mechanisms for oxygen insertion into the BM phase: i) liquid phase (NaOCl in H_2O); ii) gas phase (O_3/ O_2); iii) solid electrolyte (Y_2O_3:ZrO_2). We provide detailed structural characterization of the resulting phases, along with thermal conductivity measurements to assess the impact and reversibility of these transformations.

4.2.2.1. Liquid phase oxidation

Oxidation of $SrCoO_{2.5}$ to $SrCoO_{3-x}$ using aqueous solutions of NaOCl, Br_2, $KMnO_4$ and $Na_2S_2O_8$ has been previously reported by the research groups of Maarit Karppinen and Yuichi Shimakawa (*192*, *193*).

In this work, we immersed BM thin films of CFO and SFO in a sodium hypochlorite (NaOCl) solution containing 14% of active chlorine, diluted to 50% with deionized water. The films were soaked for 2 h at 80 ºC, under continuous stirring.

As observed in **Figure 4.7**, this process successfully converts the BM into the PV structure, for both CFO and SFO thin films, although the diffraction peak of the PV-CFO presents significantly low intensity **(Figure 4.7**a,b). Moreover, if we compare the (002) reflection of the PV-SFO (**Figure 4.7**c,d) with that shown in **Figure 4.5**, we find a reduced intensity and increased width in the diffraction peak of the PV obtained by oxidation with aqueous NaOCl solution. This indicates that the structural quality of the sample is not as good as that of the films directly synthesized in the PV phase by PLD (**Figure 4.5**).

On the other hand, complete oxygen removal from the PV, and subsequent recovery of the BM, can be achieved by thermally annealing the films at 600 ºC for 2 h, under an oxygen pressure of 10^{-6} Torr. However, again, as illustrated in **Figure 4.7**, this transformation is accompanied by a significant reduction in crystalline quality, for both CFO and SFO.

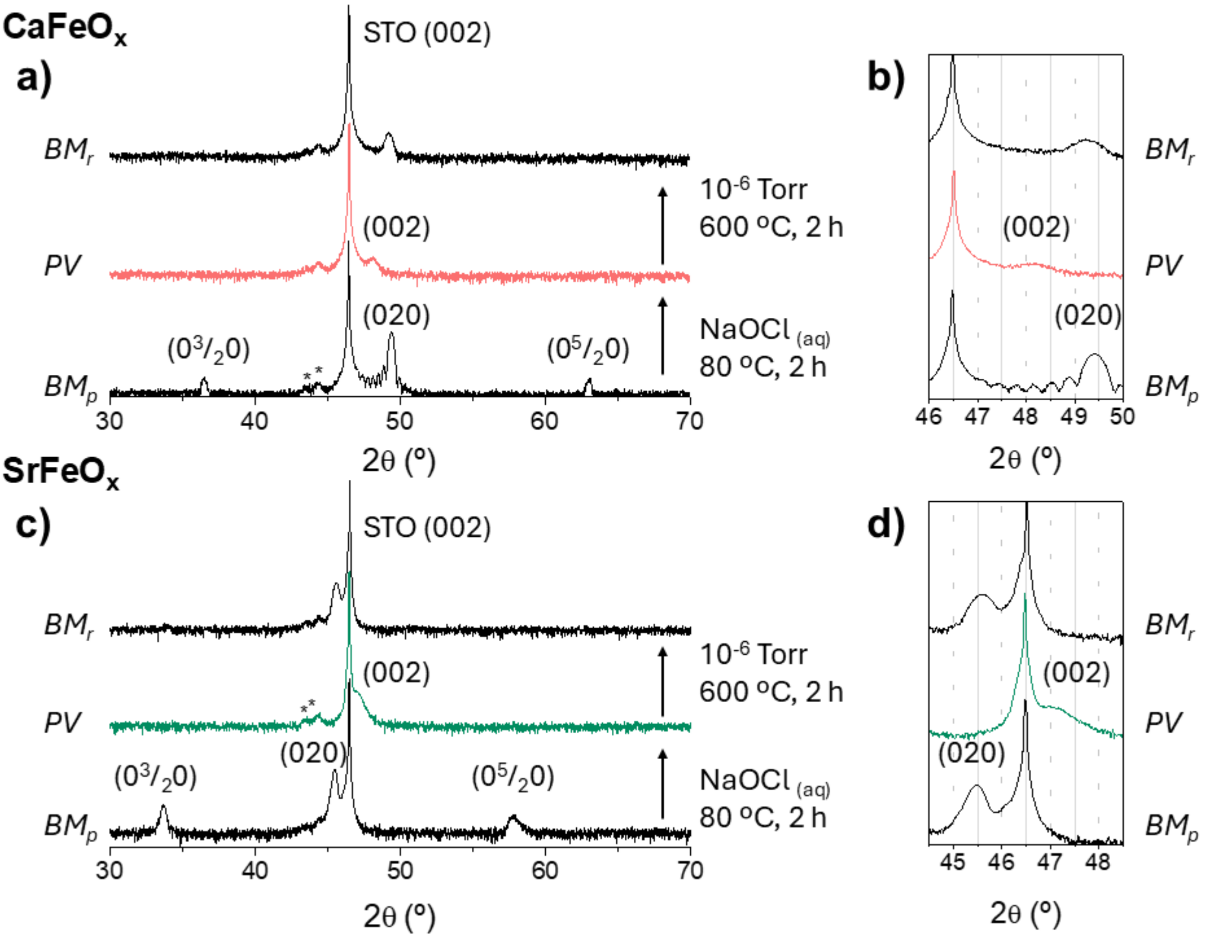

Figure 4.7. X-ray diffraction patterns of the BM-PV-BM transformation in CFO (a,b) and SFO (c,d) thin films (≈40 nm thick) using a NaOCl/H$_2$O solution as oxidant. BM$_p$ and BM$_r$ refer to the pristine and reduced BM phases, respectively. The two peaks at ≈45 ° marked with an asterisk are reflections from the tungsten of the X-ray tube. The $(0^{3}/_{2}0)$ and $(0^{5}/_{2}0)$ peaks are completely absent in the reduced BM phase of both CFO and SFO, pointing to a partial loss of long-range order. On the other hand, the (020) peak is recovered, but with decreased intensity and small displacements, as shown in b,d).

After the reduction, the main (020) Bragg reflection of the BM shows a much lower intensity and increased width compared to the original BM, as shown in **Figure 4.7**b,d. Additionally, this reflection is slightly displaced from the original diffraction angle, indicating variations in the lattice parameters relative to the pristine structure (see **Table 4.1** for the out-of-plane lattice parameters of the different phases of both CFO and SFO). For CFO, the (020) reflection shifts towards lower angles, indicating an increase of ≈0.3% in the out-of-plane lattice parameter: from 3.685(2) Å in the pristine BM to 3.696(5) Å in the reduced BM. Conversely, in SFO thin films the (020) reflection shifts towards higher angles, corresponding to a decrease of ≈0.22% in out-of-plane lattice parameter on the reduced BM obtained after wet oxidation with NaOCl.

Moreover, after reduction, the peaks corresponding to the half-order reflections ($0\,{}^{3}/_{2}\,0$) and ($0\,{}^{5}/_{2}\,0$), which are characteristic of the long-range superstructure of oxygen vacancies in the BM, are completely absent in both materials, indicating an important loss of structural crystallinity in the reduced-BM.

Table 4.1. Out-of-plane lattice parameters of CFO and SFO thin films during BM-PV-BM cycling, using NaOCl/H_2O as oxidant.

Material	BM$_p$ (Å)	PV (Å)	BM$_r$ (Å)	% BM Change
CFO	3.685(2)	3.777(6)	3.696(5)	+0.30
SFO	3.985(3)	3.855(8)	3.976(4)	-0.22

We further investigated the BM-to-PV oxidation using high resolution X-ray reciprocal space mapping, to analyze the impact of oxygen exchange in the in-plane lattice parameters. The reciprocal space maps of the pristine BM and PV phases of CFO and SFO (same samples as in **Figure 4.7**) are presented in **Figure 4.8**. These maps reveal that the BM phases grow matched to the STO substrates (**Figure 4.8**a,c). Upon wet oxidation, the structural response of the resulting PV film varies between CFO and SFO: while for SFO the oxidized PV phase retains its epitaxial matching to the STO substrate (**Figure 4.8**d), suggesting minimal strain relaxation and robust structural stability, the oxidized PV-CFO thin film exhibits partial relaxation, with an in-plane lattice parameter slightly smaller than that of the STO substrate (**Figure 4.8**b).

This different behavior of CFO and SFO thin films after oxidation with NaOCl can be attributed to the epitaxial strain imposed by the STO substrate, which is calculated using *Eq. 2.10* (see Chapter 2, section 2.2.1.2).

In the BM phase, SFO grows on STO (a_s= 3.905 Å for substrates purchased from CrysTec GmbH) substrates under compressive strain (a_f= 3.958 Å, s= -1.34%) (*194*), and chemical oxidation to PV (a_f= 3.851 Å in the bulk) (*195*) results in an equivalent in magnitude, but opposite in sign, tensile strain of +1.40%. On the other hand, CFO films in the BM structure grow on STO substates under mild tensile strain (a_f= 3.898 Å, s= +0.18%) (*99*), but transformation into the PV further increases this strain up to +3.52% (a_f= 3.772 Å) (*191*), which eventually leads to the partial relaxation of the film to an in-plane lattice parameter in between that of the bulk phase and the substrate, as observed in **Figure 4.8**b.

As a result, CFO undergoes greater epitaxial stress during oxidation/reduction cycles, which contributes to its comparatively lower stability under wet oxidation conditions. In contrast, SFO demonstrates superior structural resilience during NaOCl/H_2O oxidation. This is further supported by the higher intensity of the (020) diffraction peak in the reduced BM-SFO phase, as shown in **Figure 4.7**.

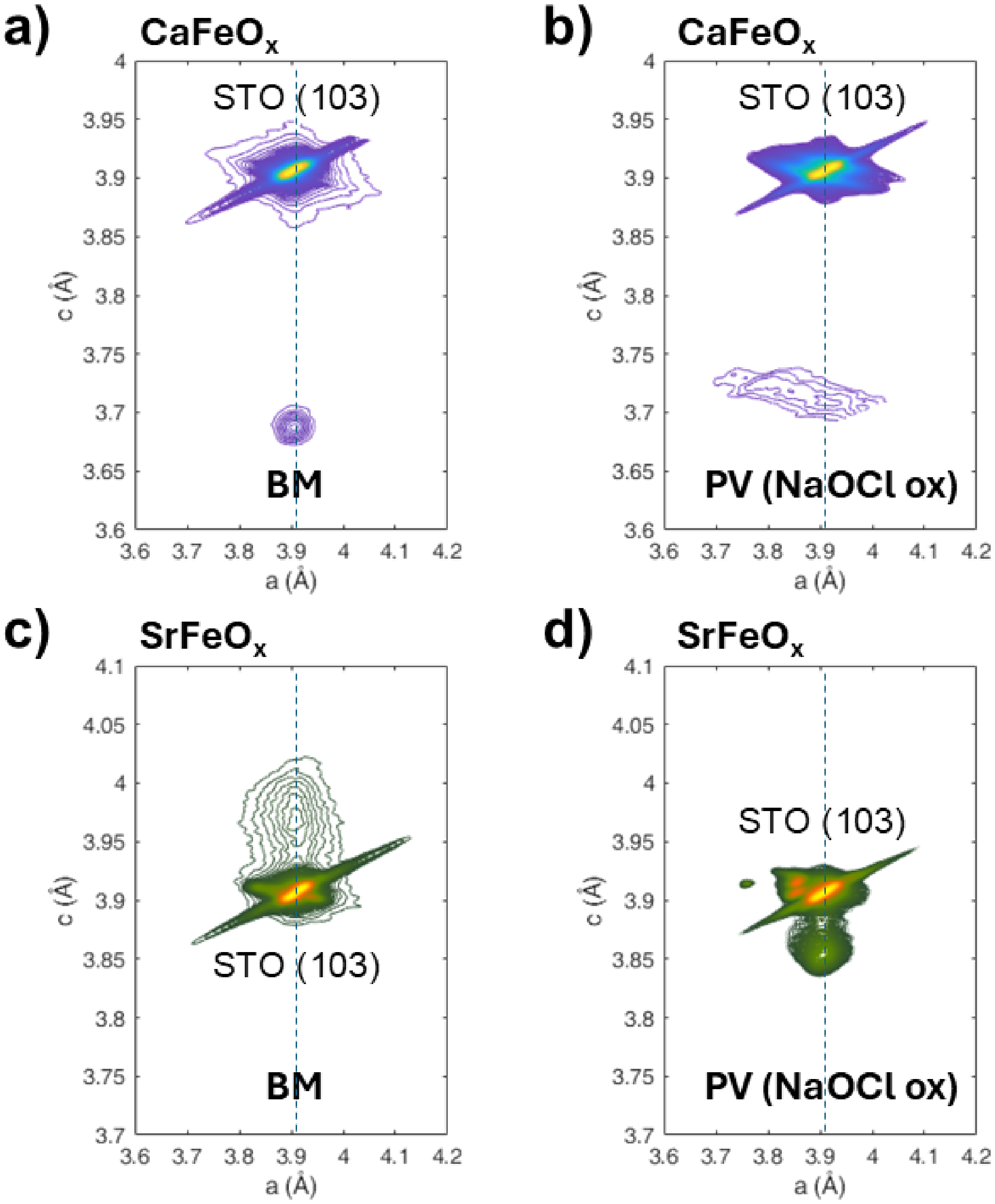

Figure 4.8. Reciprocal space maps around the (103) reflection of STO for CFO (a,b) and SFO (c,d) thin films in the BM phase and after wet oxidation with NaOCl/H_2O solutions. There is a slight relaxation in the PV CFO thin film, while in the case of SFO the film remains matched to the STO substrate during BM-PV transformation.

Furthermore, it is also important to note that the out-of-plane lattice parameter of the NaOCl oxidized PV-CFO determined from the (002) reflection (**Figure 4.7**a,b) is 3.777(6) Å (see **Table 4.1**). However, the reciprocal space map presented in **Figure 4.8**b provides an out-of-plane lattice parameter considerably lower, of the order of 3.73 Å. At this point, the origin of this discrepancy remains unclear, since the reciprocal space map was recorded in the same sample as the one shown in **Figure 4.7** (as well as in some analogous thin films, providing the same results) right after wet oxidation and X-ray diffraction experiments, thus discarding the possibility of relaxation of the structure. Additionally, sample misalignment is unlikely to be the cause of this effect provided that the peak of the STO substrate appears at the expected position. The experiment was repeated several times with identical results.

Interestingly, this behavior has only been observed in the NaOCl oxidized PV-CFO thin films, and we hypothesize that it must be related to the structural changes of CFO thin films during liquid phase oxidation.

To quantify the impact of the accumulation of defects on the microscopic reversibility of the structural transformation, we measured the thermal conductivity of the BM and PV phases using frequency domain thermoreflectance (FDTR).

Figure 4.9 presents the thermal conductivity data for CFO and SFO during topotactic transformations using NaOCl as an oxidant. To avoid problems with the Au/oxide interface, a new layer of Au was deposited after each oxidation/reduction cycle, before measuring the thermal conductivity.

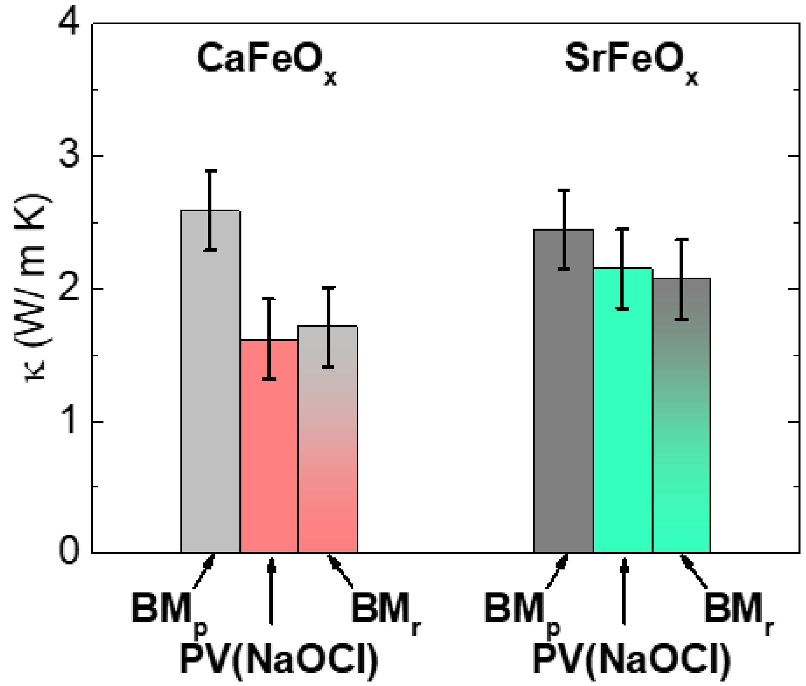

Figure 4.9. Thermal conductivity reversibility of CFO and SFO after liquid phase oxidation with NaOCl/H_2O. Transformation into the PV phase leads to a reduction in the thermal conductivity of both materials. The initial thermal conductivity state cannot be recovered after one oxidation/reduction cycle, pointing to the irreversibility of the process.

As we can observe in the figure, for both CFO and SFO the topochemical oxidation of the BM phase results in a significant reduction in thermal conductivity, ranging from 15% to 35%. This observation contradicts the ab initio predictions shown in **Figure 4.4**, which suggested that the PV-CFO phase should exhibit higher thermal conductivity than the BM.

Very importantly, extracting oxygen to go back to the BM phase does not recover the initial thermal conductivity, confirming that the structural degradation occurring during the BM-PV-BM transformation, as observed in the X-ray diffraction data (**Figure 4.7**), makes the process irreversible from thermal transport point of view. In the case of CFO, the reduced BM phase presents a thermal conductivity ≈30% below the original value; for SFO, the reduced BM shows, within the error, the same thermal conductivity as that of the oxidized perovskite.

For a detailed understanding of the effect of wet oxidation in the microstructure of the films, we performed high-resolution scanning transmission electron microscopy (STEM) on the oxidized phases of CFO and SFO. Cross-sectional lamellae of the thin films after BM-PV transformation were analyzed by high-angle annular dark field (HAADF) imaging and energy dispersive X-ray spectroscopy (EDS) in STEM. The main results are summarized in **Figure 4.10**.

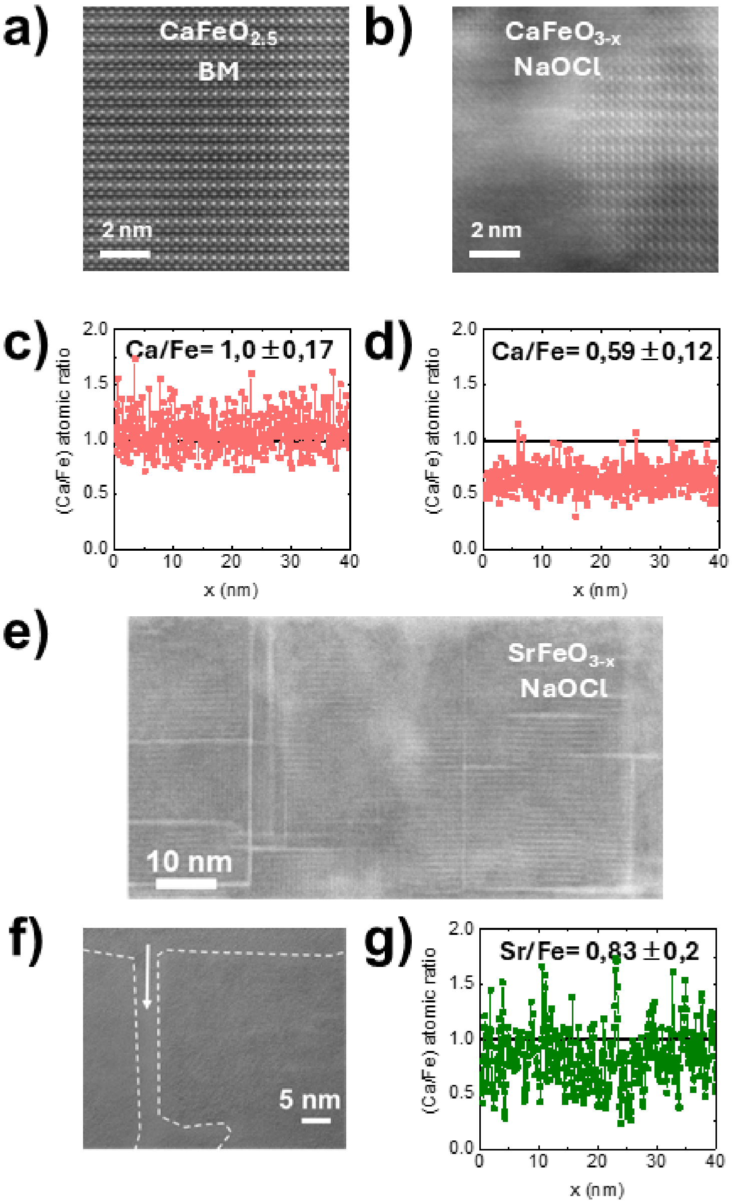

Figure 4.10. Microstructure and chemical compositions of CFO and SFO thin films. High-resolution HAADF-STEM images of the BM thin film of CFO (a), and the PV obtained by oxidation with NaOCl (b). Wet oxidation induces the formation of amorphous regions, which coexist with crystalline domains of the perovskite structure. The corresponding EDS chemical profile analysis along the films are shown under each image (c,d). The Ca/Fe ratio decreases after wet oxidation of the BM phase, confirming the partial dissolution of Ca^{2+}.The crystalline structure of the PV SFO obtained by wet oxidation is shown in the bright field (BF)-STEM image (e), displaying clear signs of amorphization but, in this case, it is restricted to the straight paths of gran boundaries (f). The EDS chemical profile analysis along the PV SFO thin film (g) shows, again, a decrease in the Sr^{2+} content, Sr/Fe ≈ 0.83 ± 0.2. These experiments were performed at the laboratory of Advanced Electron Microscopy (INL, Braga) by Dr. Enrique Carbó-Argibay.

As shown in **Figure 4.10**a, the initial BM-CFO exhibits high crystallinity, with a uniform atomic Ca/Fe ratio of ≈1 (**Figure 4.10**c). However, wet oxidation in NaOCl/H_2O results in partial amorphization of the film, creating a mixture of amorphous regions and crystalline PV domains (**Figure 4.10**b). Interestingly, the process of amorphization is accompanied by a significant reduction of the amount of Ca^{2+}, reducing the Ca/Fe ratio in the film to ≈0.59 (**Figure 4.10**d).

A similar phenomenon is observed in SFO (**Figure 4.10**e-g): wet oxidation produces the PV phase accompanied by partial amorphization, although in this case the amorphous regions are more restricted to the boundaries between crystalline nanodomains, reflecting greater structural stability compared to CFO. This stability is also reflected in a Sr/Fe atomic ratio of ≈0.83 ± 0.2.

In both cases, the partial amorphization of the thin films contributes to the reduced thermal conductivity observed in the perovskite phases (**Figure 4.9**). Amorphous regions and crystalline defects increase phonon scattering, thereby hindering heat transport. Furthermore, the observed decrease in the concentration of Ca^{2+}/Sr^{2+} ions after oxidation results in a degraded BM phase upon reduction, characterized by reduced crystallinity and variable out-of-plane lattice parameter. This structural degradation prevents the recovery of the initial thermal conductivity values, emphasizing the critical impact of ion leaching and defect formation on the reversibility and functionality of these materials.

The reduction of the Ca^{2+}/Sr^{2+} content and the partial amorphization observed during wet oxidation can be understood by examining the underlying mechanism of O^{2-} incorporation/release in negative charge-transfer oxides.

The strong oxidation potential of hypochlorite ions (^{-}OCl) is large enough to oxidize Fe^{3+} in (Ca,Sr)$FeO_{2.5}$. However, instead of producing a pure Fe^{4+} state, the oxidation predominantly results in the Fe^{3+}-$\underline{L}$ electronic configuration in (Ca,Sr)FeO_{3-x}, which is characteristic of the negative charge-transfer PV. In this situation, two competing oxidation reactions occur during the oxidation of Fe^{3+} by NaOCl in water. The first one involves the incorporation of O^{2-} ions from the hypochlorite or from the water into the oxide lattice; the chlorine in the ^{-}OCl is reduced to Cl^{-}, and Fe^{3+} is oxidized towards $Fe^{4+:}$

$$(FeO_{2.5})^{2-} + \frac{1}{2}O^{2-} \rightarrow (FeO_{3.0})^{2-} + e^{-} \qquad (1)$$

However, the progressive increase in the oxidation state of Fe leads to the creation of holes in the O 2p band, making oxygen the primary oxidized species rather than Fe, according to:

$$O^{2-} \rightarrow \frac{1}{2}O_2 + V_{\ddot{O}} + 2e^{-} \qquad (2)$$

A rapid enough generation of oxygen vacancies by this mechanism will reduce the coordination of the alkaline-earth cations (Ca^{2+} and Sr^{2+}), which, combined with their high solubility in water (*196*), can promote their leaching to the solution. This situation destabilizes the whole structure, leading to its collapse and to partial or complete amorphization (*197–200*).

If this mechanism is correct, negative charge-transfer PV oxides should undergo amorphization even in pure water, without the need for a chemical or electrochemical oxidant. The negative charge-transfer energy in the PV CFO and SFO implies a certain amount of intrinsic oxygen vacancies to balance the O_2/O^{2-} and Fe^{+4}/Fe^{+3} redox pairs. If the oxygen vacancy concentration is high enough, the reduced coordination environment of Ca^{2+} and Sr^{2+}

cations at the surface of the film will promote their partial leaching. As the cations dissolve, the oxidation state of Fe increases to keep electroneutrality, driving further electron transfer from the O 2p band and promoting the oxidation of lattice O^{2-} to molecular O_2. This process further reduces the coordination of the alkaline-earth cations, accelerating their dissolution. This self-reinforcing cycle continues until the structure fully collapses into an amorphous phase, as illustrated in **Figure 4.11**.

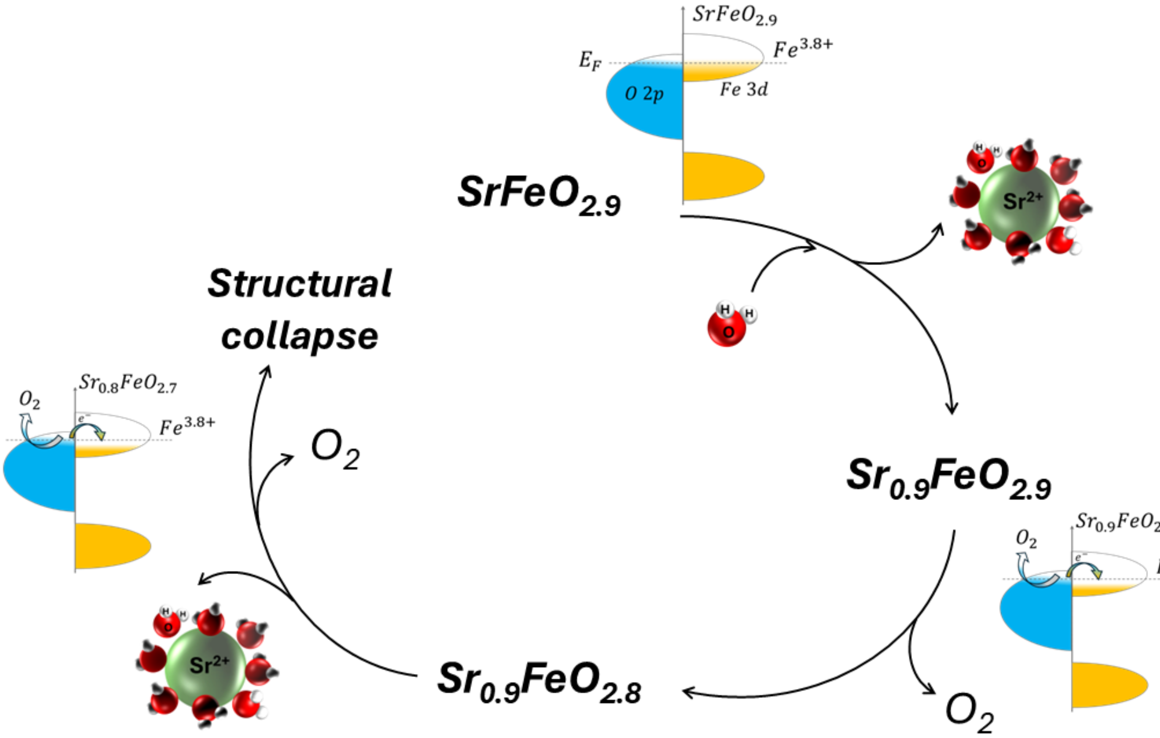

Figure 4.11. Proposed feedback mechanism for the amorphization of negative charge-transfer oxides, exemplified for SFO. Intrinsic oxygen vacancies reduce the coordination of surface Sr^{2+}, which promotes its lixiviation. This, in turn, increases the oxidation state of Fe to keep the electrical neutrality, resulting in further electron transfer from the O 2p band and O^{2-} to O_2 oxidation, as shown in the corresponding band diagrams. This cycle of Sr^{2+} leaching/ O^{2-} oxidation continues until the full collapse of the structure.

To test this hypothesis, we studied the stability in pure water of a series of oxides, with progressively higher charge-transfer energy: $SrCoO_{3-x}$ (SCO), $CaFeO_{3-x}$, $SrFeO_{3-x}$, $La_{0.6}Sr_{0.4}CoO_3$ (LSCO), $SrMnO_3$ (SMO) and $La_{0.7}Sr_{0.3}MnO_3$ (LSMO). These materials present different electronic configurations: SCO, CFO and SFO are negative charge-transfer oxides; LSCO is a positive charge-transfer oxide; and SMO, LSMO are Mott-Hubbard oxides. The relative position of O 2p and metal 3d bands for each type of material is schematized in **Figure 4.12**a-c.

In the case of Mott-Hubbard oxides, the charge-transfer energy, Δ, is larger than the Mott-Hubbard energy, U, so that the lattice oxygen is not the active redox species. In this case, an initial dissolution of a small amount of Sr^{2+} would be compensated by an increase in the oxidation state of the metal (Mn^{4+}), instead of O^{2-} to O_2 oxidation, ending the feedback loop of oxygen vacancies/ ion leaching.

Thin films of SCO, CFO, SFO, LSCO, SMO and LSMO, of comparable thickness of ≈40 nm, were immersed in deionized water at 80 ºC, pH= 6.3, for 6 h. As shown in **Figure 4.12**e, all the oxides with negative charge-transfer energy (SCO, CFO, SFO) are completely amorphized after 6 h in hot water. In contrast, LSCO, that presents a positive charge-transfer energy, only shows a reduction of intensity and broadening of the diffraction peak, signaling a partial loss of crystallinity (probably on the surface). Finally, the Mott-Hubbard oxides (SMO and LSMO) are not affected at all by immersion in water, retaining their crystalline structure.

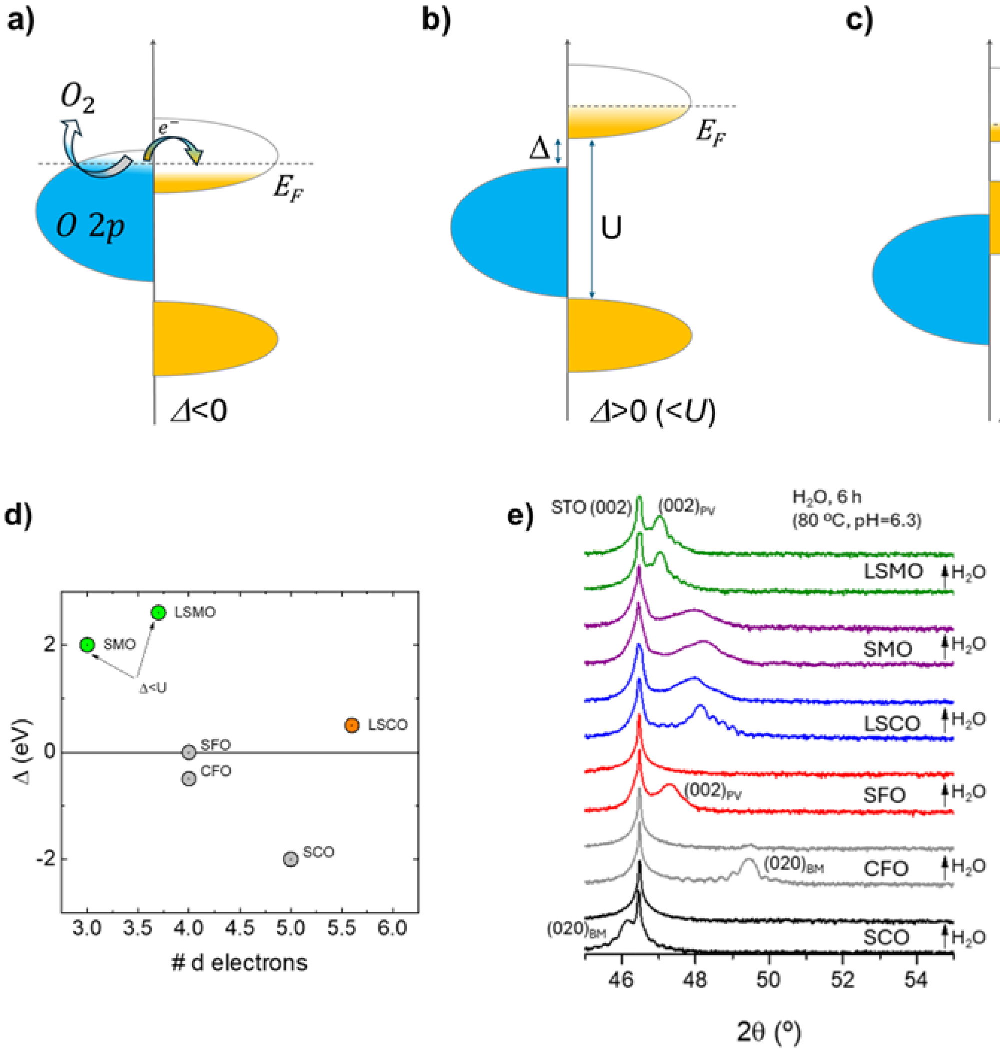

Figure 4.12. Band diagrams of negative charge-transfer (a), positive charge-transfer (b) and Mott-Hubbard (c) oxides. d) Representation of the charge-transfer energy *versus* number of 3d electrons for the oxides studied in this work. Gray, orange and green correspond to negative charge-transfer, positive charge-transfer and Mott-Hubbard oxides, respectively. In (e) we show the comparison of X-ray diffraction patterns of the oxides in (d) before and after immersion in deionized water at 80 °C for 6 h. Negative charge-transfer oxides show complete amorphization of the structure, while positive charge-transfer oxides only show a slight loss of crystallinity. Mott-Hubbard oxides are not affected by immersion in water.

This simple experiment confirms the crucial role of lattice oxygen in the spontaneous amorphization of negative charge-transfer oxides in water and provide new insights into the persistent problem of surface reconstruction observed in several perovskites during catalytic performance under anodic oxidation (*201–203*).

Also, surface amorphization was reported in films of $La_{0.5}Sr_{0.5}CoO_3$ and $SrCoO_3$ during topochemical BM-PV transformation with ionic gels, which prevented the full reversibility of the transformation (*121*, *122*, *173*). Initially, this behavior was attributed to acid etching caused by the high concentration of H^+ ions generated during the electrochemical splitting of residual H_2O molecules in the gel. However, the current findings suggest that the anions of the ionic liquid could also play a significant role by coordinating the alkaline-earth cations, triggering the amorphization of the thin films through feedback looping mechanism of alkaline-earth dissolution/oxygen lattice oxidation, like that proposed in **Figure 4.11**.

These observations highlight the intrinsic instability of negative charge-transfer oxides in polar liquids such as water. This instability fundamentally limits the reversibility of BM-to-PV transformations, making such routes unsuitable for fabricating functional, tunable devices.

4.2.2.2. Gas phase oxidation

BM- CFO thin films were oxidized to the PV phase by thermal annealing at 250 °C, for 1 hour, under flowing ozone (O_3). After this treatment, the half-order reflections and the main (020) peak of the BM disappear, and the (002) peak of the PV appears at ≈48.3 º (**Figure 4.13**a,b), corresponding to a lattice parameter of 3.761(5) Å (**Table 4.2**). The intensity and width of this peak indicate an improved crystallinity of the PV obtained via O_3 oxidation compared to that achieved through wet oxidation with NaOCl/water solution (**Figure 4.7**a). Furthermore, the slightly larger out-of-plane lattice parameter of the PV obtained after wet oxidation (3.777(6) Å) suggests lattice distortion possibly caused by defect accumulation, such as oxygen vacancies.

Subsequent thermal annealing under vacuum (600 ºC, 2 h) successfully recovered the BM phase, as indicated by the presence of the (020) diffraction peak, which retains similar intensity to that of the pristine sample, as well as by the half-order reflections $(0^{3}/_{2}0)$ and $(0^{5}/_{2}0)$, although they show reduced intensity (**Figure 4.13**a). This, along with the loss of the Laue fringes around the (020) peak (**Figure 4.13**b), points towards a partial loss of crystalline quality.

However, this degradation in crystalline quality after O_3 oxidation is not as severe as in the case of wet oxidation with NaOCl. This is evident from the 0.19% increase in the out-of-plane lattice parameter of the reduced BM phase (**Table 4.2**), compared to the 0.3% increase observed after liquid-phase oxidation (see **Table 4.1**).

In the case of SFO films, thermal annealing in oxygen (300 mTorr) is enough to transform the BM phase into PV (**Figure 4.13**c,d). The resulting PV phase exhibits high crystallinity, as evidenced by pronounced Laue oscillations around the (002) peak, characteristic of well-ordered films. The improved structural quality of SFO thin films after gas phase oxidation compared to liquid phase oxidation is also evidenced by the out-of-plane lattice parameters: as in the case of CFO, the PV obtained after wet oxidation presents a higher lattice parameter (3.855(8) Å, compared to 3.852(2) Å after O_2 oxidation), probably pointing to the presence of defects within the structure.

When the PV phase is annealed under vacuum, the BM phase is fully recovered, with the diffraction peaks retaining the original position (matching out-of-plane lattice parameter of 3.985(4) Å, **Table 4.2**) and intensities comparable to those of the pristine sample. This indicates that the BM-PV-BM transformation for SFO thin films using less aggressive conditions (O_2 instead of O_3) is highly reversible, with minimal structural degradation after one cycle.

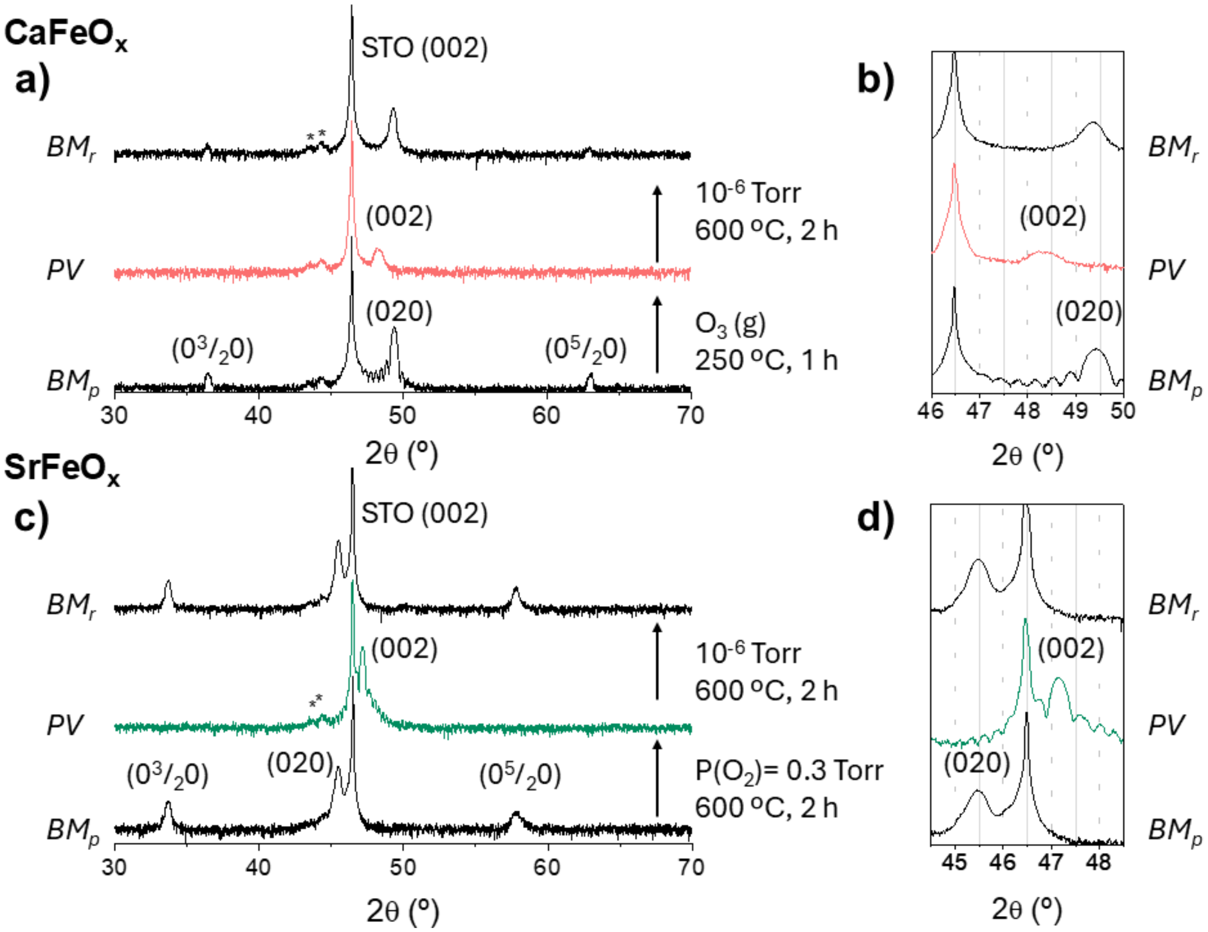

Figure 4.13. X-ray diffraction patterns of the BM-PV-BM transformation in CFO (a,b) and SFO (c,d) thin films (≈40 nm thick) using gas oxidants (O_3/O_2). BM$_p$ and BM$_r$ refer to the pristine and reduced BM phases, respectively. The two peaks at ≈45 º marked with an asterisk are reflections from the tungsten of the X-ray tube. The (020) BM peak is recovered with similar intensity to the pristine film (b,d), but with a partial loss of crystallinity in the CFO sample, as indicated by the disappearance of the Laue oscillations. The half-order reflections ($0^3/_20$ and $0^5/_20$) are now visible in the reduced BM of both materials, but with a considerable decrease in intensity for CFO.

Table 4.2. Out-of-plane lattice parameters of CFO and SFO thin films during BM-PV-BM cycling, using gas phase oxidants (O_3/O_2).

Material	BM$_p$ (Å)	PV (Å)	BM$_r$ (Å)	% BM Change
CFO	3.685(2)	3.761(5)	3.692(3)	+0.19
SFO	3.985(3)	3.852(2)	3.985(4)	0

For a better comparison of the effect of both oxidation methods on the crystalline quality of the samples, in **Figure 4.14** we show the X-ray diffraction patterns of pristine and reduced BM phases of both CFO and SFO, after one cycle of gas phase oxidation (**Figure 4.14**a,c) and liquid phase oxidation with NaOCl (**Figure 4.14**b,d). For both materials, the BM obtained after one cycle of wet oxidation loses the half-order reflections, and the (020) peak reduces its intensity, broadens and losses the Laue oscillations in the case of CFO. These effects are not so severe in the samples obtained after one gas oxidation cycle, especially in the case of O_2 (**Figure 4.14**c) which, as previously discussed, provides full structural reversibility.

It is important to note that, even though the ($0^5/_20$) peak is visible in the reduced BM-CFO after ozone oxidation (**Figure 4.14**a), it presents very low intensity compared to the initial state, pointing to a partial loss of long-range order. Furthermore, the (020) peak in the reduced BM also losses the Laue oscillations around it, although it retains considerable higher intensity compared to the reduced-BM after wet oxidation. Consequently, despite this degradation, the lattice damage is less severe compared to the BM-PV-BM cycles performed with NaOCl/H_2O.

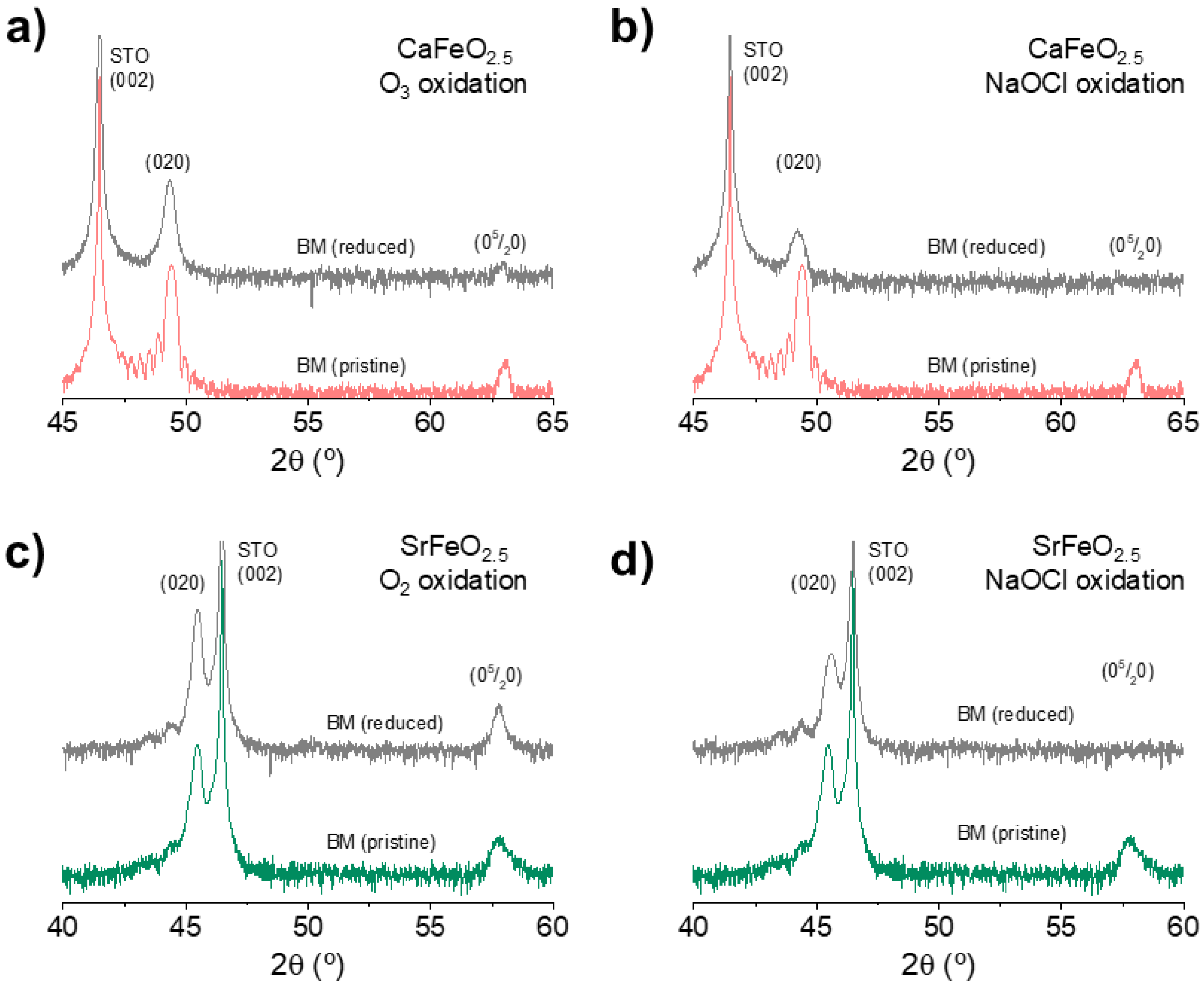

Figure 4.14. X-ray diffraction patterns of the BM phase of CFO before and after topotactic oxidation using O_3 (a) and NaOCl (b) as oxidants. The crystallinity of the brownmillerite is much better in (a), judging from the higher intensity and narrower (020) peak, as well as by the presence of half-order reflection ($0^5/_20$), which is totally absent in the NaOCl-oxidized PV. In (c) and (d) we show the X-ray diffraction patterns of BM-SFO before and after oxidation with O_2 and NaOCl, respectively. Again, the reduced BM obtained after gas phase oxidation (c) presents much better crystallinity, as indicated by the higher intensity of the (020) peak and the presence of ($0^5/_20$).

In summary, the comparison shown in **Figure 4.14** confirms that gas-phase oxidation induces fewer structural defects and preserves better lattice integrity than liquid-phase oxidation.

Reciprocal space maps provide further confirmation of the better structural stability during gas-phase oxidation (**Figure 4.15**). In this case, both CFO and SFO thin films remain perfectly matched to the STO substrate after BM-to-PV transformations with ozone (b) and oxygen (d). Notably, the PV phase of CFO obtained via ozone oxidation retains its lattice parameter, with no evidence of epitaxial relaxation.

It is important to remember that epitaxial strain in CFO changes from +0.18% (BM on STO) to +3.52% (PV on STO), but different to the samples under wet oxidation conditions, the films remain matched to the substrate during the O_3-oxidation process. This better structural integrity of CFO thin films during gas phase oxidation may be related to the Ca/Fe ratio maintained at ≈1 during transformation (as will be analyzed next), in contrast to the partial dissolution of Ca^{2+} in NaOCl/H_2O.

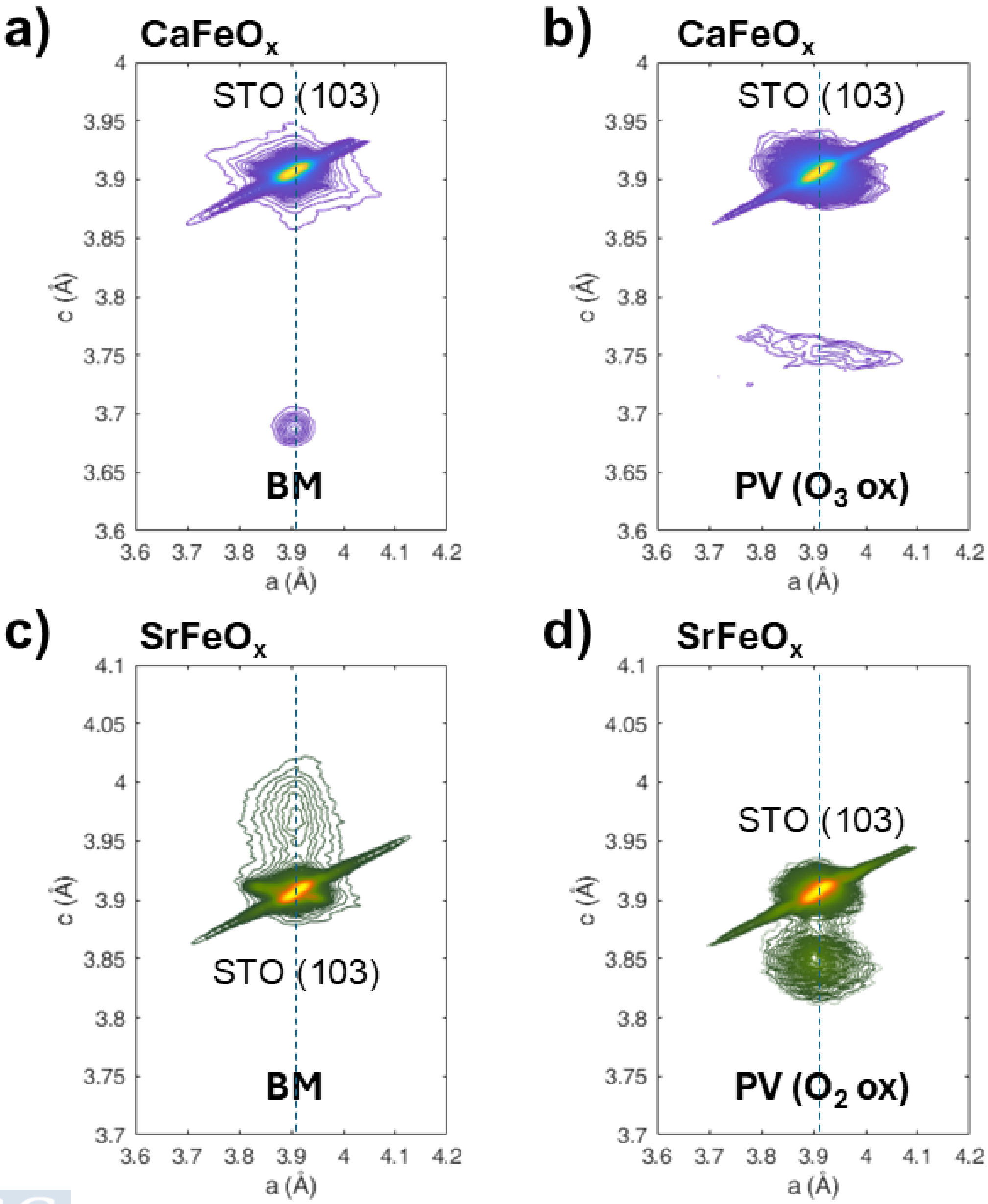

Figure 4.15. Reciprocal space maps around the (103) reflection of STO for CFO (a,b) and SFO (c,d) thin films in the BM phase and after gas phase oxidations with O_3/O_2. The thin films remain perfectly matched to the substrate during BM-PV transformation, as indicated by the in-plane lattice parameter.

High resolution STEM images and EDS composition analysis of the PV structures after gas phase oxidation are summarized in **Figure 4.16,** for both CFO and SFO thin films.

As shown in **Figure 4.16**a-d, oxidation of BM-CFO thin films with O_3 results in a well-crystallized PV that retains a Ca/Fe ratio close to 1, indicating minimal structural degradation during the oxidation process.

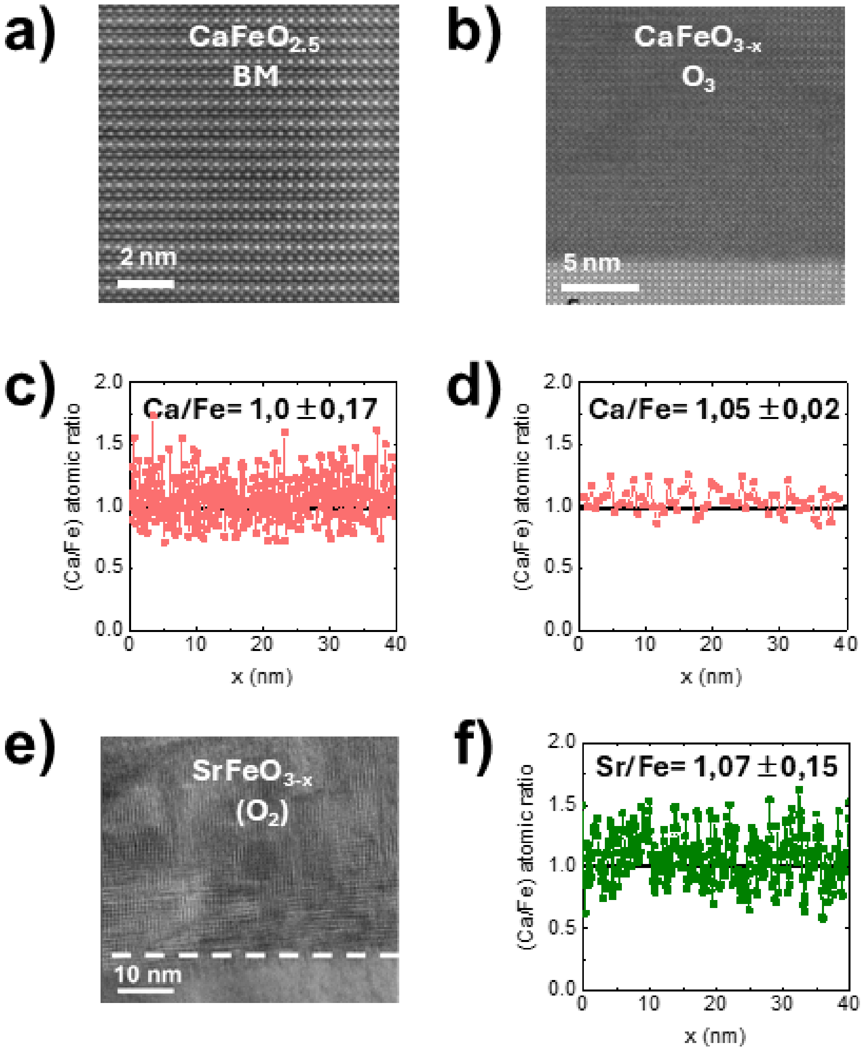

Figure 4.16. Microstructure and chemical compositions of CFO and SFO thin films. High-resolution HAADF-STEM images of the BM thin film of CFO (a), and the PV obtained by oxidation with ozone (b). The corresponding EDS chemical profile analysis along the films are shown under each image (c,d).The crystalline structure of the PV SFO obtained after thermal annealing in O_2 is shown in the TEM image (e), displaying a mosaic structure of nanodomains with different orientations. The corresponding EDS chemical profile is shown in (f). These experiments were performed by Dr. Enrique Carbó-Argibay (laboratory of Advanced Electron Microscopy at INL) and Dr. César Magén (Institute of Nanoscience and Materials of Aragón).

A similar trend is observed for SFO (**Figure 4.16**e,f): oxidation of the BM under flowing oxygen also maintains a good crystallinity, displaying PV nanodomains with different orientations. Very importantly, the Sr/Fe ratio remains approximately ≈1, further confirming that the oxidation process does not significantly alter the stoichiometry of the material.

These findings demonstrate that gas-phase oxidation methods are less aggressive and result in better structural preservation during BM-PV-BM transformations than liquid phase oxidation. This improved stability is critical for applications requiring high structural and functional reversibility, underscoring the advantages of gas-phase oxidants over wet chemical methods.

Figure 4.17 presents the thermal conductivity measurements of CFO and SFO thin films after topotactic oxidations with O_3 and O_2, respectively. As observed, the oxidation of CFO with O_3 results in a ≈30% increase in thermal conductivity, in agreement with the theoretical calculations for 40 nm thick films (**Figure 4.4**). Subsequent reduction to the BM phase recovers the initial thermal conductivity value, demonstrating a reversible switching of thermal conductivity after one cycle. However, repeating the oxidation/reduction cycle results in irreversibility issues, reflected in the significant variability and irreproducibility observed in thermal conductivity after just two cycles.

The results are qualitatively similar in SFO thin films. Thermal annealing under flowing O_2 leads to an increase in thermal conductivity during BM-to-PV transformation, and the initial thermal conductivity value can be restored through vacuum annealing (PV-to-BM), confirming the reversibility of the transition that was previously observed through X-ray diffraction (**Figure 4.13**c,d). However, after five cycles, the thermal conductivity decreases by ≈15-30% compared to the first one, preventing the full reversibility of the transformation.

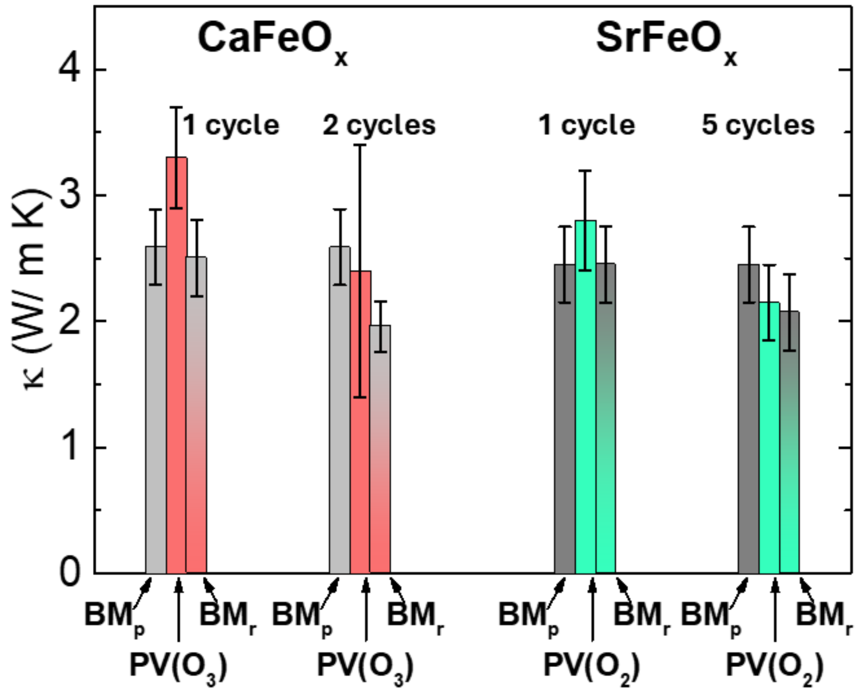

Figure 4.17. Thermal conductivity reversibility of CFO and SFO thin films (≈40 nm) after gas phase oxidation under O_3 (after the first and second oxidation/reduction cycle) and O_2 (after the first and fifth oxidation/reduction cycle). Although the thermal conductivity of CFO is reversible after one oxidation/reduction cycle with ozone, repeating the process results in the progressive accumulation of defects and incomplete transformation, leading to a reduction of thermal conductivity. Similar results are found in SFO: thermal conductivity seems reversible after one oxidation cycle with O_2, but there is a substantial reduction in thermal conductivity after five cycles.

The irreversibility of thermal conductivity after continuous BM-PV cycling is primarily due to the progressive accumulation of lattice defects during the topotactic transitions, as can be concluded from the oxidation/reduction mechanism. The process of topochemical oxidation with O_3/O_2 begins with the absorption of the oxidant molecule on the film surface, followed by electron transfer from Fe^{3+} to the antibonding molecular orbitals of O_3/O_2. This weakens the O-O bonds, facilitating the formation of O^{2-} ions that diffuse into the structure and fill the oxygen vacancies of the BM, forming the PV. Reducing the sample back to the BM structure requires the dimerization of lattice oxygen ions into either peroxide (O_2^{2-}) or superoxide (O_2^{-}) species inside the lattice, which are subsequently released as O_3 or O_2. This reduction process weakens the O-(Ca,Sr) and O-Fe bonds, and, when combined with the moderate ionic mobility at the temperature of the experiments (600 ºC), it can lead to irreversible cation segregation and defect accumulation, as observed in other oxides after repeated ion intercalation cycles (*170*, *172*).

A signal of this progressive accumulation of defects can be observed in **Figure 4.18,** which compares the X-ray diffractograms of PV CFO and SFO thin films after several oxidation-reduction cycles. In CFO, two BM-PV oxidation cycles with ozone result in incomplete structural transformation, producing a mixture of both BM and PV phases with heterogeneous domains (**Figure 4.18**a).

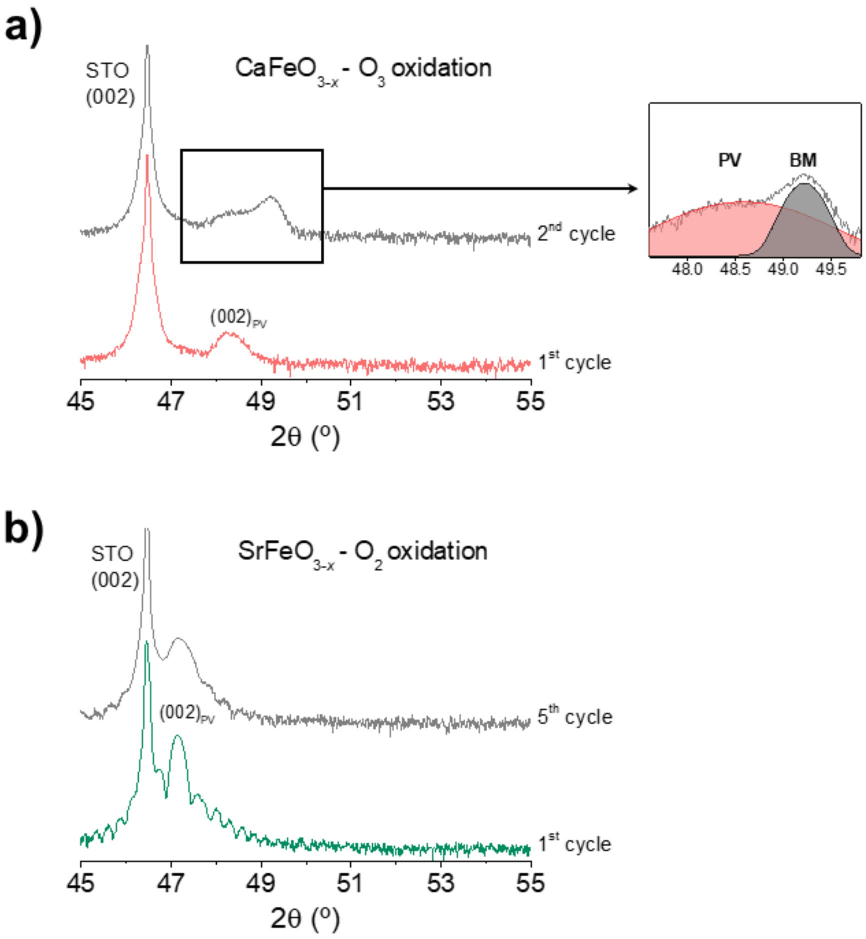

Figure 4.18. a) Comparison of the X-ray diffraction patterns of the PV CFO after two BM-PV oxidation cycles. After two cycles, there is an incomplete transformation of the BM into PV, showing a mixture of both phases. The inset shows the fitting of the diffraction peaks of each phase, corresponding to a mixture of 90% and 5% of PV and BM phases, respectively. b) Comparison of the X-ray diffraction patterns of the PV SFO after five BM-PV oxidation cycles. The (002) diffraction peak broadens and loses some of the Laue oscillations, indicating a reduction in crystalline quality.

We can estimate the proportion of BM and PV phases in **Figure 4.18**a by comparing the relative intensities of each diffraction peak to that of the pure BM and PV phases in the same film. In this case, after two oxidation/reduction cycles, there is a ≈90% of the film in the perovskite phase, while ≈5% of the film is in the brownmillerite structure. The remaining 5% corresponds to amorphous regions, probably on the boundaries between the different crystalline domains. Note that the relative intensity of the BM (020) reflection is considerably higher than that of the PV (002), which explains why the PV phase is the predominant, even though its diffraction peak is less intense.

In contrast, after five oxidation/reduction cycles in SFO, a pure perovskite structure is still obtained, retaining the initial out-of-plane lattice parameter (3.852(5) Å). However, this phase presents worse crystallinity, as indicated by the reduction in intensity of the (002) peak, loss of part of the Laue oscillations, and substantial broadening.

The irreversibility issues reported in this section, resulting from the progressive accumulation of defects during topochemical oxidation with O_3 and O_2, present a significant limitation for the design of tunable thermal devices based on this oxidation route. The degradation of material properties after repeated cycling underscores the need for strategies to minimize structural damage, in order to maintain the reversibility and performance of these devices.

4.2.2.3. Solid state oxidation

In this section, we explore the use of a solid electrolyte (yttria-stabilized zirconia, 9.5 mol% Y_2O_3 in ZrO_2, YSZ) for the reversible O^{2-} insertion/depletion into CFO and SFO thin films.

Solid ionic conductors, commonly referred to as solid electrolytes, are crystalline materials in which electric current is carried by ions instead of electrons, thus involving both charge and mass transfer. These materials rely on structural defects, such as vacancies or interstitial sites, that allow one component of the lattice –either cations or anions– to move freely. Like liquid electrolytes, solid electrolytes facilitate ion migration but offer the mechanical stability and durability of solids (*204*).

YSZ was selected for this study due to its well-established role as an oxide ion conductor, previously used as an oxygen reservoir to exchange O^{2-} ions in Co-oxides (*120*, *205–208*). In its high-temperature cubic polymorph, ZrO_2 adopts the fluorite crystal structure, which can be stabilized at room temperature by the formation of solid solutions with Y_2O_3. This stabilization implies the formation of oxygen vacancies to keep electroneutrality when Zr^{4+} ions are replaced by Y^{3+} (*158*), thus allowing O^{2-} ions to hop between empty lattice sites and resulting in ionic conduction. This ionic conductivity is favored at high temperatures (≈0.1 S/cm at 1000 ºC (*209*)) but remains at an appreciable ≈10^{-5} S/cm at 350 ºC (*205*).

In this project, we deposited several thin films of CFO and SFO (with thicknesses between 30 and 140 nm) on YSZ substrates. We deposited a ≈10 nm thick layer of 8% Gd-doped CeO_2 prior to CFO and SFO, to prevent the formation of $(Ca,Sr)ZrO_x$ at the interface, which would block the oxygen migration (see the schematic diagram of the device and the TEM image in **Figure 4.19**a,b). Oxygen intercalation/deintercalation into these films was achieved by applying electric fields to the (Ca,Sr)FeO$_X$/CeO$_2$/YSZ structure, using Al and Pt as top and bottom contacts, respectively, as illustrated in **Figure 4.19**a.

To enhance ionic conductivity across the YSZ substrate, the electric-field insertion/depletion of O^{2-} ions must be carried out at moderate temperatures. For this purpose, the devices (**Figure 4.19**a) were placed on a hot plate at 280 ºC during voltage application.

In **Figure 4.19**c we show the current and resistance variation of a BM-CFO thin film (≈140 nm) during oxidation at 280 ºC under an applied voltage of +8 V. Initially, the film transitions from a high-resistance state (BM phase, insulating) to a low-resistance state (PV phase, conductive). However, after 600 s of voltage application (indicated by the dashed blue line in the figure), before the BM-PV transition was fully completed, the hot plate was switched off, causing a rapid decrease in temperature. This temperature drop significantly reduced the ionic conductivity of the YSZ substrate, which in turn caused a gradual relaxation of the system back to its thermodynamically stable higher-resistance state (BM), despite the continued application of the voltage bias.

By monitoring the current/resistance of the film, we observed that oxygen exchange with the YSZ substrate was entirely blocked ≈5 minutes after switching off the heater, as evidenced by the stabilization of the current and resistance values. This experiment underscores the importance of using moderate temperatures to facilitate O^{2-} conductivity across the device.

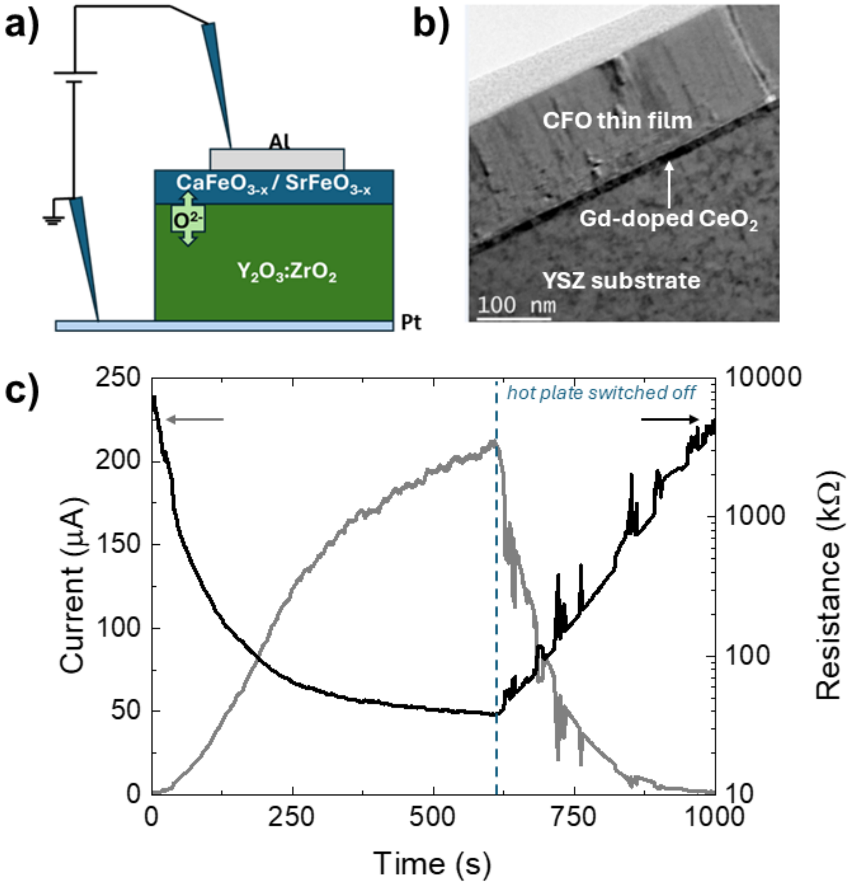

Figure 4.19. a) Scheme of the Pt/YSZ/CeO$_2$/(Ca,Sr)FeO$_x$/Al system for O^{2-} insertion/removal with electric fields. b) TEM image of a film of CFO (≈140 nm) on CeO$_2$/YSZ. Residual resist from lamellae preparation is visible on top of the CFO film. c) Stability test of a BM-CFO thin film during +8 V application at 280 °C. After ≈600 s (indicated by the dashed blue line), the hot plate is switched off, blocking the oxygen migration and resulting in the relaxation of the system towards a high-resistance state.

The electrochemical process governing this electric-field driven O^{2-} injection/depletion in $(Ca,Sr)FeO_x$ thin films occurs according to Faraday's laws of electrolysis, and it can be described by the following equilibrium reaction:

$$(Ca,Sr)FeO_{2.5} + \frac{1}{2}O^{2-} \leftrightarrow (Ca,Sr)FeO_3 + e^- \qquad (3)$$

Applying a positive voltage to the film (anode) drives its oxidation, shifting the equilibrium to the right and thereby transforming the BM phase into the PV through the incorporation of O^{2-} ions. Conversely, applying a negative voltage to the film (cathode) displaces the oxide O^{2-} ions towards the YSZ, which transforms the film back into the BM structure.

As observed in **Figure 4.20**a, the application of +8 V to a 40 nm thick BM SFO thin film, at 280 ºC, during ≈1 min, is enough to drive complete BM to PV oxidation, as indicated by the stabilization of the current. This electrochemical oxidation is accompanied by a significant change in color: from the colorless insulating BM (**Figure 4.20**b) to the metallic-like conductive PV (**Figure 4.20**c). Conversely, application of -8 V to the system reverts the structure to the original BM phase, as indicated by the value of the current (**Figure 4.20**a) and, again, by the change in color. Similar results have been found in CFO thin films of the same thickness (≈40 nm).

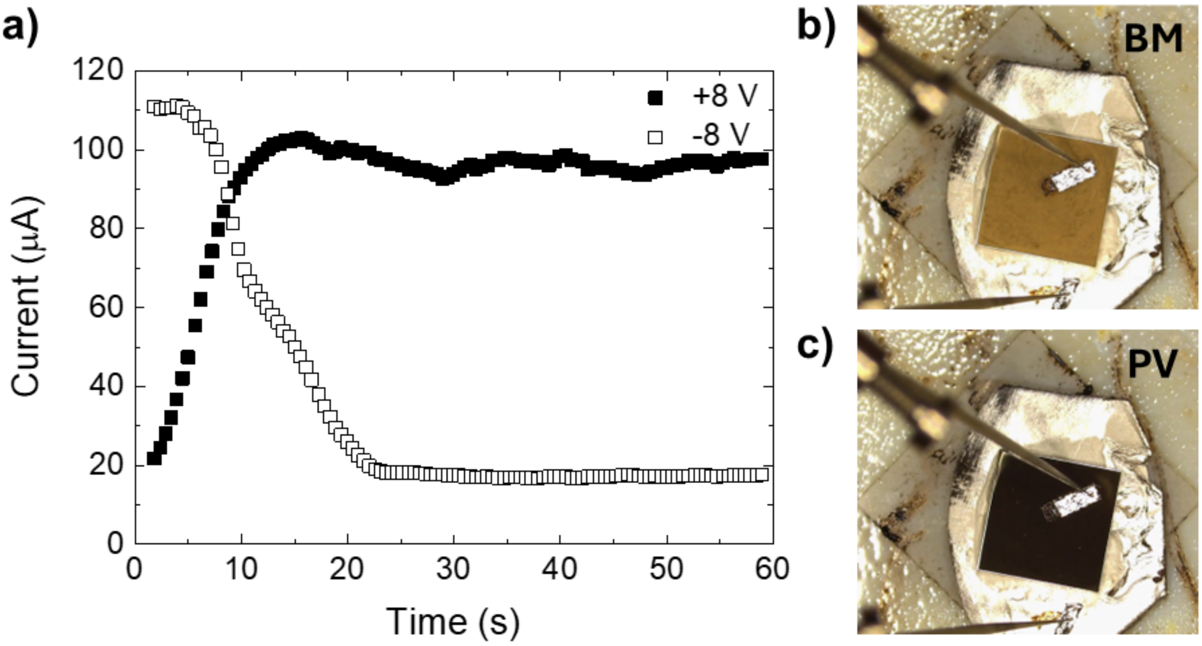

Figure 4.20. a) Current *versus* time curves of a ≈40 nm thick SFO film on CeO_2/YSZ, during the application of +8 and -8 V at a constant temperature of 280 °C, which drive topotatic oxidation and reduction, respectively. The current axis is given in absolute value. In (b,c), we show the change in color associated with such structural transitions.

The phase transition illustrated in **Figure 4.20** was further characterized by ex-situ X-ray diffraction. **Figure 4.21** presents the X-ray diffraction patterns of CFO and SFO thin films (≈40 nm thick) after undergoing BM-PV-BM transformations through the application of ±8 V. In both cases, we monitored the current *versus* time curves during voltage application at 280 ºC, waiting until complete current stabilization and change in color, as previously described. The samples were then transferred to the diffractometer for structural characterization.

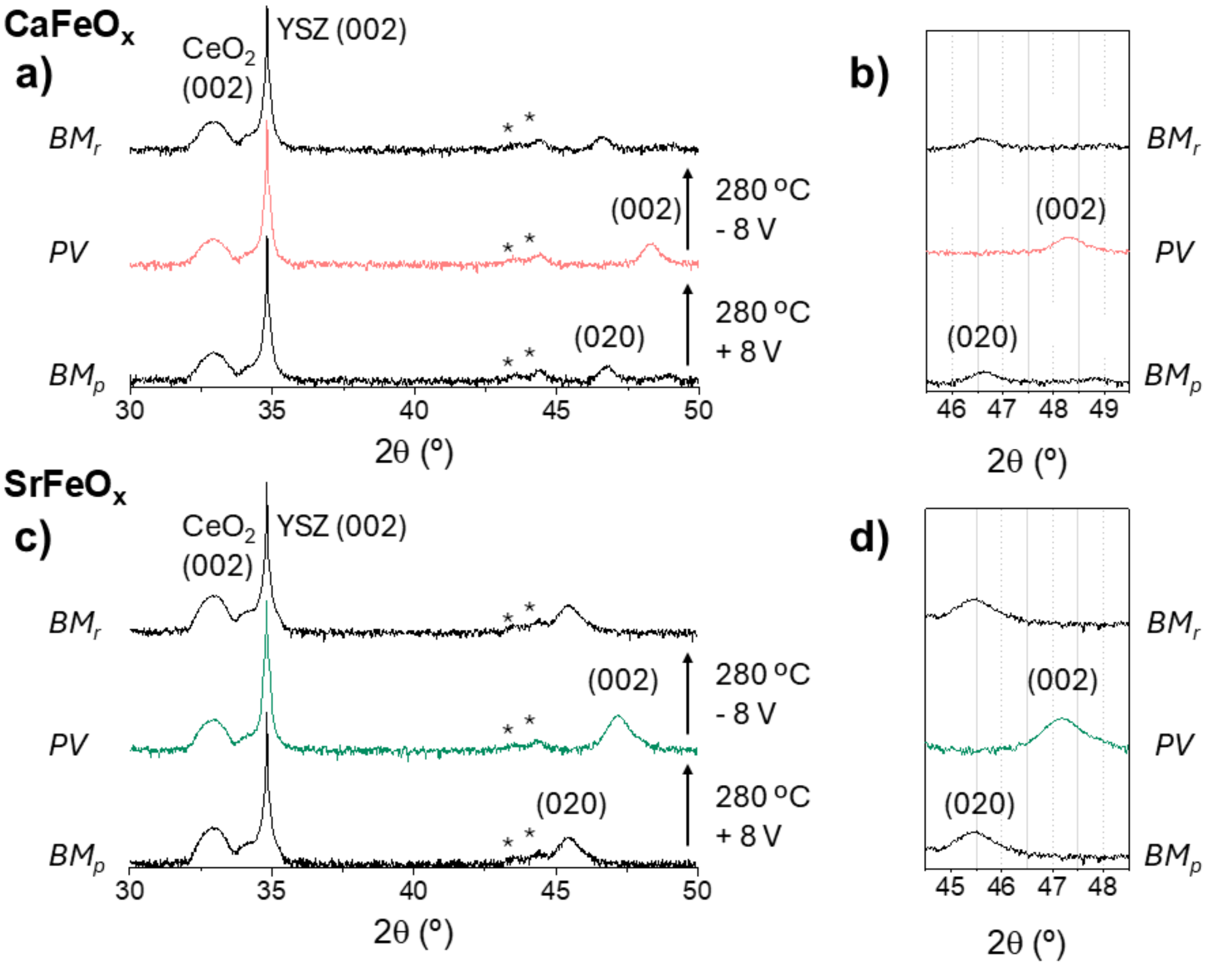

Figure 4.21. X-ray diffraction patterns of the BM-PV-BM transformation in CFO (a,b) and SFO (c,d) thin films (≈40 nm thick), after the application of ±8 V, at 280 °C, using YSZ as solid electrolyte. BM$_p$ and BM$_r$ refer to the pristine and reduced BM phases, respectively. The two peaks at ≈45 ° marked with an asterisk are reflections from the tungsten of the X-ray tube. The (020) BM peak is recovered with similar intensity to the pristine film (b,d), maintaining its original position.

As observed in **Figure 4.21**, application of +8 V to CFO (**Figure 4.21**a,b) and SFO (**Figure 4.21**c,d) thin films drives complete BM-to-PV transformation. This is evidenced by the disappearance of the (020) diffraction peak characteristic of the BM, and the emergence of the PV-(002) reflection. The corresponding lattice parameter change is from 3.895(2) Å to 3.766(4) Å for CFO, and from 3.988(5) Å to 3.849(3) Å in the case SFO (**Table 4.3**). In both cases, these lattice variations are consistent with the formation of the PV phase. However, a direct comparison with the phase transformations described in previous sections is not straightforward, as the YSZ substrate used here (lattice parameter of 5.12 Å for substrates purchased from CrysTec GmbH) differs from the STO substrates used in earlier experiments, leading to distinct epitaxial strains.

Conversely, applying -8 V to the thin films induces complete PV-to-BM reduction, restoring the initial (020) diffraction peak with intensity and position comparable to those of the pristine sample. The matching lattice parameters of the pristine and reduced BM phases (**Table 4.3**) suggest that the topotactic phase transitions induced by this method are fully reversible.

Table 4.3. Out-of-plane lattice parameters of CFO and SFO thin films after BM-PV-BM cycling through the application of ±8 V, using YSZ as solid electrolyte.

Material	BM_p (Å)	PV (Å)	BM_r (Å)	% BM Change
CFO	3.895(2)	3.766(4)	3.895(4)	0
SFO	3.988(5)	3.849(3)	3.988(6)	0

As previously demonstrated in **Figures 4.20-4.21**, the application of ±8 V to 40 nm thick SFO and CFO thin films drives complete BM-to-PV oxidation/reduction. However, the precise amount of O^{2-} exchanged in the film can be calculated through the relationship with the total amount of charge (Q) injected into the film in a time interval, t:

$$Q = \frac{I \cdot t}{e \cdot V} \qquad \textit{(Eq. 4.1)}$$

where I refers to the current intensity flowing through the sample, e is the electron charge, and V is the volume of the film. According to equation *(3)*, 0.5 O^{2-} ions per electron are incorporated into the structure. Therefore, the oxygen content of the film can be estimated from the injected electron densities.

The electrochemical reaction described in *(3)* involves one electron, so that the complete BM-PV transformation in SFO, for example, requires an electron density of around $1.75 \cdot 10^{22}$ e/cm^3, assuming a unit cell volume of $\approx 5.71 \cdot 10^{-23}$ cm^{-3} (based on the cubic perovskite with lattice parameter 3.852 Å). Therefore, the extent of the oxygen exchange and the topotactic transformation between both phases can be precisely controlled by adjusting the time during which the voltage is applied, as illustrated in **Figure 4.22**.

Applying V≥ +7 V at 280 ºC stabilizes the current after ≈1 min for 40 nm thick films (solid symbols in **Figure 4.22**a). In contrast, thicker films of about 140 nm require longer injection times, such as ≈1.5 min for 8 V (open circles in the same figure).

The application of lower voltages (from 1 to 6 V) for 1 min led to partial transformations, since the minimum electron density needed for the complete transformation (marked by a vertical dashed line in the figure) was not achieved. This results in intermediate oxidation states and varying oxygen contents of $2.5+\delta$ (where $0 < \delta < 0.5$).

As shown in **Figure 4.22**b, the application +7 or +8 V, for 1 min, to a 40 nm thick SFO film results in the full oxygenation of the structure, yielding an oxygen content of ≈3. In contrast, applying +5 V for 1 min injects an electron density of $\approx 1.3 \cdot 10^{22}$ cm^{-3} (below the required value of $1.75 \cdot 10^{22}$ e/cm^3), corresponding to ≈0.75 electrons per unit cell or ≈0.375 oxide ions (δ), achieving a total oxygen content of $2.5+\delta \approx 2.875$. This demonstrates the precise tuning of oxygen content by varying the applied voltage and duration, enabling control over the material's oxidation state and properties.

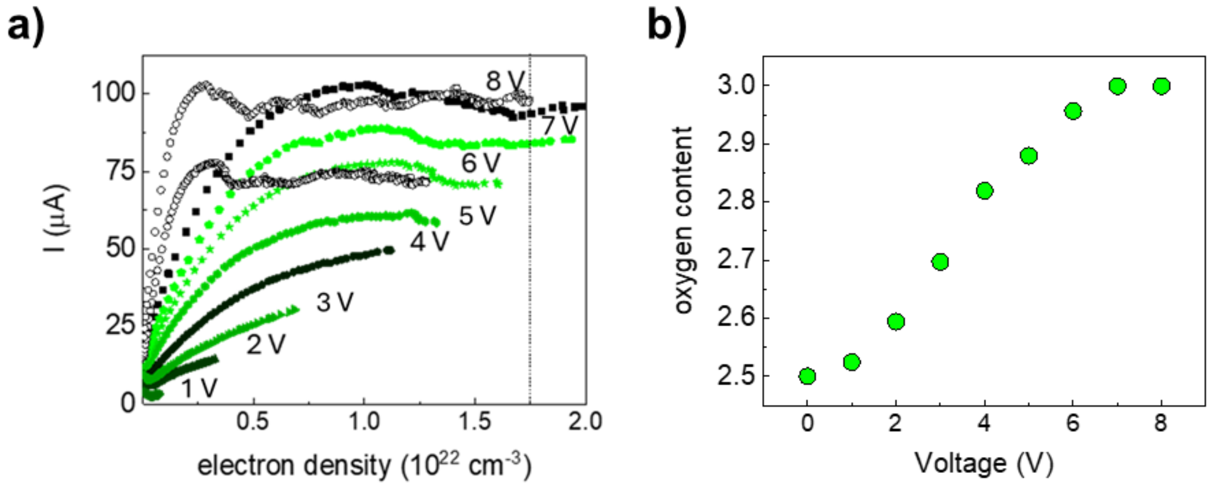

Figure 4.22. a) Current *vs* electron-density curves of a SFO thin film under different electric fields, according to *Eq. 4.1*. The solid symbols correspond to 40 nm thick films and *t*= 1 min; the open circles at 6 V and 8 V correspond to a 140 nm thick film at *t*= 1.5 min. The vertical dashed line at ≈$1.7 \cdot 10^{22}$ cm^{-3} represents the minimum electron density needed for the complete BM-to-PV oxidation, according to equation *(3)*. In (b) the calculated oxygen content after one minute of redox reaction in the films with 40 nm thickness is shown. Application of either 7 or 8 V for 1 min is enough to transform the 40 nm film of BM into a fully oxygenated PV.

The electrochemical BM-PV transformation can be also monitored using in-operando X-ray diffraction at 280 ºC, while applying alternating positive and negative voltages to our system. The main results are summarized in **Figure 4.23**a (for CFO) and **Figure 4.23**b (for SFO). In both cases, it is possible to induce reversible transformations between the brownmillerite and perovskite phases by the application of ±8 V (corresponding to an electric field of approximately ±600 kV/cm), consistent with the behavior previously observed in **Figures 4.20-4.22.**

For SFO thin films, the PV-to-BM transformation rate can be slowed down by applying intermediate voltages between the extremes of ±8 V. Under these conditions, the lattice parameter evolves continuously, revealing intermediate phases with oxygen contents of $2.5+\delta$ ($0 < \delta < 0.5$), as illustrated in **Figure 4.23**b. Conversely, the transformation from BM back to the PV phase proceeds significantly faster: even at a lower voltage of +2 V, no intermediate phases are detected during the X-ray diffraction scan time (≈8 minutes), indicating rapid oxygen incorporation.

In the case of CFO, the PV-BM transition is comparatively slower, requiring several minutes to complete. Even at ±8 V, the transformation remains incomplete during the first diffraction scan (≈8 minutes), necessitating longer voltage application times for full conversion. However, similar to SFO, the topotactic transformation in the BM to the PV direction occurs slightly faster, and it is possible to observe the coexistence of both phases at intermediate injection times (**Figure 4.23**a).

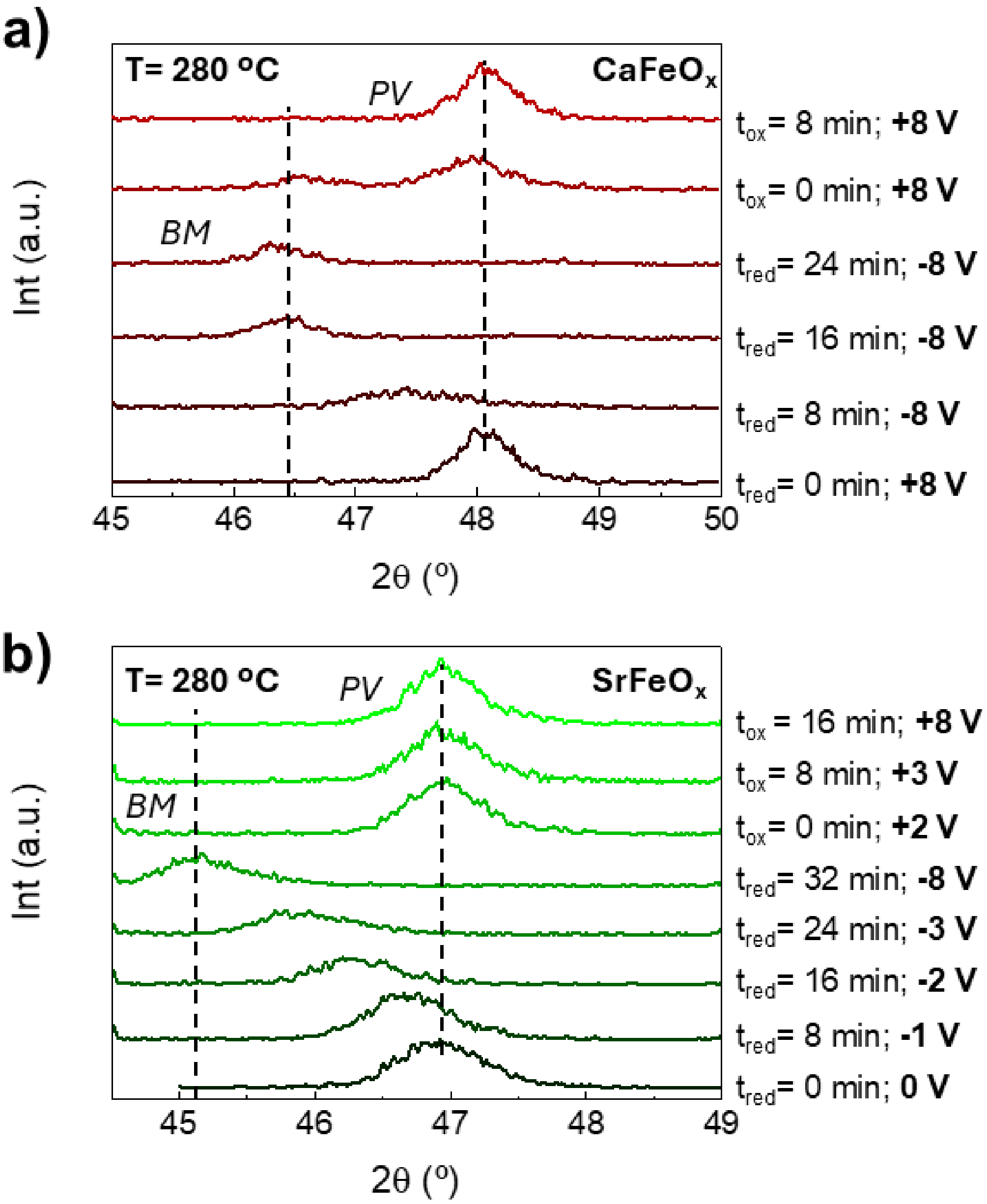

Figure 4.23. In operando X-ray diffraction patterns of the PV-BM transformation in CFO (a) and SFO (b) thin films (≈140 nm) at 280 °C, under different applied voltages, are shown. The films can be cycled between both structures dozens of times without apparent damage. Intermediate phases of SFO can be stabilized by using intermediate voltages between the extremes ±8 V. In the case of CFO, coexistence of phases can be observed during BM to PV transformation. The diffraction panels shown in (a) and (b) correspond to consecutive experiments. Each diffractogram takes 8 min to complete.

We have repeated this BM-PV-BM cycling process more than 10 times and corroborated through XRD that the topotactic transformation is completely reversible and reproducible from the structural point of view, with the diffraction peaks retaining their position (the corresponding lattice parameters are indicated in **Table 4.4**), intensity and width. Please note that the out-of-plane lattice parameters shown in this table are slightly larger than those presented in **Table 4.3**, due to the thermal expansion experienced by most oxoperovskites (*210*, *211*).

Table 4.4. Out-of-plane lattice parameters of CFO and SFO thin films obtained during in-situ BM-PV-BM cycling, at 280 °C, through the application of ±8 V using YSZ as solid electrolyte.

Material	**BM$_p$ (Å)**	**PV (Å)**	**BM$_r$ (Å)**	**% BM Change**
CFO	3.901(3)	3.778(4)	3.901(3)	0
SFO	4.016(3)	3.867(2)	4.016(4)	0

Moreover, apart from the X-ray diffraction data, EDS analysis on cross-sections of the thin films (**Figure 4.24**) also confirmed that structural integrity is maintained after repeated cycling. As shown in **Figure 4.24**b, the EDS line scan displays an invariable Ca/Fe ratio ≈1 in CFO thin films. The same results have been obtained in SFO after several oxidation/reduction cycles.

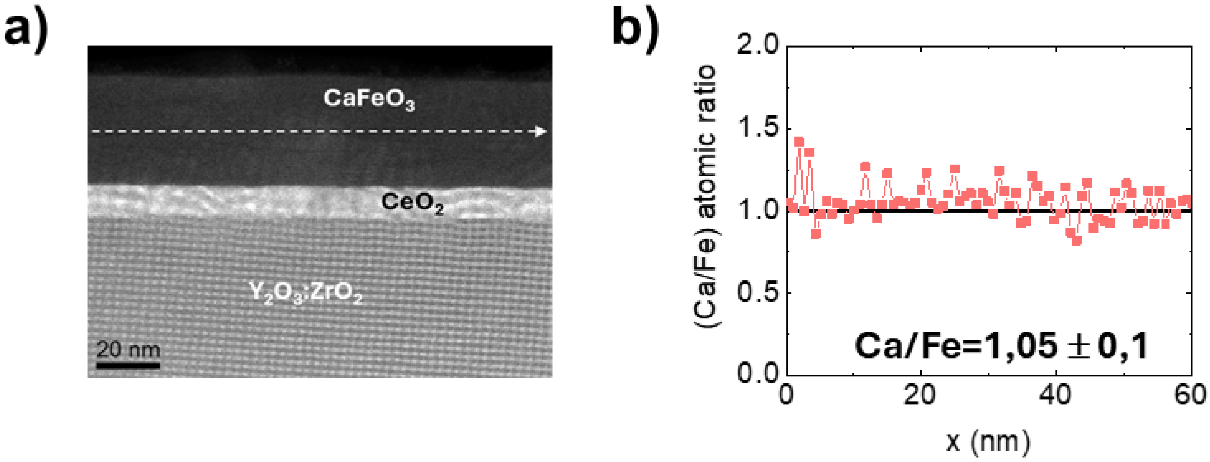

Figure 4.24. a) HAADF-STEM image of CFO thin film on CeO_2/YSZ. b) EDS line scan along the film after several oxidation/reduction cycles, and a final oxidation at +8 V to the perovskite phase. The film maintains the stoichiometric Ca/Fe ratio = 1. Experiments performed by Dr. César Magén (Institute of Nanoscience and Materials of Aragón).

We also checked these electric-field induced topotactic transformations using RSM. **Figure 4.25** shows the reciprocal space maps of 140 nm thick films of CFO (**Figure 4.25**a,b) and SFO (**Figure 4.25**c,d) after the application of positive and negative voltages (±8 V), thus characterizing the perovskite and brownmillerite phases, respectively.

In contrast to the thin films discussed in previous sections (liquid and gas phase oxidations), where CFO and SFO were grown on STO substrates (with lattice parameter a= 3.905 Å) and experienced either mild tensile or compressive strains depending on the phase, the thin films used for this study were deposited on YSZ substrates.

These YSZ substrates exhibit a significantly larger in-plane lattice parameter of 5.12 Å (for substrates purchased from CrysTec GmbH) and were coated with a ≈10 nm layer of Gd-doped CeO_2, which presents an even greater lattice parameter of 5.411 Å (*212*). The substantial lattice mismatch between these two materials (-5.4%) leads to the relaxation of the CeO_2 layer when its thickness exceeds ≈3 nm (*213*, *214*). This effect is evident in all the reciprocal space maps presented in **Figure 4.25**, where the Gd-doped CeO_2 layer adopts its bulk lattice parameter.

In order to minimize the strain, CFO and SFO thin films grow on CeO_2-coated YSZ substrates with a 45 º in-plane rotation around the [001] direction (*215*), since the lattice parameter of Gd-doped CeO_2 is more similar to $\sqrt{2}a_{pc}$ than a_{pc} (where a_{pc} represents the pseudo-cubic lattice parameter) for both CFO and SFO. Despite this structural reorganization, all CFO and SFO thin films (in both BM and PV phases) remain significantly strained, ranging from a tensile strain of ≈1.5% for the PV-CFO to a pronounced compressive strain of ≈ -3.32% for the BM-SFO. This results in the epitaxial relaxation of the thin films, as can be observed in **Figure 4.25**: CFO adopts lattice parameters between those of CeO_2 and the YSZ substrate (**Figure 4.25**a,b), while SFO thin films exhibit even greater lattice expansion (**Figure 4.25**c,d).

Notably, this relaxation persists even in thinner films (≈30 nm), indicating that the significant lattice mismatch strongly influences the structural adaptation of the films regardless of their thickness.

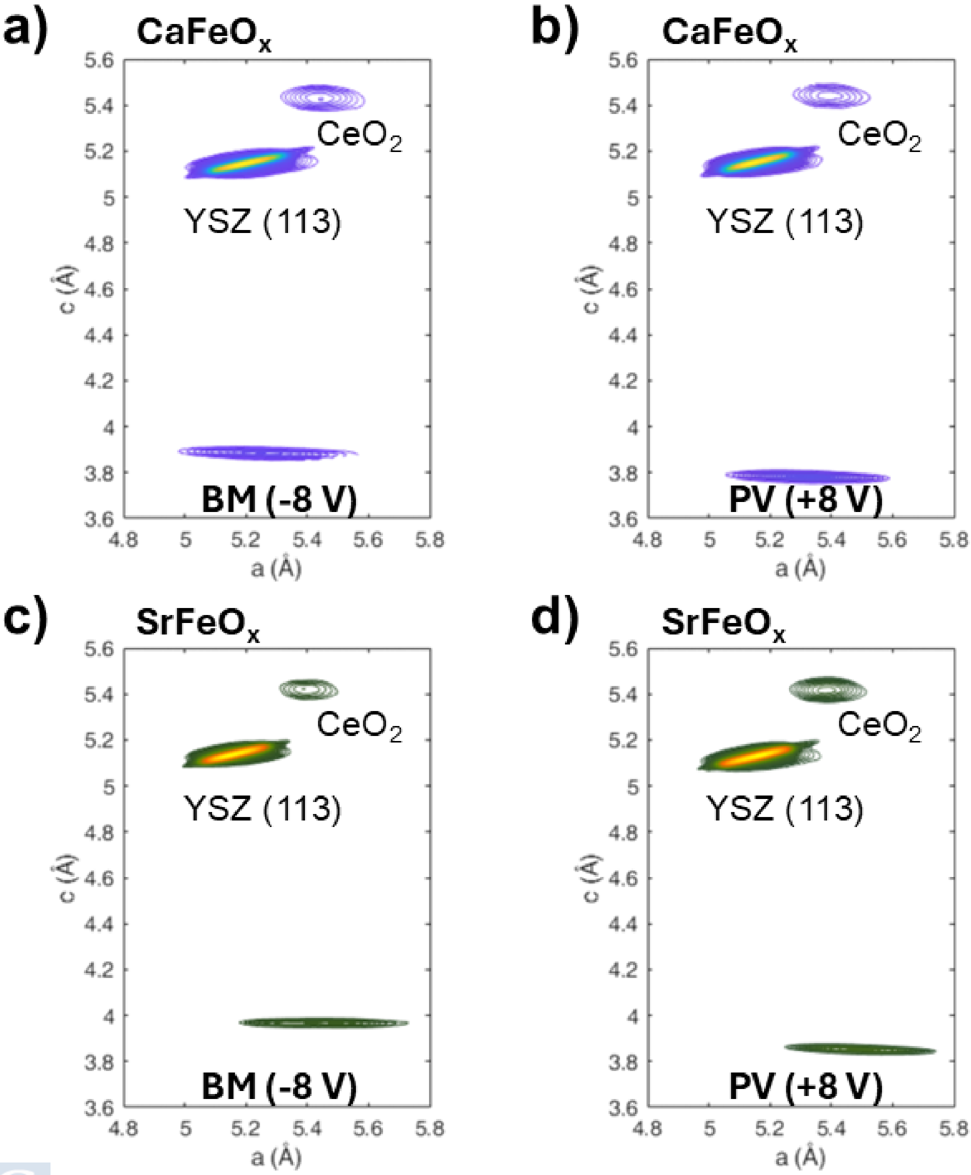

Figure 4.25. Reciprocal space maps around the (113) reflection of YSZ for 140 nm thick films of CFO (a,b) and SFO (c,d) in the BM and PV phases, after several oxidation/reduction cycles with ±8 V.

Regarding the thermal conductivity measurements, **Figure 4.26** shows the results of κ for 140 nm thick films of CFO and SFO after 10 transformation cycles, in order to ensure the reproducibility of the process. In contrast to the previous sections –where we studied CFO and SFO thin films with thicknesses up to ≈40 nm– we measured several thin films within a thickness range of 30 to 140 nm for increasing the accuracy of the thermal conductivity measurements, due to the low κ of the YSZ substrates (≈2.5 W/mK) (*10*).

As we can observe in the image (**Figure 4.26**), thermal conductivity increases by 50-60% when transforming the thin film into the PV phase, for both CFO and SFO. The application of a negative bias recovers the initial thermal conductivity value, and this cycling process can be repeated at least 10 times, maintaining this large thermal contrast in κ. This same behavior was observed within all the thickness range studied (≈30-140 nm).

It is important to note that the electrical resistance of the films varies between 3-50 Ω/cm at room temperature, depending on thickness and composition. In any case, this accounts for a maximum contribution to the thermal conductivity of ≈0.01-0.2 W/mK, which confirms that the change observed in thermal conductivity cannot be due to an electronic contribution, but due to the structural change.

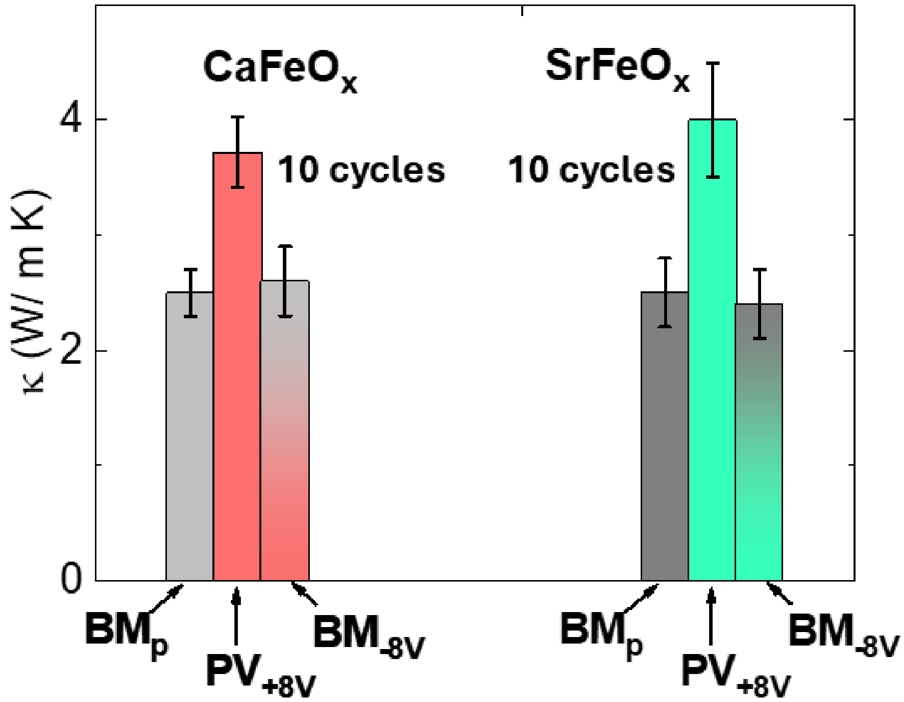

Figure 4.26. Reversibility of the thermal conductivity in the (Ca,Sr)FeO$_x$ thin films (≈140 nm) after topochemical oxidation/reduction with electric fields. The samples were cycled 10 times before performing these measurements. No degradation in thermal conductivity is observed during cycling.

Therefore, the exchange of oxide ions across the (Ca,Sr)FeO$_x$/YSZ solid interface represents the best option in terms of topochemical reversibility in negative charge-transfer oxides, allowing cycling the system for dozens of times without apparent degradation. The absence of other competing reactions, the formation of O_2 bubbles inside the structure during reduction, and the use of relatively low temperatures (280 ºC) avoids the degradation of the structure and maintains the physical properties upon repeated cycling.

Furthermore, this technique provides improved kinetics of oxygen intercalation/deintercalation. For example, Postiglione *et al.* (*173*) reported a detailed study of the kinetics of BM-PV transformation in thin films of $La_{0.5}Sr_{0.5}CoO_3$ by ion-gel gating. Contrary to our observations, they found that the BM-to-PV oxidation is slower than PV-to-BM reduction. Given the similar crystalline structures, we do not expect a large difference in the oxygen diffusion coefficient of these Co and Fe oxides. In fact, the discrepancy lies in the different oxidation mechanism of both methods: while it requires the electrochemical formation of the oxidative species (O^{2-}, O^-, etc.) and their diffusion from the surface to the interior of the film in the ion-gel method, the use of a solid electrolyte allows for the direct O^{2-} injection across the film/YSZ surface, improving the kinetics of the transformation.

4.3. CONCLUSIONS

In this chapter, we presented the use of thermal conductivity to investigate the reversibility of BM-to-PV topotactic transformations using three different oxidation methods: wet oxidation ($NaOCl/H_2O$), gas phase oxidation (O_3/O_2) and solid-state oxidation via a solid electrolyte (YSZ). These methods follow different oxidation mechanisms, as schematized in **Figure 4.27**: competing redox reactions with ^-OCl, involving lattice oxygen evolution; dissociation and reduction of surface-adsorbed O_3/O_2 molecules by direct electron transfer from $Fe^{3+/4+}$ plus diffusion of O^{2-} into the oxide lattice, and direct O^{2-} injection by an electric field across the film/YSZ interface.

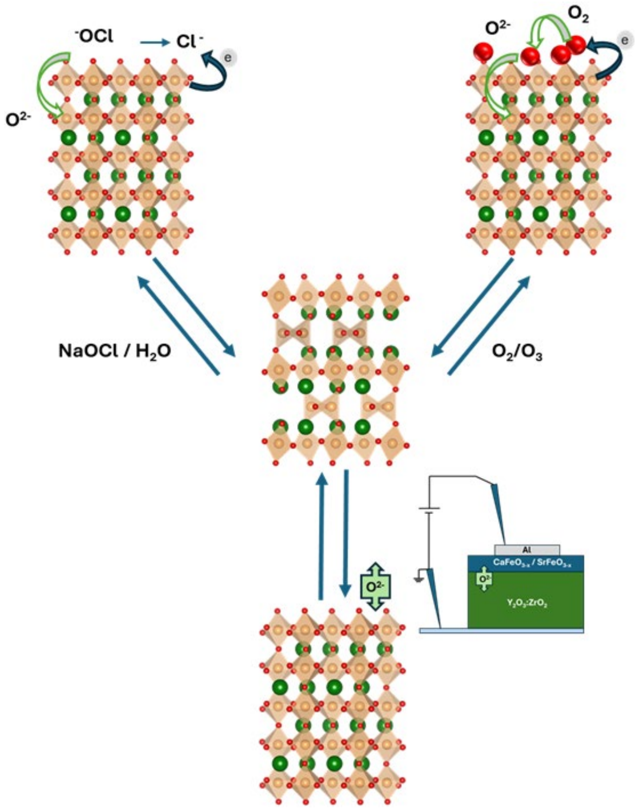

Figure 4.27. Schematic representation of the three oxidation mechanisms investigated in this chapter: liquid phase oxidation with $NaOCl/H_2O$, gas phase oxidation with O_3/O_2, and solid-state oxidation using YSZ as solid electrolyte.

These different mechanisms result in distinct chemical and structural stability, as demonstrated by the out-of-plane lattice parameters of CFO and SFO thin films after oxidation with the three methods studied, which are summarized in **Table 4.5**.

Table 4.5. Out-of-plane lattice parameters of CFO (a) and SFO (b) thin films, at room temperature, during BM-PV-BM cycling with three different oxidation mechanisms: wet oxidation (NaOCl in water), gas phase (O_3/O_2) and using a solid electrolyte (application of ±8 V).

a)

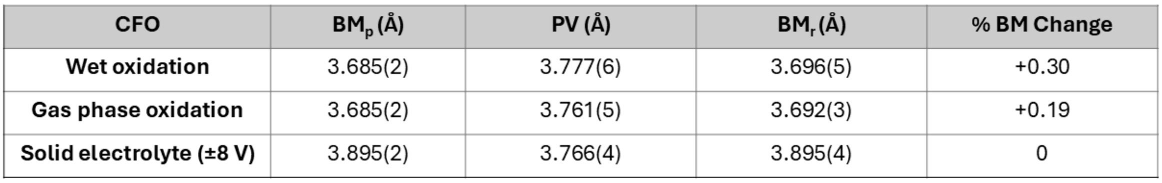

CFO	BM_p (Å)	PV (Å)	BM_r (Å)	% BM Change
Wet oxidation	3.685(2)	3.777(6)	3.696(5)	+0.30
Gas phase oxidation	3.685(2)	3.761(5)	3.692(3)	+0.19
Solid electrolyte (±8 V)	3.895(2)	3.766(4)	3.895(4)	0

b)

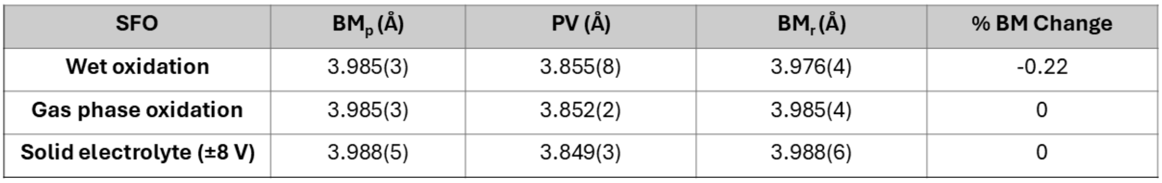

SFO	BM_p (Å)	PV (Å)	BM_r (Å)	% BM Change
Wet oxidation	3.985(3)	3.855(8)	3.976(4)	-0.22
Gas phase oxidation	3.985(3)	3.852(2)	3.985(4)	0
Solid electrolyte (±8 V)	3.988(5)	3.849(3)	3.988(6)	0

The main conclusions of our research are:

- Reversible and repeatable manipulation of physical properties of functional oxides through topochemical oxygen exchange depends very much on the oxidation pathway.
- Wet oxidation of negative charge-transfer oxides leads to structural irreversibility after one oxidation/reduction cycle, which precludes thermal switching.
- This irreversibility is due to the intrinsic instability of negative charge-transfer oxides in water (and, probably, in other polar solvents), which limits the applicability of wet methods for the fabrication of tunable devices based on these materials.
- Gas phase oxidation is a milder oxidation process, reversible after one oxidation/reduction cycle. However, repeated cycling leads to the progressive accumulation of lattice defects, impeding the reversibility of the process.
- Direct exchange of oxide ions using YSZ as solid electrolyte allows a truly reversible oxygen intercalation/deintercalation in charge-transfer oxides, providing the possibility of reversibly switching the thermal conductivity of the system.
- This electric-field assisted exchange of oxide ions is the best method for the fabrication of tunable thermal (and probably, of other type) devices.

In summary, in this chapter we emphasize the importance of selecting appropriate oxidation methods to harness the full potential of topotactic reactions in advanced materials.

5. ELECTRIC-FIELD DRIVEN THERMAL TUNING IN CHARGE-TRANSFER OXIDES

> *"In my view, all that is necessary for faith is the belief that by doing our best we shall succeed in our aims: the improvement of mankind."*
>
> ---
>
> Rosalind Franklin, English chemist and X-ray crystallographer whose research was fundamental to the discovery of the molecular structure of DNA.

The results presented in this chapter are published in:

"Electric-Field Control of the Local Thermal Conductivity in Charge Transfer Oxides" *Advanced Materials*, **2025**, 37, 2413045. https://doi.org/10.1002/adma.202413045

Noa Varela-Domínguez[1], Marcel S. Claro[1], Carlos Vázquez-Vázquez[2], Manuel Arturo López-Quintela[2] and Francisco Rivadulla*[1]

[1]CiQUS, Centro Singular de Investigación en Química Biolóxica e Materiais Moleculares, 15782-Santiago de Compostela, Spain

[2]iMATUS, Instituto de Materiales, 15782-Santiago de Compostela, Spain.

Editorial: Wiley-VCH ISSN: 1521-4095

Personal contribution: deposition of thin films and structural characterization by X-ray diffraction, AFM experiments, thermal conductivity measurements, analysis and discussion of results.

5-Year Impact Factor: 28.9. Q1 (D1) in Condensed Matter Physics.

5.1. INTRODUCTION

As discussed in the previous chapter, transition metal perovskites –and, particularly, oxygen-deficient perovskites ABO_{3-x}– naturally exhibit an intrinsic concentration of oxygen vacancies, which are relatively easy to manipulate due to the low enthalpy of oxygen vacancy formation and high oxygen exchange rate and mobility in these materials (*161*, *189*, *190*). As a result, the modulation of oxygen vacancies has been widely exploited to tune their physical and chemical properties, such as electrical conductivity (*216*), heat transport (*121*, *122*) or even triggering superconductivity (*217*).

In perovskite structures, the accumulation of oxygen vacancies can lead to two distinct outcomes. First, when vacancies are incorporated in an ordered fashion, they may drive a phase transition into a thermodynamically stable phase where the oxygen vacancies become an integral part of the new structure. Alternatively, oxygen vacancies can be accumulated in a disordered and random manner, temporarily altering the material's properties. However, the oxygen vacancies will eventually diffuse ($D \approx 5 \cdot 10^{-17}$ cm^2/s at room temperature for oxoperovskites, (*218*)), restoring the system to the original state.

In Chapter 4, we explored the first scenario in detail, underscoring how the mechanism of oxygen vacancy introduction/removal influences the reversibility of the transformation between perovskite (ABO_3) and brownmillerite ($ABO_{2.5}$) phases, with the aim of using topotactic transformations for the development of a thermal switch. In this chapter we examine the second scenario, where the random and –in principle– transient modulation of oxygen vacancies is harnessed to control thermal transport in thin films. Given the results from the previous chapter, which revealed the instability of charge-transfer oxides in liquid environments and the irreversibility issues associated with gas-phase oxidation, we will focus on the modulation of oxygen vacancies using localized electric fields.

Our research group has extensive experience in this field, having conducted multiple studies on electric-field driven oxygen vacancy modulation to tailor key physicochemical properties. For example, Sarantopoulos *et al.* (*219*) demonstrated the possibility of tuning the electrical conductivity of $CaTiO_3$ thin films by manipulating oxygen vacancies with electric fields and mechanical forces. Their work showed that the displacement of oxygen vacancies alters the local charge density, enabling transitions between high- and low-electrical conductivity states and positioning this material as a candidate for resistive switching applications.

More recently, Álvarez-Martínez *et al.* (*220*) highlighted the impact of oxygen vacancy modulation on thermal transport during resistive switching in oxides. Using $SrTiO_3$ as model system, they demonstrated that the electric-field induced accumulation/depletion of oxygen vacancies close to the oxide-metal interface during resistive switching modulates the thermal resistance at this interface.

In this chapter, we explore the modulation of thermal conductivity in transition-metal perovskite ($SrFeO_{3-x}$, $La_{0.6}Sr_{0.4}CoO_{3-x}$, $La_{0.7}Sr_{0.3}MnO_3$) thin films through the local accumulation of oxygen vacancies induced by a voltage-biased atomic force microscopy (AFM) tip.

Bias-induced AFM has proven to be a powerful and widely utilized technique for nanoscale modification of material's structure and properties. The small size of the AFM tip, typically less than 25 nm, and its proximity to the sample surface, enable the generation of exceptionally high electric fields (≈100 MV/cm) with the application of relatively low voltages (≈10 V). These intense fields can induce either permanent changes (such as electrochemical reactions or field-driven material deposition) or temporal alterations by controlling the local charge density and polarization of the material (*221*).

In the cases where permanent changes are induced, the humidity of the atmosphere allows the formation of a nanoscale water bridge between the AFM tip and the sample surface, which works as a nanoscale electrochemical cell that is laterally confined to the size of the water meniscus. The high electric fields generated through the AFM tip decompose the H_2O molecules in this water neck into reactive oxyanions that drive local anodic oxidation, producing the electrodeposition of an oxide on the sample surface (*222*, *223*). This technique, often referred to as AFM lithography, has been used to modify, permanently, the surface in semiconductors and to fabricate non-volatile functional nanostructured devices, with excellent spatial resolution (*224–227*).

On the other hand, a voltage-biased AFM tip was also used for tuning the local concentration of HO^-/H^+ surface adsorbates on the top layer of an $LaAlO_3/SrTiO_3$ interface, influencing the conductance of the interfacial 2D electron gas and locally switching between conducting and isolating states (*228*, *229*). Different types of functional devices were fabricated in this way, such as tunnel junctions and field-effect transistors (*230*), although the effect normally vanishes after a few hours under normal atmospheric conditions.

In this chapter, we present the use of a voltage-biased AFM tip to create non-volatile thermal states by inducing localized electric-field driven accumulation of oxygen vacancies in transition-metal oxides. We studied three transition-metal oxoperovskites with different electronic configurations: $SrFeO_{3-x}$ (SFO, negative charge-transfer), $La_{0.6}Sr_{0.4}CoO_{3-x}$ (LSCO, positive charge-transfer) and $La_{0.7}Sr_{0.3}MnO_3$ (LSMO, Mott-Hubbard oxide) –see **Figure 4.12**a-c for a schematic representation of their band diagrams. As it will be discussed in the next sections, we found that by optimizing the contribution of O 2p states at the Fermi level in these oxides we can create thermal states that remain stable for weeks but are completely erased by thermal annealing, returning the system to its original state. This strategy constitutes a novel application of AFM lithography and allows the fabrication of micron-size patterns with a defined value of thermal conductivity on the bare surface of the oxide thin film.

5.2. RESULTS AND DISCUSSION

5.2.1. Fabrication of the thin films

For the development of this project, we synthesized thin films (≈40 nm thick) of SFO, LSCO and LSMO on (001)-oriented $SrTiO_3$ (STO) and $(LaAlO_3)_{0.3}(Sr_2AlTaO_6)_{0.7}$ (LSAT) substrates, by PLD. The growth conditions were 100 mTorr of oxygen and a laser fluence of ≈1.5 J/cm^2 for all materials, but the deposition temperature varied from 675 ºC for SFO and LSCO to 730 ºC in the case of LSMO.

Figure 5.1 shows the X-ray diffraction patterns of the as-deposited thin films on STO. Under these growth conditions, all materials adopt the perovskite phase, exhibiting excellent crystallinity, as denoted by the pronounced Laue oscillations around the diffraction peaks.

These oscillations are particularly intense in the case of LSMO –Mott-Hubbard oxide–, since no oxygen vacancies (defects) are naturally present in the film.

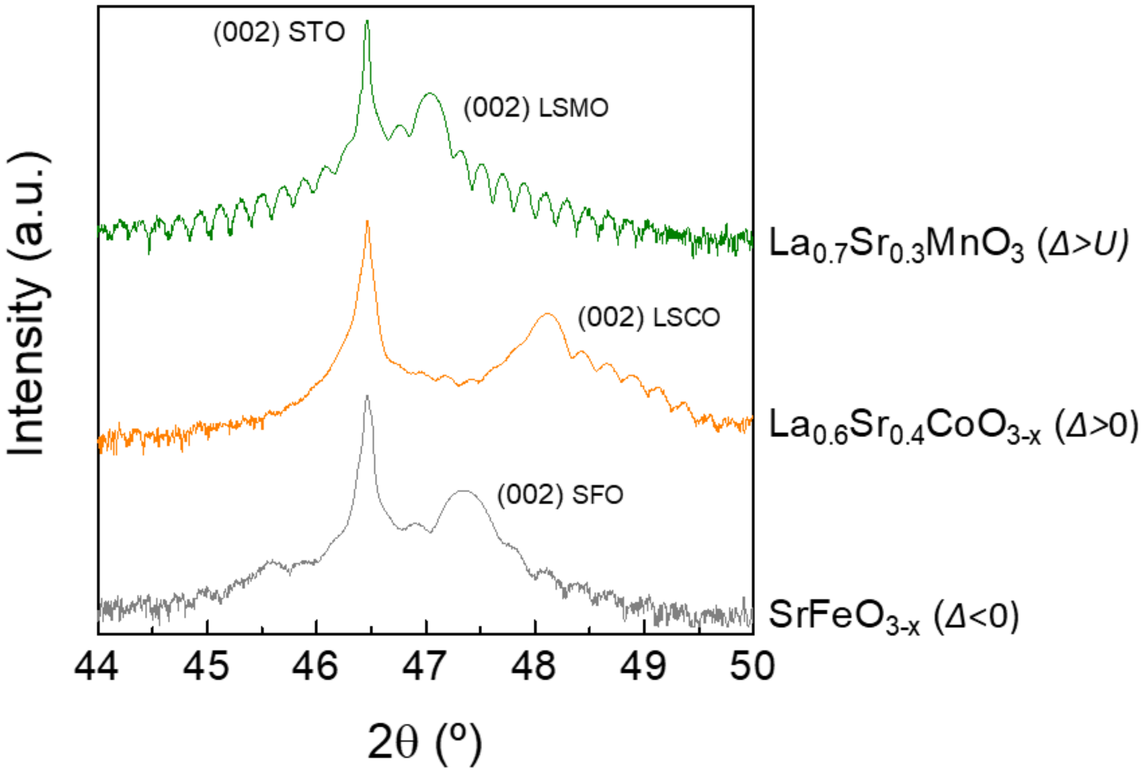

Figure 5.1. X-ray diffraction patterns of the as-deposited thin films of SFO, LSCO and LSMO (which are negative charge-transfer, positive charge-transfer and Mott-Hubbard oxides, respectively) on STO substrates.

5.2.2. Effect of the local electric field on the sample surface

In this project, we used a conductive AFM tip to apply localized electric fields on the surface of the previously described thin films. Several regions of 25 x 25 μm^2 were scanned in contact with the AFM tip biased at different voltages, using the conductive AFM mode. We hypothesize that the resulting electric fields (up to ≈100 MV/cm) should induce the local accumulation of oxygen vacancies (which are positively charged) in these regions.

The concentration of the accumulated oxygen vacancies may be controlled by adjusting the applied dose, which is determined by the voltage and the scan rate. In **Figure 5.2** we provide a comparison of a PV-SFO thin film with two different regions scanned at -10 V using different scanning rates: a 10 x 10 μm^2 square scanned at 0.3 Hz (equivalent to 3 μm/s) and a 25 x 25 μm^2 area scanned at 0.5 Hz (equivalent to 12.5 μm/s). As shown in the Raman spectra of **Figure 5.2**b, the application of -10 V at the higher scanning rate of 0.3 Hz results in the complete PV to BM transformation, as evidenced by the disappearance of the Raman peaks at 330 and 430 cm^{-1}, which are characteristic of the PV phase (*231*).

Since this project focuses on studying the effect of the local and transient accumulation of oxygen vacancies on thermal transport, all the experiments were conducted by applying different voltages (ranging from -5 V to -10 V) at a fixed scan rate of 0.5 Hz, as schematized in **Figure 5.3**a. Under these conditions, the concentration of oxygen vacancies progressively increases with the applied voltage while remaining within the regime of local accumulation, preventing a PV-to-BM structural transition (*164*).

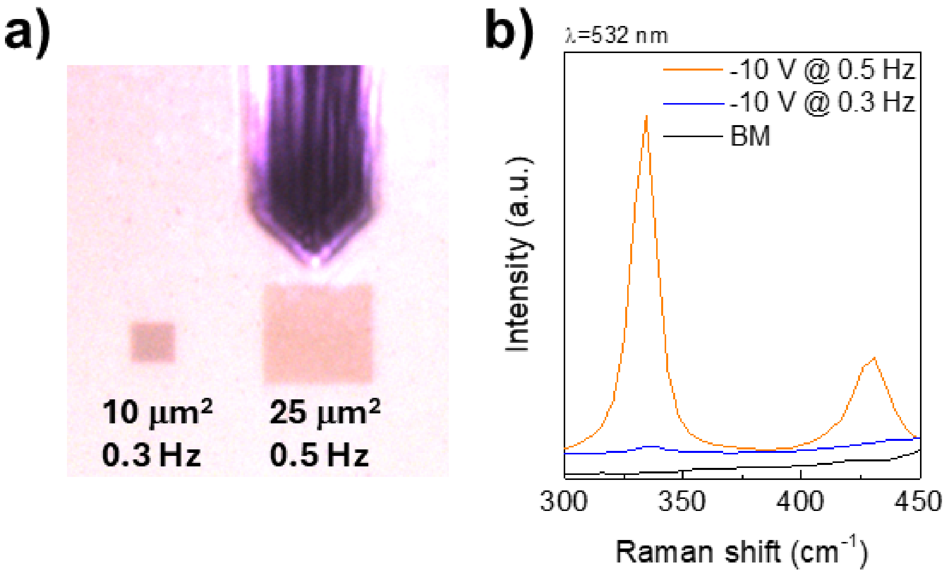

Figure 5.2. a) Optical microscopy (reflected light) image of 10 x 10 and 25 x 25 µm^2 areas of the surface of a 40 nm thick $SrFeO_{3-x}$ thin film, scanned with -10 V at 0.3 and 0.5 Hz, respectively. b) Comparison of the Raman spectra of the regions scanned at -10 V with the different scan rates, along with the Raman spectrum of an SFO thin film in the BM phase.

Figure 5.3b presents an optical microscope photograph of a SFO thin film (≈40 nm thick, deposited on STO) after scanning the surface with the different voltages. As we can see, increasing the (negative) voltage above -5 V produces a darkening of the film surface, which may be caused by the accumulation of oxygen vacancies and subsequent reduction in electrical conductivity.

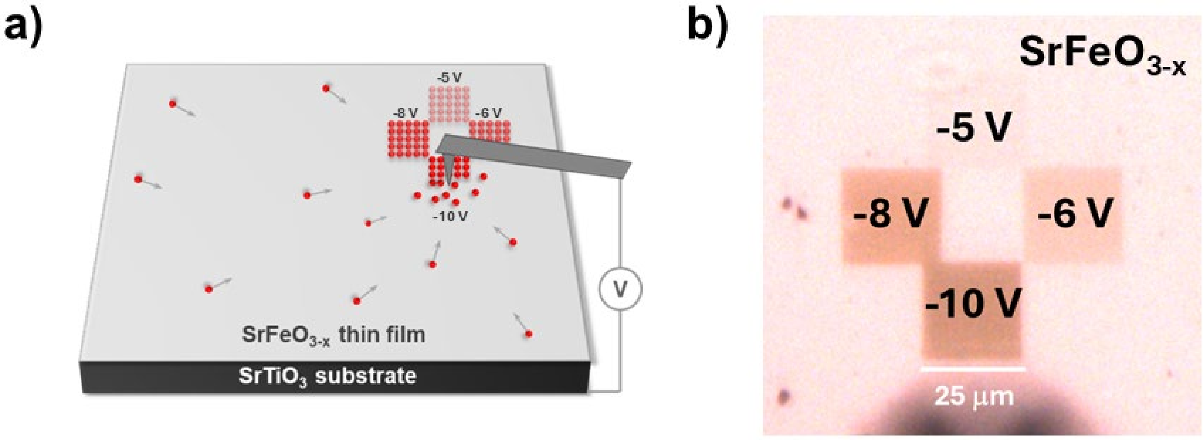

Figure 5.3. a) Schematic representation of the AFM-driven modulation of oxygen vacancies. The application of a negative bias to the sample surface induces the migration of oxygen vacancies (red balls), which are accumulated in the scanned regions. The local concentration of oxygen vacancies should vary upon the applied voltage, as represented by the different intensities of the scanned regions in the figure. b) Optical image (reflected light) of four pads of 25 x 25 µm^2 scanned with the AFM tip biased at different voltages on the surface of an SFO thin film.

Besides the observed color change, the application of localized electric fields on the SFO film also induces a surface expansion and increase in Kelvin potential in the scanned regions, as shown in **Figure 5.4**. For instance, when a voltage of -10 V is applied, the scanned area expands by approximately ≈3 nm (**Figure 5.4**a), while Kelvin surface potential increases by about ≈0.15 V (**Figure 5.4**b). In contrast, applying -6 V results in a smaller expansion of around ≈1 nm and a Kelvin potential increase of approximately ≈0.10 V (**Figure 5.4**c,d). As demonstrated in **Figure 5.4**e, both the surface height and Kelvin potential exhibit a nearly linear dependence on the applied voltage, which may be consistent with an increasing concentration of accumulated oxygen vacancies with the electric field.

In perovskites, each oxygen vacancy donates two electrons to non-bonding orbitals, resulting in the expansion of the crystalline lattice (*232*). Furthermore, this expansion is often anisotropic in epitaxial thin films, potentially enhancing the overall effect (*233*). However, the full transformation of a ≈40 nm thick film of the SFO perovskite (with out-of-plane lattice parameter of c= 3.852 Å) to the brownmillerite (c= 3.985 Å) phase implies a maximum expansion of ≈1.3 nm, well below the ≈3 nm observed here. As we will discuss later in this chapter, we ruled out the electrochemical deposition of a Sr/Fe oxide on the sample surface. Therefore, although we do not have a complete explanation of this phenomenon, we propose in this chapter that the local accumulation of oxygen vacancies is primarily responsible for this effect.

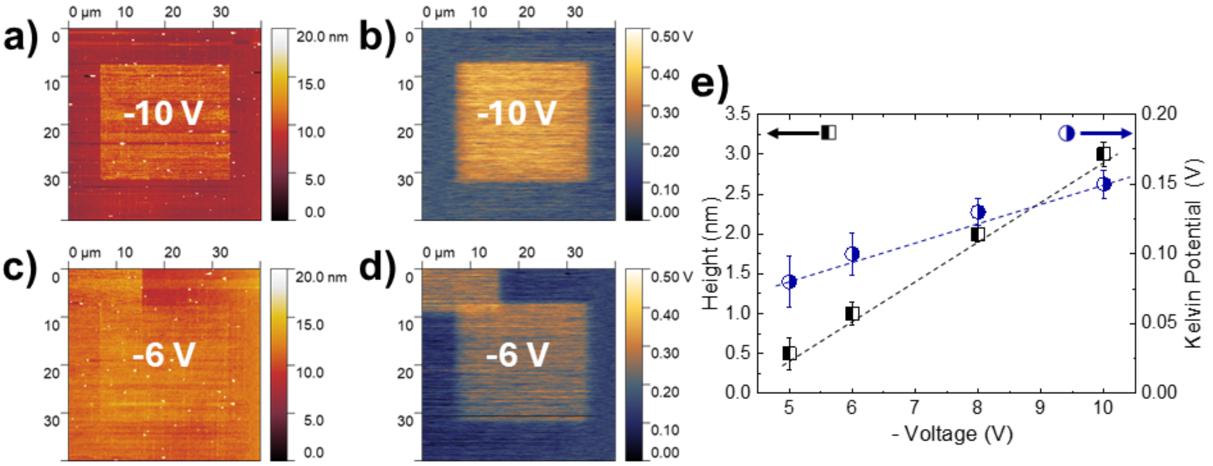

Figure 5.4. Topography (a,c) and Kelvin potential (b,d) scans of the -10 V and –6 V pads, respectively. The variation of surface expansion (black squares) and Kelvin potential (blue circles) with the applied voltage are shown in (e), displaying an almost lineal tendency in both cases. The dashed lines in the figure are guides to the eye.

This increase in local height and surface potential can be entirely eliminated by thermally annealing the thin film in air at 200 ºC for 4 h, restoring the original state and confirming the reversibility of the transformation. **Figure 5.5** illustrates the recovery of surface expansion and potential in the pad scanned at -10 V, but this behavior has been consistently observed for all the applied voltages (-5, -6, -8 and -10 V).

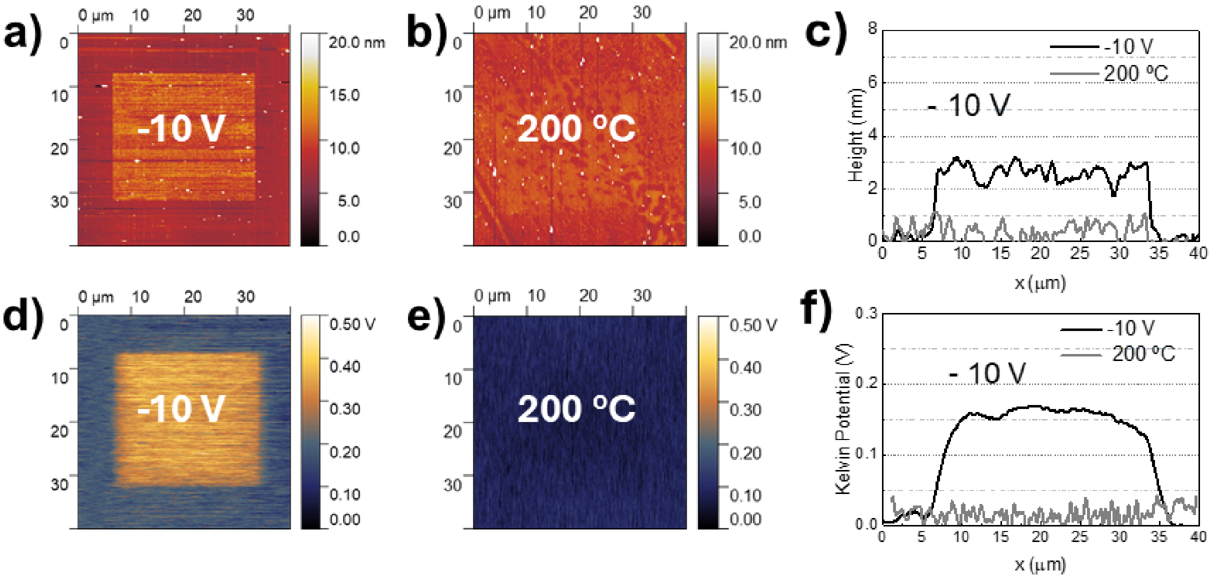

Figure 5.5. Topography (a) and Kelvin potential (d) scans of the pad modified at -10 V on a SFO thin film. The topography and Kelvin repeated on the same area after annealing the sample at 200 °C in air are shown in (b) and (e), respectively. Height and Kelvin potential line profiles along the same pad (before and after thermal annealing) are shown in (c) and (f).

The precise quantification of oxygen vacancies (and other point defects) is usually a difficult task due to their dilute concentrations (*234*). In our case, the small size of the scanned regions (25 x 25 μm^2) further complicates this analysis. Nevertheless, we estimated the maximum amount of oxygen vacancies introduced with the biased-AFM tip (at -10 V) through the analysis of the Raman spectra, shown in **Figure 5.6**.

Figure 5.6a presents the Raman spectra of an SFO thin film with several regions scanned at voltages ranging from 0 V (pristine sample) to -10 V, like those shown in **Figure 5.3**b. The Raman spectrum of the substrate (LSAT) is also added for comparison. Note that in this case the SFO thin film was grown on a LSAT substrate, to avoid the large background signal of STO (*235*).

As we can observe in the figure, the application of an electric field does not significantly alter the Raman spectra of SFO, with two prominent peaks at ≈630 and ≈700 cm^{-1} visible across all scanned regions, although they are slightly shifted towards higher frequencies upon increasing the applied voltage. These peaks correspond to Fe-O stretching modes characteristic of the PV phase, as they are forbidden in bulk BM due to symmetry constraints (*180*, *236*). As a result, these experiments further support our hypothesis that a full PV-BM transformation is not produced upon application of the electric fields at fast scanning rates (0.5 Hz, 12.5 µm/s).

In **Figure 5.6**b we show a comparison of the Raman spectra of SFO thin films with different oxygen contents, including a pristine region of the PV-SFO film, the pad scanned at -10 V, and a BM film (obtained by thermal annealing under vacuum in the PLD chamber, following the procedure described in Chapter 4). As we can see in the figure, contrary to our predictions the Raman peak at ≈700 cm^{-1} is still present, and with considerable intensity, in the epitaxial BM film (black curve), signaling some symmetry relaxation in the film. This behavior is attributed to epitaxial clamping effects, which constrain vibrational modes, coupled with stress relaxation from oxygen vacancy accumulation, ordering or clustering, potentially causing the observed hardening of the Fe-O stretching vibrations.

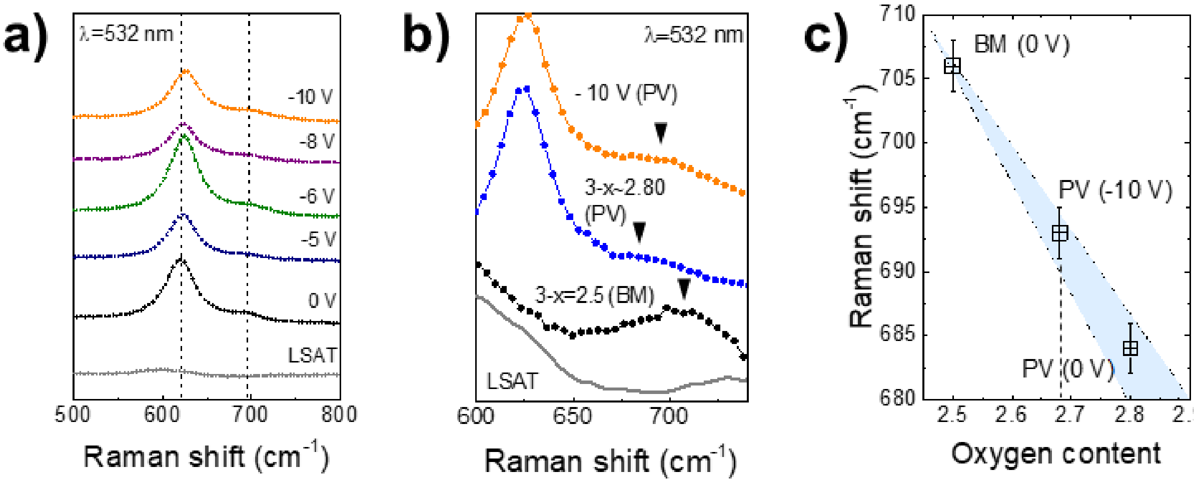

Figure 5.6. a) Evolution of the Raman spectra of an SFO thin film upon application of negative bias. The film is deposited on an LSAT substrate for the Raman experiments to avoid the broad band of STO. b) Comparison of the Raman spectra of an $SrFeO_{3-x}$ thin film in the PV phase (3-x≈ 2.82), in the BM phase (2-x= 2.5) and on the region scanned at -10 V. The LSAT spectrum is also shown for reference. c) Estimation of the oxygen content in the region scanned at -10 V from the linear dependence of the Raman peak at ≈700 cm^{-1} between the pristine PV and the BM phase. The blue-shaded region serves as a guide to the eye.

Since the 700 cm^{-1} Raman peak is present in all the three curves shown in **Figure 5.6**b, we can use its position to determine the oxygen content in the region scanned at -10 V (and thus, the concentration of oxygen vacancies introduced). Assuming a linear variation of the frequency with the oxygen composition between the BM (3-x=2.5) and pristine PV (3-x≈2.82 (*164*, *237*)), we estimate an oxygen content of 3-x≈2.68 on the pads written at -10 V (**Figure 5.6**c), meaning that the amount of oxygen vacancies introduced at this voltage is ≈0.14. This is an approximate value of the maximum concentration of oxygen vacancies introduced in the SFO thin film with our method, without inducing a phase transition.

In addition to Raman experiments, the effect of the electric field on the chemical composition of the surface was also studied using X-ray photoelectron spectroscopy (XPS). We recorded the Sr, Fe and O XPS spectra on a pristine region of the film, and on an area scanned at -10 V. The main results are presented in **Figure 5.7**.

As observed in **Figure 5.7**a, there is an inversion in the relative intensities of the Sr 3d multiplet, with the peak at ≈131 eV gaining intensity over that at ≈134 eV in the region scanned at -10 V. Since the peak at higher binding energy is characteristic of Sr-rich surfaces (*238–240*), this inversion could be indicative of a slight decrease of surface Sr on the modified area, although the change is too modest to be conclusive.

Regarding the O 1s spectrum (**Figure 5.7**b), apart from the expected contribution of lattice oxygen (purple band), there is a signal that could be attributed to the presence of hydroxide groups (cyan band) (*239*). However, no significant changes are observed upon the application of the electric field, as both peaks retain their position and relative intensities.

Lastly, the Fe 2p XPS spectra (**Figure 5.7**c) only reveal minor variations. Despite the slight displacement in the Fe $2p_{1/2}$ (≈723.5 eV) and Fe $2p_{3/2}$ (≈710 eV) peaks towards lower binding energies (≈0.7 eV) when applying the electric field –which could suggest an increase in the Fe oxidation state (*241*)–, the differences are too small to account for an electrochemical oxidation.

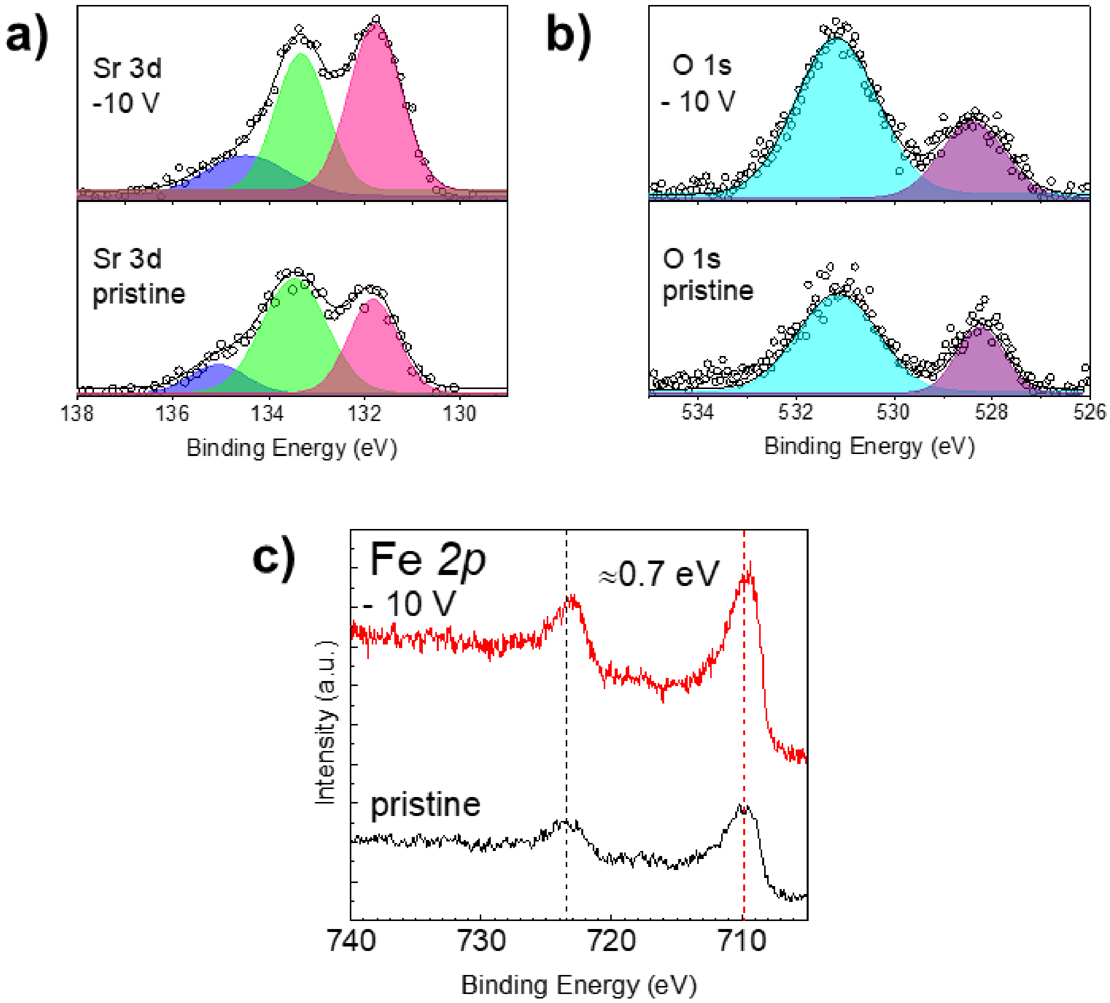

Figure 5.7. XPS spectra of a SrFeO$_{3-x}$ thin film. a) Sr 3d spectra shows a small increase in the relative intensity of the lower binding energy peak on the region scanned at -10 V, consistent with a Sr-poor surface after the application of the electric field. b) O 1s spectra presents two different bands, one corresponding to the contribution from lattice oxygen (purple peak) and another one that can be attributed to the presence of mixed hydroxide groups (cyan peak), although no significant changes are observed upon application of the voltage. c) Fe 2p spectra shows a slight displacement of Fe 2p$_{1/2}$ and 2p$_{3/2}$ peaks towards lower binding energies on the region modified with -10 V.

Therefore, the XPS spectra discards the electrodeposition of an oxide or oxohydroxide on the surface of the thin film due to local anodic oxidation when applying the negative bias. However, to further exclude the participation of adsorbed H_2O in an electrochemical reaction, we conducted additional experiments where the local application of electric fields with the biased-AFM tip was carried out under different environmental conditions: changing the relative humidity of the working atmosphere (from 8% to >60%) and after immersing both the AFM tip and sample surface in mineral oil, which contains only trace amounts of H_2O (parts per million range) (*242*).

For the low-humidity experiments, the AFM chamber underwent multiple vacuum pumping and nitrogen purge cycles until the relative humidity was reduced below 8%. To ensure stable conditions and minimize noise, the vacuum pump was switched off during AFM scanning, but post-experiment measurements confirmed that the humidity remained constant throughout the process. Conversely, for high-humidity conditions, the sample was exposed to a moisture-saturated air flux for 20 minutes immediately before scanning, promoting the formation of a thin water layer on the film surface.

For the experiments using mineral oil, the sample was preheated at 160 ºC for 10 minutes in order to remove any residual surface water before immersing both the AFM tip and the sample in mineral oil. This step ensured a continuous oil layer at the tip-sample junction, preventing the formation of a water meniscus and effectively ruling out any water-mediated electrochemical contributions to the observed surface modifications.

Figure 5.8 presents the optical microscopy images and AFM topographies of three 25 x 25 μm^2 regions of a 40 nm thick SFO film scanned at -10 V under these different environmental conditions. As we can observe in the image, the local expansion (**Figure 5.8**d) is approximately 3 nm in all cases, consistent with the results obtained under normal atmospheric conditions (RH ≈60%, **Figure 5.4**). These findings demonstrate that atmospheric humidity does not significantly influence the process, discarding the occurrence of an electrochemical reaction when applying the electric field. Consequently, the local surface expansion observed in the SFO thin film must be produced by an intrinsic effect.

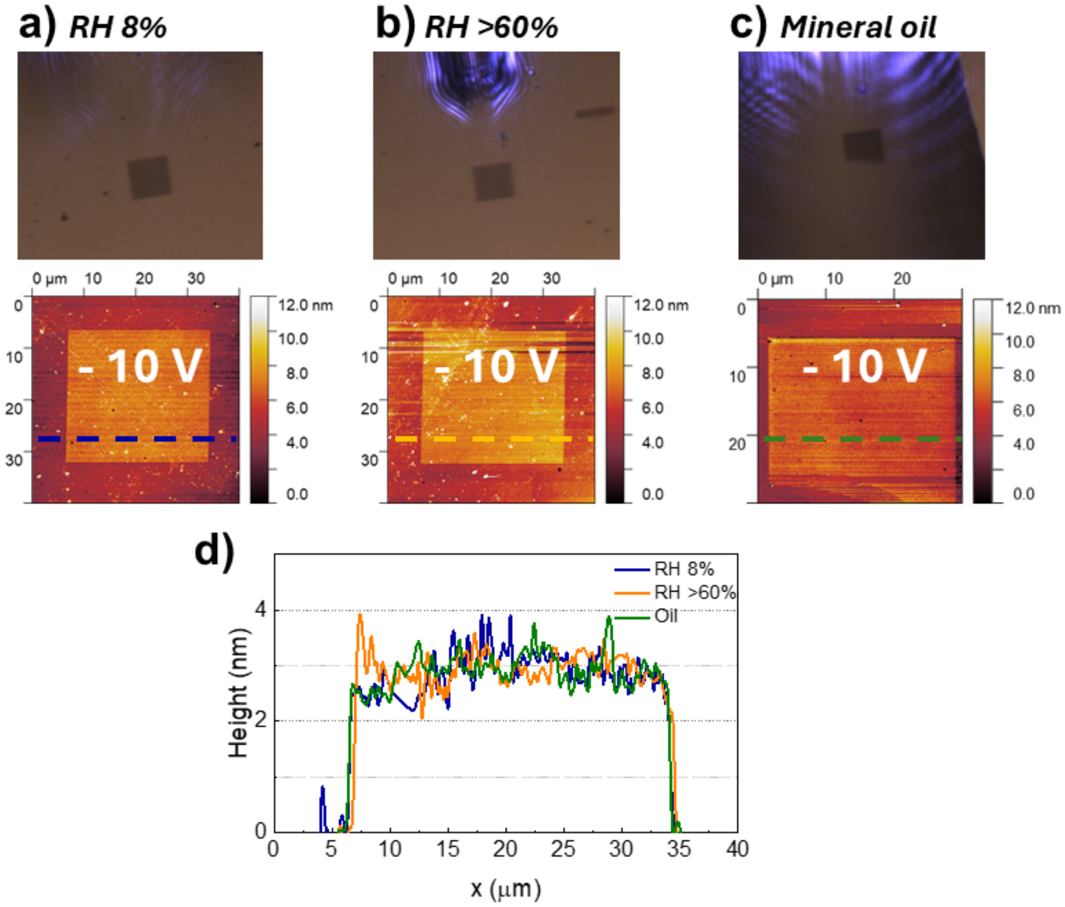

Figure 5.8. Optical microscopy (reflected light) photographs and AFM topographies of 25 x 25 μm^2 regions of the surface of a $SrFeO_{3-x}$ thin film scanned at -10 V under different conditions of relative humidity (a, b) and with the AFM tip and sample surface immersed in mineral oil (c). In (d) we show the height profile along these regions, demonstrating that the local expansion is, in all cases, around 3 nm.

Understanding the effect of the electric field on the film surface requires a detailed consideration of the electronic structure of the $SrFeO_{3-x}$ perovskite. As discussed in Chapter 4 (section 4.1), increasing the oxidation state of Fe in $SrFeO_{3-x}$ reduces the energy of the MO_{AB} band (derived from the antibonding Fe-O interaction) below the O 2p non-bonding states (refer to **Figures 4.3**b and **4.12**a for a schematic description of the band diagram). This makes the charge-transfer energy, Δ, less than zero, and the oxidation of lattice O^{2-} will compete with the oxidation of Fe^{3+}. As a result, the electric field created by the AFM tip will not only drag the existing oxygen vacancies but will also increase their concentration through local oxidation of O^{2-} anions that will be released as O_2.

All these results suggest that the generation and accumulation of oxygen vacancies underneath the voltage-biased AFM tip is responsible for the local expansion observed in SFO thin films (**Figure 5.4** and **Figure 5.8**).

On the other hand, as shown in **Figure 5.5**, thermally annealing the thin film at 200 ºC in air is enough to reincorporate oxygen back to the structure, eliminating the local expansion and returning the oxide to its original state.

This proposed mechanism of O^{2-} oxidation should be active in other charge-transfer oxides such as $La_{0.6}Sr_{0.4}CoO_{3-x}$ (LSCO), but not in the case of Mott-Hubbard oxides like $La_{0.7}Sr_{0.3}MnO_3$ (LSMO), where the active redox pair is the metal, instead of oxygen (**Figure 4.12**c). For this reason, to test our hypothesis, we scanned the surface of charge-transfer LSCO and Mott-Hubbard LSMO with the voltage-biased AFM tip, under the same conditions as SFO.

Figures 5.9-5.10 present the main results for LSCO thin films (≈40 nm thick, deposited on STO), which exhibit similar behavior to SFO. As shown in **Figure 5.9**a, the application of localized electric fields to the sample surface leads to a darkening of the scanned regions, although the effect is milder compared to SFO. However, despite this weaker optical contrast, the observed changes in surface expansion and Kelvin potential are more pronounced in LSCO, as highlighted in **Figure 5.9**b.

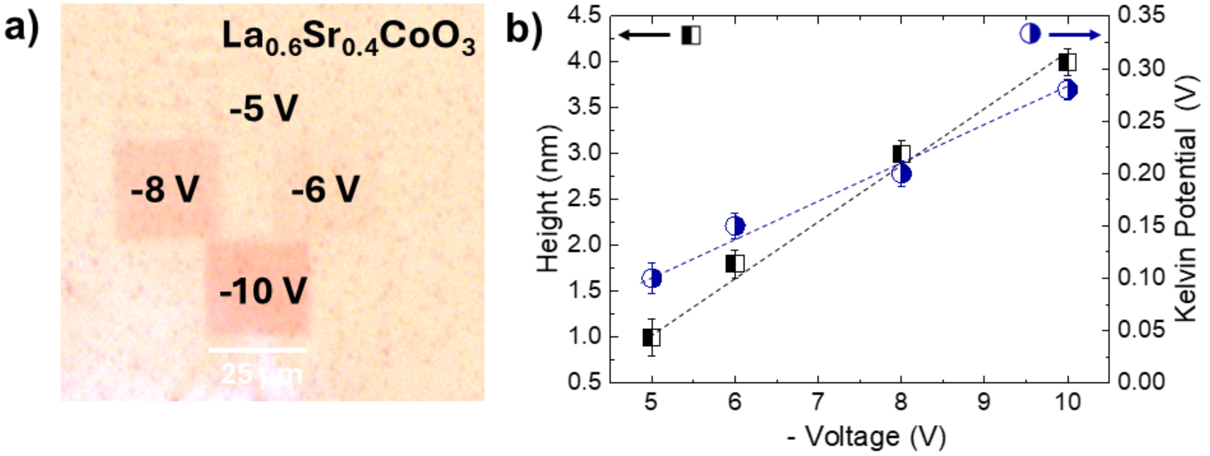

Figure 5.9. a) Optical image (reflected light) of four pads of 25 x 25 μm^2 scanned with the AFM tip biased at different voltages on the surface of a LSCO thin film. b) Variation of surface expansion (black squares) and Kelvin potential (blue circles) in the scanned pads shown in (a), displaying an almost linear tendency in both cases. The dashed lines serve as guides to the eye.

For reference, in SFO thin films surface expansion varied between ≈0.5 and 3 nm, while Kelvin potential increased from ≈0.08 to 0.15 V (**Figure 5.4**e). In contrast, LSCO exhibits a maximum surface expansion of ≈4 nm and a Kelvin potential increase of ≈0.28 V upon application of -10 V.

As in the case of SFO, these electric-field induced modifications are completely reversible, as illustrated in **Figure 5.10**. However, since the effect of the electric field on the sample surface is stronger in LSCO, higher annealing temperatures are needed to completely erase these changes. In particular, it is necessary to reach 300 ºC to fully restore both surface expansion and Kelvin potential to their original state (**Figure 5.10**c,f).

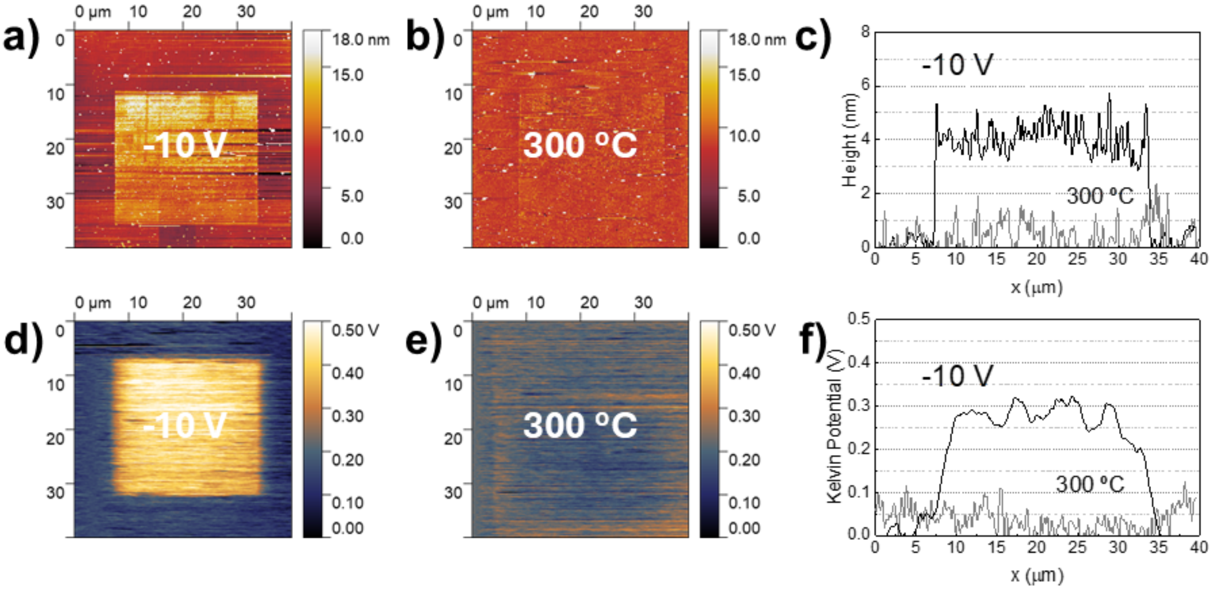

Figure 5.10. Topography (a) and Kelvin potential (d) scans of the -10 V pad on a LSCO thin film. The topography and Kelvin scans repeated in the same area after annealing the sample at 300 °C in air are shown in (b) and (e), respectively. Height and Kelvin potential line profiles along the same pad (before and after thermal annealing) are shown in (c) and (f).

In contrast, the effect of the electric field on the surface of Mott-Hubbard oxide LSMO is completely different, as shown in **Figure 5.11**. In this case, the application of localized electric fields induces only a subtle color change on the sample surface, except for -10 V, when the surface darkens considerably. Additionally, surface expansion and Kelvin potential exhibit an almost linear increase with the applied voltage up to -8 V. However, unlike SFO and LSCO where this trend is maintained across all applied voltages, the application of -10 V in LSMO breaks this pattern, leading to an exceptionally large surface expansion (≈15 nm for a 40 nm thick film) and a substantial increase in Kelvin potential (up to ≈1.3 V) (**Figure 5.11**b). These changes are significantly more pronounced than in charge-transfer oxides SFO (**Figure 5.4**) and LSCO (**Figure 5.9**).

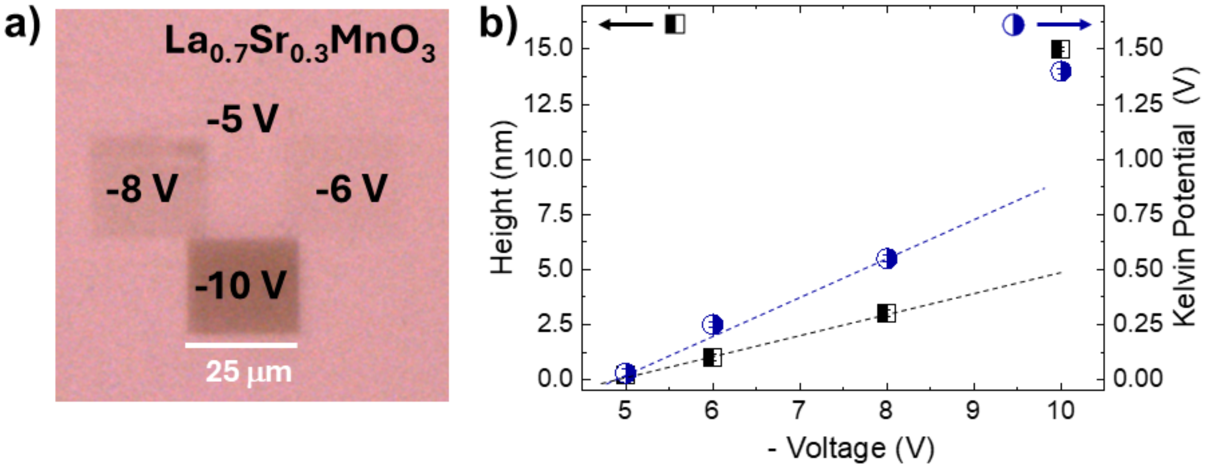

Figure 5.11. a) Optical image (reflected light) of four pads of 25 x 25 μm^2 scanned with the AFM tip biased at different voltages on the surface of a LSMO thin film (≈40 nm) deposited on STO. b) Variation of surface expansion (black squares) and Kelvin potential (blue circles) in the scanned pads shown in (a), that no longer exhibit linear tendency when voltage is increased above -8 V. The dashed lines serve as guides to the eye.

Furthermore, as shown in **Figure 5.12**, while the Kelvin potential can be fully restored after annealing (**Figure 5.12**e,f), the surface expansion remains partially irreversible: even after thermal annealing at 500 ºC, a residual height increase of ≈4 nm persists (**Figure 5.12**b,c). In contrast, for charge-transfer oxides, significantly lower temperatures (200-300 ºC) were sufficient to completely erase the effect. These findings suggest that the electric field applied with the AFM tip induces an irreversible transformation in LSMO thin films (and, by extension, in Mott-Hubbard oxides).

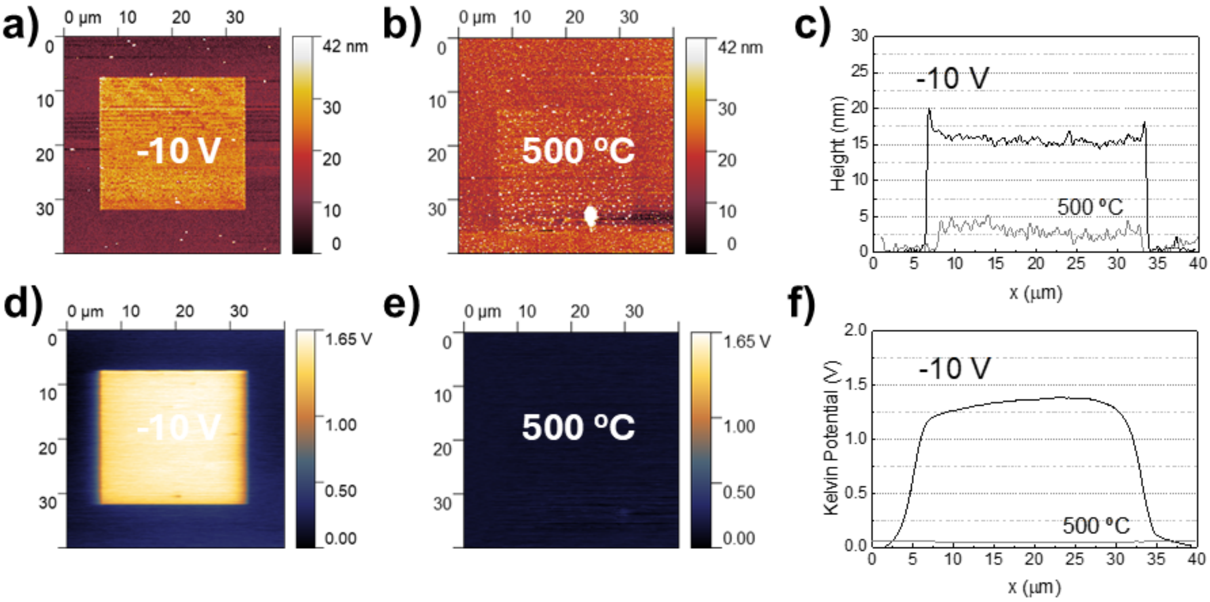

Figure 5.12. Topography (a) and Kelvin potential (d) scans of the -10 V pad on a 40 nm thick LSMO thin film. The topography and Kelvin repeated on the same area after annealing the sample at 500 ºC in air are shown in (b) and (e), respectively. Height and Kelvin potential line profiles along the same pad (before and after thermal annealing) are shown in (c) and (f), respectively.

To further investigate the origin of this pronounced surface expansion and assess the role of adsorbed water in the electric-field driven modification of Mott-Hubbard oxides, we performed additional experiments in which the LSMO surface was scanned with the AFM tip immersed in mineral oil, following the same procedure as for SFO. As presented in **Figure 5.13**, applying -10 V in absence of humidity resulted in a significantly smaller surface expansion of ≈5 nm, more similar to the effect observed in SFO and LSCO thin films (expansion of ≈3 y ≈4 nm, respectively). Additionally, the region scanned in the presence of mineral oil electrostatically attracted oil droplets, as evidenced in the optical microscope image presented in **Figure 5.13**b. This phenomenon was not observed in SFO, further indicating a different underlying mechanism.

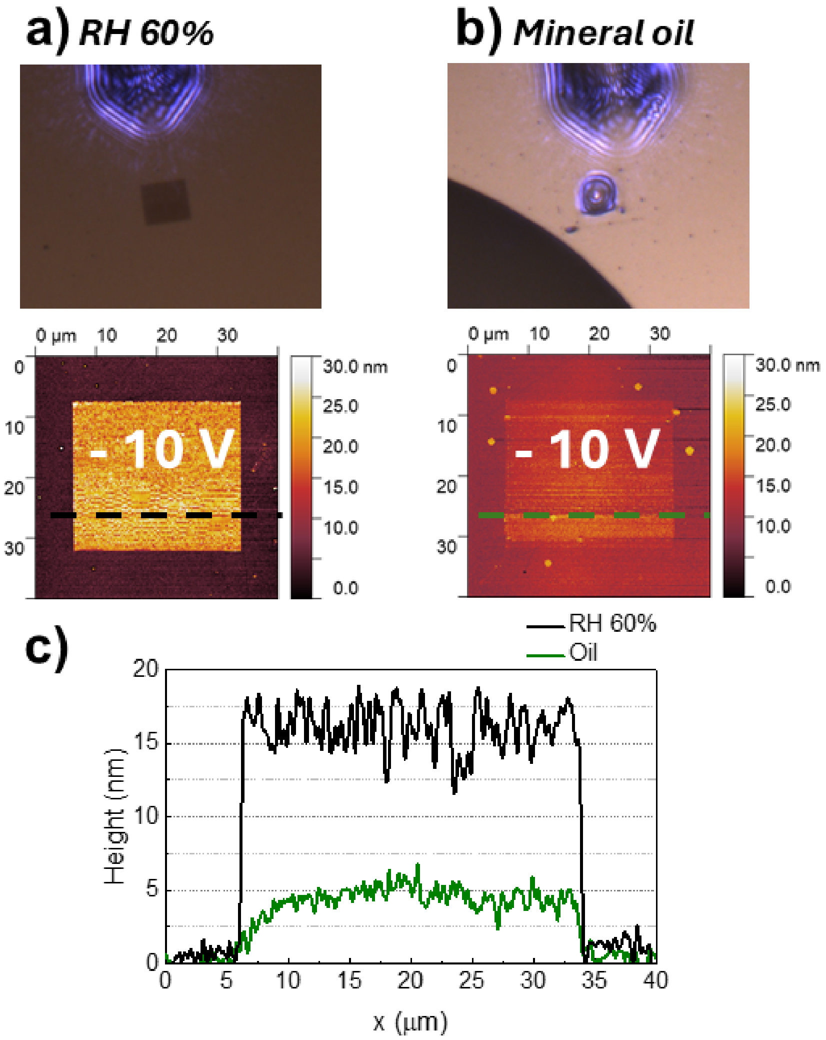

Figure 5.13. Optical microscopy (reflected light) images and AFM topographies of 25 x 25 µm^2 regions of the surface of a LSMO thin film (≈40 nm thick) scanned at -10 V under normal atmospheric conditions (a), and with the AFM tip and sample surface immersed in mineral oil (b). In (c) we show the height profiles along these regions, demonstrating that the local expansion is considerably suppressed when the electric field is applied in absence of humidity, with a maximum of ≈5 nm.

Interestingly, this expansion of ≈5 nm would have been obtained under normal atmospheric conditions if the linear trend shown in **Figure 5.11**b had continued at -10 V. These results indicate that the surface modification of Mott-Hubbard oxides may be a combination of two separate mechanisms: at lower voltages, the electric field induces the local accumulation of oxygen vacancies, and thus the observed effect is similar to that in charge-transfer oxides; however, the application of -10 V leads to an irreversible electrochemical oxidation induced by the presence of adsorbed water, as evidenced by the different behavior of LSMO upon varying the humidity levels.

To further understand the effect of localized electric fields on Mott-Hubbard oxides, we performed XPS analysis on a LSMO thin film, comparing a pristine region of the sample with an area previously modified at -10 V. The main results are summarized **in Figure 5.14**.

In this case, unlike SFO, Sr 3d spectrum does not show any changes (**Figure 5.14**a), with no noticeable variation in peak intensity or relative position. However, the O 1s spectrum (**Figure 5.14**b) now presents four different components, corresponding to lattice oxygen (purple band), surface termination oxygen (blue), oxy-hydroxide lattice oxygen (orange) and mixed hydroxide groups (cyan band). As shown in **Figure 5.14**b, the application of a negative voltage results in a considerably increase of the hydroxide band at the expense of the oxygen lattice contribution, indicating the formation of hydroxide species on the film surface.

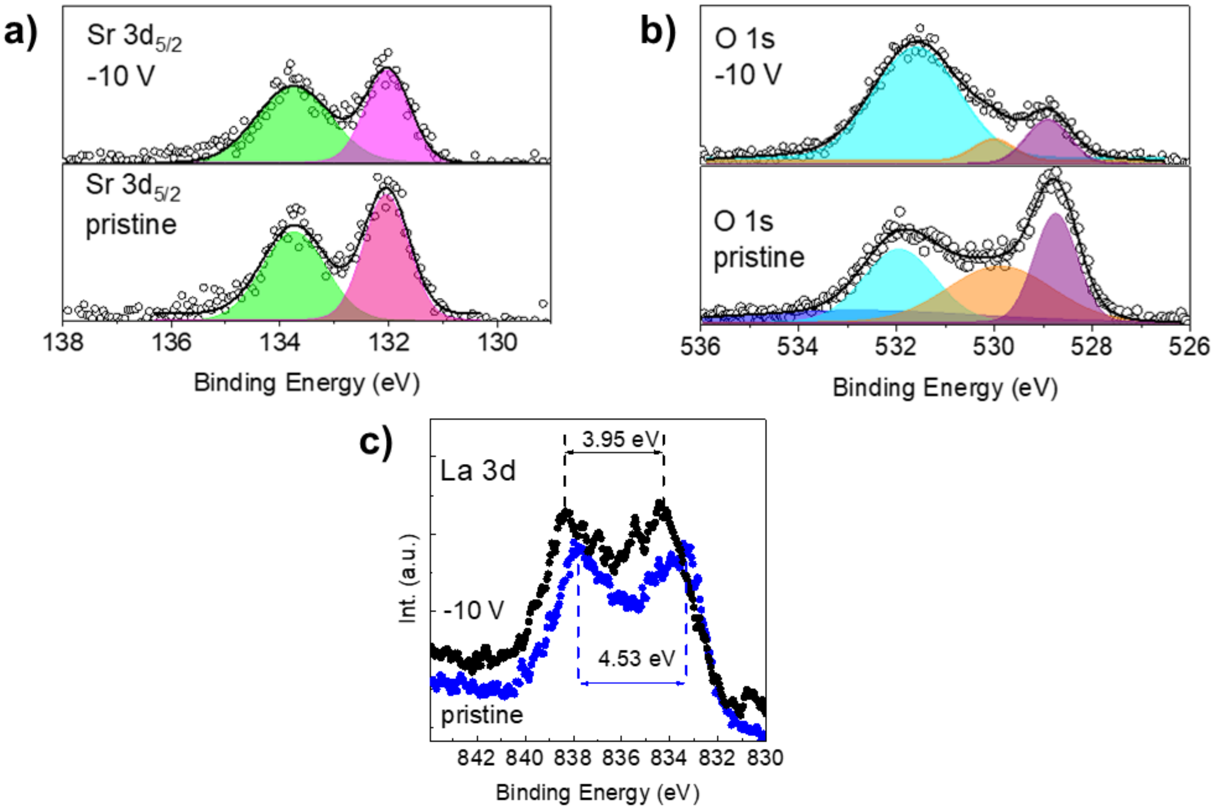

Figure 5.14. XPS spectra of a $La_{0.7}Sr_{0.3}MnO_3$ thin film, recorded on the pristine sample and on a region scanned at -10 V. Sr 3d spectrum (a) remains invariable after the application of the voltage, while the changes observed in the O 1s (b) and La 3d (c) spectra are consistent with the formation of an hydroxide on the film surface, pointing to a local electrochemical reaction with adsorbed water.

Additionally, La 3d spectrum (**Figure 5.14**c) revealed a shift in binding energy after voltage application: the La $3d_{5/2}$ multiplet splitting decreased from 4.53 eV in the pristine sample to 3.95 eV in the modified region. This observation is remarkably similar to the effects observed after the surface reconstruction of $La_{0.6}Sr_{0.4}CoO_3$ catalyst during oxygen evolution reaction (OER) operation conditions (*239*).

Therefore, the XPS data indicates that the application of localized electric fields on LSMO leads to the electrodeposition of a La and/or Mn hydroxide/oxohydroxide on the film surface, produced by electrochemical oxidation with adsorbed water under a similar mechanism to the irreversible oxidation of surface Si by AFM nanolithography (*222*). This results in the irreversible modification of Mott-Hubbard oxides upon voltage application.

So far, our results demonstrate that the high electric fields created with a voltage-biased AFM tip effectively control the local concentration of oxygen vacancies in charge-transfer oxides. We will now analyze its effect on the thermal conductivity of the oxide with the aim of exploring their viability as a thermal switch.

5.2.3. Electric-field modulation of thermal conductivity

Thermal conductivity measurements were performed by frequency domain thermoreflectance (FDTR). To gain spatial resolution during our measurements, the sample was mounted on a piezoelectric stage that can be displaced in the x, y, z axis ±100 μm, with a step of 0.1 μm. In this way, we can define a (x,y) matrix of FDTR experiments to achieve micron-size spatial resolution, thus enabling the creation of thermal conductivity maps of the regions modified with the AFM.

As detailed in Chapter 2 (section 2.2.5.2), FDTR requires the deposition of a thin transducer layer (Au, in our case) on the sample surface for the thermal conductivity measurements. Therefore, after scanning several regions of the bare surface of the thin films with the biased-AFM tip, we deposited ≈60 nm of Au on the sample surface. As shown in **Figure 5.15**a, the contrast from the modified regions observed in **Figure 5.3**b becomes invisible after Au deposition.

We performed FDTR scans over a 100 x 100 μm^2 area (step of 0.5 μm), recording the phase shift of the pump and probe lasers at six different frequencies ($\phi(\omega)$, ranging from 50 kHz to 20 MHz), selected for maximum sensitivity to the thermal conductivity of the film. In the phase-shift map at 20 MHz (**Figure 5.15**b), where the sensitivity to thermal conductivity is maximum, the regions modified by the AFM tip are now visible and with considerable contrast.

We measured the $\phi(\omega)$ curves within these modified areas, and the results are presented in **Figure 5.15**c. As we can observe in the image, the curves are progressively displaced upon increasing the negative bias, showing lower phase shifts at low frequencies and higher shifts at high frequencies. By fitting these curves to a thermal transport model, we determined the thermal conductivity values in these areas, which decreased linearly with applied voltage, reaching a maximum reduction of approximately ≈35% at -10 V (**Figure 5.15**d). This linear reduction in thermal conductivity can be explained by the local accumulation of oxygen vacancies, which progressively increases with the applied voltage as discussed in the previous section.

When fitting the phase-shift curves (**Figure 5.15**c) to the thermal transport model, the film thickness must be introduced as a fixed parameter. In this analysis, we considered both the total film thickness (≈40 nm) and the expanded thickness after AFM modification (≈43 nm at -10 V, as shown in **Figure 5.4**e). Notably, both values yielded the same thermal conductivity results, within the experimental error (**Figure 5.15**d), confirming the robustness of our measurements.

Note also that the electronic contribution to thermal conductivity of PV-SFO can be estimated from its electrical resistivity (0.05–0.1 Ω·cm at room temperature) and the Wiedemann-Franz law *(Eq. 1.7)*. In this approximation, an electronic contribution of ≈0.01 W/mK is expected. Therefore, the observed reduction in κ upon bias application cannot be attributed to an increase in the electrical resistance, but to the accumulation of point defects and their impact on phonon propagation (*243*).

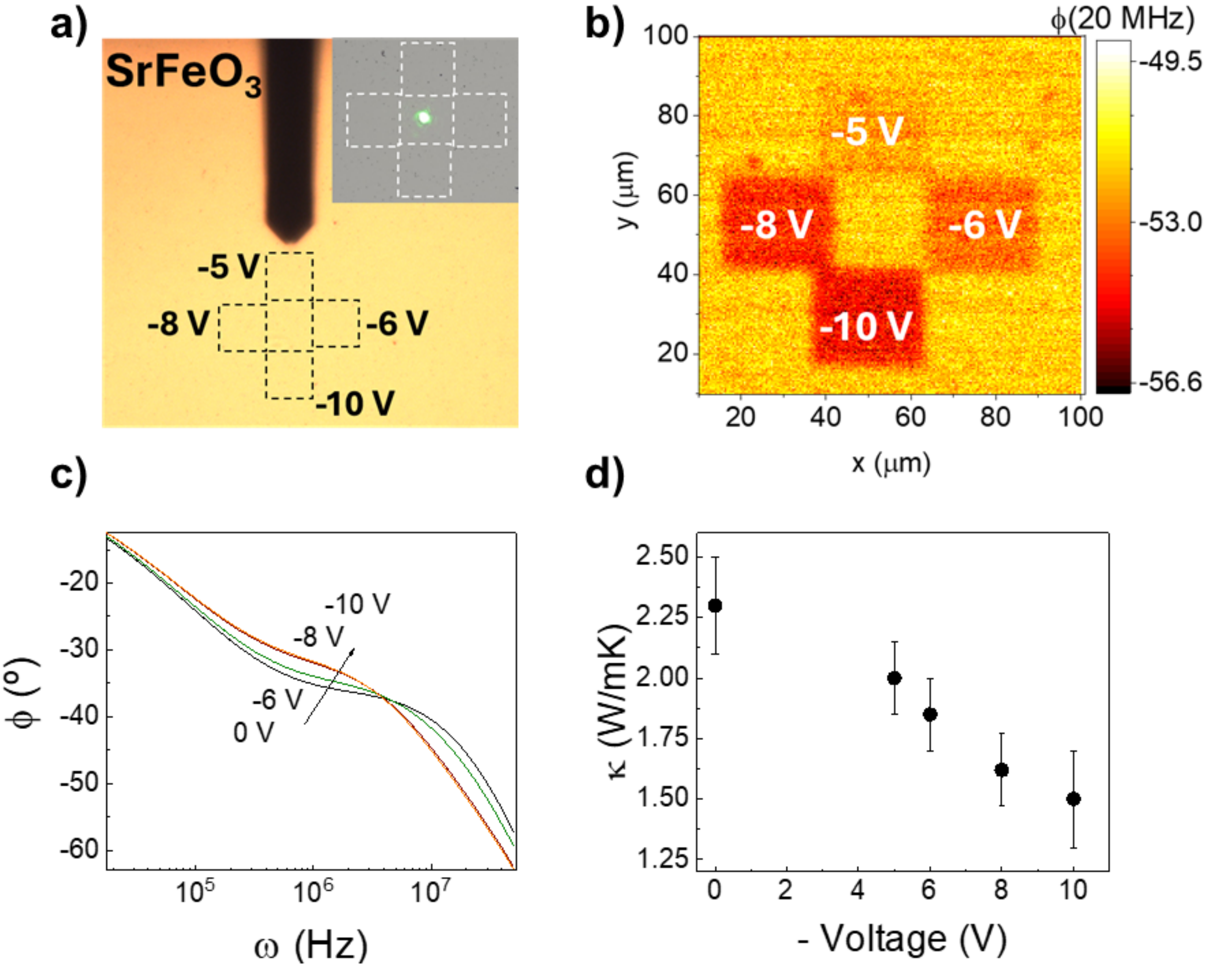

Figure 5.15. a) Optical image of the surface of a 40 nm thick SFO thin film, previously scanned with the AFM tip biased at different voltages, covered with 60 nm of Au for the FDTR measurements. The modified regions (like those shown in **Fig. 5.3**b) are not visible across the Au layer, but their approximate position is indicated by dashed squares. The shadow of the AFM cantilever is shown in the image. The inset shows a photograph of the same region captured with the FDTR camera, with the spot of the probe laser at its center. b) Phase shift map at 20 MHz obtained by scanning a region of 100 x 100 μm^2, 0.5 μm step, with the pump/probe laser beams. The four squares scanned with the AFM tip are now visible in the phase-shift map. c) Phase *vs* frequency curves measured inside each of the regions shown in (b), exhibiting a clear evolution with the applied voltage. Fitting these curves to a thermal transport model provides the local thermal conductivity, which decreases linearly with the voltage, as presented in (d).

To further analyze the spatial distribution of thermal conductivity, we generated thermal conductivity maps by fitting each pixel of the phase-shift map in **Figure 5.15**b to the thermal transport model. **Figure 5.16**a presents the resulting thermal conductivity map, together with the corresponding thermal conductivity line profiles across the modified regions (**Figure 5.16**b). As shown, all four squares created by applying different voltages are clearly distinguishable, with their intensities varying according to the applied electric field. Moreover, the line scans confirm the progressive decrease in thermal conductivity with increasing negative voltage, as previously observed in **Figure 5.15**d. This demonstrates that the thermal contrast within these regions can be effectively controlled by tuning the electric field. Additionally, these experiments reveal that the modified regions exhibit sharp boundaries in all cases, highlighting the high spatial precision achieved with this method.

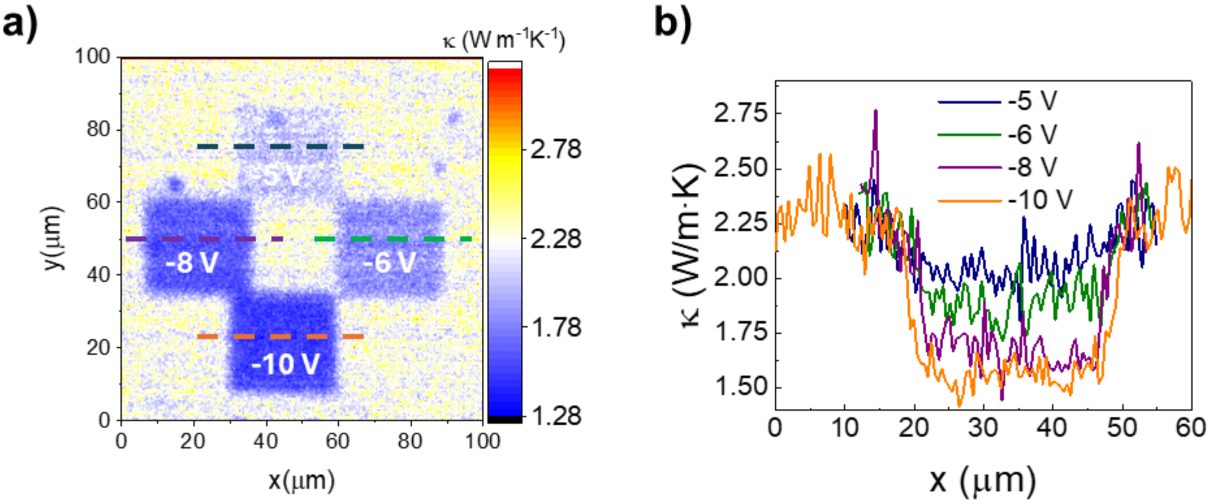

Figure 5.16. a) Thermal conductivity map of four regions of a SFO film modified with the AFM tip biased at different voltages. The map was obtained by fitting the phase-shift map at 20 MHz from **Fig 5.15**b, where the sensitivity to thermal conductivity is maximized. b) Line scans of thermal conductivity along each of these modified regions, showing the excellent control over the local thermal conductivity achieved by this method.

In the previous section, we demonstrated that the surface expansion in SFO remained unchanged (≈3 nm) upon -10 V application, regardless of atmospheric humidity levels or whether the AFM tip and sample surface were immersed in mineral oil. This ruled out the participation of adsorbed water in electrochemical transformations. However, to further validate these findings, we measured the thermal conductivity of SFO areas modified at -10 V under standard atmospheric conditions (RH 60%) and with the sample covered in mineral oil. The results are presented in **Figure 5.17**.

As observed in the figure, the thermal conductivity maps of both regions are equivalent (**Figure 5.17**b,d), with line scans displaying similar reductions in thermal conductivity of ≈35% (**Figure 5.17**e) when the sample surface was scanned at -10 V under standard atmospheric conditions (RH ≈60%) or with the AFM tip and sample surface immersed in mineral oil (absence of water). This, again, demonstrates that the changes observed in Kelvin potential, surface expansion and thermal conductivity upon application of negative bias must have an intrinsic origin, further confirming that the reduction in thermal conductivity is due to the electric-field induced accumulation of oxygen vacancies in the scanned regions.

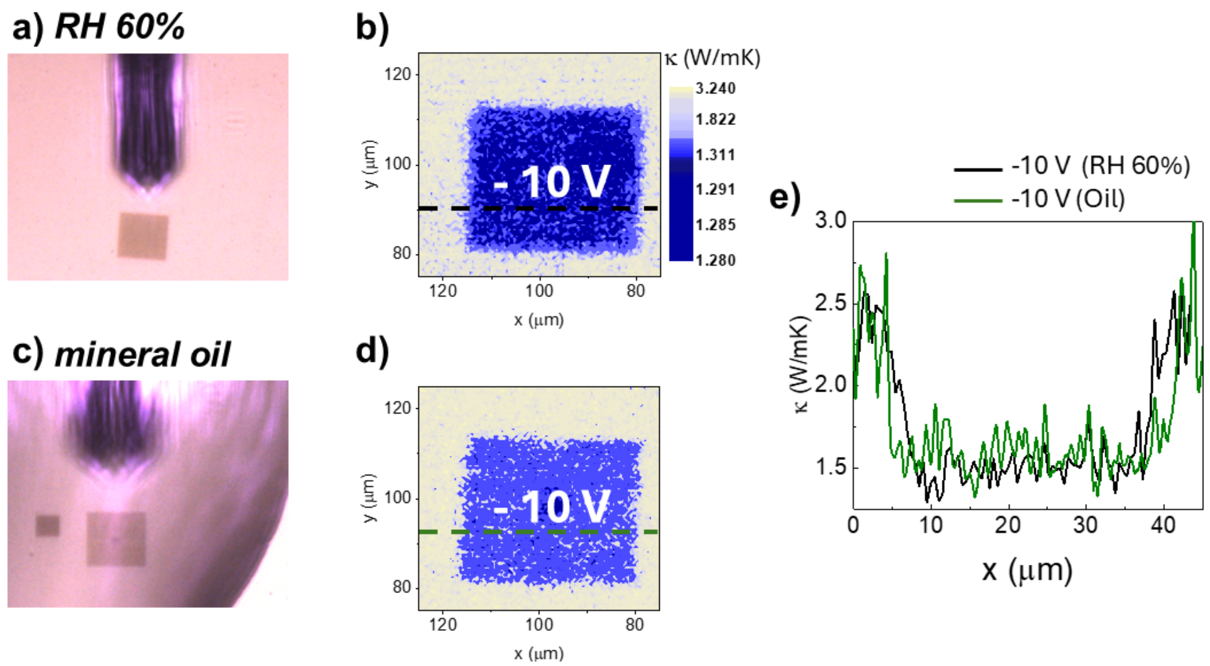

Figure 5.17. Comparison of the thermal conductivity of two regions (25 x 25 μm^2) of a SFO thin film scanned at -10 V under normal atmospheric conditions, and with the AFM tip and sample surface immersed in mineral oil. The thermal conductivity maps (b,d) and thermal conductivity profiles along the modified regions (e) highlight the equivalence of the results.

To prove the stability of the thermal states created with the AFM tip, we followed their evolution under normal atmospheric conditions and after performing thermal annealing. For this stability test, we deposited four identical SFO thin films (≈40 nm thick) in the PLD, and created the same pattern as depicted in **Figure 5.16**, consisting of four 25 x 25 μm^2 squares scanned at -5, -6, 8- and -10 V, respectively. Each sample underwent different treatments before performing thermal conductivity measurements.

The first sample was immediately coated with a 60 nm layer of Au transducer after AFM modification, followed by thermal conductivity measurement by FDTR (**Figure 5.18**a). The second sample was left under ambient laboratory conditions for one week, prior to depositing the Au transducer and measuring thermal conductivity (**Figure 5.18**b). The third sample was annealed at 200 ºC, and then Au was deposited and κ was measured (**Figure 5.18**d). Finally, the fourth sample was also subjected to thermal annealing at 200 ºC but, instead of measuring the thermal conductivity after the thermal treatment, we scanned again the same region of the film, re-writing the pattern that was erased during heating. Next, we deposited Au and measured κ (**Figure 5.18**e).

The results of the stability test are summarized in **Figure 5.18**, showing exclusively the thermal conductivity values for the region modified at -10 V, for clarity.

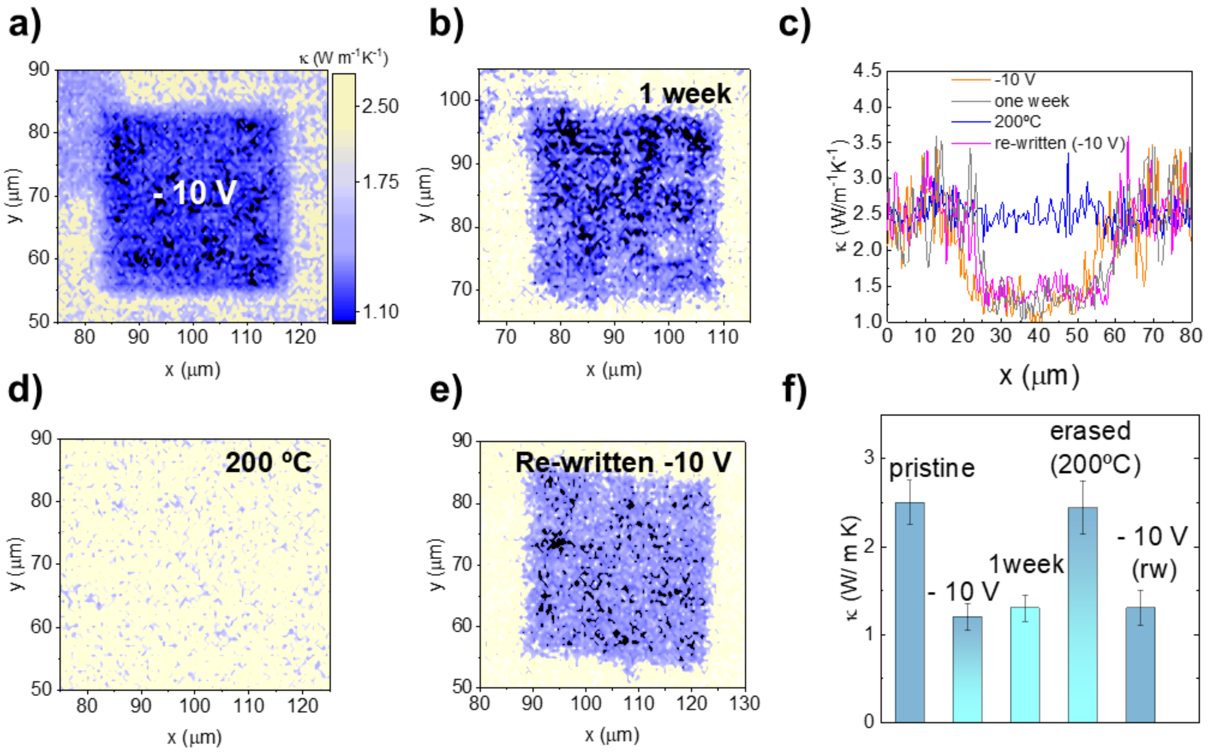

Figure 5.18. The stability of the thermal states in SFO thin films (≈40 nm) was tested by following the evolution of the area scanned at -10 V right after voltage application (a), after one week in standard atmospheric conditions (b), after thermal annealing at 200 ºC in air (d), and after erasing and rewriting at -10 V in the same area of the film (e). The line scans (c) and the histogram (f) show the local thermal conductivity in the modified regions after these processes, demonstrating the stability and reversibility of the transformation.

As observed in **Figure 5.18**, the application of -10 V to the SFO thin film leads to a reduction of ≈35 % in thermal conductivity (from ≈2.5 to 1.5 W/mK, approximately, as shown in **Figure 5.18**c,f). This reduced thermal state remains stable under normal atmospheric conditions for at least one week, but it is fully erased after thermal annealing at 200 ºC (air, for 4 h), restoring the initial thermal conductivity (**Figure 5.18**b,d). After this thermal annealing, and once the modified areas have been recovered to the original state, it is possible to re-apply the electric field, creating once again a thermal state with the same reduced thermal conductivity, within the error (**Figure 5.18**e,f). With these experiments, we demonstrate that, with the proposed AFM lithography technique, it is possible to create non-volatile thermal states in SFO with thermal contrasts of up to 35%, that can be reversed to the original state by gentle thermal annealing, allowing a new process of electric-field writing.

In order to determine if the electric-field induced accumulation of oxygen vacancies occurs in all the film thickness or just at the surface, we measured the thermal conductivity of AFM-modified regions in thicker SFO thin films (≈70 nm). As shown in **Figure 5.19**b,f, maximum reductions of 35 % were achieved, similarly to SFO thin films of ≈40 nm. Since, as previously explained, film thickness is one of the parameters introduced in the thermal transport model for fitting κ, these results demonstrate that the accumulation of oxygen vacancies (the origin of the reduced thermal conductivity) occurs across all the film thickness (at least up to 70 nm), and it is not just a surface effect.

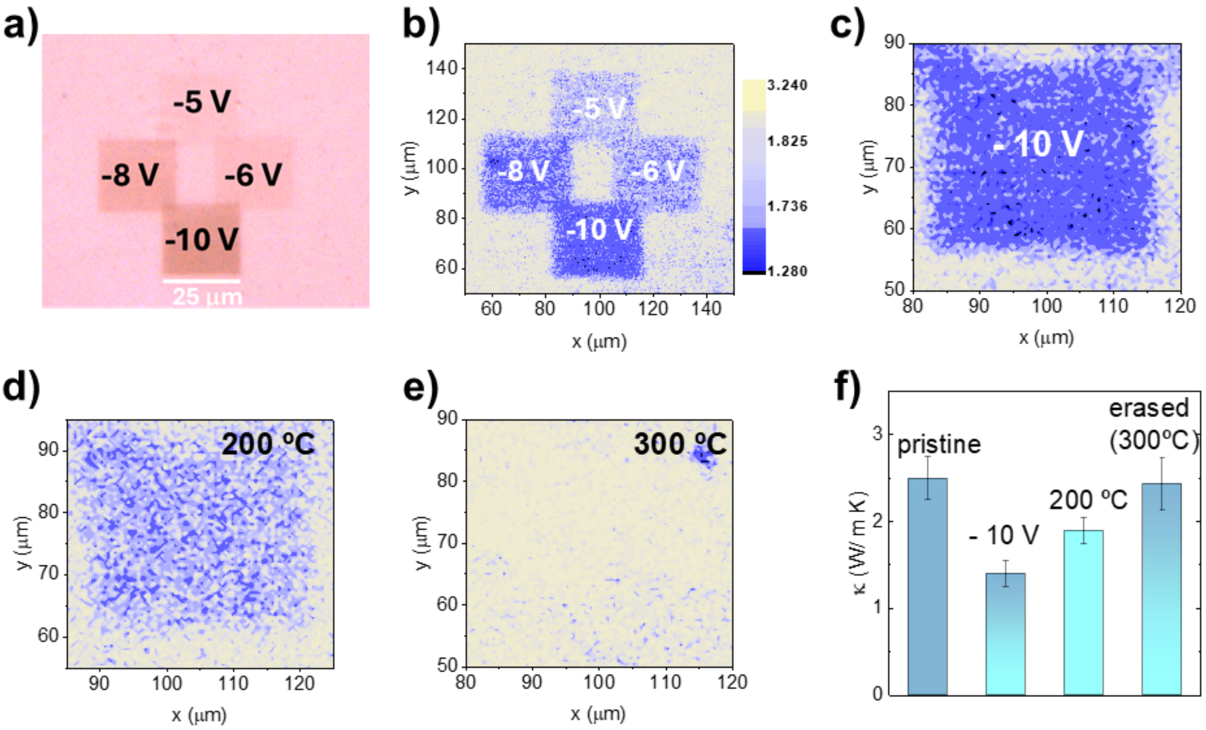

Figure 5.19. a) Optical image (reflected light) of four pads of 25 x 25 µm^2 scanned with the AFM tip biased at different voltages, on the surface of a 70 nm thick SFO thin film. b) Thermal conductivity map of the modified regions. In (c-e) we show the stability test of the written states, exemplified for the pad written at -10 V. f) Histogram showing the local thermal conductivity of the modified regions during the stability test, demonstrating the reversibility of the transformation although higher temperatures (300 °C) are needed in this case.

Again, the thermal states created on thicker films can be completely erased by performing thermal annealing, although in this case higher temperatures are needed (**Figure 5.19**c-e). At 200 ºC the initial thermal conductivity value is not recovered, being necessary to increase temperature up to 300 ºC to completely eliminate the reduced thermal state (**Figure 5.19**f). This is another indication that the accumulation of oxygen vacancies occurs throughout the entire film: higher temperatures are needed to enhance oxygen mobility across greater thicknesses.

In order to determine the maximum thermal contrast achievable with our method, we measured the thermal conductivity map of a SFO thin film (deposited on LSAT) after inducing a complete PV-to-BM transition. Following the procedure described in **Figure 5.2**, we scanned two different regions of 25 x 25 and 10 x 10 µm^2 using scan rates of 0.5 (12.5 µm/s) and 0.3 Hz (3 µm/s), respectively.

Figure 5.20b shows the measured thermal conductivity map in these two modified regions, observing a maximum reduction of thermal conductivity (≈1.0 W/mK, 58% reduction) in the area where the BM phase was obtained (10 x 10 µm^2, scanning rate of 0.3 Hz). This is the lowest thermal conductivity value that can be achieved with our method. However, repeated structural transformations may lead to the progressive accumulation of defects (as we deeply analyzed in Chapter 4), limiting the reversibility of the process. These irreversibility issues further support our approach based on local oxygen vacancy accumulation: although lower thermal contrasts are achieved with our method, it provides full reversibility and repeatability.

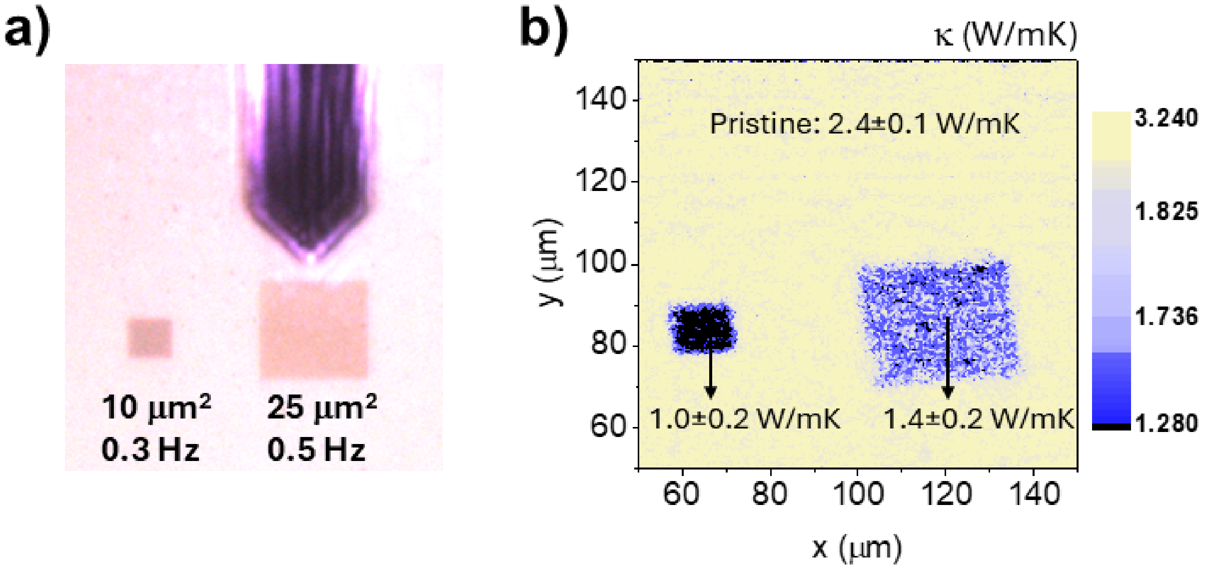

Figure 5.20. a) Optical microscopy (reflected light) image of 25 x 25 and 10 x 10 µm² areas of the surface of a 40 nm thick $SrFeO_{3-x}$ thin film (deposited on LSAT), scanned with -10 V at 0.5 and 0.3 Hz, respectively. b) Thermal conductivity map of these modified regions, demonstrating the maximum reduction in thermal conductivity for the BM phase.

Furthermore, it is worth noting that the thermal conductivity values obtained for the 40 nm thick SFO film on an LSAT substrate at a scan rate of 0.5 Hz (**Figure 5.20**) match those observed in **Figures 5.16–5.18** for an identical film grown on STO substrates. This consistency demonstrates that the reduction in thermal conductivity upon biased-AFM modification is independent of the substrate and epitaxial strain. Specifically, while SFO thin films on STO experience a tensile strain of +1.37%, this strain is reduced to +0.47% when deposited on LSAT, yet the thermal behavior remains unchanged.

The effect of the applied electric field on the thermal conductivity of charge-transfer LSCO thin films (≈40 nm) was also tested using FDTR. **Figure 5.21** presents the thermal conductivity map of the 25 x 25 µm² regions modified by the application of -5, -6, -8 and -10 V, respectively. Similarly to SFO, the application of the negative voltage leads to a continuous reduction in thermal conductivity, achieving a maximum thermal contrast of ≈55% in this case (κ≈ 0.8 W/mK for -10 V, **Figure 5.21**b). Furthermore, once again, the modified thermal states present sharp boundaries, proving the high precision of our method.

These reduced thermal states are also stable under normal atmospheric conditions, as presented in **Figure 5.22**a,b, and can be completely eliminated by performing thermal annealing in air (**Figure 5.22**c-e). However, higher annealing temperatures are needed in this case: temperature must be higher than 350 ºC to recover the initial thermal conductivity value.

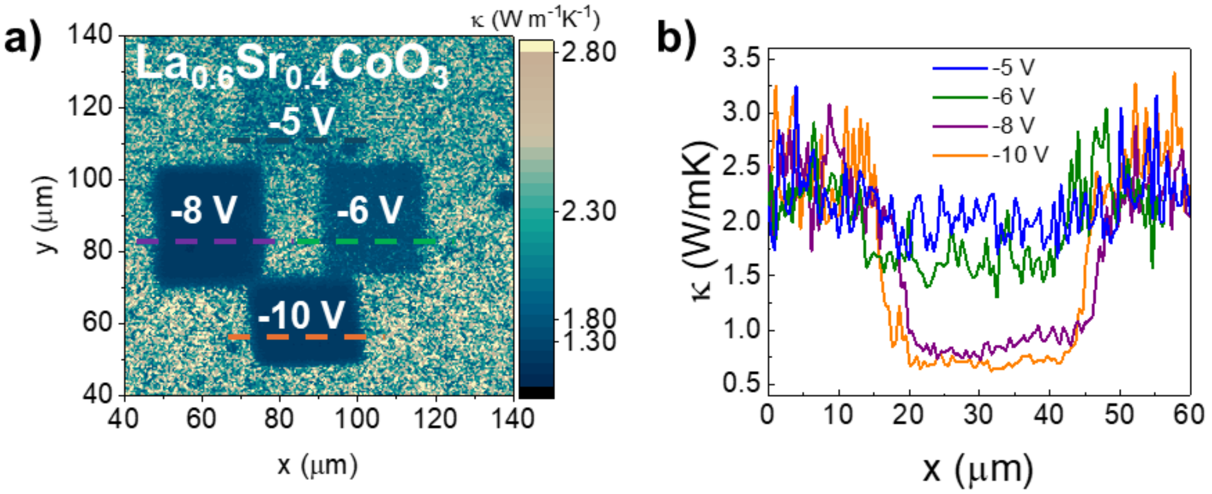

Figure 5.21. a) Thermal conductivity map of an LSCO thin film after scanning several areas of 25 x 25 μm^2 with a voltage biased-AFM tip. The line scans of the thermal conductivity along each pad are shown in b), demonstrating a maximum reduction of ≈55% for -10 V.

This result contradicts that shown in **Figure 5.10**, where only 300 ºC where needed to completely erase the surface expansion created by the AFM tip biased at -10 V. This difference is probably due to the higher sensitivity of thermal conductivity: even a small concentration of oxygen vacancies can still reduce heat transport across the film due to the increase of phonon scattering, even though the accumulation may not produce a significant expansion in the sample surface, impeding detection by AFM topography.

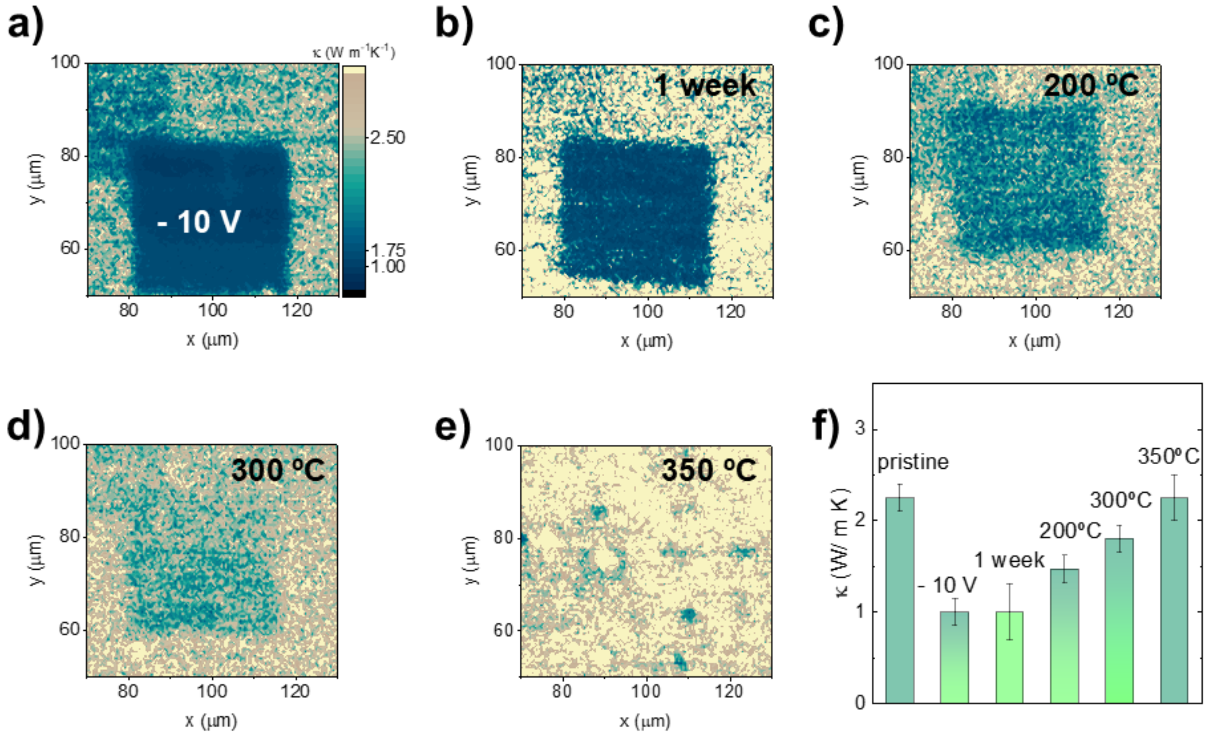

Figure 5.22. The stability of the thermal states in LSCO thin films (≈40 nm) was tested by following the evolution of the area scanned at -10 V right after voltage application (a), after one week in standard atmospheric conditions (b), and after thermal annealing in air at 200 °C (c), 300 °C (d) and 350 °C (e). The values of thermal conductivity after each treatment are shown in (f).

Finally, **Figure 5.23** summarizes the thermal conductivity results for the Mott-Hubbard oxide LSMO. As observed in **Figure 5.23**b, thermal conductivity decreases progressively with increasing negative voltage, except at -10 V, where a much sharper reduction of about 70% is observed. This drastic drop agrees with the non-linear tendency of surface expansion and Kelvin potential (**Figure 5.11**b) observed at -10 V.

Additionally, consistent with the severe and irreversible surface modifications shown in **Figure 5.12**, the application of -10 V leads to a non-reversible change in thermal conductivity. Even after thermal annealing at 500 ºC, the modified region remains clearly visible in the thermal conductivity map, and retains a thermal conductivity value ≈30% lower than the original (**Figure 5.23**c,d).

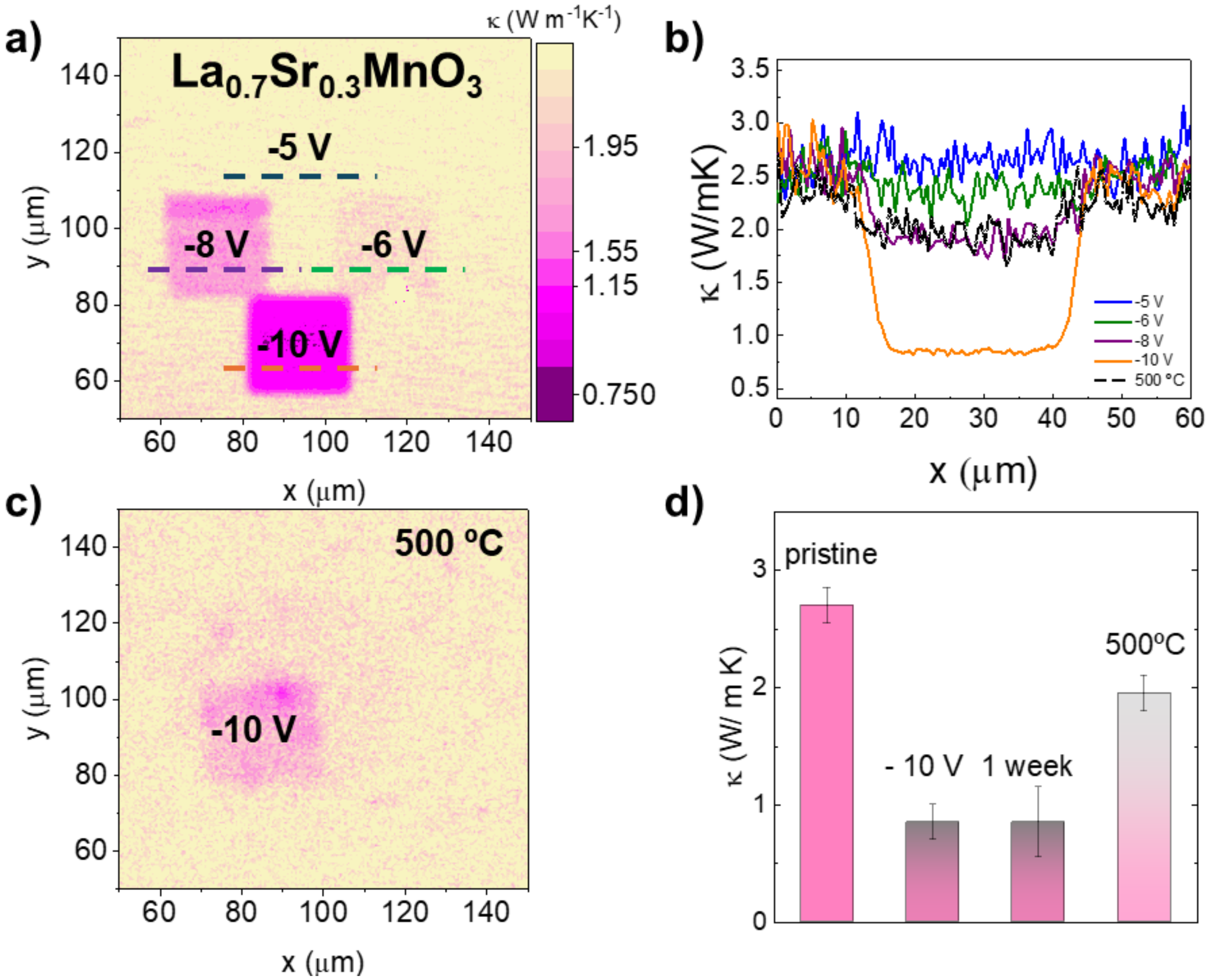

Figure 5.23. a) Thermal conductivity map of a LSMO thin film after scanning several areas of 25 x 25 μm^2 with a voltage biased-AFM tip. The line scans of the thermal conductivity along each pad are shown in (b). The stability and reversibility of the modified areas were proven by following the evolution of the -10 V pad right after modification, after one week under standard atmospheric conditions and after thermal annealing at 500 °C (c), demonstrating the irreversibility of the process. The values of thermal conductivity after each treatment are shown in (d).

These findings further highlight the critical role played by adsorbed water in Mott-Hubbard oxides, which facilitates hydroxide electrodeposition and leads to permanent modifications in both surface structure and thermal conductivity. Consequently, Mott-Hubbard oxides are unsuitable for fabricating thermal switches via electric-field modulation, as their response lacks the required reversibility for practical applications.

5.3. CONCLUSIONS

In this chapter, we investigated the reversible modulation of thermal conductivity in transition-metal perovskites using a voltage-biased AFM tip, aiming to develop a thermal switch. The key findings from our research are:

- The application of localized electric fields with a voltage-biased AFM tip effectively induces the accumulation of oxygen vacancies in perovskite thin films.
- The extent of the vacancy accumulation can be controlled with the applied dose (adjusted through voltage and scan rate), resulting either in a complete PV-BM transition or in a transient, random distribution of vacancies. However, inducing a full structural transformation often results in irreversibility issues.
- In charge-transfer oxides, the localized random accumulation of oxygen vacancies allows the creation of non-volatile thermal states, at room temperature and under ambient conditions, achieving reductions in thermal conductivity of up to 55%.
- These thermal states remain stable for weeks but can be fully erased through gentle thermal annealing in air, restoring the material to its original state and enabling reuse.
- In contrast, Mott-Hubbard oxides exhibit a combination of oxygen vacancy accumulation and surface hydroxide deposition when subjected to localized electric fields. This dual effect leads to irreversible structural changes, making these materials unsuitable for thermal switching applications.

In summary, the localized application of electric fields through a voltage-biased AFM tip enabled the creation of micron-scale patterns with reduced thermal conductivity on oxide thin films. By optimizing the contribution of the O 2p states at the Fermi level, we established non-volatile thermal states that remain stable for weeks, but that can be erased through thermal annealing. This constitutes a novel application of AFM lithography for designing reconfigurable thermal circuits, and our results demonstrate that conductive AFM-driven ionic manipulation is a promising technique for the design of the elements of a thermal circuit.

6. THERMAL TRANSPORT IN SUPERLATTICES: EFFECT OF POLAR STRUCTURES

> *“We must not forget that when radium was discovered no one knew that it would prove useful in hospitals. The work was one of pure science. And this is a proof that scientific work must not be considered from the point of view of the direct usefulness of it. It must be done for itself, for the beauty of science, and then there is always the chance that a scientific discovery may become like the radium a benefit for humanity.”*
>
> Marie Curie, first woman to win a Nobel Prize and the only person to win the Nobel in two scientific categories: Nobel Prize in Physics (1903) and Nobel Prize in Chemistry (1911).

6.1. INTRODUCTION

In ferroelectric thin films, the equilibrium polarization structure arises from the interplay between intrinsic material properties (chemical composition, crystal structure, etc.) and extrinsic factors (particularly, mechanical and electrostatic boundary conditions), resulting in broad spectrum of possible domain configurations. A canonical example is $PbTiO_3$, which typically forms classical 180 ° or 90 ° domains when epitaxially grown on appropriate substrates (*244*). However, when the electrostatic environment is altered –for instance, due to incomplete screening of bound charges at the film surface/interfaces–, strong depolarization fields can emerge, which oppose the spontaneous polarization and may destabilize these conventional domain patterns. To reduce this energetic tension, the system usually reorganizes its domain structure into more complex, and often topologically nontrivial, polarization textures that are energetically more favorable under such conditions.

This behavior is especially relevant in $PbTiO_3/SrTiO_3$ (PTO/STO) superlattices, which consist of periodically alternating thin ferroelectric (PTO) and paraelectric (STO) layers, arranged with atomic-scale precision. Within this artificial multilayer architecture, the equilibrium polarization configuration results from the delicate competition among three fundamental energy contributions (*245*):

- Electrostatic energy, associated with depolarization fields that arise when the polarization vector terminates abruptly at dielectric interfaces. To reduce this energy, the system may favor polarization configurations that curl, rotate, or alternate in such a way as to internally compensate these fields.
- Elastic energy, driven by epitaxial strain imposed by the substrate and the requirement to maintain coherent lattice matching across PTO/STO interfaces. This mechanical coupling induces further strain into the system, which can be locally relieved by polarization rotation, tilting, or domain modulation.
- Gradient energy, which is the energy cost associated with spatial variations in the polarization vector. Complex polar textures usually exhibit smooth, continuous rotations of polarization that lower electrostatic and elastic energies at the expense of increased gradient penalty.

These three energy components compete and interact across multiple length scales, and the equilibrium state is the result of minimizing the total free energy of the system. The combination of ferroelectric PTO and paraelectric STO layers in periodic superlattices constitutes a unique platform for tuning the relative importance of each contribution, giving access to a wide range of exotic topological structures that are fundamentally distinct from those found in bulk PTO.

Over the past decade, a rich variety of non-trivial polar structures have been theoretically predicted and experimentally observed in PTO/STO superlattices. Among them, polar vortices and antivortices are perhaps one of the earliest and most emblematic examples. These structures were first reported by Yadav *et al.* (*246*) in superlattices with a periodicity of 10 unit cells of STO and 10 of PTO, $[(STO)_{10}/(PTO)_{10}]$, epitaxially grown on (110) DSO substrates. By combining phase-field simulations with high-resolution TEM, the authors demonstrated that the tensile strain imposed by the substrate, together with the dielectric confinement provided by the STO layers, inhibits the formation of uniform out-of-plane polarization. Instead, the polarization within the PTO layers undergoes continuous in-plane rotation, forming periodic arrays of clockwise and counterclockwise vortex-antivortex pairs, as shown in **Figure 6.1**a. These flux-closure loops are stabilized at intermediate periodicities (typically between 10 and 20 u.c.), where the depolarization field is large enough to suppress classical domains, but the gradient energy remains low enough to allow smooth polarization textures.

Expanding on this work, Abid and coworkers (*247*) reported that by reducing the STO layer thickness up to just 4 u.c, the electrostatic boundary conditions are modified in such a way that the polar textures extend beyond the PTO layers. Specifically, in $[(PTO)_{10}/(STO)_4]$ superlattices, they observed that while the PTO layers continue to host polar vortices, polar antivortices are stabilized within the STO layers, marking the first experimental evidence of topologically non-trivial polarization textures in a nominally paraelectric layer. This discovery confirms earlier first-principles predictions by Aguado-Puente and Junquera (*248*), and highlights the important role that STO can play in the overall topological state of the superlattice when electrostatic coupling is sufficiently strong.

Closely related to vortex arrays are polar skyrmions, which are three-dimensional topological polar structures that have been observed in PTO/STO superlattices under mild compressive strain. In particular, Das *et al.* (*249*) reported the formation of room-temperature polar skyrmions in $[(PTO)_{16}/(STO)_{16}]_8$ superlattices (where 8 is the number of repetitions of the PTO/STO bilayer) on (001) STO substrates. Unlike vortices, which exhibit periodic in-plane rotation of polarization, skyrmions are characterized by a three-dimensional texture in which the polarization rotates smoothly from upward to downward across the film thickness, forming a cylindrical structure as observed in **Figure 6.1**b. Real-space mapping of the polarization vector using advanced STEM revealed that these skyrmions consist of a central core with upward out-of-plane polarization, surrounded by azimuthally rotating in-plane components, and completed by downward out-of-plane polarization at the periphery. This fully enclosed vector field resembles that of magnetic skyrmions but originates from the continuous rotation of electric dipoles.

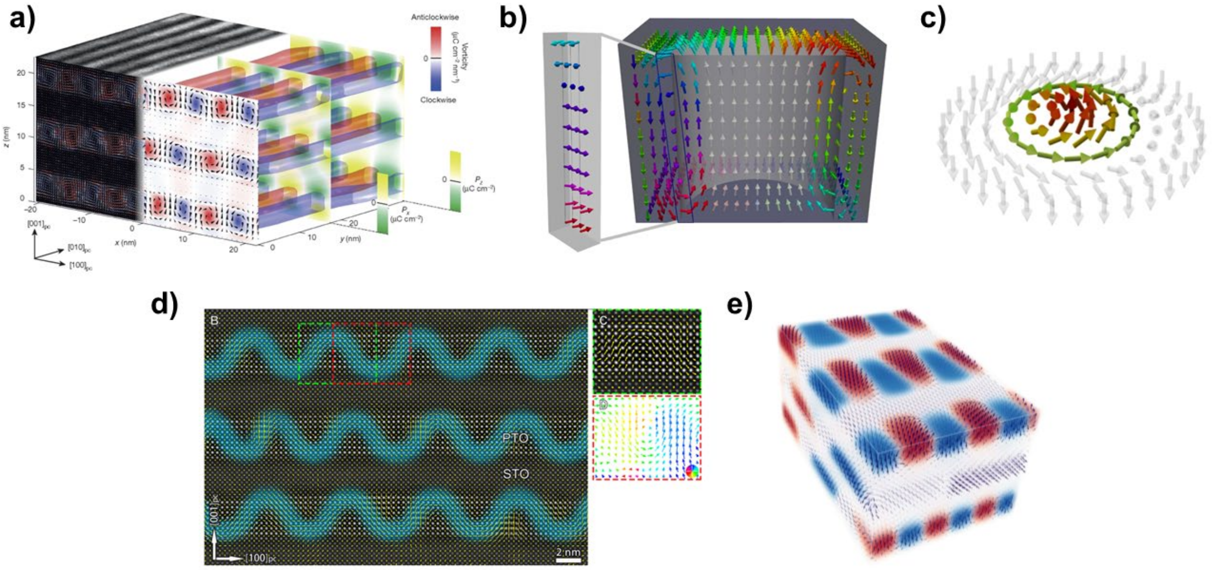

Figure 6.1. Topological polar textures stabilized in PTO/STO superlattices. a) 3D phase-field simulation (right) of vortex-antivortex arrays in a $(STO)_{10}/(PTO)_{10}$ superlattice grown on DSO, showing clockwise and counterclockwise polarization rotations. The simulated structure is accompanied by a cross-sectional STEM image with overlaid polar displacement vectors (left), and a planar-view TEM image projected onto the top plane. Reproduced with permission from ref. (*246*). Copyright (2016) Springer Nature. b) Second-principles simulation of the skyrmion structure in a PTO/STO superlattice, illustrating the continuous three-dimensional rotation of polarization from the core to the periphery. Reproduced with permission from ref. (*249*). Copyright (2019) Springer Nature. c) Schematic representation of a polar meron, a fractional topological structure formed by an out-of-plane polarized core surrounded by in-plane dipoles, lacking the out-of-plane polarization at the edge characteristic of polar skyrmions. Reproduced with permission from ref. (*250*) (CC BY 4.0 license). d) Cross-sectional HAADF-STEM image of a PTO/STO superlattice overlaid with the polar displacement vectors, revealing in-plane sinusoidal modulations in the PTO layer characteristic of electric dipole waves. Reproduced with permission from ref. (*251*) (CC BY-NC 4.0 license). e) Schematic representation of a supercrystal phase, formed by ferroelectric, ferroelastic and polar vortex sub-regions ordered in 3D. Reproduced with permission from ref. (*252*). Copyright (2019) Springer Nature.

More recently, Shao and collaborators (*250*) reported the emergence of polar merons ("half-skyrmions") in freestanding $[(PTO)_{16}/(STO)_{16}]_8$ membranes. In contrast to skyrmions, merons exhibit only partial polarization rotation, with out-of-plane polarization at the core that gradually transitions into in-plane polarization at the boundary, without surrounding antiparallel components (**Figure 6.1**c). In this study, the authors observed a temperature- and strain-induced phase transition from disordered skyrmions to an ordered lattice of polar merons. These findings further expand the catalog of polar topologies accessible in PTO/STO superlattices and illustrate their tunability via external stimuli.

An additional class of polarization textures are electric dipole waves, reported by Gong *et al.* (*251*) in $[(PTO)_7/(STO)_7]_6$ superlattices grown under tensile strain on $GdScO_3$ substrates and rapidly quenched to preserve metastable states. These structures consist of smoothly modulated head-to-tail polarization patterns that follow a sinusoidal profile along the in-plane direction

(**Figure 6.1**d). Remarkably, these dipole waves form without sharp domain walls or discontinuities, resulting in minimal gradient energy cost while still accommodating depolarization and elastic constraints. Phase-field simulations by the same authors corroborated the experimental findings, showing that dipole waves become energetically favorable beyond a critical superlattice periodicity (particularly, between 9 and 11 u.c.) and under tensile strains of ≥1.3%, so that they can also be stabilized in superlattices grown on $DyScO_3$, $SmScO_3$, and $NdScO_3$ substrates.

Finally, completing the family of complex polar configurations in PTO/STO superlattices are polar supercrystals: mesoscopic, long-range ordered structures exhibiting three-dimensional periodicity of topological polarization textures. Experimentally confirmed by Stoica *et al.* (*252*), these supercrystals arise from the self-organization of polar architectures into a lattice-like array (**Figure 6.1**e). In particular, supercrystals were observed in $(PbTiO_3)_{16}/(SrTiO_3)_{16}$ superlattices grown on (110) DSO substrates –which present polar vortices in the as-grown state, as predicted by Yadav and coworkers (*246*)–, and subsequently exposed to ultrafast laser irradiation. This optical excitation generates free carriers that partially screen the depolarization field, enabling the stabilization of a new polar configuration not accessible under equilibrium growth conditions.

Thus, by tuning the periodicity and epitaxial strain conditions, and applying thermal or optical excitation, PTO/STO superlattices can stabilize a wide variety of exotic polar configurations. These polar topologies are not only of fundamental interest but also exhibit functional properties with strong potential for different applications. Owing to their nanoscale dimensions, topological robustness, and reconfigurability under external stimuli –such as temperature or electric fields (*253–256*)–, they offer promising opportunities for non-volatile memory, multi-state logic, electrotoroidic devices, similarly to their analogues in magnetic systems (*257*, *258*).

Importantly, these polarization textures may also offer novel strategies for controlling thermal transport, an aspect that remains entirely unexplored to date. Analogous to ferroelectric domain walls, the spatial variation of polarization and the associated strain gradients inherent to topological structures could also act as effective phonon scattering centers, modifying phonon dispersion relations and limiting mean free paths. This, combined with the control over these structures achieved in PTO/STO superlattices, may constitute a promising platform for modulating lattice thermal conductivity in a non-volatile and potentially reversible manner.

In this chapter, we investigate the influence of these polar architectures on the thermal conductivity of PTO/STO superlattices and evaluate their potential for thermal switching applications. Specifically, we focus on $[(PTO)_{15}/(STO)_{15}]_m$ superlattices –with varying number of repetitions, *m*– grown on (001) STO substrates, and $[(STO)_n/(PTO)_n]_m$ superlattices –with different superlattice periodicity *n*, and number of repetitions *m*– grown on (110) DSO. Previous work by Das *et al.* (*249*) has shown that superlattices with 15 u.c. periodicity grown on STO stabilize polar skyrmions at room temperature, which can be reversibly erased by heating above 663 K (*254*), suggesting a pathway for dynamic thermal control.

In the case of the superlattices grown on DSO, they exhibit a very rich phase diagram as a function of the periodicity *n,* as reported by Yadav *et al.* (*246*) (**Figure 6.2**). For short period superlattices, the system stabilizes purely in-plane polarization components (a_1/a_2); at intermediate periodicities there is a coexistence of a_1/a_2 and vortex-antivortex arrays; and for long periods, the system transitions into flux-closure domains, consisting of discrete a-c domains forming closed loops across sharp domain walls (*259*). In this work, we synthesize and analyze superlattices across all three regions of the phase diagram.

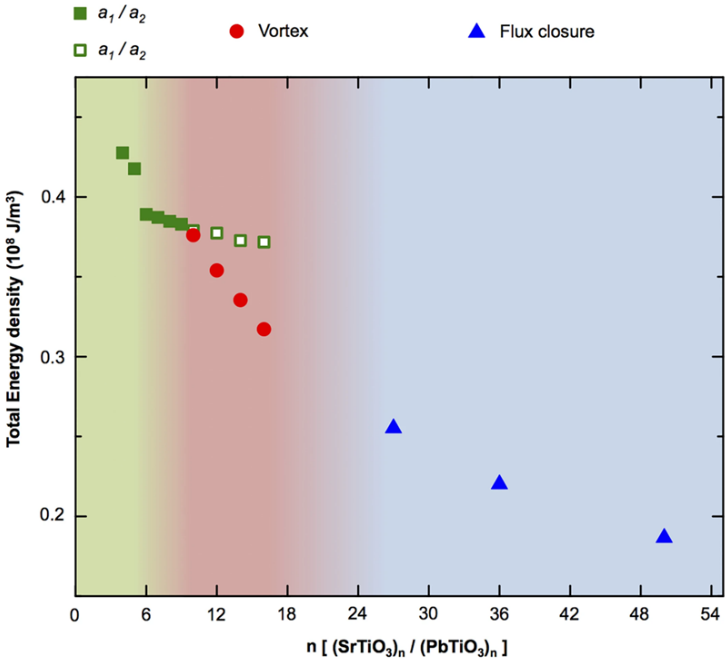

Figure 6.2. Phase-field simulated phase diagram of the equilibrium polar architectures in STO/PTO superlattices grown on DSO substrates, plotted as a function of superlattice periodicity *n* (in unit cells). Three distinct polarization states are stabilized depending on *n*: uniform in-plane polarization (a_1/a_2 domains) at short periodicities, vortex-antivortex coexistence at intermediate periodicities, and flux-closure domains at long periodicities. Reproduced with permission from ref. (*246*). Copyright (2016) Springer Nature.

6.2. RESULTS AND DISCUSSION

6.2.1. Fabrication of the superlattices

In this section, we describe the synthetic procedures followed to fabricate the PTO/STO superlattices. This process involves three main steps: the surface preparation of the substrates prior to deposition, the optimization of growth conditions for both PTO and STO layers on the selected substrates, and the final deposition of the superlattices. This whole process was conducted during a three-month research stay at the University of Wisconsin-Madison, under the supervision of Prof. Chang-Beom Eom.

6.2.1.1. Preparation of the substrates

In the previous chapters, the thin films were directly deposited on as-received commercial substrates. These substrates typically exhibit surfaces with mixed chemical termination –where both A-site and B-site cations of the ABO_3 perovskite structure coexist–, which arises from the intrinsic polarity of many perovskite oxide surfaces. Additionally, the difficulty of precisely cutting single crystals along specific crystallographic orientations, followed by mechanical polishing, often results in surfaces that are neither atomically flat nor chemically homogeneous. These characteristics, however, did not pose significant limitations for the experiments described in Chapters 4 and 5.

In contrast, the superlattices investigated in this chapter require atomically flat, single-terminated surfaces to ensure the formation of sharp interfaces and to stabilize non-trivial polar architectures –i.e., polar vortices and skyrmions. These topological structures are highly sensitive to interfacial quality and electrostatic boundary conditions, both of which are strongly determined by the substrate's surface morphology and chemical termination. For this reason, both STO and DSO substrates were subjected to specific surface treatments before deposition (*260*).

In both cases, the procedure began with ultrasonic cleaning in acetone and isopropanol (10 minutes each) to remove dust and organic residues from the substrate surface. For STO substrates, this was followed by soaking in deionized water for 30 minutes to promote surface hydration, during which SrO-rich regions are converted into $Sr(OH)_2$. After drying with nitrogen, the substrates were immersed in buffered hydrofluoric acid (BHF) –a 6:1 solution of NH_4F:HF– for 30 seconds. This etching step further promotes the formation and subsequent dissolution of $Sr(OH)_2$, thereby facilitating the development of a TiO_2-terminated surface. Following the BHF treatment, the substrates were then rinsed in water, acetone, and isopropanol, and subsequently annealed at 1000 °C for 6 hours under flowing O_2 (*261*). This thermal treatment reconstructs the surface into atomically flat terraces with step heights corresponding to a single unit cell, as confirmed by the AFM topography in **Figure 6.3**a.

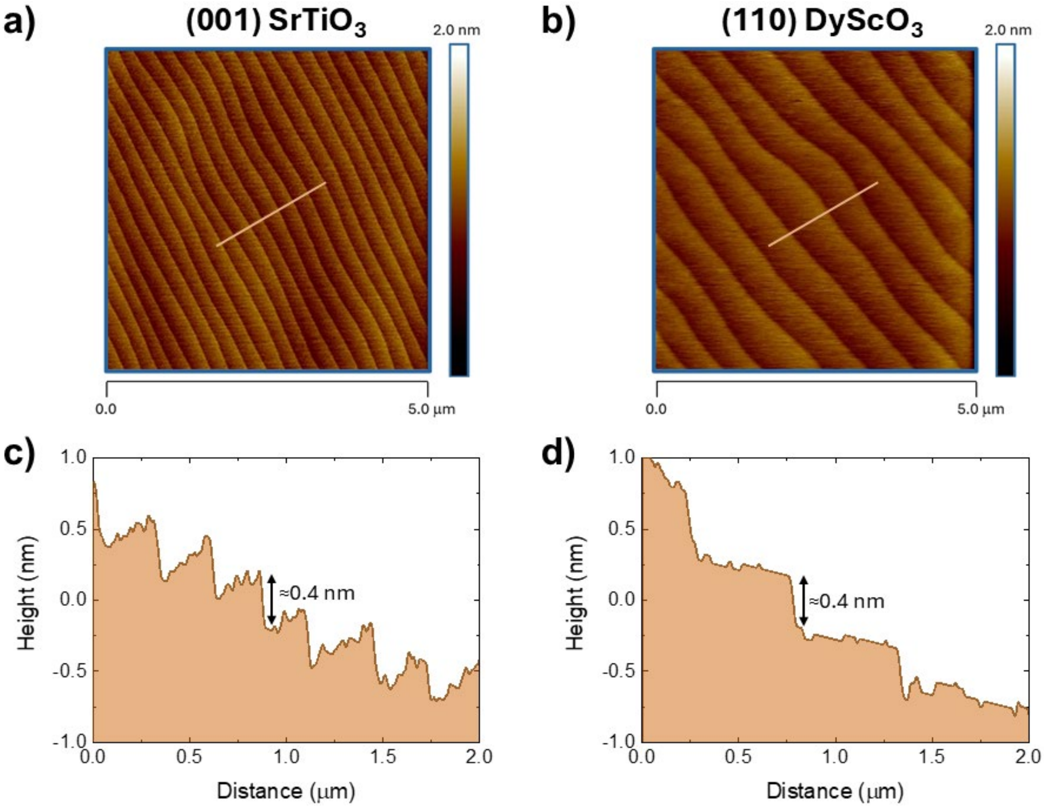

Figure 6.3. a,b) AFM topographies (5 x 5 μm^2) of treated (001) STO and (110) DSO substrates, respectively, revealing atomically flat surfaces with well-defined step-terrace structures. c,d) Corresponding height profiles extracted along the orange lines indicated in the topographic images. In both cases, the terrace step height is approximately 0.4 nm, consistent with the height of a single unit cell: 0.3905 nm for STO and 0.3942 nm for DSO. The latter corresponds to the pseudocubic lattice parameter, as DSO adopts a distorted orthorhombic structure.

Conversely, in the case of DSO, atomically flat surfaces were obtained by thermal annealing alone, without prior etching. Annealing at 1100 ºC for 4 h under flowing O_2 was sufficient to induce surface reconstruction and form well-ordered terraces, predominantly DyO-terminated, as shown in **Figure 6.3**b (*262*).

6.2.1.2. Deposition of the superlattices

Following the surface preparation of the substrates, PTO/STO superlattices were fabricated by RF magnetron sputtering. All superlattices were deposited from ceramic targets of stoichiometric $SrTiO_3$ and $Pb_{1.2}TiO_3$ (with a 20% excess of Pb to compensate for its high volatility during deposition) using a sputtering power of 100 W. A mixed working atmosphere of Ar and O_2 (85%:15% ratio) was employed, maintaining a total pressure of 200 mTorr throughout all depositions.

However, prior to the fabrication of the superlattices, it was necessary to independently optimize the growth conditions for PTO and STO on the selected substrates. A critical parameter in this process was the use of a common growth temperature for both materials per substrate type, which is essential to ensure structurally coherent interfaces and to avoid degradation effects associated with thermal cycling. Additionally, employing a single growth temperature improves process stability and reproducibility. For this purpose, individual PTO and STO thin films were grown on (001) STO and (110) DSO substrates at various temperatures. Note that the (110) orthorhombic orientation of DSO corresponds to the pseudocubic (001) orientation; this pseudocubic notation will be adopted hereafter for clarity.

The structural quality of the resulting thin films was assessed using high-resolution X-ray diffraction, including $\omega/2\theta$ scans and rocking curves, while surface morphology and roughness were examined using AFM. These techniques provided direct feedback for optimizing the deposition conditions of each material and defining the final parameters for superlattice fabrication.

The optimal growth temperature was found to depend on the substrate. On (001) STO substrates, a deposition temperature of 575 °C resulted in high-quality epitaxial films for both materials, as evidenced in **Figure 6.4**a. Under these conditions, the out-of-plane lattice parameter of PTO was measured to 4.153(6) Å, in agreement with previously reported values for c-axis oriented tetragonal PTO thin films grown under similar conditions (*48*). The corresponding (002) reflection of the STO film provided a lattice spacing of 3.91(4) Å, closely matching the bulk value of the substrate. Notably, prominent Laue oscillations are observed around the (002) Bragg reflections of both materials, indicating excellent crystalline coherence. In the PTO film, an additional high-intensity oscillation near ≈45.3 º is observed, which corresponds to a hybrid reflection arising from double diffraction involving both the film and the substrate (*263*, *264*). Such reflections are a well-established signature of atomically sharp and coherent interfaces.

AFM characterization confirmed that the films grown under these conditions exhibit atomically smooth surfaces with step-flow morphology. In both PTO and STO samples, the root-mean-square roughness remained below 0.15 nm, suitable for superlattice fabrication with sharp interfaces. **Figure 6.4**a includes the surface topography of the PTO film only; however, similar terrace structures were observed in the STO films.

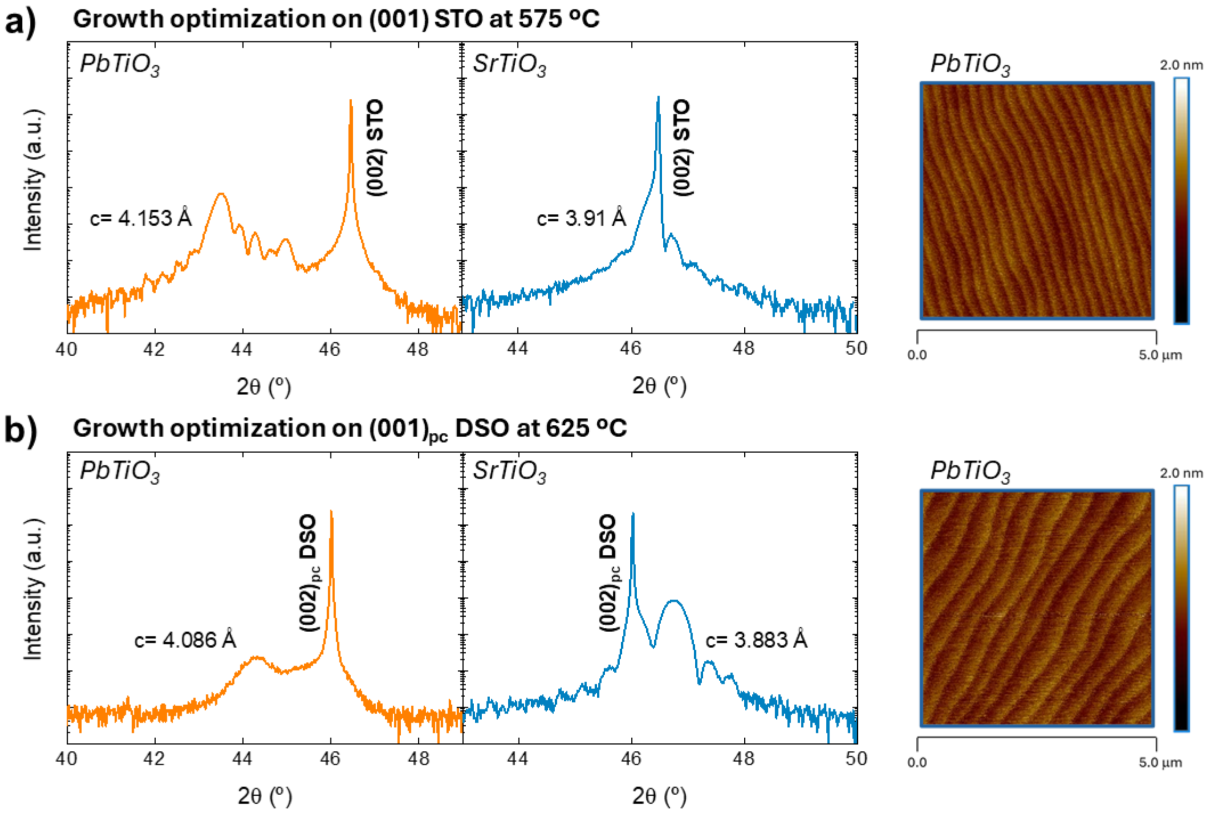

Figure 6.4. Growth optimization of PTO and STO thin films on different substrates. a) XRD ω/2θ scans of 30-nm-thick PTO (orange) and STO (blue) thin films grown on (001) STO substrates at 575 °C, showing well-defined (002) reflections and out-of-plane lattice parameters matching those found in literature. The corresponding AFM topography of the PTO surface (right) reveals atomically flat terraces with step-flow morphology. b) XRD ω/2θ scans of 30-nm-thick PTO (orange) and STO (blue) thin films grown on $(001)_{pc}$ DSO substrates at 625 °C, exhibiting sharp (002) reflections and lattice constants consistent with high crystalline quality. The associated AFM image of the PTO film confirms uniform surface morphology and step-terrace formation.

In contrast, PTO and STO films grown on DSO required a higher temperature of 625 °C to achieve comparable structural quality, as shown in **Figure 6.4**b. Under these conditions, the out-of-plane lattice parameters of PTO and STO were measured to be 4.086(2) and 3.883(5) Å, respectively, in agreement with the values reported in literature (*48*, *265*). Clear Laue oscillations around the (002) Bragg peak of STO once again confirmed the high structural coherence. AFM analysis revealed smooth surfaces in both materials, with roughness values below 0.15 nm and well-developed step-terrace morphology.

To ensure accurate control over the superlattice architecture, the individual growth rates of PTO and STO were calibrated via ex-situ XRR. This calibration enabled precise control of the thickness of each constituent layer, which is crucial for achieving the desired periodicity and maintaining coherence over multiple repetitions. These optimized growth conditions ensured reproducible deposition of high-quality PTO/STO superlattices across different substrate platforms.

Finally, under these optimized conditions, a series of $[(PTO)_n/(STO)_n]_m$ superlattices were fabricated, where *n* represents the layer thickness in unit cells and *m* is the number of bilayer repetitions. These structures, summarized in **Table 6.1**, were designed with different periodicities to promote the formation of different polar structures. Note that, for superlattices grown on (001) STO, the growth always began with an STO layer. However, for superlattices deposited on (001)$_{pc}$ DSO, the first layer was PTO.

Table 6.1. Summary of the PTO/STO superlattices grown for the development of this project, indicating the substrate type, first deposited layer, individual layer thickness (*n*), number of bilayer repetitions (*m*), expected superlattice periodicity (t_{per}), and expected total thickness.

Sample name	Substrate	1st layer	*n* PTO (u.c.)	*n* STO (u.c.)	t_{per} *(nm)*	*m*	*Thickness (nm)*
$[(PTO)_{15}/(STO)_{15}]_{10}$@STO	STO	STO	15	15	11.7	10	117
$[(PTO)_{15}/(STO)_{15}]_{15}$@STO	STO	STO	15	15	11.7	15	175.5
$[(STO)_{4}/(PTO)_{4}]_{40}$@DSO	DSO	PTO	4	4	3.12	40	124.8
$[(STO)_{4}/(PTO)_{4}]_{60}$@DSO	DSO	PTO	4	4	3.12	60	187.2
$[(STO)_{15}/(PTO)_{15}]_{10}$@DSO	DSO	PTO	15	15	11.7	10	117
$[(STO)_{15}/(PTO)_{15}]_{15}$@DSO	DSO	PTO	15	15	11.7	15	175.5
$[(STO)_{25}/(PTO)_{25}]_{6}$@DSO	DSO	PTO	25	25	19.52	6	117.1
$[(STO)_{25}/(PTO)_{25}]_{9}$@DSO	DSO	PTO	25	25	19.52	9	175.7

All the samples listed in **Table 6.1** have been structurally characterized by XRD ($\omega/2\theta$ scans, rocking curves, RSM), XRR, and AFM, among other techniques. The structural analysis of these superlattices and the characterization of their polar architectures, along with the thermal conductivity measurements, are presented in the following sections. Note that we have grown two superlattices with different total thickness for each periodicity, to improve the accuracy of the thermal transport experiments.

6.2.2. Characterization of polar skyrmions and effect on thermal transport

As discussed before, to investigate the influence of polar skyrmions on the thermal transport properties of ferroelectric superlattices, we fabricated $[(PTO)_{15}/(STO)_{15}]_m$ heterostructures on (001) STO substrates. This superlattice periodicity was selected based on previous studies reporting the stabilization of polar skyrmions at room temperature under similar epitaxial conditions (*249*, *254*). Two sets of superlattices were grown, with *m*= 10 and *m*= 15 bilayer repetitions, corresponding to total thicknesses of approximately 117 and 175 nm, respectively.

Figure 6.5 presents the structural characterization of these samples by XRD. The symmetric $\omega/2\theta$ scans (**Figures 6.5**a,b) show multiple superlattice satellite peaks ($SL_{\pm n}$) surrounding the (002) Bragg reflection, confirming the formation of well-defined periodic multilayers with coherent interfaces. The presence of high-order satellites beyond SL_{-4} further indicates long-range structural order. Additionally, Laue oscillations around the SL (002) peak in the *m*= 10 sample (inset of **Figure 6.5**a) suggest the formation of superlattices with high crystallinity and smooth interfaces, while the AFM topography shown in **Figure 6.5**b reveals a smooth, atomically flat surface, consistent with layer-by-layer growth.

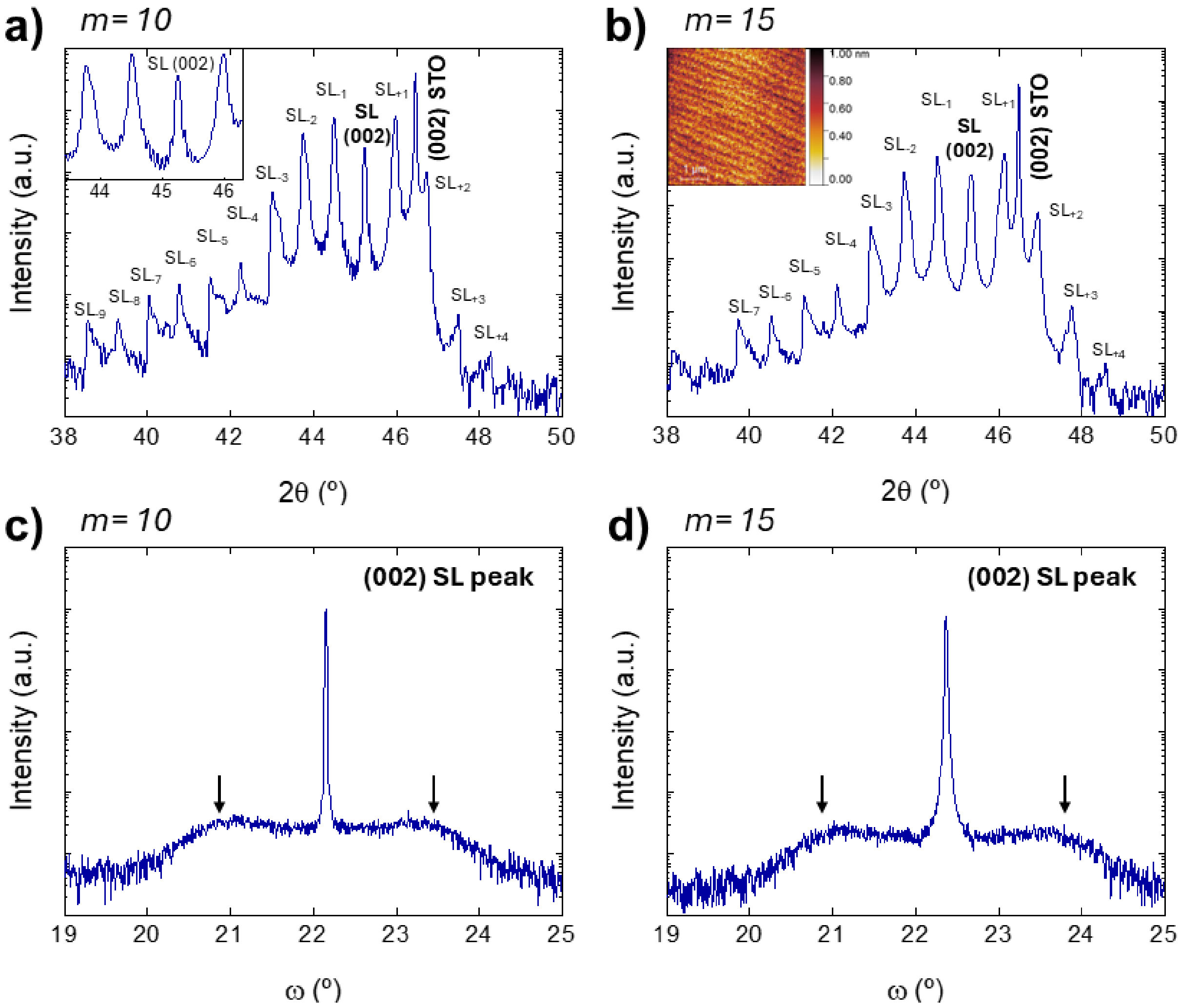

Figure 6.5. X-ray diffraction analysis of $[(PTO)_{15}/(STO)_{15}]_m$ superlattices. a,b) High-resolution ω/2θ scans around the (002) STO reflection for the samples with *m*= 10 (a) and *m*= 15 (b) repetitions, showing well-defined superlattice satellite peaks (denoted as $SL_{\pm n}$), confirming the periodic stacking of PTO and STO layers. The inset in (a) shows a magnified view of the SL (002) region, exhibiting clear Laue oscillations that confirm the high crystallinity of the superlattice. The inset in (b) shows a representative topographic AFM image, evidencing the smooth surface morphology. c,d) Rocking curves (ω scans) centered on the SL (002) Bragg peak, for *m*= 10 and *m*= 15 superlattices, respectively. The narrow FWHM and symmetric shape indicate high crystalline quality and low mosaic spread. The broad diffuse features marked with arrows in both panels suggest the presence of lateral in-plane periodicities, consistent with the presence of polar skyrmions.

The superlattice periodicity (t_{per}) of each sample was determined from the angular separation between adjacent satellite peaks using *Eq. 2.5*, yielding values of 12.84 nm for *m*= 10 and 12.06 nm for *m*= 15 (see Chapter 2, section 2.2.1.2 for details of the calculation). These slightly higher values compared to the nominal bilayer thickness of 11.7 nm (corresponding to 15 unit cells of PTO and 15 of STO), may be attributed to strain-induced expansion at the interfaces, common to superlattices under epitaxial strain (*266*).

The rocking curves (ω scans) recorded around the SL (002) peak (**Figures 6.5**c,d) show sharp, symmetric peaks with FWHM values below 0.025 °, indicating excellent crystalline quality and minimal mosaic spread. Notably, symmetric diffuse side lobes appear on both sides of the central peak (indicated by black arrows), pointing to the presence of in-plane periodic modulations, which are consistent with polarization structures such as lateral arrangements of polar skyrmions. The characteristic in-plane modulation period (d) was determined from the separation of these side peaks in reciprocal space (see *Eq. 2.6*), using *Eq. 6.1* (*267*):

$$d = \frac{2\pi}{\Delta Q_x} \qquad \text{(Eq. 6.1)}$$

The in-plane modulation period was estimated to be approximately 9.10 nm for the m= 10 sample and 8.15 nm for the m= 15 sample. These values fall within the expected periodicity of polar skyrmions previously reported by Das *et al.* (*249*), providing strong evidence for the presence of ordered polar textures in both samples. However, to further investigate these in-plane structural modulations, we acquired reciprocal space maps around the (002) Bragg reflection of the STO substrate (**Figure 6.6**). These measurements provide a two-dimensional view of the diffraction peaks, offering direct insight into periodicity and coherence on both vertical layering and lateral modulations.

As we can observe in the reciprocal space maps (**Figure 6.6**), the superlattice satellite peaks are clearly visible along the out-of-plane direction (Q_z), again confirming the regular stacking and the high-structural quality of the PTO/STO layers. The position of these satellites can be also used to determine the superlattice periodicity (*Eq. 2.11*), yielding in this case periods of 12.93 nm for m= 10 and 12.17 for m= 15 repetitions. These results are in close agreement with those calculated from the ω/2θ scans, with minor differences attributed to the uncertainty in determining the satellite peak positions.

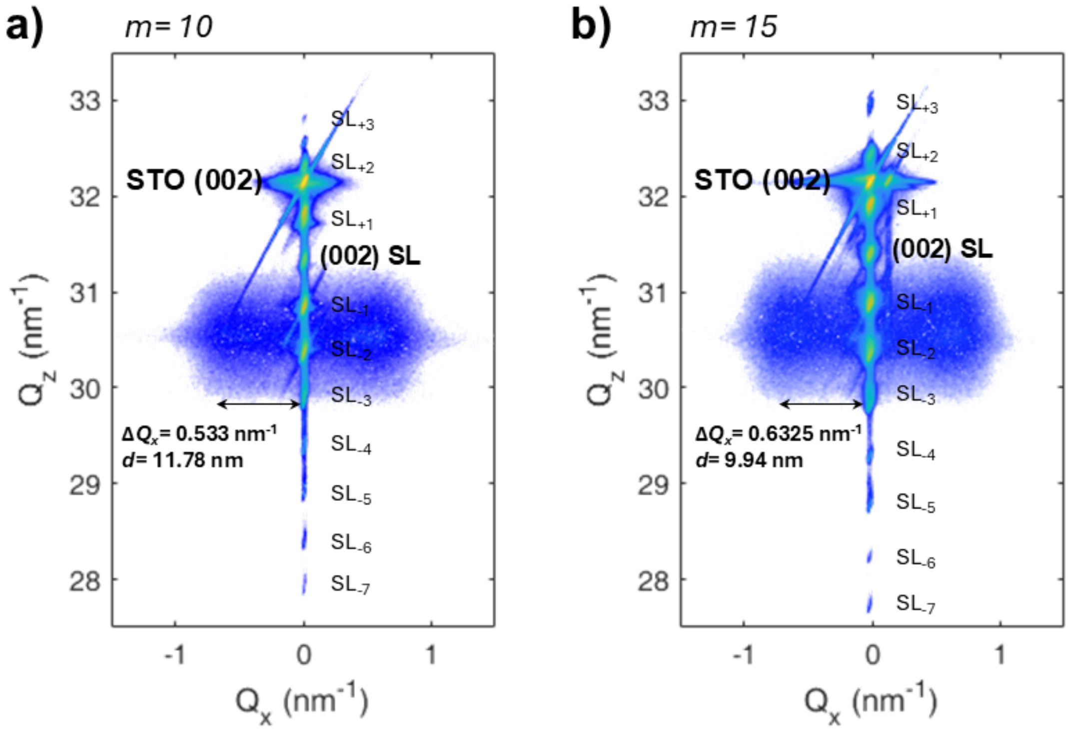

Figure 6.6. Reciprocal space maps around the (002) reflection of the STO substrate for $[(PTO)_{15}/(STO)_{15}]_m$ superlattices with m= 10 (a) and m= 15 (b) repetitions. The vertical satellites ($SL_{\pm n}$) along the out-of-plane direction (Q_z) confirm the presence of a well-defined superlattice structure in both samples. In addition, diffuse satellite signals along the in-plane direction (Q_x) reveal the presence of periodic modulations of the polarization, consistent with the formation of polar skyrmions. From the in-plane wavevector (ΔQ_x), the lateral periodicity of the skyrmion lattice is extracted as d= 11.78 nm for the m= 10 sample, and d= 9.94 nm for the m= 15 sample.

More importantly, both maps also reveal pronounced diffuse features extending along the in-plane direction (Q_x), with shape, intensity and spacing similar to those reported by Das and collaborators (*249*). These side lobes arise from periodic in-plane modulations of lattice parameter –induced by the strain field generated from the curling polarization in the skyrmions– and are consistent with the signals observed in the rocking curves (**Figures 6.5**c,d). These results reinforce the interpretation that both samples host non-trivial polar textures with long-range in-plane periodicity.

From the in-plane spacing between these signals (ΔQ_x), the corresponding real-space periodicities (d) can be determined using *Eq. 6.1*. The estimated values are 11.78 nm for m= 10 and 9.94 nm for m= 15, closely matching those obtained from the rocking curve analysis. Small deviations between both methods are expected due to the difficulty in accurately locating the position of the maxima. Notably, both experimental methods consistently show that the in-plane modulation period is smaller in the thicker sample. This reduction with increasing total thickness may indicate a trend toward denser lateral topological textures, although a direct, systematic correlation between skyrmion lattice spacing and total thickness has yet to be firmly established.

The presence of polar skyrmions was further investigated by high-resolution STEM. **Figure 6.7** shows the cross-sectional HAADF-STEM images of the superlattice with m= 15 repetitions. The low-magnification image (**Figure 6.7**a) reveals a highly ordered multilayer structure with atomically sharp interfaces, consistent with the intended periodic stacking of 15 unit cells of PTO and STO ($t_{per} \approx$12 nm). The strong contrast modulation between the alternating layers (with the PTO slabs appearing brighter due to the higher atomic number of Pb) confirms the compositional periodicity and supports the structural coherence inferred from XRD measurements.

Notably, at higher magnification (**Figure 6.7**b) additional nanoscale features emerge within the PTO layers. In particular, dark, circular contrasts are periodically distributed across the lateral direction, embedded within the brighter PTO layers. These features resemble the projected morphology of polar skyrmions, which are known to form bubble-like modulations in polarization that can alter the local scattering intensity. In particular, similar contrast signatures have been reported in cross-sectional STEM studies of skyrmion-hosting PTO/STO superlattices (*249*).

However, this initial interpretation is challenged by the polar displacement map shown in **Figure 6.7**c. This map was reconstructed from the relative atomic positions of Ti cations in both PTO and STO layers, with arrows indicating the direction and magnitude of the polarization vector. As expected for a paraelectric, the STO layers show weak, spatially uncorrelated displacements. In contrast, the PTO layers exhibit large and laterally modulated polar displacements that seem to follow a sinusoidal pattern across the in-plane direction.

This periodic lateral polarization is more consistent with the formation of dipole waves (DWs) rather than a skyrmion lattice. Supporting this interpretation, the lateral periodicity measured from reciprocal space maps (**Figure 6.6**b) is approximately 10 nm, corresponding to two adjacent contrast features in the HAADF-STEM image, as indicated in the inset of **Figure 6.7**b. In the case of polar skyrmions, the characteristic unit cell would span a single contrast feature (≈5 nm), reflecting the radial symmetry of their topological core. Therefore, the combination of HAADF contrast and polarization mapping indicates that the observed features are more accurately described as dipole waves.

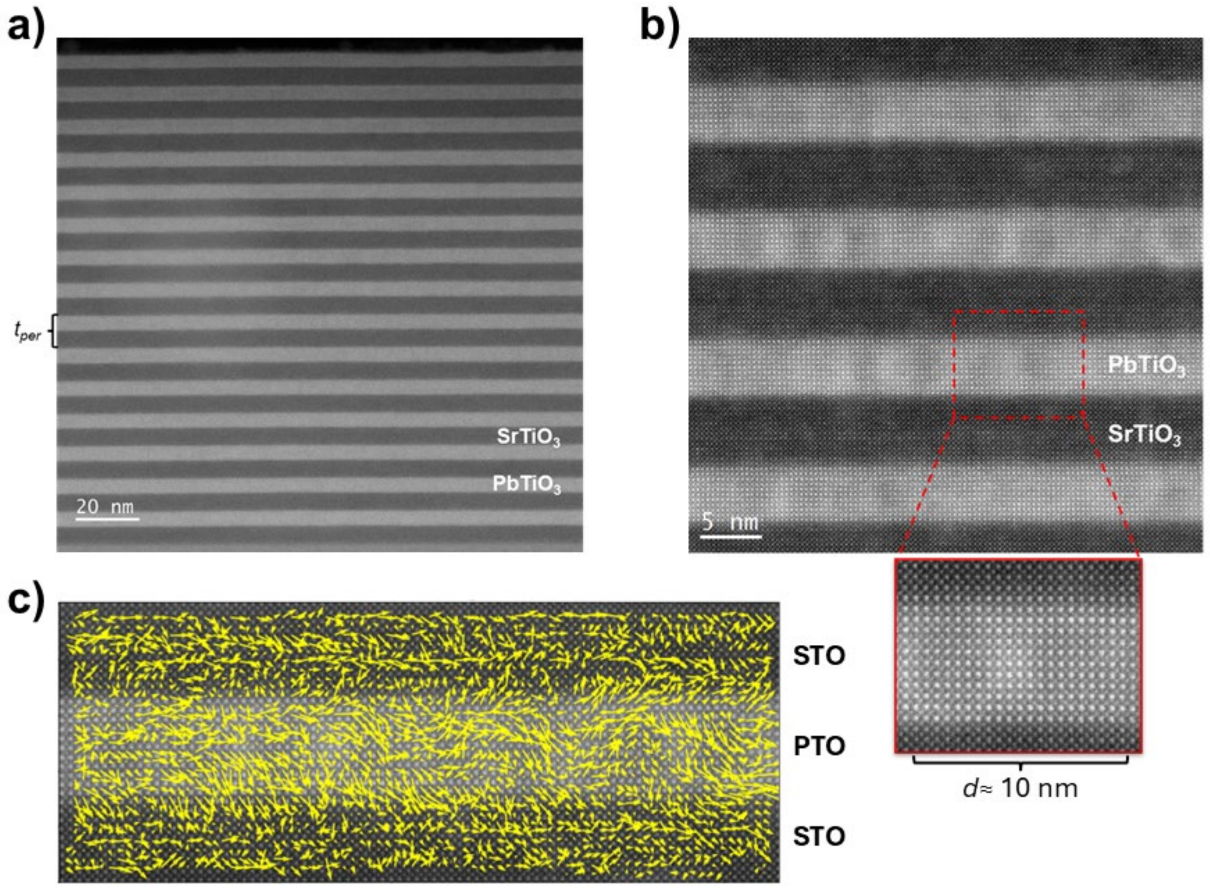

Figure 6.7. Structural characterization of the [(PTO)$_{15}$/(STO)$_{15}$]$_{15}$ superlattice by HAADF-STEM. a) Low-magnification cross-sectional image, showing well-defined periodic stacking of PTO (bright, as Pb presents higher atomic number than Sr) and STO (dark) layers, with a superlattice periodicity t_{per} of approximately 12 nm. b) High-magnification image acquired from the same region of the superlattice. Within the PTO layers, dark, nanoscale circular contrast features are observed, regularly spaced along the in-plane direction, and initially consistent with polar skyrmions. The inset provides a magnified view of a representative modulation unit ($d \approx 10$ nm, as derived from **Fig. 6.6**). c) Polar displacement map obtained from Ti cation shifts, revealing large, laterally modulated polarization in the PTO layers forming a sinusoidal pattern, more consistent with dipole waves than discrete skyrmions. The STEM images shown in (a,b) were recorded at CCiTUB (Scientific and Technological Centers of the University of Barcelona) in the framework of an ELECMI grant. The polar displacement map shown in (c) was calculated by Dr. Marcel S. Claro.

To understand how these polar architectures affect thermal transport, we performed thermal conductivity measurements using FDTR. **Figure 6.8**a shows the room-temperature thermal conductivity of the [(PTO)$_{15}$/(STO)$_{15}$]$_m$ superlattices studied in this work, along with thermal conductivity data of superlattices with similar interface density (i.e., number of interfaces per total thickness) extracted from refs. (*59*, *60*). Specifically, we include $SrTiO_3$/$CaTiO_3$ (STO/CTO, red squares), $SrTiO_3$/$BaTiO_3$ (STO/BTO, green squares) and $LaCoO_3$/$SrTiO_3$ (LCO/STO, blue square) superlattices, which span from slightly lower to slightly higher interface densities relative to our samples.

As we can observe, the PTO/STO superlattices exhibit significantly lower thermal conductivity than the STO/CTO, STO/BTO and LCO/STO superlattices, despite their structural similarity and comparable interface densities. According to the authors (*59*, *60*), these samples operate within the incoherent phonon transport regime, where thermal transport is mostly governed by particle-like phonons undergoing diffuse scattering at each interface. In this regime, thermal conductivity is primarily governed by the density and quality of the interfaces, and is expected to decrease monotonically with increasing interface density due to enhanced phonon-boundary scattering.

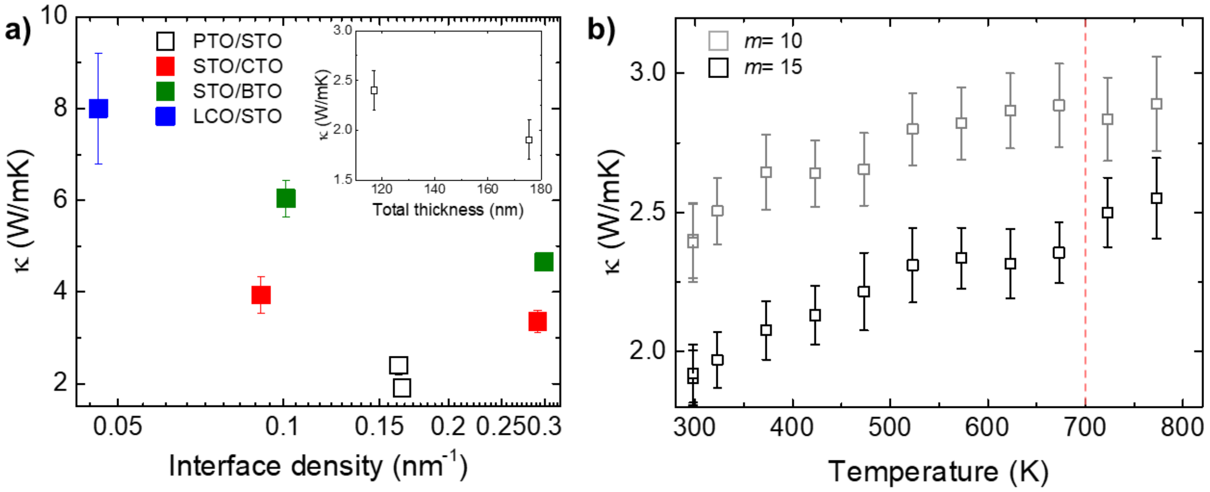

Figure 6.8. a) Room-temperature thermal conductivity of the PTO/STO superlattices with *m*= 10, 15 (black open squares), plotted as a function of interface density. For comparison, literature data for $SrTiO_3/CaTiO_3$ (red squares), $SrTiO_3/BaTiO_3$ (green squares) and $LaCoO_3/SrTiO_3$ (blue square) superlattices with similar interface densities are included (data extracted from refs. (*59*, *60*)). The inset shows the thermal conductivity of the PTO/STO superlattices studied in this work as a function of the total thickness, illustrating a clear reduction in κ with increasing the number of bilayer repetitions. b) Temperature-dependent thermal conductivity of the PTO/STO superlattices with *m*= 10 (grey) and *m*= 15 (black) repetitions. The dashed red line marks the temperature at which polar skyrmions have been reported to destabilize in similar systems.

However, the remarkably low thermal conductivity observed in our PTO/STO superlattices clearly deviate from this trend. Most notably, we observed that the thermal conductivity of the superlattices decreases with the number of bilayer repetitions (i.e., with the total thickness of the superlattice; see inset in **Figure 6.8**a), despite the interface density remaining essentially constant. This behavior is not consistent with a scenario of diffusive scattering at the interfaces, as the thermal conductivity should remain approximately constant with the superlattice thickness when the interface density is maintained.

On the other hand, there is always a remaining fraction of long-wavelength phonons that propagate coherently across the whole superlattice (*59*). In this case, random disorder at the interfaces introduces fluctuations in the lattice potential, which may induce a mobility edge and phonon localization by a similar mechanism as the Anderson localization of electrons (*268*). Although this behavior was previously observed in semiconductor superlattices with intentionally introduced random disorder at the interfaces (*269*), there are important differences with our superlattices, like the much smaller mean free path and the lack of any evident source of disorder.

For that reason, we hypothesize that the increased density of lateral polarization modulations in the thicker sample, as well as possible fluctuations in their arrangement across adjacent PTO layers or the induction of polarization in the STO layers (close to the interfaces) could be the origin of this anomalous behavior.

If these mechanisms –polarization-enhanced phonon scattering and phonon localization– play a significant role in thermal transport, one would expect the thermal conductivity to be sensitive to the presence and stability of these polar textures. Das *et al.* (*254*) previously reported that polar skyrmions in PTO/STO superlattices are thermally unstable, disappearing around ≈700 K. Although our STEM analysis revealed that the observed polarization organization more closely resembles DW patterns rather than discrete skyrmions, we performed temperature-dependent thermal conductivity measurements in our superlattices (**Figure 6.8**b) to investigate potential correlations between thermal transport and the stability of the polar architectures. For that, we used an Instec thermal stage equipped with a liquid nitrogen pump and a temperature controller.

As we can observe in the figure, the lower thermal conductivity in the superlattice with *m*= 15 is maintained across all the temperature range, reaffirming the suppressive effect of increased thickness (and possibly higher DWs density) on phonon transport. Additionally, both samples show subtly different thermal responses with temperature. The *m*= 10 superlattice follows the expected trend for nanostructures, with the thermal conductivity increasing with temperature until saturation due to the reduced thickness of the system. On the other hand, the *m*= 15 superlattice shows a modest increase in thermal conductivity after 700 K, which is the temperature at which skyrmions are reported to become unstable (marked with a dashed red line in the figure). Although this change is relatively small and may fall within experimental uncertainty, it might suggest the onset of polarization disintegration, leading to the partial recovery of propagating phonon modes previously suppressed by the lateral polarization lattice. Importantly, the thermal conductivity changes observed in both samples are reversible upon temperature cycling, indicating that the underlying polar texture and lattice structure remain stable throughout the measurements.

To directly assess the thermal stability of the polar textures in our samples, we also acquired temperature-dependent reciprocal space maps around the STO (-103) reflection for the *m*= 15 sample (**Figure 6.9**a). These measurements were carried out by Dr. José Santiso at Catalan Institute of Nanoscience and Nanotechnology (ICN2, Barcelona), who contributed to the structural investigation of the polarization architectures through temperature-dependent XRD and STEM imaging.

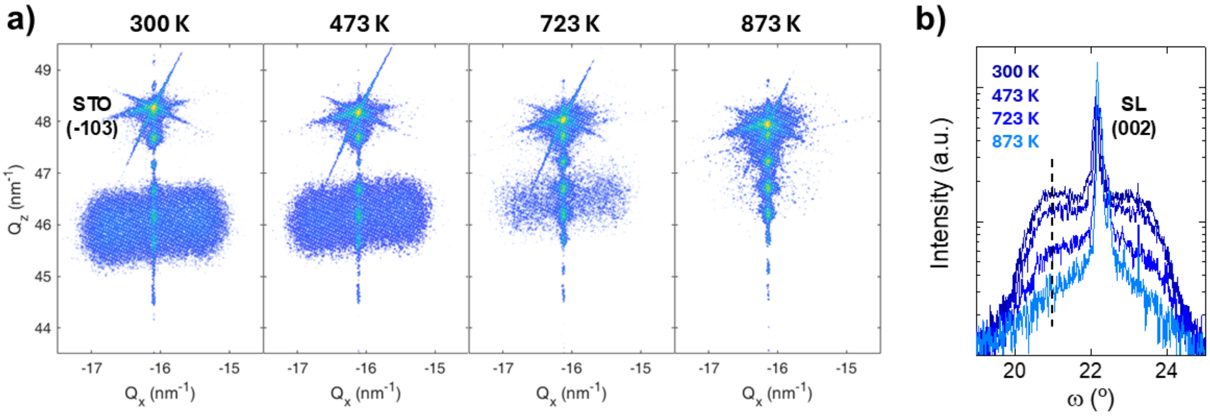

Figure 6.9. Thermal evolution of lateral polar modulations in the $[(PTO)_{15}/(STO)_{15}]_{15}$ superlattice. a) Reciprocal space maps around the STO (-103) reflection acquired at different temperatures. Pronounced side lobes along the Q_x direction are clearly visible up to 723 K, indicating the persistence of lateral periodic modulations. These features vanish at 873 K, suggesting the thermal destabilization of the polar lattice. b) Rocking curves around the SL (002) reflection at different temperatures, exhibiting a gradual attenuation of the lateral signals with increasing temperature. Complete suppression is observed at 873 K, matching the results shown in (a). These experiments were performed by Dr. José Santiso at Catalan Institute of Nanoscience and Nanotechnology (ICN2, Barcelona).

As observed in **Figure 6.9**a, the superlattice remains epitaxially matched to the substrate across all the temperature range, as evidenced by the Q_x alignment of the SL and substrate peaks. Furthermore, in agreement with the rocking curve analysis shown in **Figure 6.9**b, the characteristic side lobes initially attributed to polar skyrmions persist –with reduced intensity– up to 723 K; these features are fully suppressed only at 873 K, suggesting the complete destabilization of the lateral polar order at this elevated temperature. The deviation from the ≈700 K transition temperature reported in the literature could stem from the higher thermal stability of DW patterns or from incomplete thermal equilibration of the sample during RSM acquisition. Similar thermalization issues could also affect thermal conductivity experiments, potentially complicating the interpretation of thermal conductivity data at elevated temperatures. Unfortunately, due to operating constraints of our experimental setup, FDTR measurements cannot be performed above 800 K, which limits our ability to fully resolve the high-temperature behavior of these polar textures.

Moreover, in addition to the temperature-dependent thermal conductivity experiments discussed earlier, we also studied the stability of the polar architectures under electric fields. This investigation was motivated by previous reports by Das *et al.* (*254*) , which demonstrated that the application of electric fields of the order of ≈1500 kV/cm could destabilize and erase polar skyrmions in analogous superlattices. To explore this possibility, we fabricated a $[(PTO)_{15}/(STO)_{15}]_{15}$ superlattice on (001) STO, incorporating an intermediate 5-nm-thick $SrRuO_3$ layer to serve as bottom electrode. The top electrode consisted of an aluminum mask.

Thermal conductivity measurements were conducted under both positive and negative bias voltages, ranging from -125 V to +100 V. These values correspond to nominal electric fields of approximately -7143 kV/cm and +5714 kV/cm, respectively, assuming a uniform field across the total film thickness. As shown in **Figure 6.10**a, a slight increase in thermal conductivity was observed under both polarities. However, the current–voltage curve presented in **Figure 6.10**b revealed significant leakage currents (in the milliampere range), which likely prevented the establishment of sufficiently high internal electric fields to effectively modulate the polar architectures. Therefore, we attribute the observed changes in thermal conductivity to Joule heating during voltage application. This interpretation is further supported by the rocking curves shown in **Figure 6.10**c, where the intensity of the side lobes (corresponding to the in-plane modulations of polarization) remains unchanged under the applied bias. It is worth noting that thermal destabilization of the DW structures requires temperatures of up to 873 K (see **Figure 6.9**), far exceeding those that could plausibly be reached through electric-field-induced heating in our experimental configuration.

In summary, our combined structural and thermal analyses provide strong evidence for the presence of DW patterns in $[(PTO)_{15}/(STO)_{15}]_m$ superlattices, and suggest their potential role in suppressing thermal conductivity beyond conventional interface scattering mechanisms. However, key uncertainties persist. The precise spatial organization of the polar structures, their evolution with temperature, and the underlying mechanisms by which they interact with phonons are not yet fully understood. Furthermore, while temperature-dependent measurements hint at the potential of these systems for use in thermally tunable thermal switches, the modest thermal response observed here calls for deeper investigation. These limitations underscore the need for complementary characterization techniques, such as in-situ STEM at elevated temperatures, to directly track the evolution of polar topology and establish a definitive link between topological order and thermal transport in ferroic superlattices.

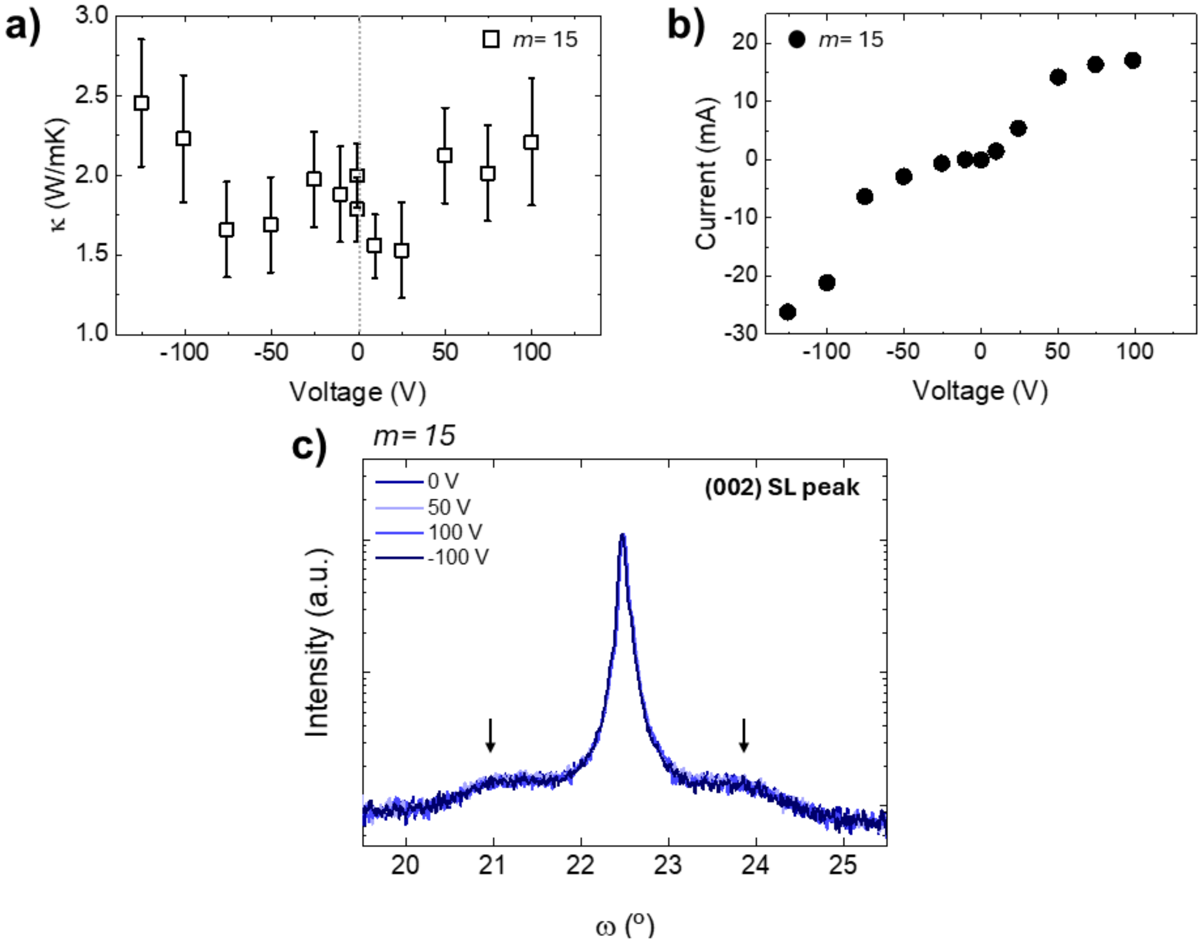

Figure 6.10. Influence of electric-field application on the thermal conductivity and polar configurations of the $[(PTO)_{15}/(STO)_{15}]_{15}$ superlattice. a) Room-temperature thermal conductivity under different applied voltages, using Al and $SrRuO_3$ as top and bottom electrodes, respectively. A modest increase in κ is observed for both positive and negative bias. b) Current-voltage curve showing significant leakage currents in the milliampere range, which prevent the formation of high internal electric fields. c) Rocking curves around the (002) SL reflection for different applied voltages. The intensity and position of the side lobes (indicated by arrows), associated with lateral polarization modulations, remain unchanged upon bias application.

6.2.3. Characterization of polar vortices and effect on thermal transport

In this section, we investigate the emergence of polar vortices and their influence on thermal transport in $[(STO)_n/(PTO)_n]_m$ superlattices epitaxially grown on $(001)_{pc}$ DSO substrates. As previously reported by Yadav *et al.* (*246*), these superlattices exhibit different polar structures depending on the superlattice periodicity *n* (see **Figure 6.2**). To systematically probe each regime of the reported phase diagram, we fabricated superlattices with three representative periodicities: *n*= 4, 15 and 25 u.c., which respectively stabilize a_1/a_2 domains, coexistence of these striped domains with polar vortices, and flux-closure configurations, respectively. For each periodicity, two different values of the repetition number *m* were chosen to yield total film thicknesses near ≈117 and ≈175 nm. A complete list of the samples synthesized for this project is provided in **Table 6.1**.

We begin our analysis with the samples exhibiting conventional polar topologies, namely the a_1/a_2 domain configuration (*n*= 4) and the flux-closure state (*n*= 25), before turning to the more complex mixed vortex regime. **Figure 6.11** presents the XRD characterization of $[(STO)_4/(PTO)_4]_{60}$ (panels a,c) and $[(STO)_{25}/(PTO)_{25}]_9$ (panels b,d) superlattices, both corresponding to a total thickness of ≈175 nm. Additional samples with fewer repetitions, specifically *m*= 40 (for *n*= 4) and *m*= 6 (for *n*= 25), were also synthesized and characterized. However, due to the similarity of their structural features to those of the thicker films, their data are omitted here for conciseness.

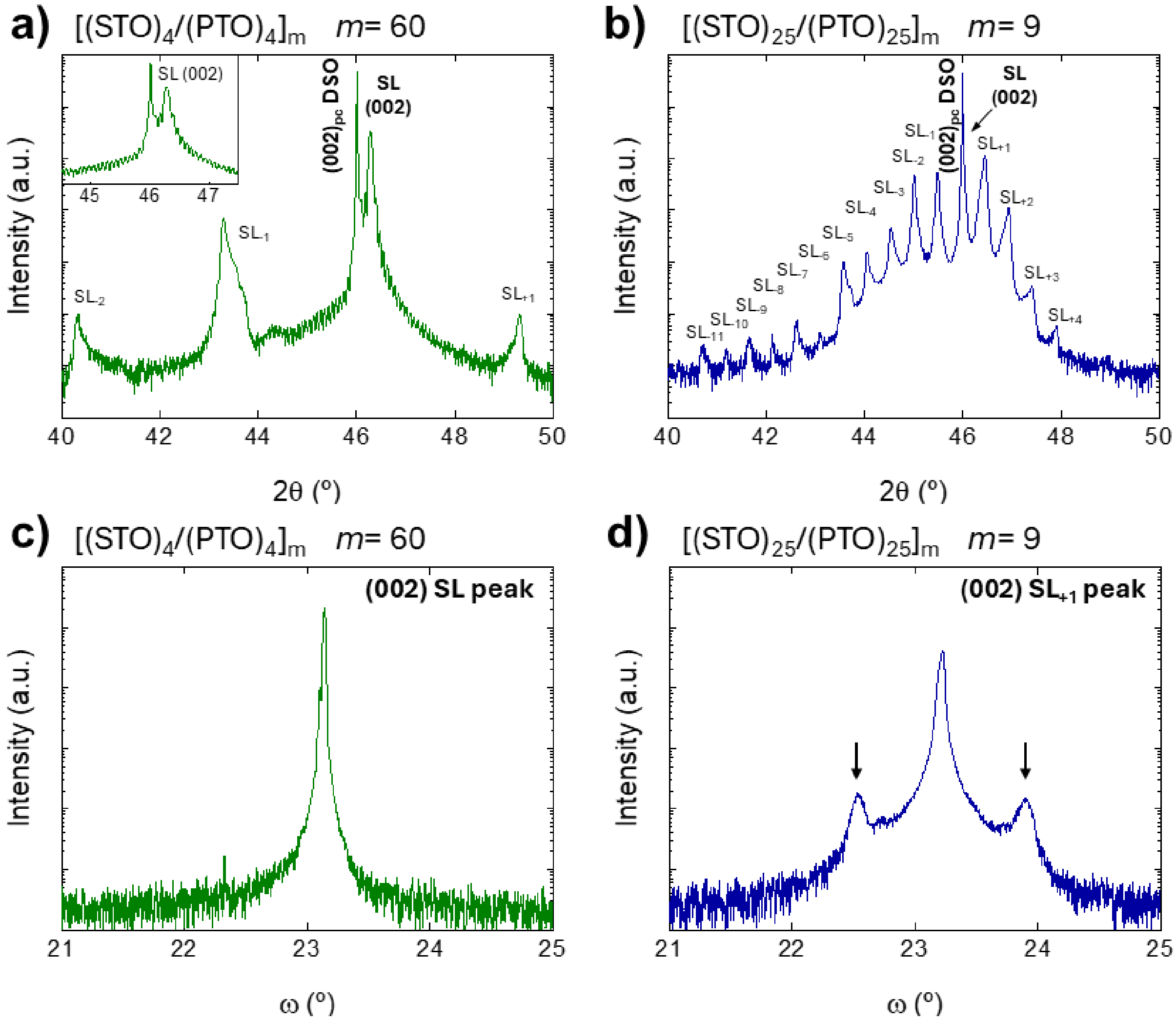

Figure 6.11. X-ray diffraction analysis of $[(STO)_4/(PTO)_4]_{60}$ (a,c) and $[(STO)_{25}/(PTO)_{25}]_9$ (b,d) superlattices grown on $(001)_{pc}$ DSO substrates. a) High-resolution ω/2θ scan of the $[(STO)_4/(PTO)_4]_{60}$ superlattice, showing sharp and well-defined satellite peaks around the (002) reflection, indicating high structural coherence and precise bilayer periodicity. The inset shows a magnified view of the SL (002) region, exhibiting clear Laue oscillations that confirm uniform thickness and interface sharpness. b) High-resolution ω/2θ scan of the $[(STO)_{25}/(PTO)_{25}]_9$ superlattice, revealing a dense series of higher-order satellite peaks (up to SL_{-11}) consistent with long bilayer periodicity and high crystallinity. c) Rocking curve centered on the SL (002) peak for the *n*= 4 sample, exhibiting a narrow FWHM, indicative of low mosaic spread and excellent crystalline quality. d) Rocking curve around the SL_{+1} satellite peak for the *n*= 25 superlattice, showing moderate broadening and a clear splitting of the peak (indicated by black arrows), suggesting in-plane domain variants or structural modulations associated with flux-closure domain formation.

Figure 6.11a shows the symmetric ω/2θ scan of the $[(STO)_4/(PTO)_4]_{60}$ superlattice. Clear and well-defined superlattice satellite peaks ($SL_{\pm1}$, SL_{-2}) are observed around the (002) reflection, indicating high structural coherence and precise control over bilayer periodicity. Moreover, the presence of Laue oscillations (see inset in **Figure 6.11**a) further confirms interface sharpness and excellent crystalline quality throughout the film. From the angular position of the satellite peaks, we extract an experimental superlattice periodicity of 3.24 nm, in good agreement with the designed bilayer periodicity of 3.12 nm (corresponding to 4/4 u.c. stacking). The position of the (002) reflection corresponds to an average out-of-plane lattice parameter of c= 3.919(3) Å, consistent with reported values for strained STO/PTO heterostructures stabilizing a_1/a_2 domain configurations (*253*).

The corresponding rocking curve around the superlattice (002) reflection, shown in **Figure 6.11**c, exhibits a sharp and symmetric peak with FWHM <0.025 º, indicative of excellent crystalline quality and minimal mosaic spread. No additional signals are observed in the scan, consistent with the stabilization of a conventional a_1/a_2 domain pattern, in which the tetragonal PTO layers adopt fully in-plane polarization under the influence of epitaxial strain imposed by the DSO substrate.

In contrast, the ω/2θ scan of the $[(STO)_{25}/(PTO)_{25}]_9$ superlattice, presented in **Figure 6.11**b, reveals a longer series of satellite peaks –extending beyond $SL_{\pm4}$–, confirming high structural coherence over large bilayer thicknesses. From the satellite spacing, a periodicity of t_{per}= 19.86 nm is obtained, closely matching the intended value of 19.52 nm. Notably, the main SL peak appears at a slightly lower angle compared to the *n*= 4 case, indicating an increased out-of-plane lattice parameter of c= 3.94(5) Å, approximately equal to that of the substrate. This expansion likely originates from the formation of flux-closure domains, which involve curling polarization vectors –separated by individual domain walls– that minimize depolarizing fields at the expense of local lattice distortions. These nonuniform polar textures may result in a net expansion of the c-axis lattice parameter when averaged over the superlattice volume.

The rocking curve of the first-order SL_{+1} peak (**Figure 6.11**d) exhibits moderate broadening relative to the *n*= 4 case, with a FWHM of 0.04 º. Although this value still corresponds to a high-quality superlattice, the increased broadening likely reflects structural inhomogeneity associated with complex domain arrangements. Additionally, the rocking curve shows a distinct splitting of the peak into two components (indicated by black arrows), absent in the *n*= 4 sample. This splitting suggests the presence of in-plane domain variants or periodic structural modulations across the superlattice thickness, consistent with the topology of flux-closure domains. From the reciprocal space separation of these components, the characteristic modulation period was calculated using *Eq. 6.1*, yielding *d*= 16.21 nm.

To gain further insight into the structure of the superlattices, reciprocal space maps around the $(002)_{pc}$ reflection of the DSO substrate were recorded (**Figure 6.12**). These measurements provide complementary information to ω/2θ scans and rocking curves, particularly regarding the presence of lateral modulations of the lattice. The reciprocal space map of the *n*= 4 superlattice (**Figure 6.12**a) reveals the presence of vertical superlattice satellites aligned along Q_z, further confirming excellent interface coherence and out-of-plane periodicity. The satellite spacing corresponds to a superlattice periodicity of 3.31 nm, closely matching the one obtained from ω/2θ scans (t_{per}= 3.24 nm). Moreover, the absence of lateral broadening or peak splitting along Q_x indicates that no detectable in-plane structural modulation is present. This observation supports the stabilization of a ferroelastic a_1/a_2 structure in which the polarization is confined in-plane, lacking out-of-plane components capable of modulating lattice along the growth direction.

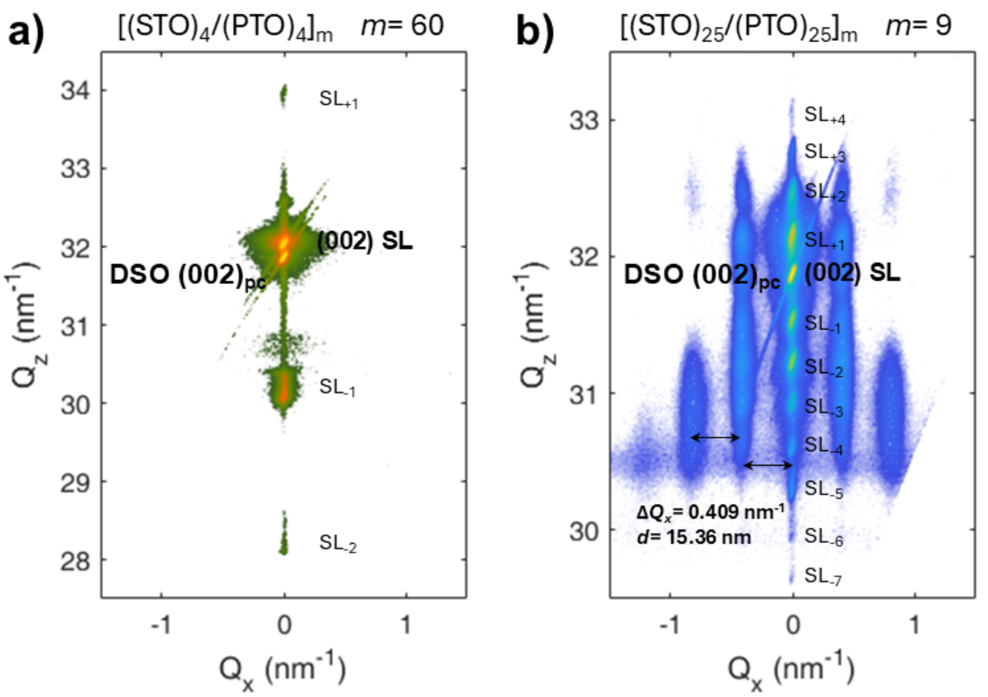

Figure 6.12. Reciprocal space maps around the $(002)_{pc}$ reflection of the DSO substrate for $[(STO)_4/(PTO)_4]_{60}$ (a) and $[(STO)_{25}/(PTO)_{25}]_9$ (b) superlattices. a) For n= 4, symmetric SL satellites are observed along Q_z, indicating an out-of-plane periodicity of t_{per}= 3.31 nm. b) For n= 25, apart from the out-of-plane superlattice periodicity (t_{per}= 20.33 nm), additional lateral satellite peaks appear at finite Q_x, revealing in-plane structural modulation with a periodicity of $d\approx$ 15.36 nm, consistent with the emergence of flux-closure domains

Conversely, the reciprocal space map of the n= 25 superlattice (**Figure 6.12**b) reveals a more complex pattern. As in the short-period superlattice, clear satellite peaks appear along the Q_z direction, indicating a well-defined and vertically modulated structure with a superlattice periodicity of t_{per}= 20.33 nm. However, in this case, additional satellite peaks are observed along the Q_x direction, equally-spaced with $\Delta Q_x\approx$ 0.409 nm^{-1}, corresponding to a real-space modulation period of $d\approx$ 15.36 nm. The simultaneous presence of vertical and lateral satellite features indicates that the superlattice exhibits structural modulations in both the out-of-plane and in-plane directions. The emergence of lateral satellites is consistent with the formation of periodic flux-closure domains, which introduce localized out-of-plane polarization components near domain closure regions, thereby modulating the lattice along the growth direction with an in-plane periodicity. This interpretation aligns with the splitting of XRD peaks previously observed in **Figure 6.11**d and supports the presence of in-plane domain variants.

To fully characterize the polarization structure of these samples and validate the interpretations derived from RSM, L-PFM measurements were conducted during a one-week research stay at the Autonomous University of Barcelona under the supervision of Prof. Jordi Sort and Dr. Eric Langenberg. In this type of PFM, the torsional oscillations of the cantilever are monitored to detect the piezoelectric response generated by in-plane polarization vectors oriented perpendicular to the cantilever axis, allowing the spatial mapping of ferroelectric domains with lateral polarization components. To enhance sensitivity and minimize imaging artifacts, measurements were performed using the Dual AC Resonance Tracking (DART) mode, which improves signal stability and sensitivity by continuously tracking the contact resonance frequency of the cantilever, enabling more accurate detection of weak piezoresponse signals.

The results of the DART L-PFM imaging for both superlattices are shown in **Figure 6.13**. For the short-period (*n*= 4) sample (**Figure 6.13**a), both the amplitude and phase maps reveal a clear stripe pattern with alternating contrast bands. This periodic contrast is consistent with the presence of ferroelastic a_1/a_2 domains, which involve 90 º in-plane polarization switching between orthogonal directions, typically $[100]_{pc}$ and $[010]_{pc}$ (*270*). The domain walls appear straight and uniformly spaced, with a characteristic domain periodicity of ≈100-120 nm. Moreover, no significant response was observed in V-PFM measurements, which are sensitive to out-of-plane polarization components. This absence of signal supports the interpretation that the polarization lies entirely in-plane, as expected for a_1/a_2 configurations stabilized by epitaxial strain on $(001)_{pc}$-oriented DSO substrates.

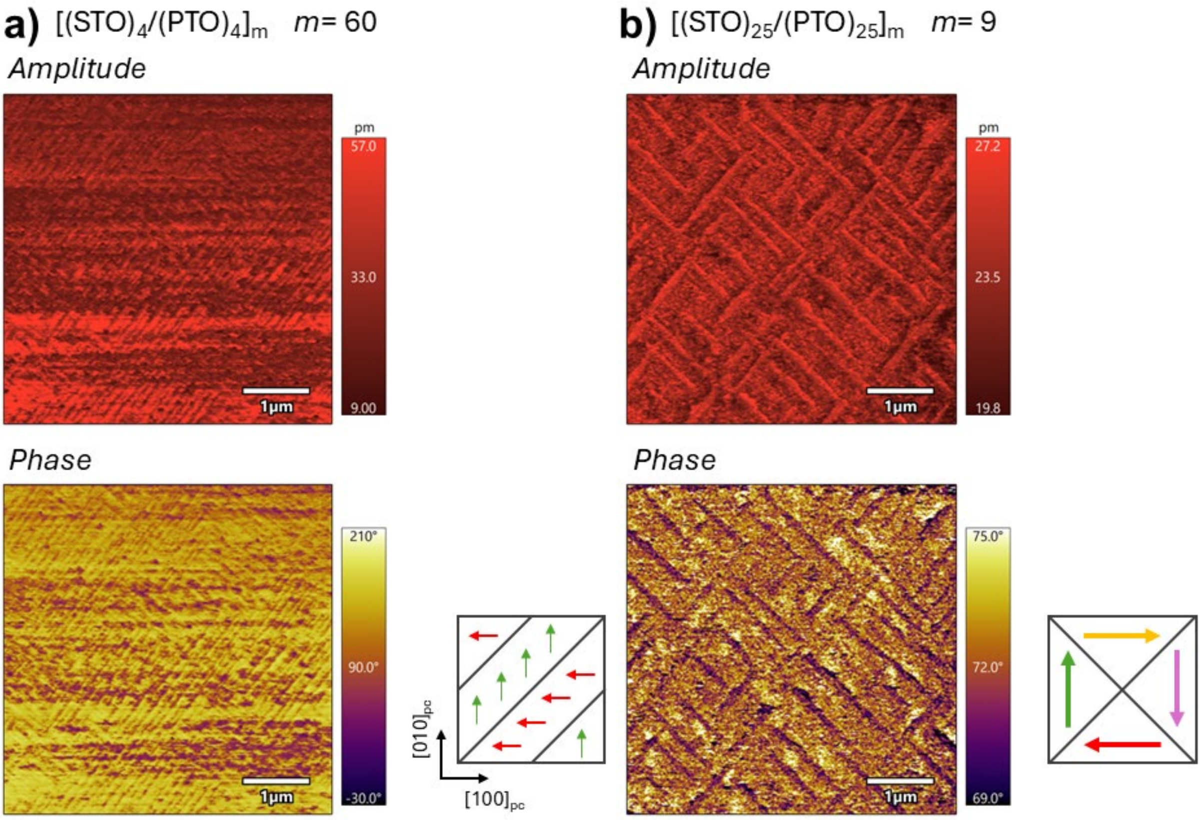

Figure 6.13. DART lateral-PFM amplitude and phase images of $[(STO)_4/(PTO)_4]_{60}$ (a) and $[(STO)_{25}/(PTO)_{25}]_9$ (b) superlattices epitaxially grown on $(001)_{pc}$ DSO substrates. a) The amplitude and phase maps show a regular stripe pattern with alternating contrast, consistent with the presence of a_1/a_2 ferroelastic domains. The scheme in the bottom panel illustrates the expected in-plane polarization configuration for this domain structure, with alternating polarization vectors along orthogonal in-plane directions. b) The amplitude and phase images for the long period (*n*= 25) sample show a more irregular and intersecting domain structure, indicative of a nontrivial in-plane polarization landscape such as flux-closure domains. The schematic inset presents a simplified projection of a flux-closure domain structure, in which the polarization rotates continuously to form closed loops involving both in-plane and out-of-plane components. It is important to note that only the in-plane components can be detected by L-PFM, and the scheme is intended as a conceptual aid rather than a direct representation of the measured signal.

In contrast, the DART L-PFM images of the long-period (n= 25) superlattice (**Figure 6.13**b) reveal a more complex and irregular domain texture. Both the amplitude and phase signals exhibit lateral contrast variations that form intersecting stripe-like features, but these features lack the long-range order and uniform periodicity observed in the short-period sample (**Figure 6.13**a). While L-PFM cannot directly resolve nanometer-scale flux-closure domains (expected periodicity of ≈16 nm according to XRD and RSM) due to the finite lateral resolution of the AFM tip (nominally ≈20 nm), the presence of modulated piezoresponse across larger areas may reflect superdomain organization or mesoscopic averaging of smaller topological structures. Although the experimentally observed features cannot be unambiguously attributed to flux-closure domains based on L-PFM alone (as the out-of-plane polarization is not detected), the presence of laterally modulated in-plane signals supports the emergence of complex polar textures in the long-period superlattice. This interpretation is consistent with complementary structural information derived from XRD and RSM.

Following the structural characterization of the superlattices, we measured their temperature-dependent thermal conductivity using FDTR to assess the influence of superlattice periodicity and polarization organization on heat transport. **Figure 6.14** presents the experimental results of two series of superlattices: $[(STO)_4/(PTO)_4]_m$ with m= 40 and 60 repetitions (corresponding to ≈117 and ≈175 nm, respectively) and $[(STO)_{25}/(PTO)_{25}]_m$ with m= 6 and 9 repetitions (again, ≈117 and ≈175 nm).

For the short-period superlattices (**Figure 6.14**a), both samples exhibit nearly identical thermal conductivity at room temperature, within the experimental error. However, as temperature increases, the thinner sample consistently shows lower thermal conductivity. This behavior suggests that, as in other oxide and semiconducting superlattices previously reported in the literature, there is a fraction of long-wavelength phonons which propagate across the whole heterostructure, and whose mean free path is limited by the total thickness. Thus, increasing the total thickness enhances their contribution to heat transport.

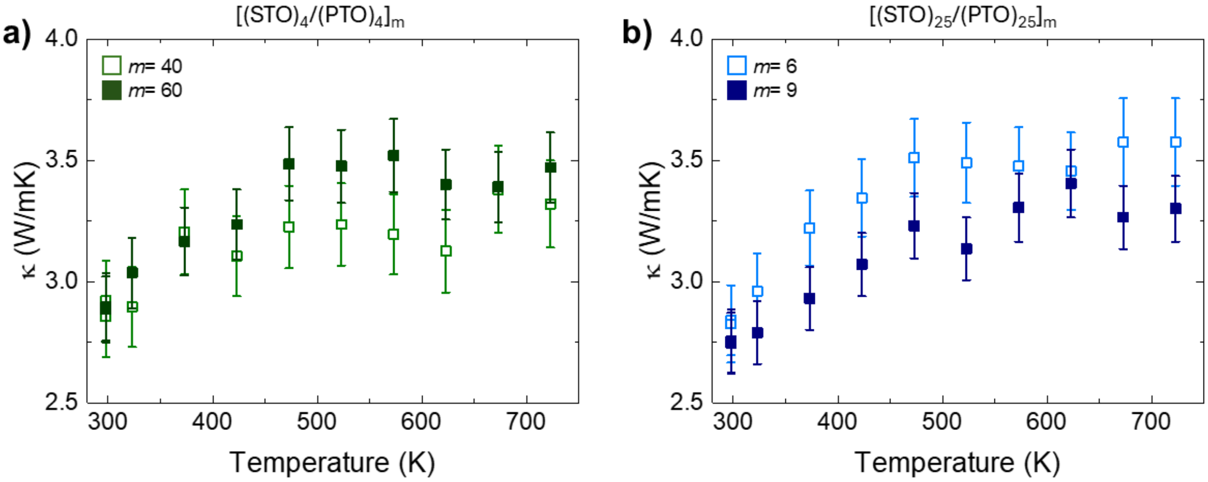

Figure 6.14. Temperature-dependent thermal conductivity of STO/PTO superlattices grown on $(001)_{pc}$ DSO substrates, measured by FDTR. a) Short-period superlattices with $[(STO)_4/(PTO)_4]_m$ architecture for m= 40 (light green squares) and m= 60 (dark green squares), corresponding to total thicknesses of ≈117 and ≈175 nm, respectively. b) Long-period superlattices with $[(STO)_{25}/(PTO)_{25}]_m$ architecture for m= 6 (light blue squares) and m= 9 (dark blue squares), also corresponding to 117 and 175 nm, respectively.

On the other hand, the long-period superlattices (**Figure 6.14**b) display the opposite trend, with the thicker sample presenting lower thermal conductivity than its thinner analogue. This is an unexpected result, but similar to the observation in the PTO/STO superlattices grown on STO substrates discussed in the previous section.

Complex domain structures, such as flux-closure domains, may introduce nanoscale lateral inhomogeneities in polarization and strain, that may act as effective phonon scattering centers or induce localization phenomena, reducing thermal conductivity more than expected from interface scattering alone.

Finally, all samples exhibit the typical temperature-dependence expected for nanostructured systems: thermal conductivity increases with temperature up to a plateau, where it saturates due to enhanced phonon-phonon scattering and the dominance of boundary-limited transport, as the phonon mean free path becomes comparable to the superlattice dimensions.

Having analyzed the short- and long-period superlattices (n= 4 and 25 u.c.), we now turn to the intermediate periodicity case (n= 15 u.c.), where polar vortex structures are expected to emerge according to the phase diagram in **Figure 6.2**. To explore this regime, we synthesized $[(STO)_{15}/(PTO)_{15}]_m$ superlattices with m= 10 and 15 repetitions, again corresponding to total thicknesses of ≈117 and 175 nm, respectively. In contrast to the previous cases, we present the full structural characterization of both samples to better resolve their polarization configuration and assess its potential impact on thermal transport.

Figure 6.15 presents the XRD analysis of $[(STO)_{15}/(PTO)_{15}]_{10}$ (panels a,c) and $[(STO)_{15}/(PTO)_{15}]_{15}$ (panels b,c) superlattices. As observed in the symmetric $\omega/2\theta$ scans (**Figures 6.15**a,b), both samples exhibit well-defined superlattice peaks (extending up to SL_{-4}) surrounding the SL (002) reflection, indicating high structural coherence and precise structural periodicity. Moreover, in the thinner sample (m= 10) clear Laue oscillations are visible around the main peak (see inset in **Figure 6.15**a), suggesting high crystallinity and the formation of sharp interfaces. Interestingly, in addition to the conventional SL satellite peaks, these diffractograms show a series of low-intensity reflections labelled as $V_{\pm n}$ –better appreciable in the m= 15 sample–, which were absent in the a_1/a_2 and flux-closure configurations discussed earlier. These secondary reflections are typically attributed to periodic modulations of polarization due to the formation of polar vortices. In particular, previous studies by Damodaran *et al.* (*253*) have demonstrated that the emergence of vortex lattices results in an effective modulation of the out-of-plane lattice parameter.

From the position of the (002) SL reflection and the zeroth-order V signal, we can estimate the out-of-plane lattice parameter of both structural components, resulting in c= 3.933(2) Å for the SL structure and c= 3.972(4) Å for the V phase. Note that these superlattices present a SL out-of-plane lattice parameter in between those determined for the n= 4 (c= 3.919(3) Å) and n= 25 (c= 3.94(5) Å) superlattices, suggesting a systematic expansion of the c-axis with increasing periodicity.

The superlattice periodicity of both samples was determined from the angular separation between the satellite peaks, yielding t_{per}= 12.05 nm for m= 10 and t_{per}= 11.63 nm for m= 15, in good agreement with the designed nominal periodicity ≈11.7 nm. The consistency across both thicknesses confirms the reproducibility of the structural modulation in this intermediate periodicity regime. Moreover, the presence of several vortex-related signals in the m= 15 superlattice allows us to extract their out-of-plane periodicity in real space, resulting in d= 11.86

nm, closely matching the superlattice periodicity (as widely reported in literature for STO/PTO superlattices hosting this type of polar architecture).

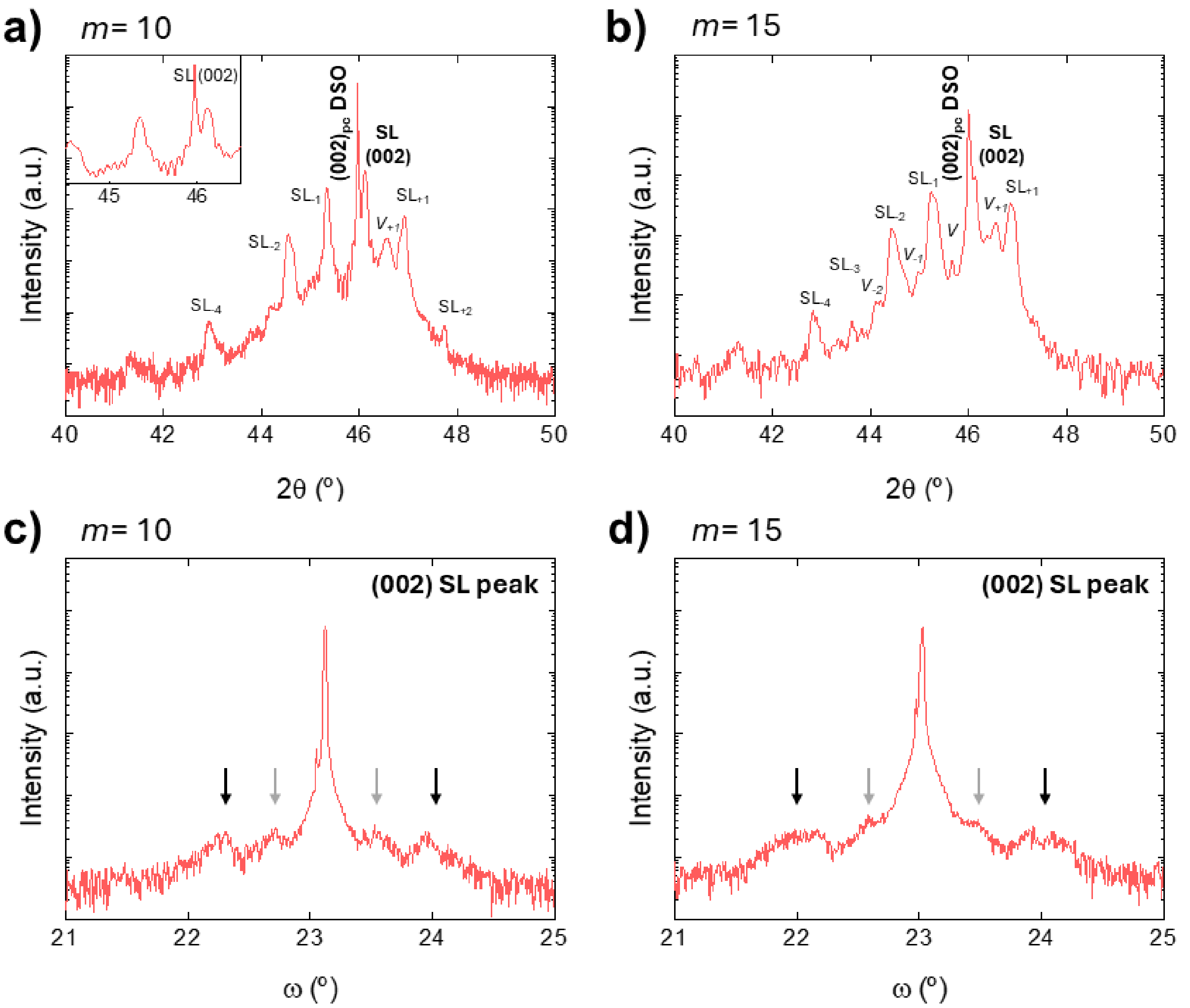

Figure 6.15. X-ray diffraction analysis of $[(STO)_{15}/(PTO)_{15}]_m$ superlattices grown on $(001)_{pc}$ DSO, with *m*= 10 (a,c,) and *m*= 15 (b,d) repetitions. a,b) High-resolution ω/2θ scans around the $(002)_{pc}$ DSO reflection, showing well-defined superlattice satellite peaks that indicate structural coherence. Additional low-intensity reflections, labelled as $V_{\pm n}$, appear between the $SL_{\pm n}$ satellites, and are attributed to periodic modulations due to polar vortex formation. The inset in (a) shows a magnified view of the SL (002) region, exhibiting clear Laue oscillations that confirm the high crystallinity of the superlattice. c,d) Rocking curves (ω scans) centered on the SL (002) Bragg peak, for *m*= 10 and *m*= 15 superlattices, respectively. The broad diffuse features marked with arrows in both panels suggest the presence of lateral in-plane periodic modulations with different characteristic lengths.

The corresponding rocking curves centered around the SL (002) peaks (**Figures 6.15**c,d) further highlight the structural complexity of these superlattices, even though both samples show symmetric peaks with FWHM≈ 0.022 °. As observed in the scans, multiple side lobes appear surrounding the (002) main peak, indicated by black and grey arrows. These lateral features suggest the presence of in-plane modulations with well-defined periodicity, likely arising from the periodic arrangement of vortex-like polar structures. Surprisingly, these side lobes result in two distinct lateral periodicities. The signals indicated by black arrows correspond to modulation periods of d_l= 13.38 nm and 11.17 nm for the *m*= 10 and *m*=15 samples, respectively, closely matching the vertical periodicity of the V phase identified in the

$\omega/2\theta$ scans. These observations support the interpretation that the d_1 modulation arises from the periodic arrangement of vortex cores, both in- and out-of-plane, as previously demonstrated by several authors (*246*, *253*). In contrast, the grey arrows correspond to longer modulation periods, yielding d_2= 25.96 nm and 27.49 nm, respectively. This second, larger in-plane periodicity may reflect a higher-order superstructure or longer-range correlation in the vortex array.

To further elucidate the domain structure and polarization modulations in these samples, we recorded reciprocal space maps around the symmetric $(002)_{pc}$ reflection of the DSO substrate. As shown in **Figure 6.16**, both samples exhibit a clear series of vertically aligned satellite peaks, confirming excellent structural periodicity along the out-of-plane (Q_z) direction. From the vertical spacing between these features, we estimated superlattice periodicities of t_{per}= 12.31 nm (m= 10) and t_{per}=12.02 nm (m= 15), in excellent agreement with the values obtained from $\omega/2\theta$ scans (t_{per}= 12.05 nm and 11.63 nm for m= 10 and 15, respectively), with minor differences arising from the uncertainties in determining the peak position across both techniques.

Beyond vertical coherence, both reciprocal space maps display additional diffuse signals at finite in-plane Q_x positions (marked by black arrows), symmetrically distributed around the main SL (002) peak, consistent with the formation of periodically ordered polar vortex structures. The lateral spacing between these signals (ΔQ_x) corresponds real-space modulation periods of d_1= 11.70 for m= 10 and d_1= 10.53 nm for m= 15, closely matching the vortex periodicity estimated from the rocking curve analysis (**Figure 6.15**c,d). Although the out-of-plane V satellites observed in the $\omega/2\theta$ scans are not clearly resolved in the reciprocal space maps –likely due to overlapping with the SL satellites–, the presence of these lateral modulations confirms the existence of an ordered vortex lattice with lateral periodicity approximately equal to the bilayer thickness. Moreover, as observed in the SLs grown on STO (analyzed in the previous section), the in-plane vortex density increases with the number of bilayer repetitions, reflecting the tendency of these topological structures to self-organize more tightly in thicker superlattices.

Interestingly, in addition to the V-related diffuse scattering, a second family of satellite peaks emerges –marked by grey arrows in **Figure 6.16**– which exhibit both in-plane (Q_x) and out-of-plane (Q_z) ordering. It is worth noting that, differently to the n= 25 superlattices –which present several satellite signals along Q_x arising from the presence of flux-closure domains, as shown in **Figure 6.12**b– the different lateral signals observed in **Figure 6.16** are not equally spaced, meaning that they correspond to different in-plane periodicities, d_1 and d_2, rather than higher-order harmonics of the V-lattice. These observations agree with the multi-periodic features observed in the rocking curves (**Figure 6.15**c,d), reinforcing the presence of two distinct lateral modulations.

The real-space periodicities associated with this second set of satellites were determined from the in-plane (Q_x) and out-of-plane (Q_z) spacings. For the thinner sample (m= 10), these modulations correspond to in-plane and out-of-plane periodicities of 31.38 nm and 12.64 nm, respectively. For the thicker sample (m= 15), the estimated periodicities are 26.62 nm (in-plane) and 12.23 nm (out-of-plane). These modulations, being significantly larger than the vortex lattice constants, suggest the emergence of a long-range superstructure.

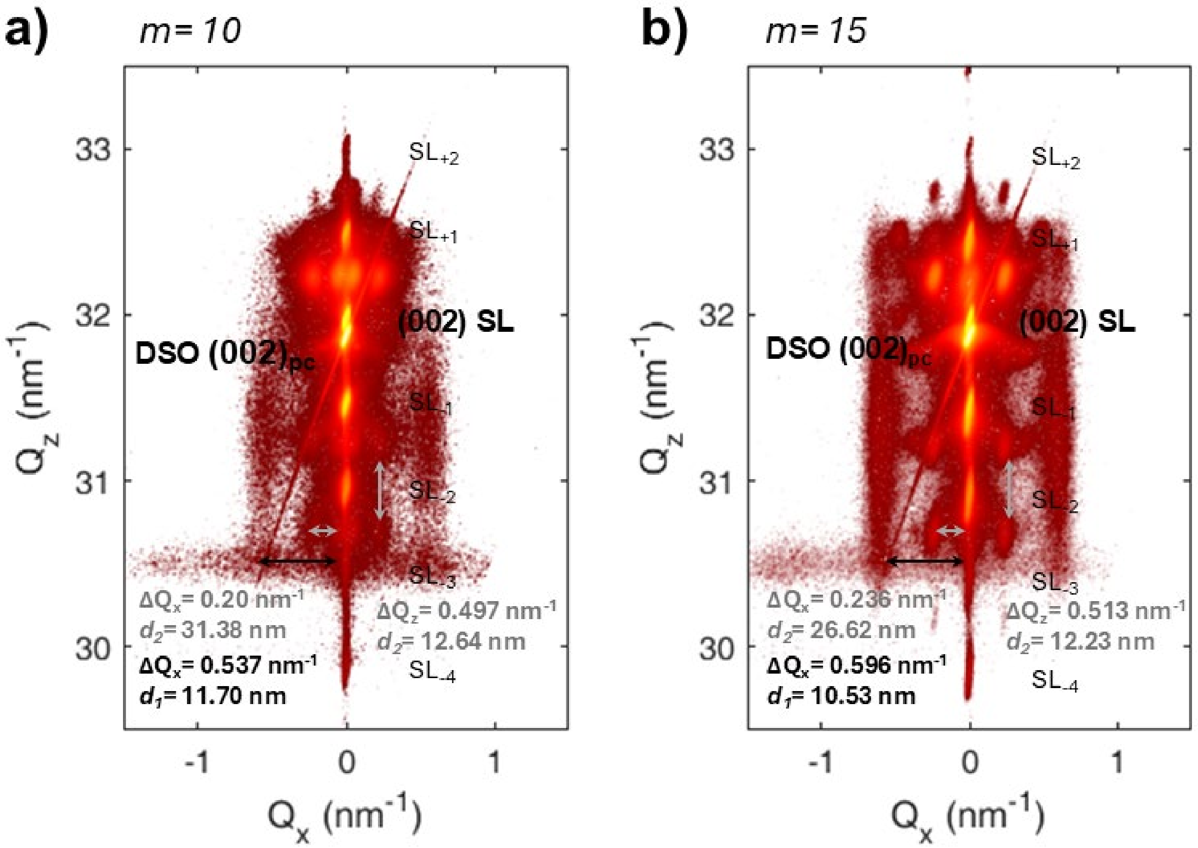

Figure 6.16. Reciprocal space maps around the symmetric (002)$_{pc}$ reflection of the DSO substrate for [(STO)$_{15}$/(PTO)$_{15}$]$_m$ superlattices with m= 10 (a) and m= 15 (b) repetitions. Both maps show well-defined vertical SL satellite peaks along Q_z, confirming the regular stacking of the superlattices with periodicities (t_{per}) of 12.31 and 12.02 nm, respectively. In addition to these features, diffuse lateral satellites at finite Q_x positions (black arrows) reveal the presence of in-plane modulations consistent with the formation of ordered polar vortex arrays. The corresponding lateral periodicities are 11.70 nm (m= 10) and 10.53 nm (m= 15), matching the vortex lattice spacing extracted from rocking curve analysis. A second family of satellites (grey arrows) emerges at intermediate Q_x and Q_z positions, indicating additional structural modulations with both in-plane and out-of-plane periodicities, as indicated in the image. These features are attributed to the formation of a three-dimensional polar supercrystal (SC) phase, characterized by the long-range periodic arrangement of vortex structures in both lateral and vertical directions.

In fact, such additional satellite features are consistent with the formation of a supercrystal (SC) phase –a higher-order superstructure characterized by arrangement of vortices into a periodic 3D array. A schematic representation of this state is shown in **Figure 6.1**e.

This supercrystal phase has been previously reported by Stoica *et al.* (*252*, *255*) in (STO)$_{16}$/(PTO)$_{16}$ superlattices grown in (001)$_{pc}$ DSO after sub-picosecond pulsed optical illumination. The authors reported that this system exhibits a mixture of polar vortices and conventional a$_1$/a$_2$ domains in the as-grown state, as widely demonstrated in analogous systems. However, optical illumination with sub-picosecond pulse excitation using light above the PTO bandgap led to the generation of free carriers at the PTO/STO interfaces, which partially reduce the interfacial depolarization fields. Under this optical stimulation, the system evolves into a stable structure with long-range nanoscale polar order, consisting of polar vortices that are intertwined in three dimensions with an orthorhombic supercell of approximately 30 x 25 x 11 nm^3 –closely matching the in-plane and out-of-plane periodicities extracted from our reciprocal space maps (30 x 12 nm^2).

However, the authors report that the transformation of the pristine mixed a_1/a_2 and vortex state into the SC phase led to the evolution of the diffraction pattern from distinct V and SL peaks into a unified set of SC satellites, signaling the full transformation into the supercrystal phase. As shown in **Figure 6.15**a,b, our $\omega/2\theta$ scans still exhibit contributions from both superlattice and vortex-related reflections. This observation suggests that our samples may exhibit a coexistence of regions with disordered vortices and areas where they locally organize into a SC arrangement.

Notably, this SC phase has also been reported in ferroelectric-metal $PbTiO_3/SrRuO_3$ superlattices deposited on $(001)_{pc}$ DSO in as grown conditions (*271*), formed in this case by the three-dimensional arrangement of horizontal and vertical flux-closure domains, rather than polar vortices. However, to the best of our knowledge, our study represents the first experimental observation of spontaneous SC phase formation in symmetric STO/PTO superlattices without the need for external optical stimulation. Given the non-equilibrium nature of these structures, subtle variations of the deposition conditions during growth may alter the charge density of STO, which can migrate and screen the depolarization fields at the interface and produce an effect similar to the charges generated by optical stimulation.

To further investigate the polar textures present in these samples, we initially attempted to characterize the domain configurations using DART L-PFM, as applied to the n= 4 and n= 25 superlattices. However, the presence of surface contamination and particulate matter on these films prevented the acquisition of reliable phase or amplitude contrast. As a result, detailed nanoscale domain analysis was instead carried out via STEM. These experiments were performed by Dr. José Santiso (ICN2, Barcelona).

Figure 6.17 presents the cross-sectional HAADF-STEM characterization of the m= 15 sample. The low-magnification image in **Figure 6.17**a reveals a well-ordered multilayer structure consistent with the intended 15/15 u.c. stacking sequence, with a periodicity of $t_{per}\approx$ 12 nm in the vertical direction. The clear contrast between the alternating layers confirms the compositional periodicity and supports the structural coherence inferred from XRD measurements.

The fast Fourier transform (FFT) of this image (**Figure 6.17**b) exhibits two sets of satellite reflections, one corresponding to the vertical superlattice periodicity and another reflecting the lateral superstructure around the main reflections (better appreciable in the zoomed regions of **Figure 6.17**b). By applying a selective FFT mask that filters out the vertical satellites and retains only the lateral diffuse features, we obtained the image shown in **Figure 6.17**c. This filtered reconstruction reveals an alternating contrast pattern confined within the PTO layers, consistent with an in-plane modulation of polarization. In several regions, the modulations appear to be coupled across adjacent PTO layers through the paraelectric STO, with varying in-phase and anti-phase coupling. Nevertheless, no long-range coherence between adjacent PTO slabs is observed, at least from the STEM image, suggesting that interlayer coupling is only locally correlated. The lateral periodicity extracted from these modulations is approximately 10 nm, in good agreement with the vortex lattice spacing determined from RSM (**Figure 6.16**b).

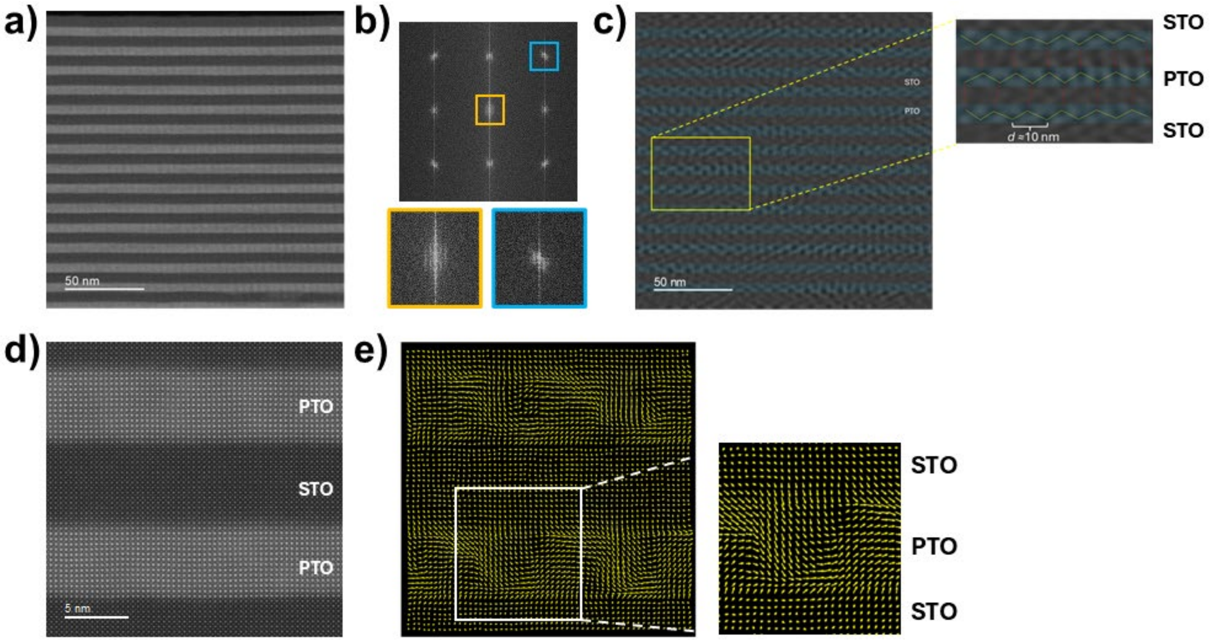

Figure 6.17. Structural characterization of the $[(STO)_{15}/(PTO)_{15}]_{15}$ superlattice grown on $(001)_{pc}$ DSO by STEM. a) Low-magnification cross-sectional HAADF-STEM image, showing well-defined periodic stacking of PTO (bright, as Pb presents higher atomic number than Sr) and STO (dark) layers, with a superlattice periodicity $t_{per} \approx 12$ nm. b) FFT pattern of the image in (a), showing two sets of satellite reflections: vertical satellites corresponding to the superlattice periodicity, and lateral satellites indicative of in-plane polarization modulation. The insets show magnified regions of the FTT image to better highlight these satellites. c) Filtered image obtained from FFT masking, isolating the lateral modulation components and revealing alternating contrast patterns within the PTO layers. These modulations exhibit a lateral periodicity of ≈10 nm and extend across multiple PTO layers in selected regions, suggesting local 3D organization of the polarization texture. d) High-magnification HAADF-STEM image, showing atomic column resolution across the PTO and STO layers. The atomically sharp interfaces and uniform contrast confirm the high crystalline quality and chemical modulation of the multilayer structure. e) Polar displacement map extracted from the atomic positions of Ti cations. As expected, STO layers show minimal displacement, while PTO layers display a sinusoidal in-plane modulation of polarization consistent with dipole-wave configurations. The modulation period (≈10 nm) matches the values extracted from RSM experiments. Data and analysis provided by Dr. José Santiso (ICN2, Barcelona).

However, no evidence of extended regions exhibiting the larger periodicity associated with the SC was observed across the lamella. This absence may stem from the inherent instability of the SC phase during specimen preparation, as reported by Stoica and coworkers (*252*), or from the relaxation of elastic constraints due to the reduced thickness of the lamella. This highlights a key challenge in the characterization of these complex polar states through direct visualization: their extreme sensitivity to strain and boundary effects that may be severely affected by the preparation of the lamellae and the conditions during observation. For instance, while Yadav *et al.* (*246*) reported the stabilization of polar vortices in $[(STO)_{10}/(PTO)_{10}]_{10}$ superlattices grown on $(001)_{pc}$ DSO substrates, Tan and collaborators (*270*) demonstrated that the as-grown films exhibit conventional a_1/a_2 domains, and the vortex lattice only emerges after the preparation of the lamella, as the system transitions from biaxial to uniaxial strain. These discrepancies underscore the sensitive nature of topological polar textures and their strong dependence on sample environment and geometry.

A higher magnification image, with atomic column resolution, is shown in **Figure 6.17**d, demonstrating the excellent crystalline quality of the sample and the formation of atomically sharp interfaces. A corresponding polar displacement map is presented in **Figure 6.17**e, derived from precise measurements of the relative positions of Ti cations in both PTO and STO. As expected for the paraelectric phase, the Ti displacements within the STO layers are small and disordered. However, consistent with the findings in the superlattices grown on STO (originally expected to host polar skyrmions), the PTO layers exhibit large polar displacements that organize into a lateral sinusoidal modulation, resembling dipole waves (DWs) rather than closed-loop vortices, contrary to previous reports in similar systems. The periodicity of this horizontal arrangement is around 10 nm, which is in close agreement with the XRD measured values.

This sinusoidal polarization arrangement has been previously observed in STO/PTO superlattices grown on DSO substrates and rapidly quenched to room temperature after deposition, as reported by Gong *et al.* (*251*). In their work, the formation of dipolar wave configurations was attributed to a non-equilibrium cooling process, which kinetically stabilized metastable polarization textures before the system could fully relax into its thermodynamically favored state (i.e., polar vortex lattice). This procedure may be consistent with our growth conditions: although the heating power was progressively reduced after deposition, the cooling rate was not actively controlled, potentially leading to a similarly rapid quench. Nevertheless, these authors predicted the stabilization of the DWs in superlattices with relatively short periodicities, up to *n*= 11 u.c per layer.

Recent results by Wang and collaborators (*272*) have shed light on the connection between dipole waves and vortex structures. Using phase-field simulations and angle-resolved PFM, they demonstrated that polar vortices can be understood as the superposition of two orthogonal DWs. In this framework, the emergence of a pure DW pattern rather than a closed-loop vortex configuration could result from the suppression of one of the two orthogonal wave components. This suppression may be driven by local variations in strain, electrostatic boundary conditions, or defects, all of which can lift the degeneracy between the two modes and stabilize a unidirectional polarization modulation.

Following the structural characterization of the intermediate-periodicity superlattices with *m*= 10 and 15 repetitions, we investigated their thermal transport properties using FDTR, to evaluate how these polar textures –DWs and their 3D ordering into a polar SC phase– influence the effective thermal conductivity.

Figure 6.18a summarizes the room-temperature thermal conductivity of all the STO/PTO superlattices grown on DSO substrates studied in this section, plotted as a function of the superlattice periodicity (*n*= 4, 15 and 25 u.c.). As observed in the figure, the superlattices with *n*= 15 exhibit the lowest thermal conductivity among the series, despite having an intermediate interface density. This reduction is especially pronounced in the *m*= 15 sample (total thickness of ≈175 nm), which displays the minimum thermal conductivity across all the measured superlattices.

This pronounced decrease in thermal conductivity for the intermediate period superlattices cannot be solely attributed to interface scattering or film thickness. Instead, it points toward the influence of the polar superstructures discussed before. In contrast to the trivial a_1/a_2 stripe domains (*n*= 4) or flux-closure architectures (*n*= 25), the *n*= 15 samples host a more complex polarization texture, based on sinusoidal DWs which are three-dimensionally arranged into a polar supercrystal phase. This SC configuration introduces long-range periodic modulations in both in-plane and out-of-plane directions, generating a spatially varying polarization and strain landscape, which may enhance phonon scattering.

As in the superlattices grown on STO substrates, the thicker samples show a smaller thermal conductivity, consistent with localization phenomena, like the Anderson localization (*269*) discussed in the previous section.

Moreover, the very low thermal conductivity observed for the *m*= 15 superlattice can be rationalized by the higher density and spatial coherence of the SC phase, as evidenced by the more intense satellite peaks in the reciprocal space map (**Figure 6.16**). These observations support the idea that the degree of 3D polar ordering directly influences phonon transport, providing a tunable mechanism for thermal conductivity control.

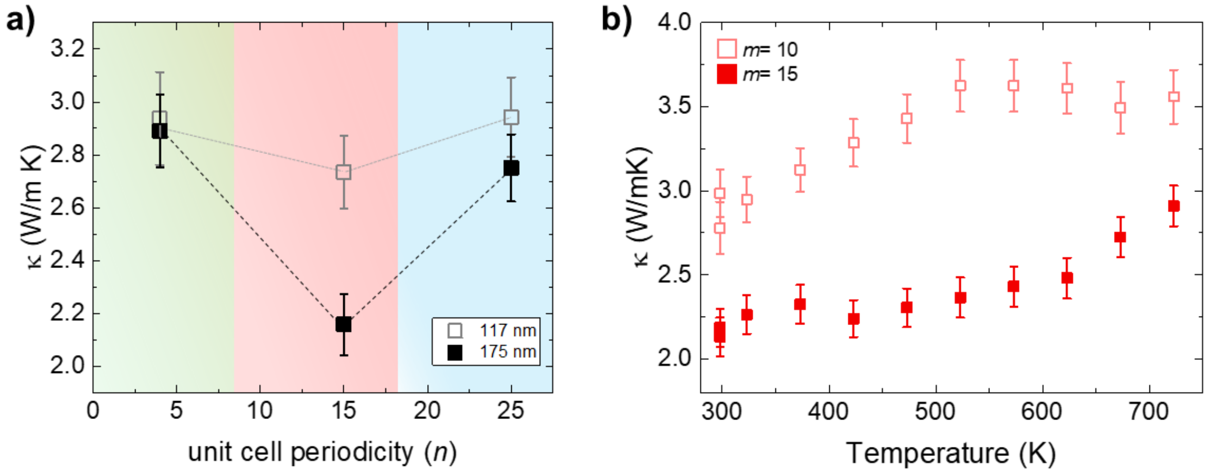

Figure 6.18. Thermal conductivity of $[(STO)_n/(PTO)_n]_m$ superlattices grown on $(001)_{pc}$ DSO substrates. a) Room-temperature thermal conductivity as a function of superlattice periodicity *n*, for two different total thicknesses: ≈117 nm (open squares) and ≈175 nm (solid squares). The lowest thermal conductivity is observed for *n*= 15 superlattices despite their intermediate interface density, highlighting the role of 3D polar arrangement. b) Temperature-dependent thermal conductivity for the *n*= 15 superlattices with *m*= 10 and 15 repetitions, showing distinct thermal behavior. The thinner sample (open squares) shows the expected trend for nanostructures, while the thicker sample (solid squares) exhibits suppressed thermal conductivity across the full temperature range.

In addition to the room-temperature measurements, we also performed temperature-dependent FDTR experiments on the *n*= 15 superlattices, from room temperature up to ≈770 K, as shown in **Figure 6.18**b. As we can observe in the figure, the *m*= 10 superlattice exhibits the same behavior as all the samples previously discussed in this chapter, with a progressive increase in thermal conductivity with temperature up to saturation. However, the thicker (*m*= 15) sample presents a markedly different temperature-dependent response: its thermal conductivity remains anomalously low across the entire temperature range, exhibiting a modest increase with temperature and slowly approaching the thermal conductivity of the *m*= 10 sample at high temperatures. Notably, the curve presents three different regimes (see also **Figure 6.19**b): an initial plateau where thermal conductivity remains nearly constant (within experimental uncertainty) up to ≈450-500 K, followed by a mild slope increase up to ≈620 K, and a more abrupt rise thereafter.

This behavior follows the evolution of polar domains, as demonstrated by the temperature-dependent reciprocal space mapping shown in **Figure 6.19**a. All superlattice satellite peaks remain vertically aligned with the substrate reflection throughout the whole temperature range, confirming the preservation of epitaxial matching up to the highest measured temperatures. However, the satellite signals associated with the SC (indicated by grey arrows in **Figure 6.19**a) persist only up to approximately ≈473 K, becoming indetectable at higher temperatures. In contrast, the satellites corresponding to the DWs (marked by black arrows in **Figure 6.19**a) maintain a significant intensity up to 473 K, gradually vanishing thereafter and completely disappearing between 573 and 673 K.

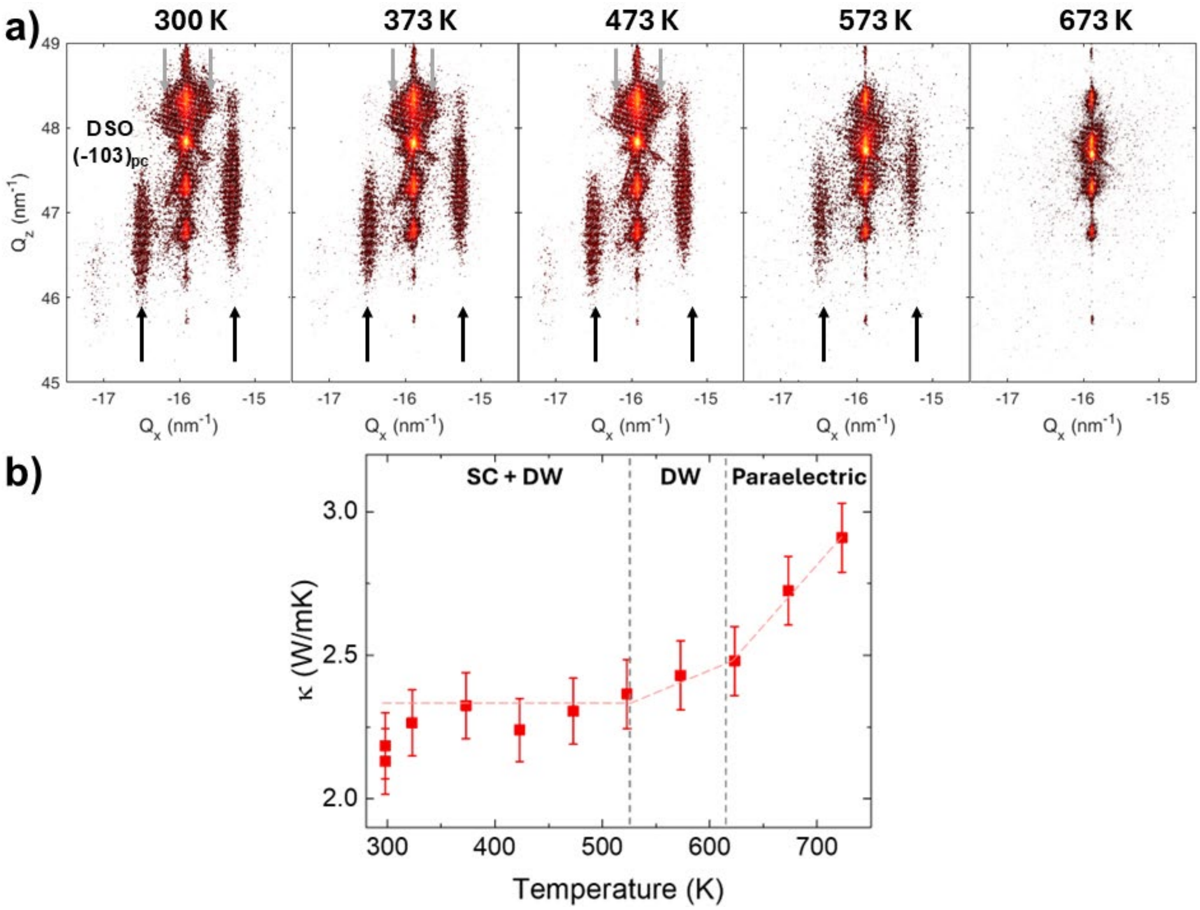

Figure 6.19. Thermal evolution of the polar textures and thermal conductivity in the *m*= 15 superlattice. a) Temperature-dependent reciprocal space maps acquired around the (-103)$_{pc}$ reflection of the DSO substrate. Grey and black arrows indicate the satellite signals associated with the polar supercrystal (SC) and dipole wave (DW) phases, respectively. The intensity and persistence of these features reveal distinct phase transitions upon heating. Due to experimental constraints, each map was acquired with a reduced integration time (total measurement time of ≈2 hours), leading to lower-intensity signals compared to the high-resolution map shown in **Fig. 6.16**b (acquired over 9 hours). Nevertheless, the key features related to the polar textures are still clearly discernible. b) Temperature-dependent thermal conductivity, showing three distinct regimes that correlate with the structural transitions observed in (a): SC + DW coexistence below ≈525 K, DW-only configuration between ≈525–625 K, and paraelectric behavior above ≈625 K. The RSM experiments shown in (a) were conducted by Dr. José Santiso at Catalan Institute of Nanoscience and Nanotechnology (ICN2, Barcelona).

Based on these observations, three distinct temperature regimes can be defined:

i) From room temperature to ≈525 K: coexistence of the SC and DWs phases, with both contributing to the polar organization.
ii) From 525 to 625 K: SC phase is no longer observed, so that only DWs persist in the sample.
iii) Above 675 K: complete disappearance of DWs, indicating the transition into a paraelectric state.

These observations are in agreement with previous experiments on the thermal stability of optically induced SC phases in STO/PTO superlattices, where the SC structure vanishes around 470 K and the transition to the paraelectric phase occurs between 650-700 K, depending on the history of optical excitation (*252*, *255*). However, a key difference is observed: in those studies, once the SC phase is thermally suppressed, it does not reappear upon cooling, and the system reverts to its original mixed a_1/a_2 and vortex domain state. In contrast, our superlattices fully recover the SC-associated satellite signals upon cooling to room temperature, indicating that in our case the SC phase represents a thermodynamically stable ground state, rather than a metastable configuration triggered by external stimuli.

More importantly, the phase regimes extracted from RSM are consistent with the thermal behavior of the m= 15 sample, as highlighted in **Figure 6.19**b. The nearly constant thermal conductivity observed up to ≈525 K correlates with the coexistence of SC and DW phases, which provide a highly disordered and anharmonic environment for phonon transport. Between 525-625 K, as the SC phase disappears and only DWs remain, the thermal conductivity begins to increase modestly, reflecting the reduced phonon scattering efficiency in the absence of 3D order. Above 625 K, when DWs vanish and the sample becomes paraelectric, a pronounced rise in thermal conductivity is observed, consistent with a more ordered lattice and diminished phonon scattering from polar textures. Importantly, this thermal response is fully reversible: upon cooling, the original thermal conductivity is restored, indicating that no permanent structural changes occur during the thermal cycling. This reversibility underscores the potential of polar topologies as active elements for dynamic thermal control.

The origin of the different thermal behavior observed in m= 10 and m= 15 superlattices, despite both presenting the same periodicity (n= 15) and similar polar structures, is unknown. However, we hypothesize that enhanced suppression of thermal conductivity in the m= 15 sample is due to its greater spatial coherence and higher density of the SC phase, as evidenced by more intense lateral satellite signals in RSM (**Figure 6.16**). This would suggest that not only the presence, but also the degree of long-range 3D ordering of polar structures, plays a critical role in phonon scattering and thermal transport modulation.

In summary, these results underscore the possibility of using complex polar architectures –such as dipole waves and supercrystals– to reversibly modulate heat transport in STO/PTO superlattices (and, probably, in other ferroelectric systems) through thermal stimuli. Moreover, since many of these polar architectures can be switched by electric fields (*253–256*, *273*), this approach opens a promising route for the development of solid-state thermal switches.

6.3. CONCLUSIONS

In this chapter, we investigated the influence of complex polar topologies on the thermal transport properties of PTO/STO superlattices, aiming to evaluate their viability as active thermal switching platforms. By systematically tuning the epitaxial strain and superlattice periodicity, we have stabilized a wide range of polar configurations –including conventional a_1/a_2 stripe domains, flux-closure configurations, and more exotic topological states such as dipole waves and their three-dimensional organization into a polar supercrystal. These polar configurations exhibit distinct structural characteristics, thermal stability, and effect on phonon-mediated heat transport. The main conclusions of our work are:

- While previous studies reported the stabilization of polar skyrmions in PTO/STO superlattices grown under compressive strain on (001) STO substrates, our results indicate the formation of laterally modulated dipole waves with a characteristic periodicity of ≈10 nm, rather than isolated skyrmion cores.
- Similarly, $[(STO)_{15}/(PTO)_{15}]_m$ superlattices grown on $(001)_{pc}$ DSO, which were expected to host polar vortices, instead stabilize a dense lattice of dipole waves that spontaneously self-assemble into a polar supercrystal. This constitutes the first evidence of spontaneous supercrystal formation in STO/PTO superlattices without the need for external optical excitation.
- All the studied superlattices exhibit remarkably low thermal conductivities –regardless of their polar configuration– compared to nanostructures with similar interface densities. This underscores the dominant role of internal polar ordering in phonon scattering, beyond traditional interfacial effects.
- For a fixed superlattice periodicity, thermal conductivity decreases with increasing total thickness, except for the samples exhibiting conventional a_1/a_2 domains (n= 4 on DSO). This counterintuitive trend may arise from increased polarization density or from the emergence of phonon localization phenomena, such as Anderson localization, driven by complex polar textures.
- All the samples, except for the thicker n= 15 superlattice, exhibit the expected temperature-dependent thermal conductivity for nanostructures. In contrast, this last sample shows an anomalously low thermal conductivity across the whole temperature range, with three distinct regimes that match the phase transitions observed in the reciprocal space maps. This underscores the crucial role of polar ordering –in particular 3D polar organizations– on thermal conductivity.
- Unlike previously reported on photoinduced SC phases, the polar supercrystal in our samples fully recovers after thermal cycling This stability enables repeatable and reversible control of thermal conductivity with temperature, a key requirement for thermal switching applications.

In summary, our findings demonstrate that engineering polar topologies –particularly through 3D polar ordering– offers a powerful route to actively modulate thermal conductivity in ferroelectric superlattices through thermal stimuli. The interplay between polarization structure, epitaxial strain, and phonon transport opens up new opportunities for designing reconfigurable thermal devices, such as non-volatile thermal switches. Moreover, given the electric-field responsiveness of many of these polar states, this strategy paves the way for multifunctional thermal management technologies rooted in topological ferroelectricity.

7. CONCLUDING REMARKS AND OUTLOOK

> *"Always remember that you are absolutely unique. Just like everyone else."*
>
> Margaret Mead, American cultural anthropologist. She was a pioneer of anthropological feminism and the sexual revolution.

The main motivation of this thesis was to contribute to the field of active thermal management by developing and characterizing materials capable of undergoing reversible thermal conductivity switching in response to external stimuli. To address this objective, four distinct strategies were investigated (Chapters 3-6), each based on a different physical mechanism and material platform. Collectively, these approaches demonstrated that heat conduction can be actively and reversibly modulated through rational materials design. Furthermore, they underscored the extraordinary sensitivity of thermal conductivity to subtle variations in structural order, chemical composition, and ferroelectric polarization, highlighting its potential not only as a transport property usable in devices, but also as an indirect probe of internal material's structure. The general conclusions derived from these studies are:

- Photoresponsive azobenzene derivatives enable light-induced reversible modulation of thermal conductivity near room temperature. The switching kinetics and thermal contrast can be controlled by varying the length of the alkyl side chain and the initial phase (i.e., crystalline solid or liquid crystal), which influence molecular mobility and packing. Moreover, the use of these azo-derivatives as photoactive dopants in liquid crystalline matrices allow bi-directional thermal switching, with a moderate thermal contrast and fast switching times. These results illustrate the viability of low-power, optically reconfigurable thermal materials based on soft-matter systems.

- The reversibility of brownmillerite-to-perovskite topotactic transformations in negative charge-transfer oxides is strongly dependent on the oxidation pathway. Our findings show that these oxides are inherently unstable in aqueous environments, which limits their applicability in liquid-phase systems such as oxide-based electrodes. Additionally, we found that among the oxidation strategies investigated (liquid phase, gas phase and solid state), only solid-state electrochemical oxidation with a YSZ solid electrolyte enabled truly reversible O^{2-} insertion and extraction. This approach led to robust and repeatable thermal conductivity switching with high ON/OFF ratios, underscoring the critical role of controlled ionic exchange in achieving functional reversibility in these systems.

- The application of localized electric fields through an atomic force microscopy tip provides a precise means to engineer oxygen vacancy distributions in negative charge-transfer oxides, yielding non-volatile states of reduced thermal conductivity. These states, erasable by mild thermal annealing in air, demonstrated exceptional stability and reusability under ambient conditions. This represents a novel approach to writing and erasing thermal functionality with micrometer resolution, offering a pathway toward the fabrication of thermal logic circuits. The contrasting behavior of Mott-Hubbard systems, which undergo irreversible degradation under the same conditions, further highlights the need for careful materials selection based on electronic structure.

- The internal polarization topology of ferroelectric superlattices plays a dominant role in phonon scattering. A wide range of polar configurations (including stripe domains, flux-closure patterns, dipole waves, and three-dimensional polar supercrystals) was stabilized in PTO/STO superlattices through epitaxial strain and periodicity engineering. All configurations exhibited remarkably low thermal conductivities, well below those expected from interface scattering alone. Notably, the spontaneous formation of 3D polar supercrystals correlated with anomalous thermal behavior and phase transitions, suggesting the presence of polarization-enhanced phonon scattering or localization. The full thermal reversibility of these polar textures, combined with their responsiveness under electric fields, points to topological order as a powerful and previously underexplored strategy for controlling heat flow in solids.

Altogether, the results presented in this thesis demonstrate that dynamic modulation of thermal conductivity can be achieved through a diverse range of mechanisms, each offering different advantages in terms of thermal contrast, reversibility, tunability, and spatial resolution. These findings collectively establish a set of material design and functional principles for the development of future thermal switches and contribute to the broader scientific goal of treating heat as an actively controllable property, rather than a passive consequence of material composition. By bridging soft matter, complex oxides, and ferroic architectures, this work lays the foundation for the development of adaptive, programmable, and multifunctional thermal materials –critical components for the next generation of intelligent thermal technologies.

ANNEX I

In this annex we provide the complete experimental procedure followed for the synthesis and purification of the 4,4’-dialkyloxy-3-methylazobenzenes studied in Chapter 3.

Synthesis of 4,4’-dihydroxy-3-methylazobenzene

In a 100 mL round bottom flask 3.01 g of 4-aminophenol (27.49 mmol, 1.00 equiv.) were dissolved in 35.0 mL of 2.5 M $HCl_{(aq)}$, and the obtained solution was cooled in an ice bath. Over this solution, 2.27 g of $NaNO_2$ (32.99 mmol, 1.20 equiv) in 3.0 mL of deionized water were added dropwise for 5 minutes, and the mixture was stirred for 15 minutes at 0 ºC. Then, 2.97 g of *o*-cresol (27.49 mmol, 1.00 equiv.), previously dissolved in 11.0 mL of a $NaOH_{(aq)}$ solution (20%), were added slowly under stirring at 0 ºC. The mixture was allowed to reach room temperature and then stirred overnight. The reaction mixture was acidified with 1 M $HCl_{(aq)}$ and extracted with ethyl acetate (3 × 20 mL). The combined organic phase was dried over anhydrous $MgSO_4$, and the solvent was removed under vacuum. The crude mixture was purified by flash chromatography over silica gel (1:2 ethyl acetate/hexane) to give the desired product as a brown solid (2.53 g, 40% yield). ^{1}H-RMN (300 MHz, DMSO-d_6) δ 10.08 (s, 1H), 10.04 (s, 1H), 7.70 (d, J = 8.23 Hz, 2H), 7.61 (s, 1H), 7.55 (d, J = 8.53 Hz, 1H), 6.90 (m, 3H), 2.20 (s, 3H).

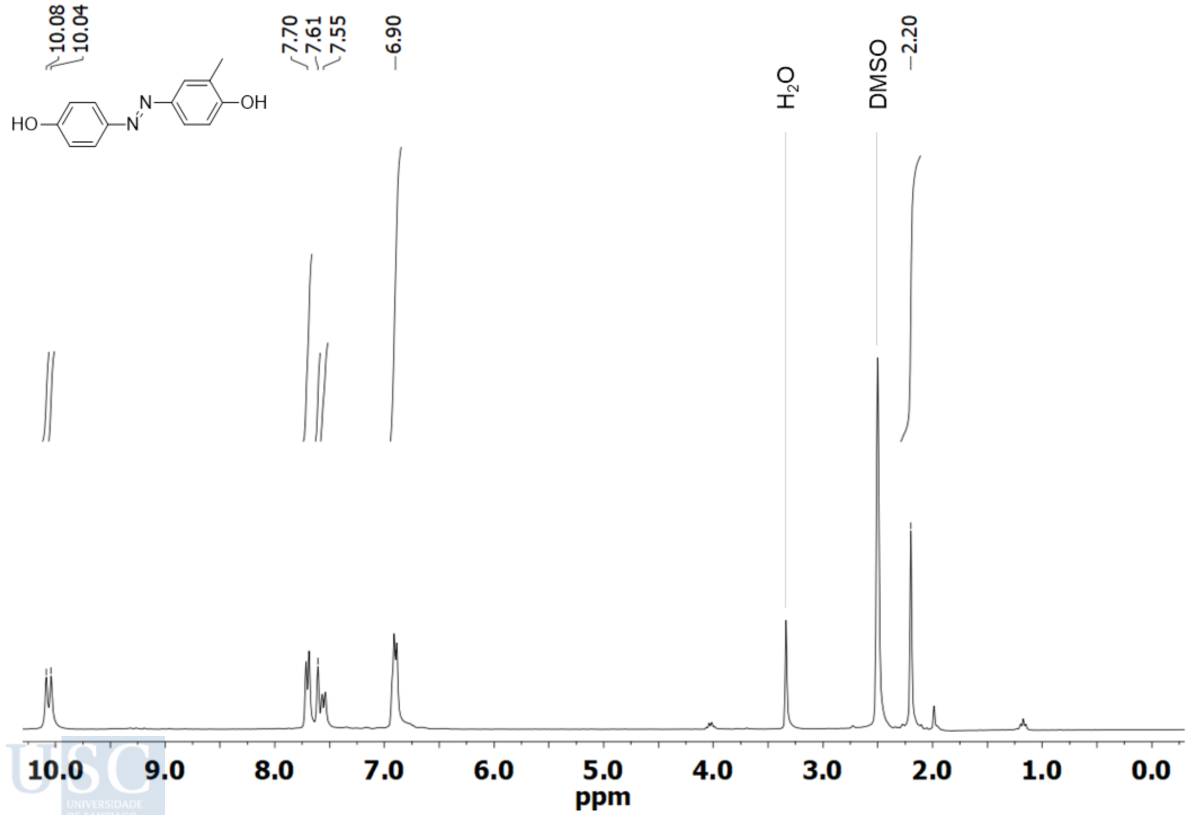

Synthesis of 4,4'-dipropyloxy-3-methylazobenzene

A mixture of 4,4'-dihydroxy-3-methylazobenzene (0.3 g, 1.31 mmol, 1.00 equiv.), 1-bromopropane (0.37 g, 3.01 mmol, 2.30 equiv.), K_2CO_3 (0.38 g, 2.75 mmol, 2.10 equiv.), and a catalytic amount of potassium iodide in 15.0 mL of N,N-dimethylformamide was heated at 70 ºC for 24 h. The reaction mixture was cooled down to room temperature and then acidified with 1 M $HCl_{(aq)}$ until precipitation of a yellow solid. The yellow solid was then isolated by filtration and washed with deionized water. The solid was dissolved in chloroform, dried over $MgSO_4$, and the solvent removed under reduced pressure. The crude material was purified by flash chromatography over silica gel (1:9 ethyl acetate/hexane) to give 4,4'-dipropyloxy-3-methylazobenzene as a yellow powder (0.32 g, 78% yield). ^{1}H-RMN (300 MHz, $CDCl_3$) δ 7.87 (d, *J* = 8.46 Hz, 2H), 7.74 (m, 2H), 6.99 (d, *J* = 9.27 Hz, 2H) 6.90 (d, *J* = 9.20 Hz, 1H), 4.00 (m, 4H), 2.31 (s, 3H), 1.86 (m, 4H), 1.08 (m, 6H).

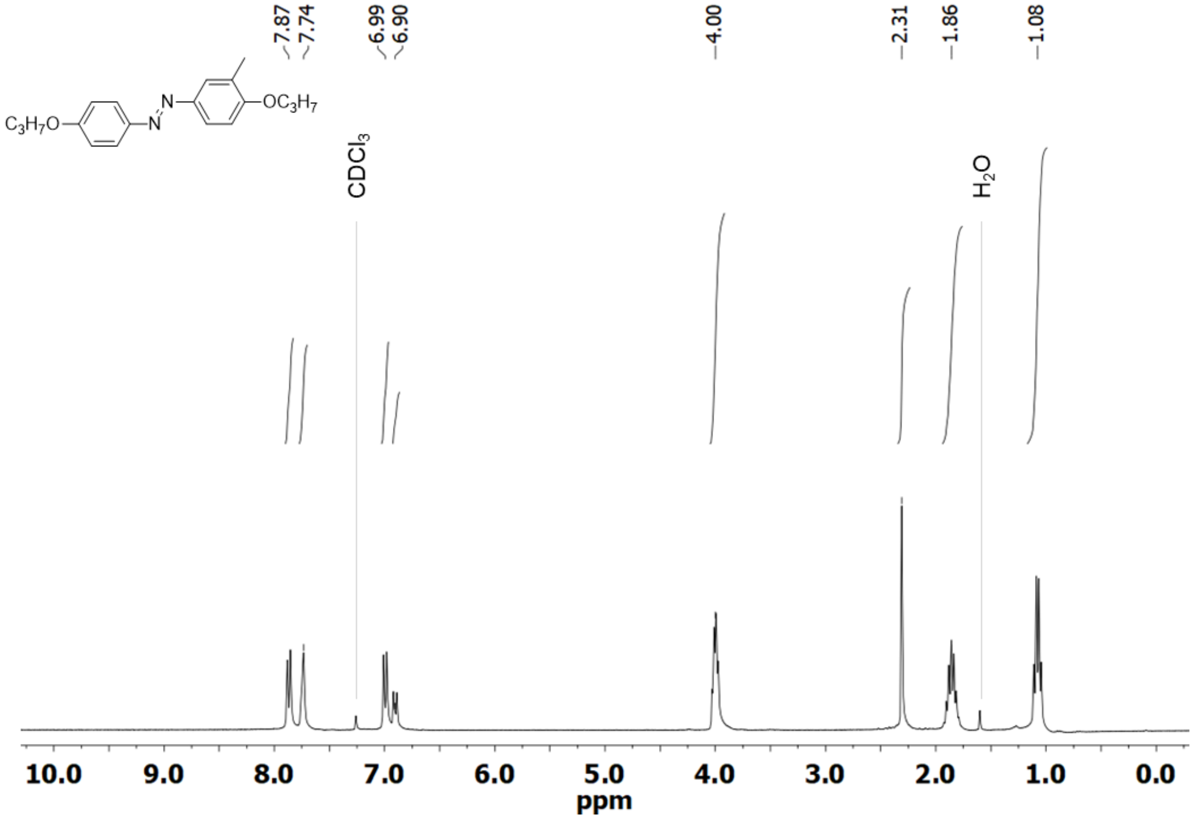

Synthesis of 4,4’-dipentyloxy-3-methylazobenzene

A mixture of 4,4’-dihydroxy-3-methylazobenzene (0.325 g, 1.42 mmol, 1.00 equiv.), 1-bromopentane (0.495 g, 3.28 mmol, 2.30 equiv.), K_2CO_3 (0.411 g, 2.98 mmol, 2.10 equiv.), and a catalytic amount of potassium iodide in 16.25 mL of N,N-dimethylformamide was heated under argon atmosphere at 95 ºC for 24 h. The reaction mixture was cooled down to room temperature and neutralized using 1 M $HCl_{(aq)}$ until an orange solid is precipitated. The orange precipitate was isolated by filtration and washed with deionized water. The solid was dissolved in dichloromethane, dried over $MgSO_4$, and the solution was concentrated under reduced pressure. The crude material was purified by gradient flash chromatography over silica gel (5:95 to 20:80 ethyl acetate/hexane) to give 4,4’-dipentyloxy-3-methylazobenzene as an orange powder (0.352 g, 67% yield). ^{1}H-RMN (500 MHz, $CDCl_3$) δ 7.85 (d, *J* = 8.93 Hz, 2H), 7.73 (m, 2H), 6.98 (d, *J* = 8.52 Hz, 2H), 6.90 (d, *J* = 9.26 Hz, 1H), 4.05 (m, 4H), 2.30 (s, 3H), 1.84 (m, 4H), 1.44 (m, 8H), 0.96 (m, 6H).

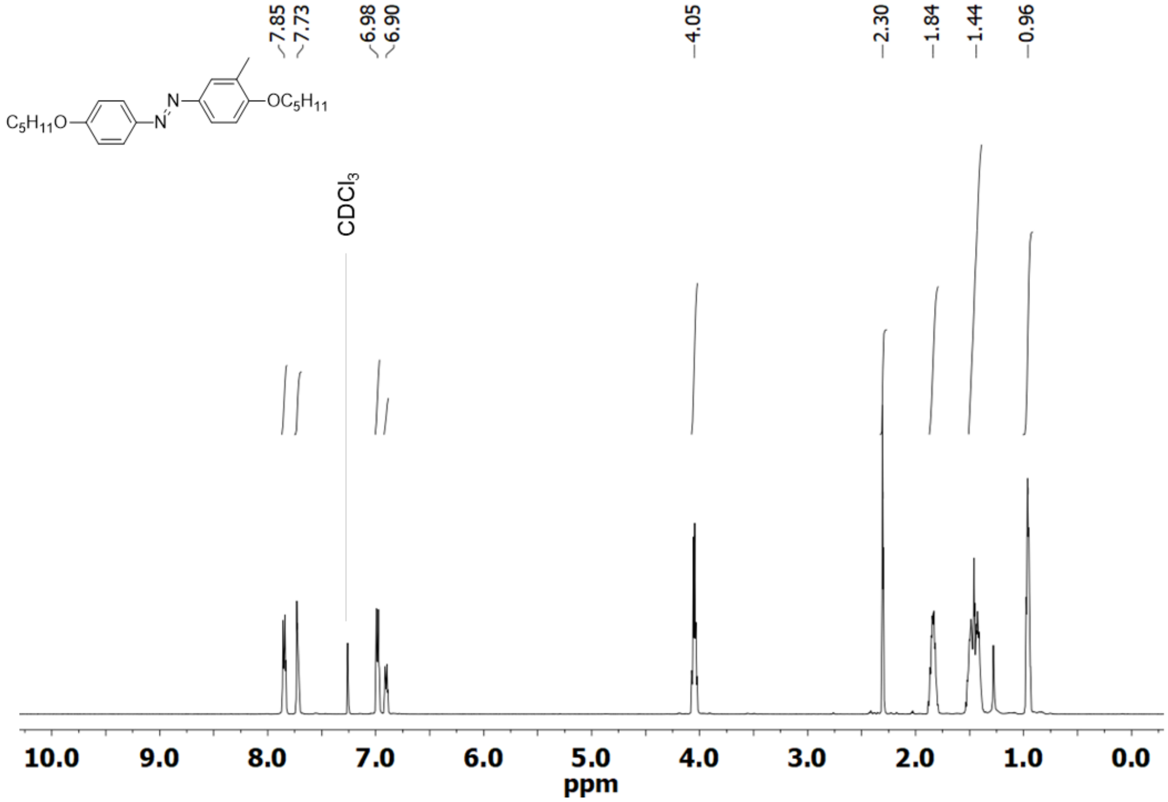

Synthesis of 4,4'-dihexyloxy-3-methylazobenzene

A mixture of 4,4'-dihydroxy-3-methylazobenzene (0.30 g, 1.31 mmol, 1.00 equiv.), 1-bromohexane (0.497 g, 3.01 mmol, 2.30 equiv.), K_2CO_3 (0.379 g, 2.75 mmol, 2.10 equiv.), and a catalytic amount of potassium iodide in 15 mL of N,N-dimethylformamide was heated at 120 ºC for 24 h. The reaction mixture was cooled down to room temperature and neutralized using 1 M $HCl_{(aq)}$ until an orange precipitate is obtained. The orange precipitate was isolated by filtration and washed with deionized water. The solid was dissolved in chloroform, dried over $MgSO_4$, and the solution was concentrated under reduced pressure. The residue was recrystallized from methanol to afford 4,4'-dihexyloxy-3-methylazobenzene as an orange solid (0.415 g, 80% yield). ^{1}H-RMN (300 MHz, $CDCl_3$) δ 7.85 (d, *J* = 8.86 Hz, 2H), 7.73 (m, 2H), 6.98 (d, *J* = 8.90 Hz, 2H), 6.90 (d, *J* = 9.39 Hz, 1H), 4.04 (m, 4H), 2.30 (s, 3H), 1.82 (m, 4H), 1.54 (m, 4H), 1.36 (m, 8H), 0.92 (m, 6H).

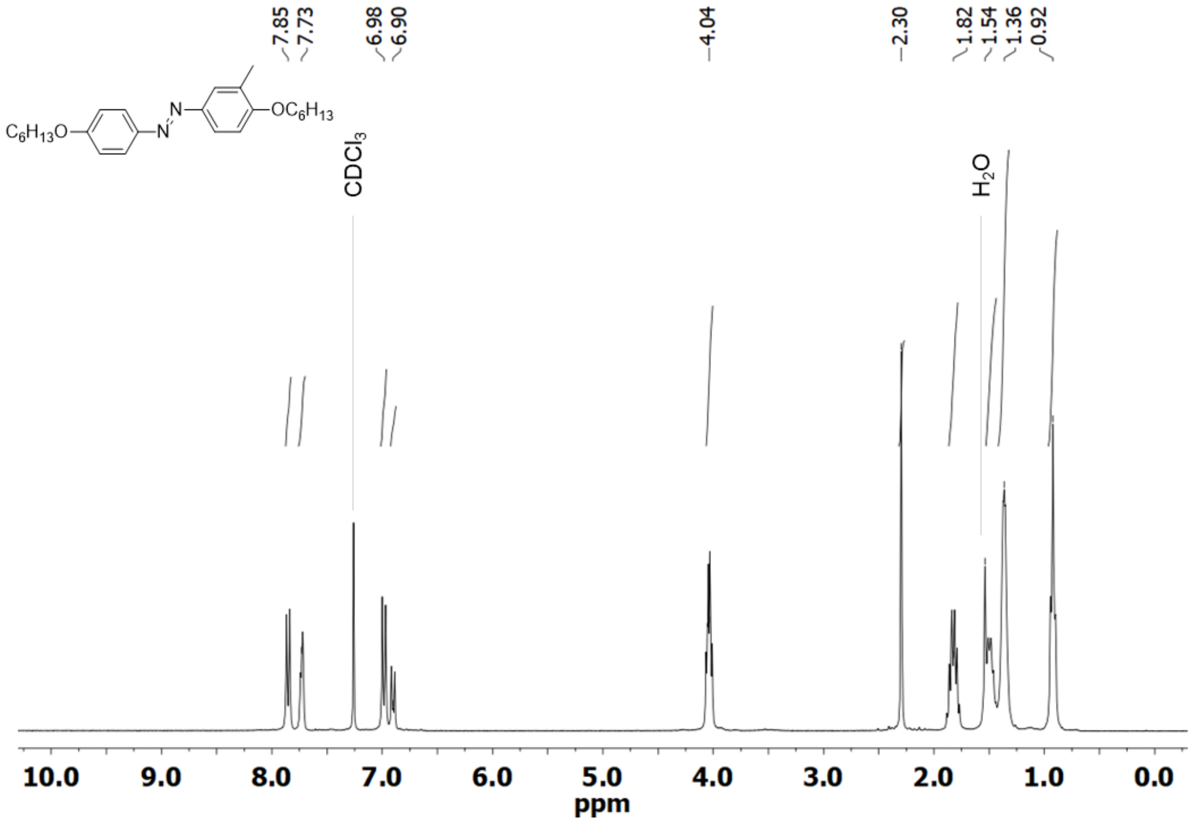

Synthesis of 4,4’-dioctyloxy-3-methylazobenzene

A mixture of 4,4’-dihydroxy-3-methylazobenzene (0.8 g, 3.50 mmol, 1.00 equiv.), 1-bromooctane (1.55 g, 8.05 mmol, 2.30 equiv.), K_2CO_3 (1.21 g, 8.75 mmol, 2.50 equiv.), and a catalytic amount of potassium iodide in 40 mL of N,N-dimethylformamide was heated to 100 ºC for 24 h. The reaction mixture was cooled down to room temperature, neutralized using 1 M $HCl_{(aq)}$, and the aqueous phase was extracted with diethyl ether (3 × 20 mL). The combined organic phase was washed with water (1 × 20 mL) and brine (1 × 20 mL). The organic phase was dried over $MgSO_4$, and the solvent was evaporated under reduced pressure. The residue was purified by flash chromatography on silica gel (1:9 diethyl ether/hexane) to give 4,4’-dioctyloxy-3-methylazobenzene as an orange solid (1.11 g, 70% yield). ^{1}H-RMN (300 MHz, $CDCl_3$) δ 7.86 (d, *J* = 7.87 Hz, 2H), 7.73 (m, 2H), 6.99 (d, *J* = 8.96 Hz, 2H), 6.90 (d, *J* = 9.40 Hz, 1H), 4.03 (m, 4H), 2.30 (s, 3H), 1.83 (m, 4H), 1.49 (m, 4H), 1.32 (m, 16H), 0.90 (m, 6H).

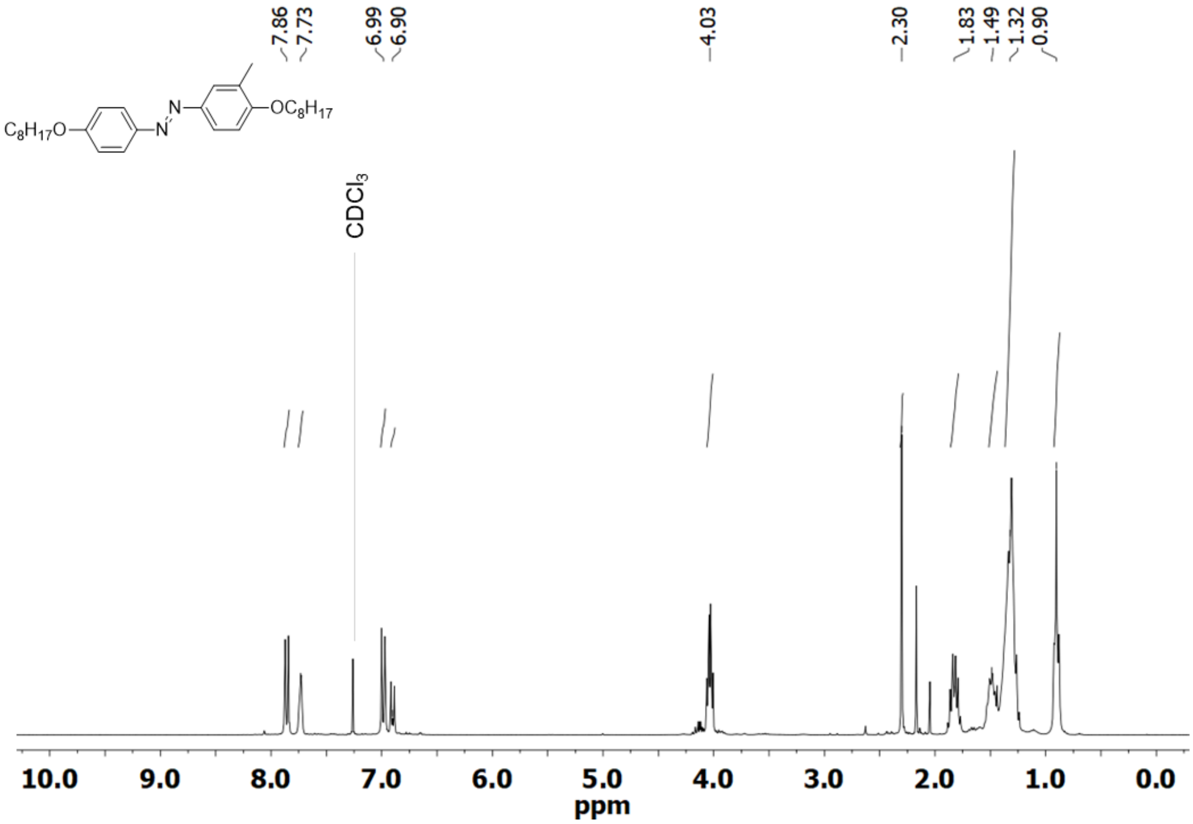

Synthesis of 4,4’-didecyloxy-3-methylazobenzene

A mixture of 4,4’-dihydroxy-3-methylazobenzene (0.442 g, 1.94 mmol, 1.00 equiv.), 1-bromodecane (0.96 g, 4.36 mmol, 2.25 equiv.), K_2CO_3 (2.15 g, 15.5 mmol, 8.00 equiv.), and a catalytic amount of potassium iodide in 24 mL of N,N-dimethylformamide was heated at 95 ºC for 24 h. The reaction mixture was cooled down to room temperature, neutralized using 1 M $HCl_{(aq)}$ and then extracted with chloroform (3 × 20 mL). The combined organic phase was washed with water (1 × 20 mL) and brine (1 × 20 mL). The organic phase was dried over $MgSO_4$ and the solvent evaporated under reduced pressure. The residue was purified by flash chromatography over silica gel (gradient from 100% hexane to 100% ethyl acetate) to give 4,4’-didecyloxy-3-methylazobenzene as a yellow solid (0.8 g, 80% yield). ^{1}H-RMN (300 MHz, $CDCl_3$) δ 7.85 (d, J = 8.80 Hz, 2H), 7.73 (m, 2H), 6.98 (d, J = 8.95 Hz, 2H), 6.90 (d, J = 9.48 Hz, 1H), 4.03 (m, 4H), 2.30 (s, 3H), 1.82 (m, 4H), 1.49 (m, 4H), 1.31 (m, 24H), 0.89 (m, 6H).

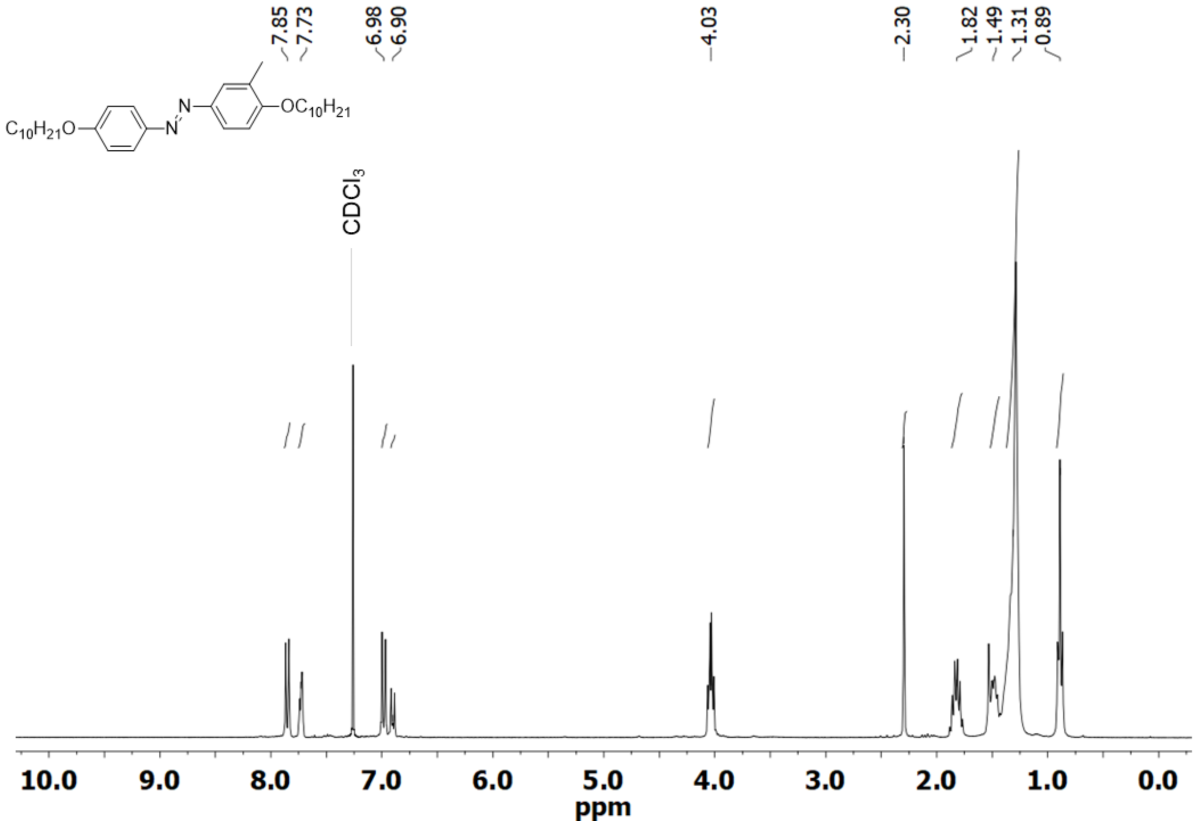

Synthesis of 4,4’-ditetradecyloxy-3-methylazobenzene

A mixture of 4,4’-dihydroxy-3-methylazobenzene (0.801 g, 3.50 mmol, 1.00 equiv.), 1-bromotetradecane (2.23 g, 8.05 mmol, 2.30 equiv.) K_2CO_3 (1.21 g, 8.75 mmol, 2.50 equiv.), and a catalytic amount of potassium iodide in 40 mL of N,N-dimethylformamide was heated at 95 ºC for 24 h. The reaction mixture was cooled to room temperature, neutralized using 1 M $HCl_{(aq)}$ and then extracted with diethyl ether (3 × 20 mL). The combined organic phase was washed with water (1 × 20 mL) and brine (1 × 20 mL). The organic phase was dried over $MgSO_4$, and the solvent evaporated under reduced pressure. The residue was dissolved in diethyl ether/hexane (1:9) and filtrated through a short pad of silica gel to give 4,4’-ditetradecyloxy-3-methylazobenzene as an orange powder (1.48 g, 68% yield). ^{1}H-RMN (500 MHz, $CDCl_3$) δ 7.85 (d, *J* = 8.91 Hz, 2H), 7.72 (m, 2H), 6.98 (d, *J* = 8.94 Hz, 2H), 6.90 (d, *J* = 9.26 Hz, 1H), 4.05 (m, 4H), 2.30 (s, 3H), 1.83 (m, 4H), 1.49 (m, 4H), 1.34 (m, 40H), 0.90 (m, 6H).

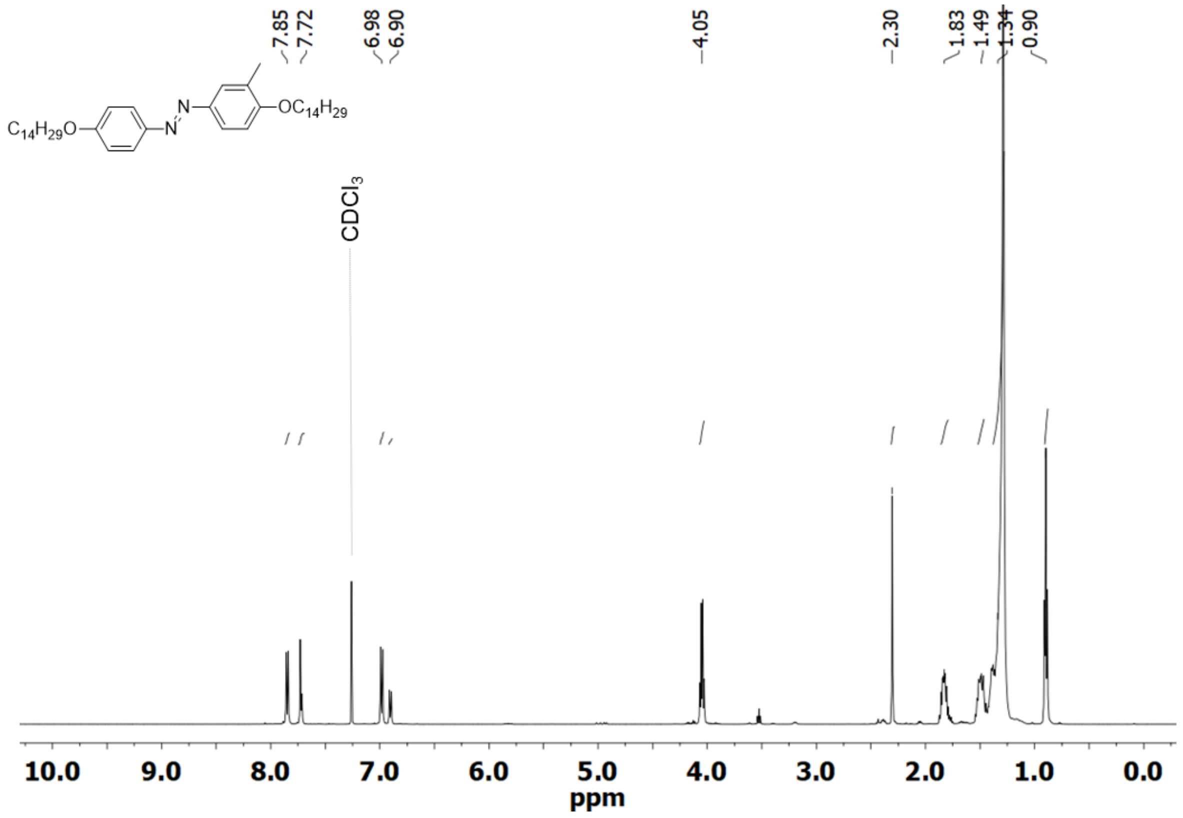

ANNEX II: RESUMO EN GALEGO

A consecución dunha xestión eficiente da enerxía térmica constitúe un desafío fundamental en múltiples ámbitos tecnolóxicos. Con todo, as esixencias en termos de transporte térmico varían significativamente en función da aplicación: nos dispositivos electrónicos de alta potencia, é necesario disipar de maneira eficaz o calor xerado durante o seu funcionamento, o que require o uso de materiais con alta condutividade térmica; pola contra, en aplicacións como o illamento térmico, a refrixeración ou os dispositivos termoeléctricos –nos que resulta esencial manter un gradiente de temperatura– son precisos materiais con condutividades térmicas extremadamente baixas.

Historicamente, o transporte de calor foi considerado unha propiedade pasiva dos materiais, determinada por parámetros intrínsecos como a composición química, a estrutura cristalina ou a concentración de defectos. En consecuencia, os materiais eran deseñados para presentar condutividades térmicas altas ou baixas segundo a súa funcionalidade prevista. Non obstante, a posibilidade de modular de forma dinámica o transporte térmico (é dicir, conmutar entre estados de alta e baixa condutividade térmica segundo se requira) suporía unha verdadeira revolución na xestión térmica adaptativa e na electrónica de baixo consumo. Do mesmo xeito que os semicondutores transformaron a electrónica ao permitir a modulación controlada do transporte eléctrico, un avance análogo no campo térmico pasaría por materiais cuxa condutividade poida ser controlada externamente.

Porén, a manipulación precisa do transporte térmico é moito máis complexa que o control do transporte eléctrico. A diferenza da corrente eléctrica, que pode circular selectivamente a través de condutores e ser detida por illantes, todos os materiais conducen calor, en maior ou menor medida, o que dificulta enormemente o seu control. Ademais, o estudo do transporte térmico enfronta diversas limitacións, tanto teóricas como experimentais. No plano teórico, cómpre considerar a coexistencia de distintos portadores de enerxía –como fonóns, electrón, magnóns, etc.–, cuxo comportamento varía segundo o sistema; ademais, as interaccións entre estes portadores son difíciles de modelar, e a resistencia térmica nas interfaces entre materiais diferentes (como metais, óxidos ou semicondutores) resulta especialmente complexa de predicir. Por outra banda, na escala nanométrica, o transporte térmico pasa dun réxime difusivo a un réxime balístico, para o cal os modelos clásicos (como a lei de Fourier) deixan de ser válidos. No plano experimental, a universalidade da condución térmica fai difícil illar os mecanismos específicos de transporte; ademais, a medida da condutividade en mostras con xeometrías non ideais introduce incertezas significativas, e as técnicas actuais atopan limitacións para caracterizar con precisión o fluxo térmico en sistemas cada vez máis miniaturizados.

Neste contexto, esta tese ten como obxectivo contribuír ao avance no campo da xestión do calor mediante a exploración do control activo do transporte térmico en mesofases e películas delgadas de óxidos complexos, coa intención de reformular o papel da condutividade térmica como unha magnitude funcional e modulable, máis alá da súa tradicional consideración como unha propiedade pasiva asociada á estrutura do material. O propósito xeral deste traballo é desenvolver interruptores térmicos, entendidos como materiais nos que a condutividade térmica poida ser modulada de maneira precisa e reversible baixo demanda, mediante a aplicación de estímulos externos. Estes materiais adaptativos ofrecen un gran potencial para a implementación de novas funcionalidades, como illamentos térmicos conmutables ou memorias térmicas baseadas no control do fluxo de calor.

Para acadar esta meta, exploráronse catro estratexias complementarias, cada unha baseada nun mecanismo físico específico e aplicada nun tipo de material distinto. Estas catro liñas de investigación, que constitúen os capítulos centrais do traballo (Capítulos 3-6), son:

i) Conmutación da condutividade térmica en mesofases mediante luz UV/Vis.
ii) Uso de reaccións topotácticas reversibles para a modulación térmica en películas delgadas de óxidos complexos.
iii) Control da condutividade térmica en óxidos de transferencia de carga a través da modulación local da concentración de vacantes de osíxeno mediante campos eléctricos.
iv) Enxeñaría de topoloxías polares para a regulación do transporte térmico en superredes ferroeléctricas epitaxiais.

O desenvolvemento destes proxectos require o uso combinado de diversas técnicas de síntese e caracterización, que se describen brevemente a continuación.

Metodoloxía experimental e técnicas de caracterización

Dada a diversidade de materiais e mecanismos abordados nesta tese foi necesario empregar un conxunto amplo de técnicas de síntese e caracterización, co fin de obter un control preciso sobre a composición, estrutura e propiedades térmicas dos sistemas analizados.

No Capítulo 3 investigouse a modulación da condutividade térmica en mesofases baseadas en derivados de azobenceno. Estes compostos foron sintetizados mediante unha ruta multietapa de síntese orgánica, que consiste na formación inicial dun núcleo azobencénico funcionalizado, seguida da súa alquilación mediante bromuros de cadeas lineais. De esta forma, sintetizáronse derivados de azobenceno con diferentes lonxitudes de cadea alquílica, entre 3 de 14 átomos de carbono, o que permitiu controlar a estabilización dunha fase de cristal líquido a temperaturas intermedias para os compostos con 8 e 10 átomos de carbono. A caracterización estrutural destas moléculas realizouse mediante espectroscopia de resonancia magnética de protón (^{1}H-NMR), co fin de garantir a súa pureza estrutural. Esta caracterización foi complementada con calorimetría diferencial de varrido (DSC), para determinar as transicións de fase que estes compostos experimentan ao variar a temperatura; e microscopia óptica de luz polarizada (POM), para identificar a natureza das diferentes fases (sólido cristalino, cristal líquido ou líquido isotrópico).

As películas delgadas de óxidos complexos (xeralmente, materiais con estrutura tipo perovskita ABO_3) estudados nos Capítulos 4 e 5 foron sintetizados mediante deposición por láser pulsado (PLD), unha técnica de deposición física en fase vapor que permite o crecemento epitaxial controlado dos materiais a partir de brancos cerámicos multicatiónicos. Neste proceso, un láser de alta enerxía é empregado para ablacionar o material do branco, xerando unha pluma de plasma dirixido que permite a deposición do material desexado sobre substratos monocristalinos a temperaturas controladas. A técnica destaca pola súa capacidade para transferir de maneira estequiométrica a composición do branco ao substrato, así como pola súa compatibilidade con atmosferas reactivas. En particular, as deposicións realizáronse en atmosferas controladas de O_2, para garantir a correcta incorporación de osíxeno nas estruturas finais. Ademais, para asegurar o crecemento uniforme das películas delgadas, tanto o branco como substrato se mantiveron en rotación continuada durante a deposición.

No Capítulo 6, por outra banda, as superredes epitaxiais de $PbTiO_3/SrTiO_3$ (PTO/STO) foron sintetizadas durante unha estadía de investigación na Universidade de Wisconsin-Madison (supervisada polo Prof. Chang-Beom Eom) mediante a técnica de pulverización catódica por magnetrón ("*RF magnetron sputtering"*) en configuración *off-axis*. Neste proceso, empregamos un plasma de argon ionizado que bombardea dous brancos cerámicos (PTO e STO) dispostos formando 90° respecto ao substrato, permitindo así a deposición alternada de capas de ambos materiais. A presenza dun campo magnético mellora a eficiencia da ionización e estabiliza o plasma, favorecendo unha deposición reproducible e controlada a escala atómica.

A caracterización estrutural das películas delgadas e superredes realizouse mediante técnicas de difracción e reflectividade de raios X (XRD e XRR). A difracción de raios X proporcionou información sobre os parámetros de rede e calidade cristalina das diferentes mostras a través de scans $\omega/2\theta$, ω-scans, e mapas de espazo recíproco (RSM), permitindo tamén a avaliación do estado epitaxial das películas. Pola súa banda, a reflectividade de raios X foi empregada para determinar o grosor, rugosidade e densidade dos filmes e multicapas a partir da análise das oscilacións de Kiessig e do axuste dos datos experimentais a modelos matemáticos.

A nivel morfolóxico e funcional, empregouse a microscopia de forzas atómicas (AFM) en diferentes modos de operación. En particular, utilizouse AFM convencional para caracterizar a topografía superficial e a rugosidade dos substratos e películas delgadas. Ademais, aplicáronse técnicas avanzadas baseadas en AFM para estudar propiedades eléctricas e ferroeléctricas a escala local. En particular, o uso do modo condutor do AFM (C-AFM) permitiu a aplicación de campos eléctricos a través da punta do AFM, mentres que a microscopia de sonda Kelvin (KPFM) foi empregada para cartografar a distribución de potencial superficial e estudar a estabilidade das modificacións inducidas mediante C-AFM. Para o estudo dos dominios ferroeléctricos e texturas topolóxicas nas superredes de PTO/STO, realizáronse experimentos de microscopia de piezoresposta (PFM), durante unha estadía de investigación na Universidade Autónoma de Barcelona.

Por último, a caracterización térmica levouse a cabo mediante dúas técnicas principais, escollidas en función do tipo de mostra. Para os compostos moleculares estudados no Capítulo 3 empregouse o método 3ω, adaptado no grupo de investigación para medir líquidos e mesofases. Esta técnica baséase no uso dunha resistencia metálica (no noso caso, Pt), que actúa tanto como sensor como calefactor. Cando se aplica unha corrente alterna (AC), xéranse unha serie de oscilacións térmicas a partir das cales pode determinarse a condutividade térmica do sistema. Para os sistemas de películas delgadas e superredes (Capítulos 4 a 6), empregouse a técnica de termoreflectancia no dominio da frecuencia (FDTR), unha técnica óptica non destrutiva baseada na modulación de dous láseres (*pump/probe*) a través dunha capa transdutora de Au. A partir do desfase entre ambos láseres é posible determinar a condutividade térmica do sistema. Ademais, a montaxe experimental inclúe un soporte piezoeléctrico para o posicionamento preciso da mostra con resolución micrométrica (polo que é posible medir a condutividade térmica con resolución espacial) e unha celda Intec realizar medidas a diferentes temperaturas.

Este conxunto metodolóxico permitiu abordar, desde unha perspectiva multidisciplinar, os mecanismos estruturais e térmicos que gobernan a modulación activa da condutividade térmica nos diferentes sistemas estudados, garantindo unha análise robusta e exhaustiva dos resultados experimentais que se presentan nas seccións seguintes.

Conmutación da condutividade térmica en mesofases mediante luz UV/Vis.

A primeira liña de traballo (presentada no Capítulo 3) céntrase no estudo de mesofases baseadas en azobenceno, que experimentan unha isomerización *trans-cis* inducida por luz ao seren expostas a radiación UV/Vis. Esta transformación estrutural reversible altera o empaquetamento molecular e as interaccións intermoleculares, influíndo así no transporte térmico.

Neste traballo, variamos sistematicamente a lonxitude da cadea alquílica dos derivados de azobenceno, o que nos permitiu estabilizar fases de cristal líquido a temperaturas intermedias para as cadeas de 8 e 10 átomos de carbono. Esta optimización posibilitou analizar a isomerización *trans*/*cis* durante ciclos de iluminación UV/Vis, en función tanto da lonxitude da cadea alquílica como da fase inicial do sistema (sólido cristalino ou cristal líquido). Desta forma, foi posible optimizar tanto a velocidade de resposta como o contraste térmico asociado ao cambio de fase. En concreto, os maiores contrastes térmicos observáronse a temperatura ambiente para a cadea de 10 átomos de carbono, cun cambio de condutividade térmica próximo ao 35 %; con todo, este efecto vén acompañado dunha resposta lenta, no rango das horas. Aumentando a temperatura de iluminación –de modo que o sistema se atope inicialmente na fase de cristal líquido– conséguese acelerar a resposta, aínda que a costa dun menor contraste térmico, que neste caso ronda o 10 %.

Co obxectivo de combinar grandes contrastes térmicos con altas velocidades de resposta, exploramos a incorporación destes derivados de azobenceno como dopantes fotoactivos en matrices comerciais de cristais líquidos. Partimos da hipótese de que a isomerización das moléculas dopantes podería desestabilizar a orde estrutural da matriz hóspede, modulando así a condutividade térmica do conxunto. Esta estratexia permitiunos demostrar que a isomerización das moléculas de azobenceno induciu cambios bidireccionais na condutividade térmica, cunha resposta rápida, alta estabilidade e excelente ciclabilidade. Estes resultados establecen a luz como un estímulo eficaz, sen contacto, para o control dinámico do fluxo de calor en materiais brandos.

Uso de reaccións topotácticas reversibles para a modulación térmica en películas delgadas de óxidos complexos.

A segunda liña de investigación, desenvolvida no Capítulo 4, céntrase na exploración de transicións de fase redox topotácticas como mecanismo funcional para modular o transporte térmico en películas delgadas de óxidos de transferencia de carga negativa. En concreto, estudouse a conversión reversible entre as estruturas brownmillerita (Ca,Sr)FeO$_{2.5}$ e perovskita (Ca,Sr)FeO$_3$. Esta transformación implica un proceso de inserción/extracción de ións O^{2-} na rede cristalina, que altera substancialmente a conectividade estrutural, a simetría e, en consecuencia, as propiedades físicas do material, incluída a condutividade térmica. A natureza topotáctica destas transicións –nas que se conserva a continuidade estrutural entre as fases inicial e final– permite (a priori) modificar o estado funcional do sistema sen comprometer a súa integridade mecánica ou estrutural, o que as converte nun enfoque altamente atractivo para dispositivos conmutables.

Para avaliar a viabilidade deste mecanismo para o desenvolvemento de interruptores térmicos, estudáronse tres rutas de oxidación complementarias: a oxidación química en disolución acuosa ($NaOCl/H_2O$), a oxidación en fase gasosa (O_3/O_2) e a oxidación electroquímica mediante un electrólito sólido (YSZ). Os resultados revelaron que a reversibilidade da transición brownmillerita-perovskita depende de maneira crítica da ruta de oxidación escollida.

En concreto, observouse que a oxidación química en disolución acuosa conduce á degradación irreversible da estrutura cristalina, debido á inestabilidade inherente dos óxidos de transferencia de carga en medios líquidos. A oxidación en fase gasosa ofrece unha mellor estabilidade estrutural, pero a acumulación progresiva de defectos acaba provocando problemas de irreversibilidade tras varios ciclos de oxidación/redución. Pola contra, a oxidación electroquímica mediante un electrólito sólido de YSZ permite a inserción/extracción completamente reversible de O^{2-}, resultando nun cambio estable e repetible da condutividade térmica cun contraste térmico próximo a ≈2. Neste caso, o fluxo directo de ións O^{2-} a través do electrólito, impulsado pola aplicación dun potencial eléctrico, permite oxidar ou reducir o material de forma controlada e sen degradación da rede.

Estes achados revelan o papel esencial do control iónico na estabilización de estados térmicos non volátiles en óxidos, e ofrecen un camiño prometedor cara ao deseño de memorias térmicas ou dispositivos de conmutación baseados en oxidación/redución topotáctica.

Control da condutividade térmica en óxidos de transferencia de carga a través da modulación local da concentración de vacantes de osíxeno mediante campos eléctricos.

A terceira estratexia, presentada no Capítulo 5, céntrase no control da concentración de vacantes de osíxeno mediante a aplicación de campos eléctricos en películas delgadas de óxidos de transferencia de carga, concretamente en $SrFeO_{3-x}$ e $La_{0.6}Sr_{0.4}CoO_{3-x}$. Para tal fin, aplicáronse campos eléctricos localizados mediante a punta dun microscopio de forza atómica (AFM), o que permitiu inducir a acumulación controlada de vacantes de osíxeno en rexións específicas do material. A introdución controlada destes defectos ten un efecto directo sobre a condutividade térmica, reducíndoa significativamente nas zonas afectadas sen danar a morfoloxía superficial nin comprometer a integridade estrutural do material. Este enfoque permite escribir patróns térmicos de forma micrométrica, creando áreas funcionalmente distintas con diferentes propiedades de transporte de calor, algo semellante ao almacenamento ou procesamento de información en dispositivos electrónicos.

Os estados modificados resultaron ser estables baixo condicións ambientais, demostrando carácter non volátil. Ademais, puideron ser completamente revertidos mediante un leve quentamento en aire, o que posibilita o borrado e reescritura de patróns térmicos de forma controlada. En contraste, óxidos con comportamento de tipo Mott-Hubbard, como $La_{0.7}Sr_{0.3}MnO_3$, experimentaron degradacións irreversibles baixo as mesmas condicións, subliñando a importancia de seleccionar adecuadamente os materiais en función da súa estrutura electrónica.

A capacidade de escribir, borrar e reprogramar estados térmicos de maneira non destrutiva mediante campos eléctricos localizados introduce un novo paradigma no ámbito da xestión térmica activa, con importantes implicacións para o desenvolvemento de memorias térmicas, lóxica baseada en calor e dispositivos de computación fonónica. Esta metodoloxía combina resolución espacial, reversibilidade funcional e estabilidade temporal, ofrecendo unha ruta viable para a modulación dinámica do transporte de calor en dispositivos a escala nanométrica.

Ao permitir a manipulación precisa do fluxo térmico sen alterar fisicamente a superficie nin recorrer a transformacións estruturais permanentes, este enfoque representa un avance significativo cara á implementación de arquitecturas térmicas intelixentes, reconfigurables e integrables en sistemas electrónicos avanzados.

Enxeñaría de topoloxías polares para a regulación do transporte térmico en superredes ferroeléctricas epitaxiais.

A cuarta e última estratexia desenvolvida nesta tese preséntase no Capítulo 6. Neste caso, investigouse a modulación do transporte térmico mediante a manipulación de arquitecturas polares en superredes ferroeléctricas epitaxiais de PbTiO$_3$/SrTiO$_3$ (PTO/STO). A través do axuste preciso da tensión epitaxial (controlada a través da elección do substrato) e da periodicidade da superrede, foi posible estabilizar unha ampla variedade de arquitecturas polares, incluíndo dominios ferroeléctricos convencionais do tipo a$_1$/a$_2$ ou patróns de peche de fluxo (dominios *flux-closure*), e texturas polares máis complexas como ondas dipolares (*dipole waves*) e supercristais tridimensionais.

A hipótese que motivou este estudo partía da premisa de que a presenza de distribucións espaciais non triviais da polarización –particularmente aquelas con rotación continua ou modulación lateral a escala nanométrica– pode actuar como fonte de dispersión para os fonóns, afectando así de maneira directa ao transporte térmico. Estes patróns introducen gradientes internos de tensión, campos eléctricos locais e barreiras de simetría que interfiren co desprazamento colectivo dos fonóns.

As medidas de condutividade térmica amosaron que estas superredes de PTO/STO presentan condutividades térmicas sistematicamente inferiores ás de sistemas similares con densidades de interfaces comparables. Este comportamento atribúese a unha dispersión fonónica intensificada, causada pola rotación continua da polarización, os gradientes laterais de tensión e as inhomoxeneidades dipolares a escala nanométrica intrínsecas ás texturas de polarización. Ademais, observouse que a organización tridimensional da polarización nunha estrutura de supercristal conduce a unha redución adicional da condutividade térmica, evidenciando un novo grao de liberdade para a manipulación do fluxo de calor mediante o deseño de arquitecturas ferroeléctricas complexas. Asemade, estas estruturas son termicamente inestables e responden á temperatura de forma reversible, o que permite a implementación de interruptores térmicos sensibles á temperatura baseados en mecanismos ferroeléctricos.

En conxunto, este capítulo demostra que a topoloxía da polarización pode empregarse como parámetro de deseño para controlar de maneira activa e funcional a condutividade térmica en materiais ferroeléctricos. Estes resultados abren unha nova liña de investigación na intersección entre ferroelectricidade, transporte de fonóns e enxeñaría de materiais intelixentes, na que a manipulación de texturas polares emerxe como unha ferramenta prometedora para o deseño de dispositivos térmicos programables, adaptativos e de alta resolución espacial.

Conclusións xerais

Conxuntamente, os resultados presentados nesta tese demostran que a modulación activa da condutividade térmica pode acadarse mediante unha gran variedade de mecanismos materiais, cada un con características propias en termos de contraste, reversibilidade, velocidade de resposta, resolución espacial e estabilidade a longo prazo. Ademais, estes estudos poñen de manifesto a notable sensibilidade da condutividade térmica fronte a variacións sutís na orde estrutural, na estequiometría e na configuración da polarización ferroeléctrica, o que subliña o seu valor non só como magnitude funcional en dispositivos, senón tamén como ferramenta indirecta para sondar o estado interno dos materiais a escala nanométrica.

Nun plano máis amplo, esta tese contribúe ao establecemento dun novo marco conceptual no que a condutividade térmica deixa de ser unha simple consecuencia pasiva da natureza dun material, para converterse nunha propiedade activamente sintonizable e funcionalmente útil. A posibilidade de controlar o transporte térmico con precisión, de forma reversible e con estimulación externa, abre a porta a novas aplicacións en tecnoloxías de enerxía, electrónica flexible, sensores intelixentes, illamentos adaptativos ou computación baseada en calor.

Máis aló das aplicacións inmediatas, este traballo establece un conxunto de principios de deseño e fundamentos físicos que servirán de guía para futuras investigacións no ámbito do desenvolvemento de interruptores térmicos e da modulación controlada do transporte de calor.

BIBLIOGRAPHY

1. A. L. Moore, L. Shi, Emerging challenges and materials for thermal management of electronics. *Materials Today* **17**, 163–174 (2014).

2. D. G. Cahill, W. K. Ford, K. E. Goodson, G. D. Mahan, A. Majumdar, H. J. Maris, R. Merlin, S. R. Phillpot, Nanoscale thermal transport. *J Appl Phys* **93**, 793–818 (2003).

3. X. Qian, J. Zhou, G. Chen, Phonon-engineered extreme thermal conductivity materials. *Nat Mater* **20**, 1188–1202 (2021).

4. J. F. Rivadulla Fernández, *Termodinámica Estadística y Fenómenos de Transporte* (USC editora manuais, Santiago de Compostela, 2017).

5. S. J. Blundell, K. M. Blundell, *Concepts in Thermal Physics* (Oxford University Press, Great Britain, ed. 2nd, 2010).

6. P. Atkins, J. De Paula, *Physical Chemistry* (W. H. Freeman and Company, New York, ed. 9th, 2010).

7. R. A. Matula, Electrical resistivity of copper, gold, palladium, and silver. *J Phys Chem Ref Data* **8**, 1147–1298 (1979).

8. E. G. Childs, J. Ericks, Lewis, R. L. Powell, *Thermal Conductivity of Solids at Room Temperature and below: A Review and Complication of the Literature* (National Bureau of Standards, 1973).

9. N. F. Muhamad, R. A. Maulat Osman, M. S. Idris, M. N. Mohd Yasin, Physical and electrical properties of SrTiO3 and SrZrO3. *EPJ Web Conf* **162**, 01052 (2017).

10. E. Langenberg, E. Ferreiro-Vila, V. Leborán, A. O. Fumega, V. Pardo, F. Rivadulla, Analysis of the temperature dependence of the thermal conductivity of insulating single crystal oxides. *APL Mater* **4**, 104815 (2016).

11. K. Kadoya, N. Matsunaga, A. Nagashima, Viscosity and Thermal Conductivity of Dry Air in the Gaseous Phase. *J Phys Chem Ref Data* **14**, 947–970 (1985).

12. P. Debye, Zur Theorie der spezifischen Wärmen. *Ann Phys* **344**, 789–839 (1912).

13. D. T. Morelli, G. A. Slack, "High lattice thermal conductivity solids" in *High Thermal Conductivity Materials*, S. L. Shindé, J. S. Goela, Eds. (Springer, New York, 2006), pp. 37–68.

14. P. G. Klemens, Thermal Conductivity and Lattice Vibrational Modes. *Solid State Physics - Advances in Research and Applications* **7**, 1–98 (1958).

15. J. M. Ziman, *Principles of the Theory of Solids* (Cambridge University Press, ed. 2nd, 1972).

16. S. Shin, Q. Wang, J. Luo, R. Chen, Advanced Materials for High-Temperature Thermal Transport. *Adv Funct Mater* **30**, 1–23 (2020).

17. C. T. Walker, R. O. Pohl, Phonon scattering by point defects. *Physical Review* **131**, 1433–1442 (1963).

18. H. B. G. Casimir, Note on the conduction of heat in crystals. *Physica* **5**, 495–500 (1938).

19. P. G. Klemens, The scattering of low-frequency lattice waves by static imperfections. *Proceedings of the Physical Society. Section A* **68**, 1113–1128 (1955).

20. S. Kuma, M. M. Woldemariam, Structural, Electronic, Lattice Dynamic, and Elastic Properties of SnTiO3 and PbTiO3 Using Density Functional Theory. *Advances in Condensed Matter Physics* **2019**, 3176148 (2019).

21. E. T. Ritz, N. A. Benedek, Interplay between Phonons and Anisotropic Elasticity Drives Negative Thermal Expansion in PbTiO3. *Phys Rev Lett* **121**, 255901 (2018).

22. K. Nishida, M. Osada, J. Sakai, N. Ito, T. Katoda, R. Ikariyama, H. Funakubo, H. Moriwake, T. Yamamoto, Oxygen vacancies in PbTiO3 thin films probed by resonant Raman spectroscopy. *Journal of the Ceramic Society of Japan* **121**, 598–601 (2013).

23. L. Iglesias, A. Sarantopoulos, C. Magén, F. Rivadulla, Oxygen vacancies in strained SrTiO3 thin films: Formation enthalpy and manipulation. *Phys Rev B* **95**, 165138 (2017).

24. Z. Zhang, P. Wu, L. Lu, C. Shu, Study on vacancy formation in ferroelectric PbTiO3 from ab initio. *Appl Phys Lett* **88**, 142902 (2006).

25. J. Sakai, J. M. C. Roque, P. Vales-Castro, J. Padilla-Pantoja, G. Sauthier, J. Santiso, Pulsed laser deposition of epitaxial non-doped PbTiO3 thin films from PbO-TiO2 mosaic targets. *Coatings* **11**, 662 (2021).

26. D. Bolmatov, V. V. Brazhkin, K. Trachenko, The phonon theory of liquid thermodynamics. *Sci Rep* **2**, 421 (2012).

27. J. Frenkel, *Kinetic Theory of Liquids* (Oxford University Press, 1946).

28. K. Trachenko, V. V. Brazhkin, Collective modes and thermodynamics of the liquid state. *Reports on Progress in Physics* **79**, 016502 (2015).

29. L. Qun-Fang, L. Rui-Sen, N. Dan-Yan, H. Yu-Chun, Thermal conductivities of some organic solvents and their binary mixtures. *J Chem Eng Data* **42**, 971–974 (1997).

30. C. López-Bueno, D. Bugallo, V. Leborán, F. Rivadulla, Sub-µL measurements of the thermal conductivity and heat capacity of liquids. *Physical Chemistry Chemical Physics* **20**, 7277–7281 (2018).

31. L. Manjunatha, H. Takamatsu, J. J. Cannon, Atomic-level breakdown of Green–Kubo relations provides new insight into the mechanisms of thermal conduction. *Sci Rep* **11**, 5597 (2021).

32. J. Kang, L. Wang, First-Principles Green-Kubo Method for Thermal Conductivity Calculations. *Phys Rev B* **96**, 020302(R) (2017).

33. J. Bosse, W. Gotze, M. Lucke, Mode Coupling Theory of Simple Clasical Fluids. *Phys Rev A (Coll Park)* **17**, 434–446 (1978).

34. G. A. Slack, S. Galginaitis, Thermal conductivity and phonon scattering by magnetic impurities in CdTe. *Physical Review* **133**, A253 (1964).

35. M. Asen-Palmer, K. Bartkowski, E. Gmelin, M. Cardona, A. Zhernov, A. Inyushkin, A. Taldenkov, V. Ozhogin, Thermal conductivity of germanium crystals with different isotopic compositions. *Phys Rev B Condens Matter Mater Phys* **56**, 9431–9447 (1997).

36. J. Qu, A. Balvanz, S. Baranets, S. Bobev, P. Gorai, Computational design of thermoelectric alloys through optimization of transport and dopability. *Mater Horiz* **9**, 720–730 (2022).

37. B. Abeles, D. S. Beers, G. D. Cody, J. P. Dismukes, Thermal Conductivity of Ge-Si Alloys at High Temperatures. *Physical Review* **125**, 44–46 (1962).

38. W. Kim, J. Zide, A. Gossard, D. Klenov, S. Stemmer, A. Shakouri, A. Majumdar, Thermal conductivity reduction and thermoelectric figure of merit increase by embedding nanoparticles in crystalline semiconductors. *Phys Rev Lett* **96**, 045901 (2006).

39. B. Poudel, Q. Hao, Y. Ma, Y. Lan, A. Minnich, B. Yu, X. Yan, D. Wang, A. Muto, D. Vashaee, X. Chen, J. Liu, M. S. Dresselhaus, G. Chen, Z. Ren, High-thermoelectric performance of nanostructured bismuth antimony telluride bulk alloys. *Science (1979)* **320**, 634–638 (2008).

40. M. N. Luckyanova, D. Chen, W. Ma, H. L. Tuller, G. Chen, B. Yildiz, Thermal conductivity control by oxygen defect concentration modification in reducible oxides: The case of Pr0.1Ce0.9O2-δ thin films. *Appl Phys Lett* **104**, 061911 (2014).

41. C. Yu, M. L. Scullin, M. Huijben, R. Ramesh, A. Majumdar, Thermal conductivity reduction in oxygen-deficient strontium titanates. *Appl Phys Lett* **92**, 191911 (2008).

42. B. Duan, Y. Li, J. Li, Y. Gao, P. Zhai, J. Yang, Z. Lu, H. Yang, H. Wang, G. Li, Regulation of oxygen vacancy and reduction of lattice thermal conductivity in ZnO ceramic by high temperature and high pressure method. *Ceram Int* **46**, 26176–26181 (2020).

43. Z. Qu, T. D. Sparks, W. Pan, D. R. Clarke, Thermal conductivity of the gadolinium calcium silicate apatites: Effect of different point defect types. *Acta Mater* **59**, 3841–3850 (2011).

44. D. Bugallo, E. Langenberg, E. Ferreiro-Vila, E. H. Smith, C. Stefani, X. Batlle, G. Catalan, N. Domingo, D. G. Schlom, F. Rivadulla, Deconvolution of Phonon Scattering by Ferroelectric Domain Walls and Point Defects in a PbTiO3Thin Film Deposited in a Composition-Spread Geometry. *ACS Appl Mater Interfaces* **13**, 45679–45685 (2021).

45. A. Sarantopoulos, D. Saha, W. L. Ong, C. Magén, J. A. Malen, F. Rivadulla, Reduction of thermal conductivity in ferroelectric SrTiO3 thin films. *Phys Rev Mater* **4**, 1–5 (2020).

46. M. Royo, C. Escorihuela-Sayalero, J. Íñiguez, R. Rurali, Ferroelectric domain wall phonon polarizer. *Phys Rev Mater* **1**, 051402(R) (2017).

47. J. A. Seijas-Bellido, C. Escorihuela-Sayalero, M. Royo, M. P. Ljungberg, J. C. Wojdeł, J. Íñiguez, R. Rurali, A phononic switch based on ferroelectric domain walls. *Phys Rev B* **96**, 140101(R) (2017).

48. E. Langenberg, D. Saha, M. E. Holtz, J. J. Wang, D. Bugallo, E. Ferreiro-Vila, H. Paik, I. Hanke, S. Ganschow, D. A. Muller, L. Q. Chen, G. Catalan, N. Domingo, J. Malen, D. G. Schlom, F. Rivadulla, Ferroelectric Domain Walls in PbTiO3 Are Effective Regulators of Heat Flow at Room Temperature. *Nano Lett* **19**, 7901–7907 (2019).

49. E. Langenberg, H. Paik, E. H. Smith, H. P. Nair, I. Hanke, S. Ganschow, G. Catalan, N. Domingo, D. G. Schlom, Strain-Engineered Ferroelastic Structures in PbTiO3 Films and Their Control by Electric Fields. *ACS Appl Mater Interfaces* **12**, 20691–20703 (2020).

50. A. Sood, R. Cheaito, T. Bai, H. Kwon, Y. Wang, C. Li, L. Yates, T. Bougher, S. Graham, M. Asheghi, M. Goorsky, K. E. Goodson, Direct Visualization of Thermal Conductivity Suppression Due to Enhanced Phonon Scattering Near Individual Grain Boundaries. *Nano Lett* **18**, 3466–3472 (2018).

51. H. S. Yang, G. R. Bai, L. J. Thompson, J. A. Eastman, Interfacial thermal resistance in nanocrystalline yttria-stabilized zirconia. *Acta Mater* **50**, 2309–2317 (2002).

52. A. Filatova-Zalewska, Z. Litwicki, K. Moszak, W. Olszewski, K. Opołczyńska, D. Pucicki, J. Serafińczuk, D. Hommel, A. Jeżowski, Anisotropic thermal conductivity of AlGaN/GaN superlattices. *Nanotechnology* **32**, 075707 (2021).

53. G. Chen, C. L. Tien, X. Wu, J. S. Smith, Thermal diffusivity measurement of GaAs/AlGaAs thin-film structures. *J Heat Transfer* **116**, 325–331 (1994).

54. X. Y. Yu, G. Chen, A. Verma, J. S. Smith, Temperature dependence of thermophysical properties of GaAs/AlAs periodic structure. *Appl Phys Lett* **67**, 3554–3556 (1995).

55. T. Yao, Thermal properties of AlAs/GaAs superlattices. *Appl Phys Lett* **51**, 1798–1800 (1987).

56. G. Chen, Non-Fourier phonon heat conduction at the microscale and nanoscale. *Nature Reviews Physics* **3**, 555–569 (2021).

57. M. Maldovan, Phonon wave interference and thermal bandgap materials. *Nat Mater* **14**, 667–674 (2015).

58. M. N. Luckyanova, J. Garg, K. Esfarjani, A. Jandl, M. T. Bulsara, A. J. Schmidt, A. J. Minnich, S. Chen, M. S. Dresselhaus, Z. Ren, E. a Fitzgerald, G. Chen, Coherent Phonon Heat Conduction in Superlattices. *Science (1979)* **338**, 936–939 (2012).

59. D. Bugallo, E. Langenberg, E. Carbó-Argibay, N. Varela Dominguez, A. O. Fumega, V. Pardo, I. Lucas, L. Morellón, F. Rivadulla, Tuning Coherent-Phonon Heat Transport in LaCoO3/SrTiO3 Superlattices. *Journal of Physical Chemistry Letters* **12**, 11878–11885 (2021).

60. J. Ravichandran, A. K. Yadav, R. Cheaito, P. B. Rossen, A. Soukiassian, S. J. Suresha, J. C. Duda, B. M. Foley, C. H. Lee, Y. Zhu, A. W. Lichtenberger, J. E. Moore, D. A. Muller, D. G. Schlom, P. E. Hopkins, A. Majumdar, R. Ramesh, M. A. Zurbuchen, Crossover from incoherent to coherent phonon scattering in epitaxial oxide superlattices. *Nat Mater* **13**, 168–172 (2014).

61. M. V. Simkin, G. D. Mahan, Minimum Thermal Conductivity of Superlattices. *Phys Rev Lett* **84**, 927–930 (2000).

62. M. Maldovan, Sound and heat revolutions in phononics. *Nature* **503**, 209–217 (2013).

63. J. Maire, R. Anufriev, R. Yanagisawa, A. Ramiere, S. Volz, M. Nomura, Heat conduction tuning by wave nature of phonons. *Sci Adv* **3**, 1–6 (2017).

64. J. K. Yu, S. Mitrovic, D. Tham, J. Varghese, J. R. Heath, Reduction of thermal conductivity in phononic nanomesh structures. *Nat Nanotechnol* **5**, 718–721 (2010).

65. N. Zen, T. A. Puurtinen, T. J. Isotalo, S. Chaudhuri, I. J. Maasilta, Engineering thermal conductance using a two-dimensional phononic crystal. *Nat Commun* **5**, 3435 (2014).

66. R. Juneja, A. K. Singh, Rattling-Induced Ultralow Thermal Conductivity Leading to Exceptional Thermoelectric Performance in AgIn5S8. *ACS Appl Mater Interfaces* **11**, 33894–33900 (2019).

67. G. Nolas, J. Cohn, G. A. Slack, Effect of partial void filling on the lattice thermal conductivity of skutterudites. *Phys Rev B Condens Matter Mater Phys* **58**, 164–170 (1998).

68. T. Takabatake, K. Suekuni, T. Nakayama, E. Kaneshita, Phonon-glass electron-crystal thermoelectric clathrates: Experiments and theory. *Rev Mod Phys* **86**, 669–716 (2014).

69. M. Christensen, A. B. Abrahamsen, N. B. Christensen, F. Juranyi, N. H. Andersen, K. Lefmann, J. Andreasson, C. R. H. Bahl, B. B. Iversen, Avoided crossing of rattler modes in thermoelectric materials. *Nat Mater* **7**, 811–815 (2008).

70. C. López-Bueno, M. Suárez-Rodríguez, A. Amigo, F. Rivadulla, Hydrophobic solvation increases thermal conductivity of water. *Physical Chemistry Chemical Physics* **22**, 21094–21098 (2020).

71. J. Jia, S. Li, X. Chen, Y. Shigesato, Emerging Solid–State Thermal Switching Materials. *Adv Funct Mater* **34**, 2406667 (2024).

72. K. Yuan, J. Shi, W. Aftab, M. Qin, A. Usman, F. Zhou, Y. Lv, S. Gao, R. Zou, Engineering the Thermal Conductivity of Functional Phase-Change Materials for Heat Energy Conversion, Storage, and Utilization. *Adv Funct Mater* **30**, 1904228 (2020).

73. H. Kizuka, T. Yagi, Temperature dependence of thermal conductivity of VO2 thin folms across metal-insulator transition. *Jpn J Appl Phys* **54**, 053201 (2015).

74. C. López-Bueno, M. R. Bittermann, B. Dacuña-Mariño, A. L. Llamas-Saiz, M. Del Carmen Giménez-López, S. Woutersen, F. Rivadulla, Low temperature glass/crystal transition in ionic liquids determined by H-bond Vs. coulombic strength. *Physical Chemistry Chemical Physics* **22**, 20524–20530 (2020).

75. R. Zheng, J. Gao, J. Wang, G. Chen, Reversible temperature regulation of electrical and thermal conductivity using liquid-solid phase transitions. *Nat Commun* **2**, 289 (2011).

76. J. Yang, Y. Yang, S. W. Waltermire, X. Wu, H. Zhang, T. Gutu, Y. Jiang, Y. Chen, A. A. Zinn, R. Prasher, T. T. Xu, D. Li, Enhanced and switchable nanoscale thermal conduction due to van der Waals interfaces. *Nat Nanotechnol* **7**, 91–95 (2012).

77. X. Meng, T. Pandey, J. Jeong, S. Fu, J. Yang, K. Chen, A. Singh, F. He, X. Xu, J. Zhou, W. P. Hsieh, A. K. Singh, J. F. Lin, Y. Wang, Thermal Conductivity Enhancement in MoS2 under Extreme Strain. *Phys Rev Lett* **122**, 155901 (2019).

78. T. Du, Z. Xiong, L. Delgado, W. Liao, J. Peoples, R. Kantharaj, P. R. Chowdhury, A. Marconnet, X. Ruan, Wide range continuously tunable and fast thermal switching based on compressible graphene composite foams. *Nat Commun* **12**, 4915 (2021).

79. H. Babaei, K. R. Meihaus, J. R. Long, Reversible Thermal Conductivity Switching Using Flexible Metal-Organic Frameworks. *Chemistry of Materials* **35**, 6220–6226 (2023).

80. J. J. Wang, Y. Wang, J. F. Ihlefeld, P. E. Hopkins, L. Q. Chen, Tunable thermal conductivity via domain structure engineering in ferroelectric thin films: A phase-field simulation. *Acta Mater* **111**, 220–231 (2016).

81. J. F. Ihlefeld, B. M. Foley, D. A. Scrymgeour, J. R. Michael, B. B. McKenzie, D. L. Medlin, M. Wallace, S. Trolier-Mckinstry, P. E. Hopkins, Room-temperature voltage tunable phonon thermal conductivity via reconfigurable interfaces in ferroelectric thin films. *Nano Lett* **15**, 1791–1795 (2015).

82. B. M. Foley, M. Wallace, J. T. Gaskins, E. A. Paisley, R. L. Johnson-Wilke, J. W. Kim, P. J. Ryan, S. Trolier-Mckinstry, P. E. Hopkins, J. F. Ihlefeld, Voltage-Controlled Bistable Thermal Conductivity in Suspended Ferroelectric Thin-Film Membranes. *ACS Appl Mater Interfaces* **10**, 25493–25501 (2018).

83. K. Aryana, J. A. Tomko, R. Gao, E. R. Hoglund, T. Mimura, S. Makarem, A. Salanova, M. S. Bin Hoque, T. W. Pfeifer, D. H. Olson, J. L. Braun, J. Nag, J. C. Read, J. M. Howe, E. J. Opila, L. W. Martin, J. F. Ihlefeld, P. E. Hopkins, Observation of solid-state bidirectional thermal conductivity switching in antiferroelectric lead zirconate (PbZrO3). *Nat Commun* **13**, 1573 (2022).

84. C. Liu, Y. Si, H. Zhang, C. Wu, S. Deng, Y. Dong, Y. Li, M. Zhuo, N. Fan, B. Xu, P. Lu, L. Zhang, X. Lin, X. Liu, J. Yang, Z. Luo, S. Das, L. Bellaiche, Y. Chen, Z. Chen, Low voltage–driven high-performance thermal switching in antiferroelectric PbZrO3 thin films. *Science (1979)* **382**, 1265–1269 (2023).

85. J. Cho, M. D. Losego, H. G. Zhang, H. Kim, J. Zuo, I. Petrov, D. G. Cahill, P. V. Braun, Electrochemically tunable thermal conductivity of lithium cobalt oxide. *Nat Commun* **5**, 4035 (2014).

86. A. Sood, F. Xiong, S. Chen, H. Wang, D. Selli, J. Zhang, C. J. McClellan, J. Sun, D. Donadio, Y. Cui, E. Pop, K. E. Goodson, An electrochemical thermal transistor. *Nat Commun* **9**, 4510 (2018).

87. Z. Bian, Q. Yang, M. Yoshimura, H. J. Cho, J. Lee, H. Jeen, T. Endo, Y. Matsuo, H. Ohta, Solid-State Electrochemical Thermal Transistors with Strontium Cobaltite-Strontium Ferrite Solid Solutions as the Active Layers. *ACS Appl Mater Interfaces* **15**, 23512–23517 (2023).

88. Y. Norikane, E. Uchida, S. Tanaka, K. Fujiwara, H. Nagai, Photoinduced Phase Transitions in Rod-shaped Azobenzene with Different Alkyl Chain Length. *J. Photopolym. Sci. Technol.* **29**, 149–157 (2016).

89. Y. Norikane, E. Uchida, S. Tanaka, K. Fujiwara, E. Koyama, R. Azumi, H. Akiyama, H. Kihara, M. Yoshida, Photoinduced crystal-to-liquid phase transitions of azobenzene derivatives and their application in photolithography processes through a solid-liquid patterning. *Org Lett* **16**, 5012–5015 (2014).

90. N. A. Shepelin, Z. P. Tehrani, N. Ohannessian, C. W. Schneider, D. Pergolesi, T. Lippert, A practical guide to pulsed laser deposition. *Chem Soc Rev* **52**, 2294–2321 (2023).

91. D. P. Norton, "Pulsed laser deposition of complex materials: progress towards applications" in *Pulsed Laser Deposition of Thin Films*, R. Eason, Ed. (Jon Wiley & Sons, Hoboken, New Jersey, 2007), pp. 3–31.

92. M. A. Khan, T. P. Comyn, A. J. Bell, Deposition of PbTiO3 films on Pt/Si substrates using pulsed laser deposition. *J Eur Ceram Soc* **28**, 591–597 (2008).

93. P. J. Kelly, R. D. Arnell, Magnetron sputtering: A review of recent developments and applications. *Vacuum* **56**, 159–172 (2000).

94. M. Dawber, "Sputtering techniques for epitaxial growth of complex oxides" in *Epitaxial Growth of Complex Metal Oxides*, G. Koster, M. Huijben, G. Rijnders, Eds. (Woodhead Publishing, 2015), pp. 31–45.

95. Y. Deng, W. Chen, B. Li, C. Wang, T. Kuang, Y. Li, Physical vapor deposition technology for coated cutting tools: A review. *Ceram Int* **46**, 18373–18390 (2020).

96. C. B. Eom, J. Z. Sun, K. Yakamoto, A. F. Marshall, K. E. Luther, T. H. Geballe, S. S. Laderman, In situ grown YBa2Cu3O7-d thin films from single-target magnetron sputtering. *Appl Phys Lett* **55**, 595–597 (1989).

97. M. Sardela, "X-ray Diffraction and Reflectivity" in *Practical Materials Characterization*, M. Sardela, Ed. (Springer, New York, 2014), pp. 1–42.

98. M. Birkholz, *Thin Film Analysis by X-Ray Scattering* (Wiley-VCH, Weinheim, 2006).

99. C. B. Vanpeteghem, R. J. Angel, J. Zhao, N. L. Ross, G. J. Redhammer, F. Seifert, The effect of oxygen vacancies and aluminium substitution on the high-pressure properties of brownmillerite-structured Ca2Fe2-xAlxO5. *Phys Chem Miner* **35**, 493–504 (2008).

100. G. Binnig, C. F. Quate, C. Gerber, Atomic Force Microscope. *Phys Rev Lett* **56**, 930–933 (1986).

101. Park Systems, *NX10 User's Manual* (2018; www.parksystems.co.jp).

102. B. Bhushan, O. Marti, "Scanning Probe Microscopy - Principle of Operation, Instrumentation and Probes" in *Springer Handbook of Nanotechnology*, B. Bhushan, Ed. (Springer Berlin Heidelberg, Berlin, 2004), pp. 573–612.

103. W. Melitz, J. Shen, A. C. Kummel, S. Lee, Kelvin probe force microscopy and its application. *Surf Sci Rep* **66**, 1–27 (2011).

104. A. Gruverman, S. V. Kalinin, Piezoresponse force microscopy and recent advances in nanoscale studies of ferroelectrics. *J Mater Sci* **41**, 107–116 (2006).

105. A. Gruverman, M. Alexe, D. Meier, Piezoresponse force microscopy and nanoferroic phenomena. *Nat Commun* **10**, 1661 (2019).

106. A. D. Skoog, F. J. Holler, S. R. Crouch, *Principles of Instrumental Analysis* (Cengage Learning, Boston, USA, ed. 7th, 2018).

107. G. W. H. Höhne, W. F. Hemminger, H.-J. Flammersheim, *Differential Scanning Calorimetry* (Springer Berlin Heidelberg, Berlin, ed. 2nd, 2003).

108. B. Outram, *Liquid Crystals* (IOP Publishing, 2018).

109. D. G. Cahill, Thermal conductivity measurement from 30 to 750 K: The 3ω method. *Review of Scientific Instruments* **61**, 802–808 (1990).

110. S. M. Lee, D. G. Cahill, Heat transport in thin dielectric films. *J Appl Phys* **81**, 2590–2595 (1997).

111. D. G. Cahill, R. O. Pohl, Thermal conductivity of amorphous solids above the plateau. *Phys Rev B* **35**, 4067–4073 (1987).

112. A. J. Schmidt, R. Cheaito, M. Chiesa, A frequency-domain thermoreflectance method for the characterization of thermal properties. *Review of Scientific Instruments* **80**, 094901 (2009).

113. A. Schmidt, M. Chiesa, X. Chen, G. Chen, An optical pump-probe technique for measuring the thermal conductivity of liquids. *Review of Scientific Instruments* **79**, 064902 (2008).

114. C. Yuan, R. Hanus, S. Graham, A review of thermoreflectance techniques for characterizing wide bandgap semiconductors' thermal properties and devices' temperatures. *J Appl Phys* **132**, 220701 (2022).

115. J. Yang, C. Maragliano, A. J. Schmidt, Thermal property microscopy with frequency domain thermoreflectance. *Review of Scientific Instruments* **84**, 104904 (2013).

116. D. G. Cahill, Analysis of heat flow in layered structures for time-domain thermoreflectance. *Review of Scientific Instruments* **75**, 5119–5122 (2004).

117. Y. Takahashi, H. Akiyama, Heat capacity of gold from 80 to 1000 K. *Thermochim Acta* **109**, 105–109 (1986).

118. R. M. Costescu, M. A. Wall, D. G. Cahill, Thermal conductance of epitaxial interfaces. *Phys Rev B Condens Matter Mater Phys* **67**, 054302 (2003).

119. Y. K. Koh, Y. Cao, D. G. Cahill, D. Jena, Heat-transport mechanisms in superlattices. *Adv Funct Mater* **19**, 610–615 (2009).

120. Q. Yang, H. J. Cho, Z. Bian, M. Yoshimura, J. Lee, H. Jeen, J. Lin, J. Wei, B. Feng, Y. Ikuhara, H. Ohta, Solid-State Electrochemical Thermal Transistors. *Adv Funct Mater* **33**, 2214939 (2023).

121. Q. Lu, S. Huberman, H. Zhang, Q. Song, J. Wang, G. Vardar, A. Hunt, I. Waluyo, G. Chen, B. Yildiz, Bi-directional tuning of thermal transport in SrCoOx with electrochemically induced phase transitions. *Nat Mater* **19**, 655–662 (2020).

122. Y. Zhang, W. M. Postiglione, R. Xie, C. Zhang, H. Zhou, V. Chaturvedi, K. Heltemes, H. Zhou, T. Feng, C. Leighton, X. Wang, Wide-range continuous tuning of the thermal

conductivity of La0.5Sr0.5CoO3-δ films via room-temperature ion-gel gating. *Nat Commun* **14**, 2626 (2023).

123. T. Ishibe, T. Kaneko, Y. Uematsu, H. Sato-Akaba, M. Komura, T. Iyoda, Y. Nakamura, Tunable Thermal Switch via Order–Order Transition in Liquid Crystalline Block Copolymer. *Nano Lett* **22**, 6105–6111 (2022).

124. R. Shrestha, Y. Luan, S. Shin, T. Zhang, X. Luo, J. S. Lundh, W. Gong, M. R. Bockstaller, S. Choi, T. Luo, R. Chen, K. Hippalgaonkar, S. Shen, High-contrast and reversible polymer thermal regulator by structural phase transition. *Sci Adv* **5**, 1–8 (2019).

125. T. Zhang, T. Luo, High-contrast, reversible thermal conductivity regulation utilizing the phase transition of polyethylene nanofibers. *ACS Nano* **7**, 7592–7600 (2013).

126. J. A. Tomko, A. Pena-Francesch, H. Jung, M. Tyagi, B. D. Allen, M. C. Demirel, P. E. Hopkins, Tunable thermal transport and reversible thermal conductivity switching in topologically networked bio-inspired materials. *Nat Nanotechnol* **13**, 959–964 (2018).

127. S. Krause, B. L. Feringa, Towards artificial molecular factories from framework-embedded molecular machines. *Nat Rev Chem* **4**, 550–562 (2020).

128. B. L. Feringa, R. A. Van Delden, N. Koumura, E. M. Geertsema, Chiroptical Molecular Switches. *Chem Rev* **100**, 1789–1816 (2000).

129. B. L. Feringa, N. Koumura, R. A. Van Delden, M. K. J. Ter Wiel, Light-driven molecular switches and motors. *Appl Phys A Mater Sci Process* **75**, 301–308 (2002).

130. C. N. Stindt, S. Crespi, R. Toyoda, M. F. Hilbers, J. Kemmink, P. van der Meulen, W. J. Buma, B. L. Feringa, Activating a light-driven molecular motor by metal complexation. *Chem* **9**, 2337–2348 (2023).

131. J. Shin, J. Sung, M. Kang, X. Xie, B. Lee, K. Min, T. J. White, Light-triggered thermal conductivity switching in azobenzene polymers. *Proc Natl Acad Sci U S A* **116**, 5973–5978 (2019).

132. X. Wei, T. Luo, Effect of side-chain π–π stacking on the thermal conductivity switching in azobenzene polymers: a molecular dynamics simulation study. *Physical Chemistry Chemical Physics* **24**, 10272–10279 (2022).

133. I. L. Ngo, S. Jeon, C. Byon, Thermal conductivity of transparent and flexible polymers containing fillers: A literature review. *Int J Heat Mass Transf* **98**, 219–226 (2016).

134. M. L. Huber, A. H. Harvey, *Thermal Conductivity of Gases* (CRC-Press, Boca Raton, 2011).

135. C. Uher, "Thermal conductivity of metals" in *Thermal Conductivity. Physics of Solids and Liquids* (Springer, 2004), pp. 21–91.

136. S. Shen, A. Henry, J. Tong, R. Zheng, G. Chen, Polyethylene nanofibres with very high thermal conductivities. *Nat Nanotechnol* **5**, 251–255 (2010).

137. V. Singh, T. L. Bougher, A. Weathers, Y. Cai, K. Bi, M. T. Pettes, S. A. McMenamin, W. Lv, D. P. Resler, T. R. Gattuso, D. H. Altman, K. H. Sandhage, L. Shi, A. Henry, B.

A. Cola, High thermal conductivity of chain-oriented amorphous polythiophene. *Nat Nanotechnol* **9**, 384–390 (2014).

138. M. Grundler, T. Derieth, A. Heinzel, Polymer compounds with high thermal conductivity. *AIP Conf Proc* **1779**, 030015 (2016).

139. H. Rau, "Photoisomerization of azobenzenes" in *Photoreactive Organic Thin Films* (Elsevier, 2002), pp. 3–47.

140. S. Sun, S. Liang, W. C. Xu, G. Xu, S. Wu, Photoresponsive polymers with multi-Azobenzene groups. *Polym Chem* **10**, 4389–4401 (2019).

141. E. Blasco, M. Piñol, C. Berges, C. Sánchez-Somolinos, L. Oriol, "Smart polymers for optical data storage" in *Smart Polymers and Their Applications* (Woodhead Publishing Limited, 2014), pp. 510–548.

142. T. Ikeda, O. Tsutsumi, Optical Switching and Image Storage by Means of Azobenzene Liquid-Crystal Films. *Science (1979)* **268**, 1873–1875 (1995).

143. T. Yamamoto, Y. Norikane, H. Akiyama, Photochemical liquefaction and softening in molecular materials, polymers, and related compounds. *Polym J* **50**, 551–562 (2018).

144. G. G. Nair, S. K. Prasad, U. S. Hiremath, C. V. Yelamaggad, Effect of light on the polarization of a banana-shaped achiral compound doped with a photoactive azobenzene material. *J Appl Phys* **90**, 48–52 (2001).

145. C. H. Legge, G. R., Mitchell, Photo-induced phase transitions in azobenzene-doped liquid crystals. *J. Phys. D: Appl. Phys.* **25**, 492–499 (1992).

146. H. K. Bisoyi, Q. Li, Light-Driven Liquid Crystalline Materials: From Photo-Induced Phase Transitions and Property Modulations to Applications. *Chem Rev* **116**, 1509–15166 (2016).

147. R. Eelkema, M. M. Pollard, J. Vicario, N. Katsonis, B. S. Ramon, B. C. W. M., D. J. Broer, B. L. Feringa, Nanomotor rotates microscale objects. *Nature* **440**, 163 (2006).

148. M. Moniruzzaman, J. D. R. Talbot, C. J. Sabey, G. F. Fernando, The use of H NMR and UV-vis measurements for quantitative determination of trans/cis isomerization of a photo-responsive monomer and its copolymer. *J Appl Polym Sci* **100**, 1103–1112 (2006).

149. M. J. Stephen, J. P. Straley, Physics of liquid crystals. *Rev Mod Phys* **46**, 617–704 (1974).

150. X. Wei, Z. Wang, Z. Tian, T. Luo, Thermal Transport in Polymers: A Review. *J Heat Transfer* **143**, 072101 (2021).

151. M. Marinelli, F. Mercuri, S. Foglietta, U. Zammit, F. Scudieri, Anisotropic heat transport in the octylcyanobiphenyl (8CB) liquid crystal. *Phys Rev E* **54**, 1604 (1996).

152. G. Ahlers, D. S. Cannell, L. I. Berge, S. Sakurai, Thermal conductivity of the nematic liquid crystal 4-n-pentyl-4'-cyanobiphenyl. *Phys Rev E* **49**, 545–553 (1994).

153. C. Fehr, P. Dieudonné, J. Primera, T. Woignier, J. L. Sauvajol, E. Anglaret, Solid state polymorphism of liquid crystals in confined geometries. *The European Physical Journal E* **12**, 13–16 (2003).

154. J. Thoen, H. Marynissen, W. Van Dael, Temperature dependence of the enthalpy and the heat capacity of the liquid-crystal octylcyanobiphenyl (8CB). *Phys Rev A (Coll Park)* **26**, 2886–2905 (1982).

155. J. R. Günter, H.-R. Oswald, Attempt to a Systematic Classification of Topotactic Reactions. *Bull Inst Chem Res Kyoto Univ* **53**, 249–255 (1975).

156. F. K. Lotgering, Topotactical reactions with ferrimagnetic oxides having hexagonal crystal structures-I. *Journal of Inorganic and Nuclear Chemistry* **9**, 113–123 (1959).

157. R. D. Shannon, R. C. Rossi, Definition of Topotaxy. *Nature* **202**, 1000–1001 (1964).

158. A. R. West, *Solid State Chemistry and Its Applications* (Wiley, ed. 2nd, 2014).

159. K. Mizushima, P. C. Jones, P. J. Wiseman, J. B. Goodenough, LixCoO2 (0<x<1): a new cathode material for batteries of high enery density. *Solid State Ion* **3–4**, 171–174 (1981).

160. M. G. S. R. Thomas, P. G. Bruce, J. B. Goodenough, Lithium mobility in the layered oxide Li1-xCoO2. *Solid State Ion* **17**, 13–19 (1985).

161. Y. L. Lee, J. Kleis, J. Rossmeisl, S. H. Yang, D. Morgan, Prediction of solid oxidefuel cell cathode activity with first-principles descriptors. *Energy Environ Sci* **4**, 3966–3970 (2011).

162. M. Feng, J. Li, S. Zhang, A. Pofelski, R. El Hage, C. Klewe, A. T. N'diaye, P. Shafer, Y. Zhu, G. Galli, I. K. Schuller, Y. Takamura, Hydrogen-Induced Topotactic Phase Transformations of Cobaltite Thin Films. *Journal of Physical Chemistry C* **128**, 17124–17133 (2024).

163. S. He, O. Petracic, V. Lauter, L. Cao, Y. Zhou, M. L. Weber, J. Schubert, O. Concepción, R. Dittmann, R. Waser, T. Brückel, F. Gunkel, La0.6Sr0.4CoO3−δ Films Under Deoxygenation: Magnetic And Electronic Transitions Are Apart from The Structural Phase Transition. *Adv Funct Mater* **34**, 2313208 (2024).

164. E. Ferreiro-Vila, S. Blanco-Canosa, I. Lucas del Pozo, H. B. Vasili, C. Magén, A. Ibarra, J. Rubio-Zuazo, G. R. Castro, L. Morellón, F. Rivadulla, Room-Temperature AFM Electric-Field-Induced Topotactic Transformation between Perovskite and Brownmillerite SrFeOx with Sub-Micrometer Spatial Resolution. *Adv Funct Mater* **29**, 1901984 (2019).

165. Y. Gu, K. Xu, C. Song, X. Zhong, H. Zhang, H. Mao, M. S. Saleem, J. Sun, W. Liu, Z. Zhang, F. Pan, J. Zhu, Oxygen-Valve Formed in Cobaltite-Based Heterostructures by Ionic Liquid and Ferroelectric Dual-Gating. *ACS Appl Mater Interfaces* **11**, 19584–19595 (2019).

166. A. Khare, D. Shin, T. S. Yoo, M. Kim, T. D. Kang, J. Lee, S. Roh, I. H. Jung, J. Hwang, S. W. Kim, T. W. Noh, H. Ohta, W. S. Choi, Topotactic Metal–Insulator Transition in Epitaxial SrFeOx Thin Films. *Advanced MaterialsMaterials* **29**, 1606566 (2017).

167. R. D. Chakraborty, W. M. Postiglione, S. Ghosh, K. A. Mkhoyan, C. Leighton, V. E. Ferry, Optical Properties of Electrochemically Gated La1−xSrxCoO3−δ as a Topotactic Phase-Change Material. *Adv Opt Mater* **11**, 2300098 (2023).

168. H. Jeen, W. S. Choi, M. D. Biegalski, C. M. Folkman, I. C. Tung, D. D. Fong, J. W. Freeland, D. Shin, H. Ohta, M. F. Chisholm, H. N. Lee, Reversible redox reactions in an epitaxially stabilized SrCoO x oxygen sponge. *Nat Mater* **12**, 1057–1063 (2013).

169. T. Yamamoto, S. Kawaguchi, T. Kosuge, A. Sugai, N. Tsunoda, Y. Kumagai, K. Beppu, T. Ohmi, T. Nagase, K. Higashi, K. Kato, K. Nitta, T. Uruga, S. Yamazoe, F. Oba, T. Tanaka, M. Azuma, S. Hosokawa, Emergence of Dynamically-Disordered Phases During Fast Oxygen Deintercalation Reaction of Layered Perovskite. *Advanced Science* **10**, 2301876 (2023).

170. K. McColl, S. W. Coles, P. Zarabadi-Poor, B. J. Morgan, M. S. Islam, Phase segregation and nanoconfined fluid O2 in a lithium-rich oxide cathode. *Nat Mater* **23**, 826–833 (2024).

171. M. Batuk, D. Vandemeulebroucke, M. Ceretti, W. Paulus, J. Hadermann, Topotactic redox cycling in SrFeO2.5+δ explored by 3D electron diffraction in different gas atmospheres. *J Mater Chem A Mater* **11**, 213–220 (2023).

172. J. J. Marie, R. A. House, G. J. Rees, A. W. Robertson, M. Jenkins, J. Chen, S. Agrestini, M. Garcia-Fernandez, K. J. Zhou, P. G. Bruce, Trapped O2 and the origin of voltage fade in layered Li-rich cathodes. *Nat Mater* **23**, 818–825 (2024).

173. W. M. Postiglione, G. Yu, V. Chaturvedi, H. Zhou, K. Heltemes, A. Jacobson, M. Greven, C. Leighton, Mechanisms of Hysteresis and Reversibility across the Voltage-Driven Perovskite-Brownmillerite Transformation in Electrolyte-Gated Ultrathin La0.5Sr0.5CoO3−δ. *ACS Appl Mater Interfaces* **16**, 19184–19197 (2024).

174. Y. Li, W. Guo, D. I. Stroe, H. Zhao, P. Kjær Kristensen, L. Rosgaard Jensen, K. Pedersen, L. Gurevich, Evolution of aging mechanisms and performance degradation of lithium-ion battery from moderate to severe capacity loss scenarios. *Chemical Engineering Journal* **498**, 155588 (2024).

175. X. Wang, H. Zhong, S. Xi, W. S. V. Lee, J. Xue, Understanding of Oxygen Redox in the Oxygen Evolution Reaction. *Advanced Materials* **34**, 2107956 (2022).

176. C. Yang, A. Grimaud, Factors controlling the redox activity of Oxygen in perovskites: From theory to application for catalytic reactions. *Catalysts* **7**, 149 (2017).

177. J. B. Goodenough, Metallic oxides. *Progress in Solid State Chemistry* **5**, 145–399 (1971).

178. J. B. Goodenough, *Magnetism and the Chemical Bond* (John Wiley & Sons, New York, 1963).

179. J. Hombo, Y. Matsumoto, T. Kawano, Electrical conductivities of SrFeO3-δ and BaFeO3-δ perovskites. *J Solid State Chem* **84**, 138–143 (1990).

180. O. I. Barkalov, S. V. Zaitsev, V. D. Sedykh, Strontium ferrite SrFeO3-δ (2.50 ≤ 3-δ ≤ 2.87) studied by Raman and Mössbauer spectroscopy. *Solid State Commun* **354**, 114912 (2022).

181. L. Karvonen, M. Valkeapää, R. S. Liu, J. M. Chen, H. Yamauchi, M. Karppinen, O-K and Co-L XANES study on oxygen intercalation in perovskite SrCoO3-δ. *Chemistry of Materials* **22**, 70–76 (2010).

182. H. Taguchi, M. Shimada, M. Koizumi, The effect of oxygen vacancy on the magnetic properties in the system SrCoO3-δ (0 < δ < 0.5). *J Solid State Chem* **29**, 221–225 (1979).

183. J. R. Petrie, C. Mitra, H. Jeen, W. S. Choi, T. L. Meyer, F. A. Reboredo, J. W. Freeland, G. Eres, H. N. Lee, Strain Control of Oxygen Vacancies in Epitaxial Strontium Cobaltite Films. *Adv Funct Mater* **26**, 1564–1570 (2016).

184. J. B. Torrance, P. Lacorre, C. Asavaroengchai, R. M. Metzger, Why are some oxides metallic, while most are insulating? *Physica C Supercond* **182**, 351–364 (1991).

185. J. Suntivich, W. T. Hong, Y. L. Lee, J. M. Rondinelli, W. Yang, J. B. Goodenough, B. Dabrowski, J. W. Freeland, Y. Shao-Horn, Estimating hybridization of transition metal and oxygen states in perovskites from O K -edge X-ray absorption spectroscopy. *Journal of Physical Chemistry C* **118**, 1856–1863 (2014).

186. J. Zaane, G. A. Sawatzky, Band Gaps and Electronic Structure of Transition-Metal Compounds. *Phys Rev Lett* **55**, 418–421 (1985).

187. S. Chowdhury, A. Jana, M. Kuila, V. R. Reddy, R. J. Choudhary, D. M. Phase, Negative Charge-Transfer Energy in SrCoO2.5 Thin Films: An Interplay between O-2p Hole Density, Charge-Transfer Energy, Charge Disproportionation, and Ferromagnetic Ordering. *ACS Appl Electron Mater* **2**, 3859–3870 (2020).

188. A. E. Bocquet, A. Fujimori, T. Mizokawa, T. Saitoh, H. Namatame, S. Suga, N. Kimizuka, Y. Takeda, M. Takano, Electronic structure of SrFe4+O3 and related Fe perovskite oxides. *Phys Rev B* **45**, 1561–1570 (1992).

189. A. Rothschild, W. Menesklou, H. L. Tuller, E. Ivers-Tiffée, Electronic structure, defect chemistry, and transport properties of SrTi1-xFexO3-y solid solutions. *Chemistry of Materials* **18**, 3651–3659 (2006).

190. T. Das, J. D. Nicholas, Y. Qi, Long-range charge transfer and oxygen vacancy interactions in strontium ferrite. *J Mater Chem A Mater* **5**, 4493–4506 (2017).

191. T. Takeda, R. Kanno, Y. Kawamoto, M. Takano, S. Kawasaki, T. Kamiyama, F. Izumi, Metal-semiconductor transition, charge disproportionation, and low-temperature structure of Ca(1-x)Sr(x)FeO3 synthesized under high-oxygen pressure. *Solid State Sci* **2**, 673–687 (2000).

192. L. Karvonen, S. Räsänen, H. Yamauchi, M. Karppinen, Chemical oxidation of SrCoO3-δ. *Chem Lett* **36**, 1176–1177 (2007).

193. N. Ichikawa, M. Iwanowska, M. Kawai, C. Calers, W. Paulus, Y. Shimakawa, Reduction and oxidation of SrCoO2.5 thin films at low temperatures. *Dalton Transactions* **41**, 10507–10510 (2012).

194. M. Schmidt, S. J. Campbell, Crystal and magnetic structures of Sr2Fe2O5 at elevated temperature. *J Solid State Chem* **156**, 292–304 (2001).

195. J. P. Hodges, S. Short, J. D. Jorgensen, X. Xiong, B. Dabrowski, S. M. Mini, C. W. Kimball, Evolution of oxygen-vacancy ordered crystal structures in the perovskite series Sr(n)Fe(n)O(3n-1) (n = 2, 4, 8, and ∞), and the relationship to electronic and magnetic properties. *J Solid State Chem* **151**, 190–209 (2000).

196. S. Deublein, S. Reiser, J. Vrabec, H. Hasse, A set of molecular models for alkaline-earth cations in aqueous solution. *Journal of Physical Chemistry B* **116**, 5448–5457 (2012).

197. S. Hao, M. Liu, J. Pan, X. Liu, X. Tan, N. Xu, Y. He, L. Lei, X. Zhang, Dopants fixation of Ruthenium for boosting acidic oxygen evolution stability and activity. *Nat Commun* **11**, 5368 (2020).

198. C. Wu, X. Wang, Y. Tang, H. Zhong, X. Zhang, A. Zou, J. Zhu, C. Diao, S. Xi, J. Xue, J. Wu, Origin of Surface Reconstruction in Lattice Oxygen Oxidation Mechanism Based-Transition Metal Oxides: A Spontaneous Chemical Process. *Angewandte Chemie - International Edition* **62** (2023).

199. B. Han, A. Grimaud, L. Giordano, W. T. Hong, O. Diaz-Morales, L. Yueh-Lin, J. Hwang, N. Charles, K. A. Stoerzinger, W. Yang, M. T. M. Koper, Y. Shao-Horn, Iron-Based Perovskites for Catalyzing Oxygen Evolution Reaction. *Journal of Physical Chemistry C* **122**, 8445–8454 (2018).

200. X. Wang, H. Zhong, S. Xi, W. S. V. Lee, J. Xue, Understanding of Oxygen Redox in the Oxygen Evolution Reaction. *Advanced Materials* **34**, 2107956 (2022).

201. A. Grimaud, O. Diaz-Morales, B. Han, W. T. Hong, Y. L. Lee, L. Giordano, K. A. Stoerzinger, M. T. M. Koper, Y. Shao-Horn, Activating lattice oxygen redox reactions in metal oxides to catalyse oxygen evolution. *Nat Chem* **9**, 457–465 (2017).

202. E. Fabbri, M. Nachtegaal, T. Binninger, X. Cheng, B. J. Kim, J. Durst, F. Bozza, T. Graule, R. Schäublin, L. Wiles, M. Pertoso, N. Danilovic, K. E. Ayers, T. J. Schmidt, Dynamic surface self-reconstruction is the key of highly active perovskite nano-electrocatalysts for water splitting. *Nat Mater* **16**, 925–931 (2017).

203. H. Wang, T. Zhai, Y. Wu, T. Zhou, B. Zhou, C. Shang, Z. Guo, High-Valence Oxides for High Performance Oxygen Evolution Electrocatalysis. *Advanced Science* **10**, 2301706 (2023).

204. H. Rickert, Solid Ionic Conductors: Principles and Applications. *Angewandte Chemie International Edition in English* **17**, 37–46 (1978).

205. A. Chatterjee, J. M. Caicedo, B. Ballesteros, J. Santiso, An in operando study of chemical expansion and oxygen surface exchange rates in epitaxial GdBaCo2O5.5 electrodes in a solid-state electrochemical cell by time-resolved X-ray diffraction. *J Mater Chem A Mater* **6**, 12430–12439 (2018).

206. Q. Yang, H. J. Cho, H. Jeen, H. Ohta, Macroscopic Visualization of Fast Electrochemical Reaction of SrCoOx Oxygen Sponge. *Adv Mater Interfaces* **6**, 1901260 (2019).

207. Q. Lu, B. Yildiz, Voltage-Controlled Topotactic Phase Transition in Thin-Film SrCoOx Monitored by in Situ X-ray Diffraction. *Nano Lett* **16**, 1186–1193 (2016).

208. Q. Lu, Y. Chen, H. Bluhm, B. Yildiz, Electronic Structure Evolution of SrCoOx during Electrochemically Driven Phase Transition Probed by in Situ X-ray Spectroscopy. *Journal of Physical Chemistry C* **120**, 24148–24157 (2016).

209. Y. Yamamura, S. Kawasaki, H. Sakai, Molecular dynamics analysis of ionic conduction mechanism in yttria-stabilized zirconia. *Solid State Ion* **126**, 181–189 (1999).

210. M. D. Biegalski, J. H. Haeni, S. Trolier-McKinstry, D. G. Schlom, C. D. Brandle, A. J. Ven Graitis, Thermal expansion of the new perovskite substrates DyScO3 and GdScO3. *J Mater Res* **20**, 952–958 (2005).

211. D. de Ligny, P. Richet, High-temperature heat capacity and thermal expansion of SrTiO3 and SrZrO3 perovskites. *Phys Rev B Condens Matter Mater Phys* **53**, 3013–3022 (1996).

212. J. M. Siqueira Júnior, L. F. Brum Malta, F. M. S. Garrido, T. Ogasawara, M. E. Medeiros, Raman and Rietveld structural characterization of sintered alkaline earth doped ceria. *Mater Chem Phys* **135**, 957–964 (2012).

213. C. Balaji Gopal, M. García-Melchor, S. C. Lee, Y. Shi, A. Shavorskiy, M. Monti, Z. Guan, R. Sinclair, H. Bluhm, A. Vojvodic, W. C. Chueh, Equilibrium oxygen storage capacity of ultrathin CeO2-δ depends non-monotonically on large biaxial strain. *Nat Commun* **8**, 15360 (2017).

214. Y. Shi, S. C. Lee, M. Monti, C. Wang, Z. A. Feng, W. D. Nix, M. F. Toney, R. Sinclair, W. C. Chueh, Growth of Highly Strained CeO2 Ultrathin Films. *ACS Nano* **10**, 9938–9947 (2016).

215. C. Chen, D. Chen, Y. Gao, Z. Shao, F. Ciucci, Computational and experimental analysis of Ba0.95La 0.05FeO3-δ as a cathode material for solid oxide fuel cells. *J Mater Chem A Mater* **2**, 14154–14163 (2014).

216. P. Nizet, F. Chiabrera, N. López-Pintó, N. Alayo, P. Langner, S. Valencia, A. Fraile-Rodríguez, F. Baiutti, A. Smekhova, A. Morata, J. Sort, A. Tarancón, Analog control of electrical conductivity in La0.5Sr0.5FeO3-x through oxygen deficiency induced magnetic transition. *Appl Phys Rev* **11**, 041426 (2024).

217. D. Li, K. Lee, B. Y. Wang, M. Osada, S. Crossley, H. R. Lee, Y. Cui, Y. Hikita, H. Y. Hwang, Superconductivity in an infinite-layer nickelate. *Nature* **572**, 624–627 (2019).

218. L. Iglesias, A. Gómez, M. Gich, F. Rivadulla, Tuning Oxygen Vacancy Diffusion through Strain in SrTiO3 Thin Films. *ACS Appl Mater Interfaces* **10**, 35367–35373 (2018).

219. A. Sarantopoulos, W. L. Ong, J. A. Malen, F. Rivadulla, Effect of epitaxial strain and vacancies on the ferroelectric-like response of CaTiO3 thin films. *Appl Phys Lett* **113**, 182902 (2018).

220. V. Álvarez-Martínez, R. Ramos, V. Leborán, A. Sarantopoulos, R. Dittmann, F. Rivadulla, Interfacial Thermal Resistive Switching in (Pt,Cr)/SrTiO3 Devices. *ACS Appl Mater Interfaces* **16**, 15043–15049 (2024).

221. R. Garcia, A. W. Knoll, E. Riedo, Advanced scanning probe lithography. *Nat Nanotechnol* **9**, 577–587 (2014).

222. J. A. Dagata, W. Tseng, J. Bennett, C. J. Evans, J. Schneir, H. H. Harary, Selective-area epitaxial growth of gallium arsenide on silicon substrates patterned using a scanning tunneling microscope operating in air. *Appl Phys Lett* **57**, 2437–2439 (1990).

223. J. A. Dagata, T. Inoue, J. Itoh, K. Matsumoto, H. Yokoyama, Role of space charge in scanned probe oxidation. *J Appl Phys* **84**, 6891–6900 (1998).

224. X. N. Xie, H. J. Chung, H. Xu, X. Xu, C. H. Sow, A. T. S. Wee, Probe-induced native oxide decomposition and localized oxidation of 6H-SiC (0001) surface: an atomic force microscopy investigation. *J Am Chem Soc* **126**, 7665–7675 (2004).

225. E. S. Snow, G. G. Jernigan, P. M. Campbell, The kinetics and mechanism of scanned probe oxidation of Si. *Appl Phys Lett* **76**, 1782–1784 (2000).

226. R. Held, S. Lüscher, T. Heinzel, K. Ensslin, W. Wegscheider, Fabricating tunable semiconductor devices with an atomic force microscope. *Appl Phys Lett* **75**, 1134–1136 (1999).

227. S. Masubuchi, M. Arai, T. MacHida, Atomic force microscopy based tunable local anodic oxidation of graphene. *Nano Lett* **11**, 4542–4546 (2011).

228. C. Cen, S. Thiel, G. Hammerl, C. W. Schneider, K. E. Andersen, C. S. Hellberg, J. Mannhart, J. Levy, Nanoscale control of an interfacial metal-insulator transition at room temperature. *Nat Mater* **7**, 298–302 (2008).

229. F. Bi, D. F. Bogorin, C. Cen, C. W. Bark, J. W. Park, C. B. Eom, J. Levy, "Water-cycle" mechanism for writing and erasing nanostructures at the LaAlO3/SrTiO3 interface. *Appl Phys Lett* **97**, 173110 (2010).

230. C. Cen, S. Thiel, J. Mannhart, J. Levy, Oxide nanoelectronics on demand. *Science (1979)* **323**, 1026–1030 (2009).

231. D. Mohan Radheep, K. Shanmugapriya, B. Palanivel, R. Murugan, Magnetic field-induced switching of magnetic ordering in SrFeO3−δ. *Appl Phys A Mater Sci Process* **122**, 1–5 (2016).

232. U. Aschauer, R. Pfenninger, S. M. Selbach, T. Grande, N. A. Spaldin, Strain-controlled oxygen vacancy formation and ordering in CaMnO3. *Phys Rev B Condens Matter Mater Phys* **88**, 054111 (2013).

233. M. Tyunina, O. Pacherova, T. Kocourek, A. Dejneka, Anisotropic chemical expansion due to oxygen vacancies in perovskite films. *Sci Rep* **11**, 15247 (2021).

234. Y. Sun, J. Yang, S. Li, D. Wang, Defect engineering in perovskite oxide thin films. *Chemical Communications* **57**, 8402–8420 (2021).

235. H. W. Jang, A. Kumar, S. Denev, M. D. Biegalski, P. Maksymovych, C. W. Bark, C. T. Nelson, C. M. Folkman, S. H. Baek, N. Balke, C. M. Brooks, D. A. Tenne, D. G. Schlom, L. Q. Chen, X. Q. Pan, S. V. Kalinin, V. Gopalan, C. B. Eom, Ferroelectricity in strain-free SrTiO3 thin films. *Phys Rev Lett* **104**, 197601 (2010).

236. E. Sediva, J. L. M. Rupp, Raman spectra and defect chemical characteristics of Sr(Ti,Fe)O3−y solid solution of bulk pellets vs. thin films. *J Mater Chem A Mater* **11**, 26752–26763 (2023).

237. E. Sediva, T. Defferriere, N. H. Perry, H. L. Tuller, J. L. M. Rupp, In Situ Method Correlating Raman Vibrational Characteristics to Chemical Expansion via Oxygen Nonstoichiometry of Perovskite Thin Films. *Advanced Materials* **31**, 1902493 (2019).

238. W. T. Hong, K. A. Stoerzinger, E. J. Crumlin, E. Mutoro, H. Jeen, H. N. Lee, Y. Shao-Horn, Near-Ambient Pressure XPS of Higherature Surface Chemistry in Sr2Co2O5 Thin Films. *Top Catal* **59**, 574–582 (2016).

239. M. L. Weber, G. Lole, A. Kormanyos, A. Schwiers, L. Heymann, F. D. Speck, T. Meyer, R. Dittmann, S. Cherevko, C. Jooss, C. Baeumer, F. Gunkel, Atomistic Insights into Activation and Degradation of La0.6Sr0.4CoO3-δ Electrocatalysts under Oxygen Evolution Conditions. *J Am Chem Soc* **144**, 17966–17979 (2022).

240. D. G. Popescu, N. Barrett, C. Chirila, I. Pasuk, M. A. Husanu, Influence of hole depletion and depolarizing field on the BaTiO3/La0.6Sr0.4MnO3 interface electronic structure revealed by photoelectron spectroscopy and first-principles calculations. *Phys Rev B Condens Matter Mater Phys* **92**, 235442 (2015).

241. A. Shahzad, J. Ali, M. W. Ullah, K. Aziz, M. A. Javed, F. Hussain, S. Manan, K. A. Khan, T. Alomayri, W. A. R. M, G. Yang, Fe-based dual-center heterogeneous catalyst assisted with reduced graphene oxide for the activation of peroxymonosulfate. *Adv Compos Hybrid Mater* **6**, 185 (2023).

242. C. Noël, L. Wouters, K. Paredis, U. Celano, T. Hantschel, Oil as an Enabler for Efficient Materials Removal in Three-Dimensional Scanning Probe Microscopy Applications. *Front Mech Eng* **7**, 797962 (2021).

243. X. Wu, J. Walter, T. Feng, J. Zhu, H. Zheng, J. F. Mitchell, N. Biškup, M. Varela, X. Ruan, C. Leighton, X. Wang, Glass-Like Through-Plane Thermal Conductivity Induced by Oxygen Vacancies in Nanoscale Epitaxial La0.5Sr0.5CoO3−δ. *Adv Funct Mater* **27**, 1704233 (2017).

244. C. Lichtensteiger, M. Hadjimichael, E. Zatterin, C. P. Su, I. Gaponenko, L. Tovaglieri, P. Paruch, A. Gloter, J. M. Triscone, Mapping the complex evolution of ferroelastic/ferroelectric domain patterns in epitaxially strained PbTiO3 heterostructures. *APL Mater* **11**, 061126 (2023).

245. X. Guo, L. Zhou, B. Roul, Y. Wu, Y. Huang, S. Das, Z. Hong, Theoretical Understanding of Polar Topological Phase Transitions in Functional Oxide Heterostructures: A Review. *Small Methods* **6**, 2200486 (2022).

246. A. K. Yadav, C. T. Nelson, S. L. Hsu, Z. Hong, J. D. Clarkson, C. M. Schlepuëtz, A. R. Damodaran, P. Shafer, E. Arenholz, L. R. Dedon, D. Chen, A. Vishwanath, A. M. Minor, L. Q. Chen, J. F. Scott, L. W. Martin, R. Ramesh, Observation of polar vortices in oxide superlattices. *Nature* **530**, 198–201 (2016).

247. A. Y. Abid, Y. Sun, X. Hou, C. Tan, X. Zhong, R. Zhu, H. Chen, K. Qu, Y. Li, M. Wu, J. Zhang, J. Wang, K. Liu, X. Bai, D. Yu, X. Ouyang, J. Wang, J. Li, P. Gao, Creating polar antivortex in PbTiO3/SrTiO3 superlattice. *Nat Commun* **12**, 2054 (2021).

248. P. Aguado-Puente, J. Junquera, Structural and energetic properties of domains in PbTiO3/SrTiO3 superlattices from first principles. *Phys Rev B Condens Matter Mater Phys* **85**, 184105 (2012).

249. S. Das, Y. L. Tang, Z. Hong, M. A. P. Gonçalves, M. R. McCarter, C. Klewe, K. X. Nguyen, F. Gómez-Ortiz, P. Shafer, E. Arenholz, V. A. Stoica, S. L. Hsu, B. Wang, C. Ophus, J. F. Liu, C. T. Nelson, S. Saremi, B. Prasad, A. B. Mei, D. G. Schlom, J. Íñiguez,

P. García-Fernández, D. A. Muller, L. Q. Chen, J. Junquera, L. W. Martin, R. Ramesh, Observation of room-temperature polar skyrmions. *Nature* **568**, 368–372 (2019).

250. Y. T. Shao, S. Das, Z. Hong, R. Xu, S. Chandrika, F. Gómez-Ortiz, P. García-Fernández, L. Q. Chen, H. Y. Hwang, J. Junquera, L. W. Martin, R. Ramesh, D. A. Muller, Emergent chirality in a polar meron to skyrmion phase transition. *Nat Commun* **14**, 1355 (2023).

251. F. H. Gong, Y. L. Tang, Y. L. Zhu, H. Zhang, Y. J. Wang, Y. T. Chen, Y. P. Feng, M. J. Zou, B. Wu, W. R. Geng, Y. Cao, X. L. Ma, Atomic mapping of periodic dipole waves in ferroelectric oxide. *Sci Adv* **7**, eabg5503 (2021).

252. V. A. Stoica, N. Laanait, C. Dai, Z. Hong, Y. Yuan, Z. Zhang, S. Lei, M. R. McCarter, A. Yadav, A. R. Damodaran, S. Das, G. A. Stone, J. Karapetrova, D. A. Walko, X. Zhang, L. W. Martin, R. Ramesh, L. Q. Chen, H. Wen, V. Gopalan, J. W. Freeland, Optical creation of a supercrystal with three-dimensional nanoscale periodicity. *Nat Mater* **18**, 377–383 (2019).

253. A. R. Damodaran, J. D. Clarkson, Z. Hong, H. Liu, A. K. Yadav, C. T. Nelson, S. L. Hsu, M. R. McCarter, K. D. Park, V. Kravtsov, A. Farhan, Y. Dong, Z. Cai, H. Zhou, P. Aguado-Puente, P. Garcia-Fernandez, J. Iniguez, J. Junquera, A. Scholl, M. B. Raschke, L. Q. Chen, D. D. Fong, R. Ramesh, L. W. Martin, Phase coexistence and electric-field control of toroidal order in oxide superlattices. *Nat Mater* **16**, 1003–1009 (2017).

254. S. Das, Z. Hong, V. A. Stoica, M. A. P. Gonçalves, Y. T. Shao, E. Parsonnet, E. J. Marksz, S. Saremi, M. R. McCarter, A. Reynoso, C. J. Long, A. M. Hagerstrom, D. Meyers, V. Ravi, B. Prasad, H. Zhou, Z. Zhang, H. Wen, F. Gómez-Ortiz, P. García-Fernández, J. Bokor, J. Íñiguez, J. W. Freeland, N. D. Orloff, J. Junquera, L. Q. Chen, S. Salahuddin, D. A. Muller, L. W. Martin, R. Ramesh, Local negative permittivity and topological phase transition in polar skyrmions. *Nat Mater* **20**, 194–201 (2021).

255. C. Dai, V. A. Stoica, S. Das, Z. Hong, L. W. Martin, R. Ramesh, J. W. Freeland, H. Wen, V. Gopalan, L. Q. Chen, Tunable Nanoscale Evolution and Topological Phase Transitions of a Polar Vortex Supercrystal. *Advanced Materials* **34**, 2106401 (2022).

256. R. Zhu, Z. Jiang, X. Zhang, X. Zhong, C. Tan, M. Liu, Y. Sun, X. Li, R. Qi, K. Qu, Z. Liu, M. Wu, M. Li, B. Huang, Z. Xu, J. Wang, K. Liu, P. Gao, J. Wang, J. Li, X. Bai, Dynamics of Polar Skyrmion Bubbles under Electric Fields. *Phys Rev Lett* **129**, 107601 (2022).

257. R. Tomasello, E. Martinez, R. Zivieri, L. Torres, M. Carpentieri, G. Finocchio, A strategy for the design of skyrmion racetrack memories. *Sci Rep* **4**, 1–7 (2014).

258. A. Fert, V. Cros, J. Sampaio, Skyrmions on the track. *Nat Nanotechnol* **8**, 152–156 (2013).

259. Z. Hong, A. R. Damodaran, F. Xue, S. L. Hsu, J. Britson, A. K. Yadav, C. T. Nelson, J. J. Wang, J. F. Scott, L. W. Martin, R. Ramesh, L. Q. Chen, Stability of Polar Vortex Lattice in Ferroelectric Superlattices. *Nano Lett* **17**, 2246–2252 (2017).

260. A. Biswas, C. H. Yang, R. Ramesh, Y. H. Jeong, Atomically flat single terminated oxide substrate surfaces. *Prog Surf Sci* **92**, 117–141 (2017).

261. J. J. Peng, C. S. Hao, H. Y. Liu, Y. Yan, Two-step treatment to obtain single-terminated SrTiO3 substrate and the related difference in both LaAlO3 film growth and electronic property. *AIP Adv* **11**, 085303 (2021).

262. R. Dirsyte, J. Schwarzkopf, G. Wagner, R. Fornari, J. Lienemann, M. Busch, H. Winter, Thermal-induced change in surface termination of DyScO3 (110). *Surf Sci* **604**, L55–L58 (2010).

263. C. Weymann, C. Lichtensteiger, S. Fernandez-Peña, A. B. Naden, L. R. Dedon, L. W. Martin, J. M. Triscone, P. Paruch, Full Control of Polarization in Ferroelectric Thin Films Using Growth Temperature to Modulate Defects. *Adv Electron Mater* **6**, 2000852 (2020).

264. E. H. Smith, P. D. C. King, A. Soukiassian, D. G. Ast, D. G. Schlom, Hybrid reflections from multiple x-ray scattering in epitaxial oxide films. *Appl Phys Lett* **111**, 131903 (2017).

265. J. H. Haeni, et al. et al., Room-Temperature Ferroelectricity in Strained SrTiO3. *Nature* **430**, 758–761 (2004).

266. M. Nemoz, F. Semond, S. Rennesson, M. Leroux, S. Bouchoule, G. Patriarche, J. Zuniga-Perez, Interdiffusion of Al and Ga in AlN/AlGaN superlattices grown by ammonia-assisted molecular beam epitaxy. *Superlattices Microstruct* **150**, 106801 (2021).

267. F. H. Gong, Y. L. Tang, Y. J. Wang, Y. T. Chen, B. Wu, L. X. Yang, Y. L. Zhu, X. L. Ma, Absence of critical thickness for polar skyrmions with breaking the Kittel's law. *Nat Commun* **14**, 3376 (2023).

268. Y. Ni, S. Volz, Evidence of phonon Anderson localization on the thermal properties of disordered atomic systems. *J Appl Phys* **130**, 190901 (2021).

269. M. N. Luckyanova, J. Mendoza, H. Lu, B. Song, S. Huang, J. Zhou, M. Li, Y. Dong, H. Zhou, J. Garlow, L. Wu, B. J. Kirby, A. J. Grutter, A. A. Puretzky, Y. Zhu, M. S. Dresselhaus, A. Gossard, G. Chen, Phonon localization in heat conduction. *Sci Adv* **4**, eaat9460 (2018).

270. C. Tan, Y. Dong, Y. Sun, C. Liu, P. Chen, X. Zhong, R. Zhu, M. Liu, J. Zhang, J. Wang, K. Liu, X. Bai, D. Yu, X. Ouyang, J. Wang, P. Gao, Z. Luo, J. Li, Engineering polar vortex from topologically trivial domain architecture. *Nat Commun* **12**, 4620 (2021).

271. M. Hadjimichael, Y. Li, E. Zatterin, G. A. Chahine, M. Conroy, K. Moore, E. N. O. Connell, P. Ondrejkovic, P. Marton, J. Hlinka, U. Bangert, S. Leake, P. Zubko, Metal–ferroelectric supercrystals with periodically curved metallic layers. *Nat Mater* **20**, 495–502 (2021).

272. J. Wang, R. Gao, S. Tang, S. Dong, M. Liang, J. Yang, S. Zhang, H. Huang, General principle of ferroelectric topological domain formation. *Sci Adv* **11**, eadu6223 (2025).

273. Z. Hong, S. Das, C. Nelson, A. Yadav, Y. Wu, J. Junquera, L. Q. Chen, L. W. Martin, R. Ramesh, Vortex Domain Walls in Ferroelectrics. *Nano Lett* **21**, 3533–3539 (2021)

RIGHTS AND PERMISSIONS

PUBLICATIONS DERIVED FROM THIS THESIS

The publications derived from this thesis, which are partially reproduced in chapters 3, 4 and 5, do not require permission for non-commercial purposes, as they are all published under open-access Creative Commons licenses.

"Light-induced bi-directional switching of thermal conductivity in azobenzene-doped liquid crystal mesophases" *Journal of Materials Chemistry C*, **2023**, 11, 4588-4594. https://doi.org/10.1039/D3TC00099K

Noa Varela-Domínguez, Carlos López-Bueno, Alejandro López-Moreno, Marcel S. Claro, Gustavo Rama, Víctor Leborán, María del Carmen Giménez-López, and Francisco Rivadulla*

This article is published under the CC BY-NC 3.0 license, which allows sharing and adapting the material for non-commercial purposes, provided that appropriate credit is given, and any modifications are indicated, if applicable.

"Exploring Topochemical Oxidation Reactions for Reversible Tuning of Thermal Conductivity in Perovskite Fe Oxides" *Chemistry of Materials*, **2024**, 36, 10249-10258. https://doi.org/10.1021/acs.chemmater.4c02023

Noa Varela-Domínguez, Marcel S. Claro, Enrique Carbó-Argibay, César Magén and Francisco Rivadulla*

This article is published under the CC BY 4.0 license, which allows sharing and adapting the material provided that appropriate credit is given, and any modifications are indicated, if applicable.

"Electric-Field Control of the Local Thermal Conductivity in Charge Transfer Oxides" *Advanced Materials*, **2025**, 37, 2413045. https://doi.org/10.1002/adma.202413045

Noa Varela-Domínguez, Marcel S. Claro, Carlos Vázquez-Vázquez, Manuel Arturo López-Quintela and Francisco Rivadulla*

This article is published under the CC BY-NC-ND 4.0 license, which allows sharing the material for non-commercial purposes, provided that appropriate credit is given.

TABLES AND FIGURES

Figure 2.15b

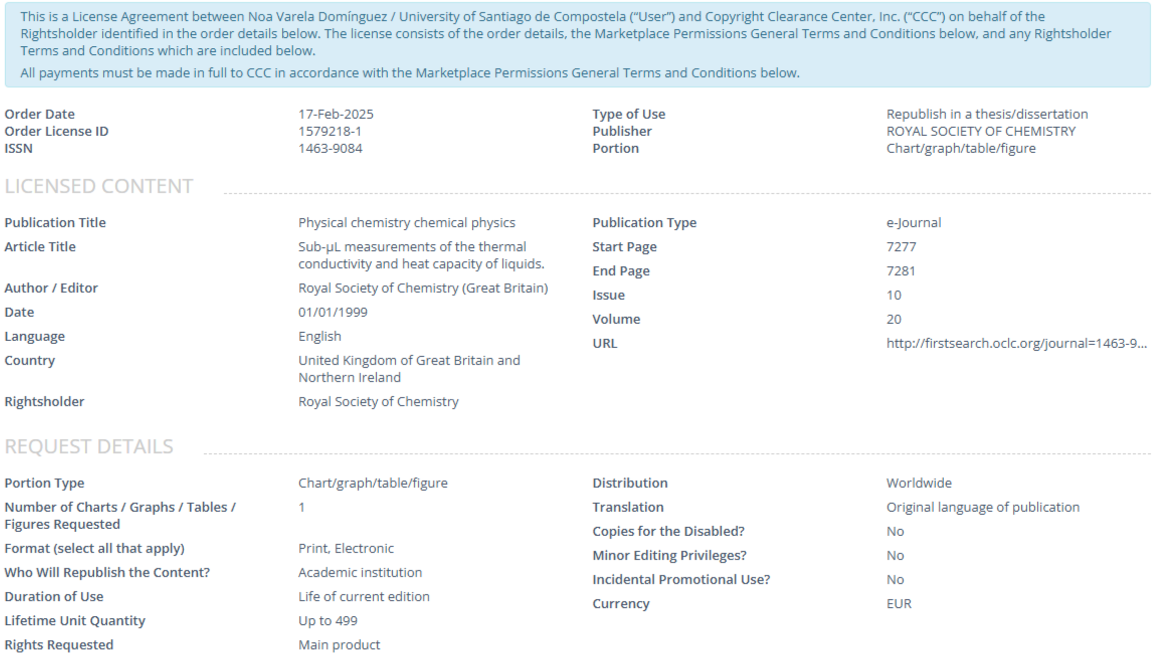

This is a License Agreement between Noa Varela Domínguez / University of Santiago de Compostela ("User") and Copyright Clearance Center, Inc. ("CCC") on behalf of the Rightsholder identified in the order details below. The license consists of the order details, the Marketplace Permissions General Terms and Conditions below, and any Rightsholder Terms and Conditions which are included below.

All payments must be made in full to CCC in accordance with the Marketplace Permissions General Terms and Conditions below.

Order Date	17-Feb-2025	**Type of Use**	Republish in a thesis/dissertation
Order License ID	1579218-1	**Publisher**	ROYAL SOCIETY OF CHEMISTRY
ISSN	1463-9084	**Portion**	Chart/graph/table/figure

LICENSED CONTENT

Publication Title	Physical chemistry chemical physics	**Publication Type**	e-Journal
Article Title	Sub-μL measurements of the thermal conductivity and heat capacity of liquids.	**Start Page**	7277
		End Page	7281
Author / Editor	Royal Society of Chemistry (Great Britain)	**Issue**	10
Date	01/01/1999	**Volume**	20
Language	English	**URL**	http://firstsearch.oclc.org/journal=1463-9...
Country	United Kingdom of Great Britain and Northern Ireland		
Rightsholder	Royal Society of Chemistry		

REQUEST DETAILS

Portion Type	Chart/graph/table/figure	**Distribution**	Worldwide
Number of Charts / Graphs / Tables / Figures Requested	1	**Translation**	Original language of publication
		Copies for the Disabled?	No
Format (select all that apply)	Print, Electronic	**Minor Editing Privileges?**	No
Who Will Republish the Content?	Academic institution	**Incidental Promotional Use?**	No
Duration of Use	Life of current edition	**Currency**	EUR
Lifetime Unit Quantity	Up to 499		
Rights Requested	Main product		

Figure 3.1b

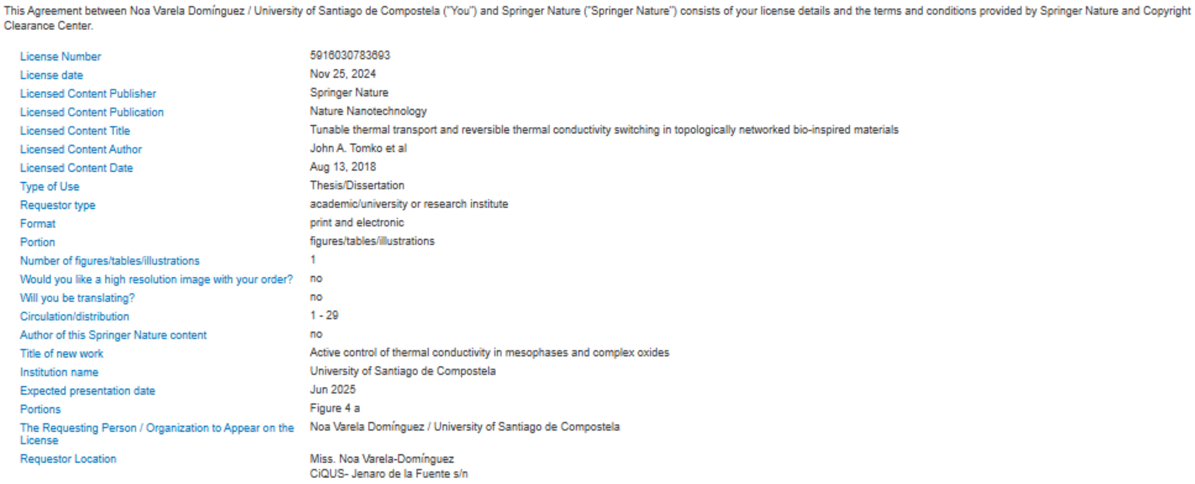

This Agreement between Noa Varela Domínguez / University of Santiago de Compostela ("You") and Springer Nature ("Springer Nature") consists of your license details and the terms and conditions provided by Springer Nature and Copyright Clearance Center.

License Number	5916030783693
License date	Nov 25, 2024
Licensed Content Publisher	Springer Nature
Licensed Content Publication	Nature Nanotechnology
Licensed Content Title	Tunable thermal transport and reversible thermal conductivity switching in topologically networked bio-inspired materials
Licensed Content Author	John A. Tomko et al
Licensed Content Date	Aug 13, 2018
Type of Use	Thesis/Dissertation
Requestor type	academic/university or research institute
Format	print and electronic
Portion	figures/tables/illustrations
Number of figures/tables/illustrations	1
Would you like a high resolution image with your order?	no
Will you be translating?	no
Circulation/distribution	1 - 29
Author of this Springer Nature content	no
Title of new work	Active control of thermal conductivity in mesophases and complex oxides
Institution name	University of Santiago de Compostela
Expected presentation date	Jun 2025
Portions	Figure 4 a
The Requesting Person / Organization to Appear on the License	Noa Varela Domínguez / University of Santiago de Compostela
Requestor Location	Miss. Noa Varela-Domínguez CiQUS- Jenaro de la Fuente s/n

---

Figure 3.3

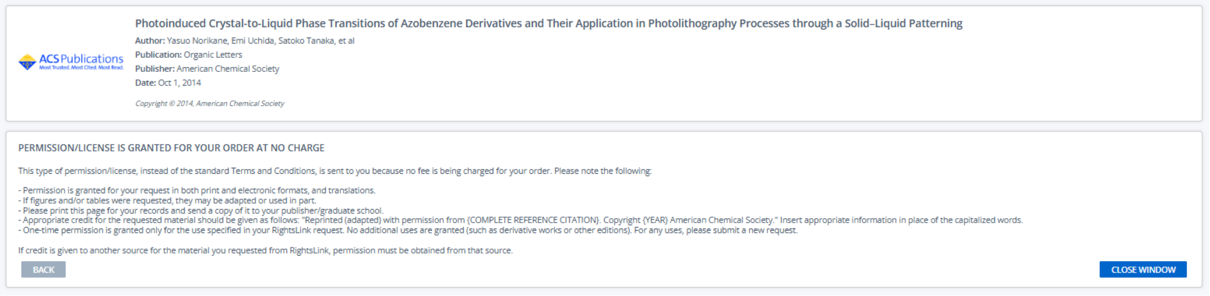

Photoinduced Crystal-to-Liquid Phase Transitions of Azobenzene Derivatives and Their Application in Photolithography Processes through a Solid–Liquid Patterning

Author: Yasuo Norikane, Emi Uchida, Satoko Tanaka, et al
Publication: Organic Letters
Publisher: American Chemical Society
Date: Oct 1, 2014

Copyright © 2014, American Chemical Society

PERMISSION/LICENSE IS GRANTED FOR YOUR ORDER AT NO CHARGE

This type of permission/license, instead of the standard Terms and Conditions, is sent to you because no fee is being charged for your order. Please note the following:

- Permission is granted for your request in both print and electronic formats, and translations.
- If figures and/or tables were requested, they may be adapted or used in part.
- Please print this page for your records and send a copy of it to your publisher/graduate school.
- Appropriate credit for the requested material should be given as follows: "Reprinted (adapted) with permission from {COMPLETE REFERENCE CITATION}. Copyright {YEAR} American Chemical Society." Insert appropriate information in place of the capitalized words.
- One-time permission is granted only for the use specified in your RightsLink request. No additional uses are granted (such as derivative works or other editions). For any uses, please submit a new request.

If credit is given to another source for the material you requested from RightsLink, permission must be obtained from that source.

Figure 3.7

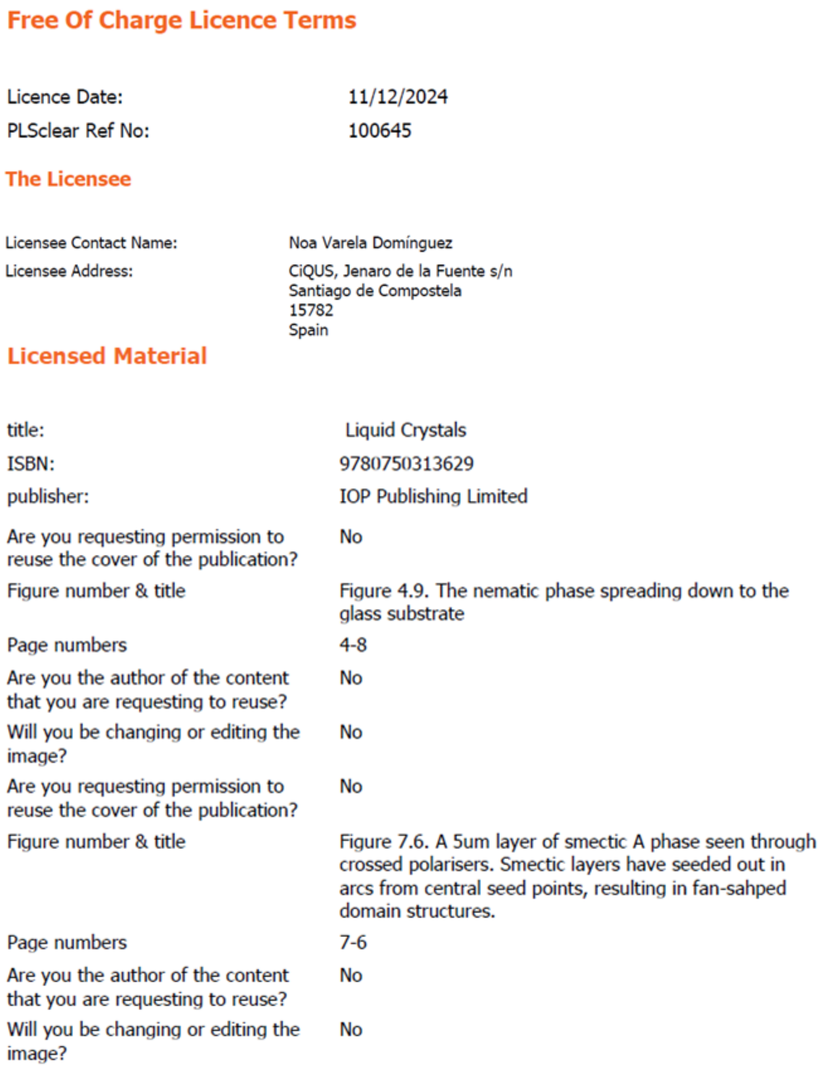

Free Of Charge Licence Terms

Licence Date:	11/12/2024
PLSclear Ref No:	100645

The Licensee

Licensee Contact Name:	Noa Varela Domínguez
Licensee Address:	CiQUS, Jenaro de la Fuente s/n Santiago de Compostela 15782 Spain

Licensed Material

title:	Liquid Crystals
ISBN:	9780750313629
publisher:	IOP Publishing Limited
Are you requesting permission to reuse the cover of the publication?	No
Figure number & title	Figure 4.9. The nematic phase spreading down to the glass substrate
Page numbers	4-8
Are you the author of the content that you are requesting to reuse?	No
Will you be changing or editing the image?	No
Are you requesting permission to reuse the cover of the publication?	No
Figure number & title	Figure 7.6. A 5um layer of smectic A phase seen through crossed polarisers. Smectic layers have seeded out in arcs from central seed points, resulting in fan-sahped domain structures.
Page numbers	7-6
Are you the author of the content that you are requesting to reuse?	No
Will you be changing or editing the image?	No

Figure 3.19

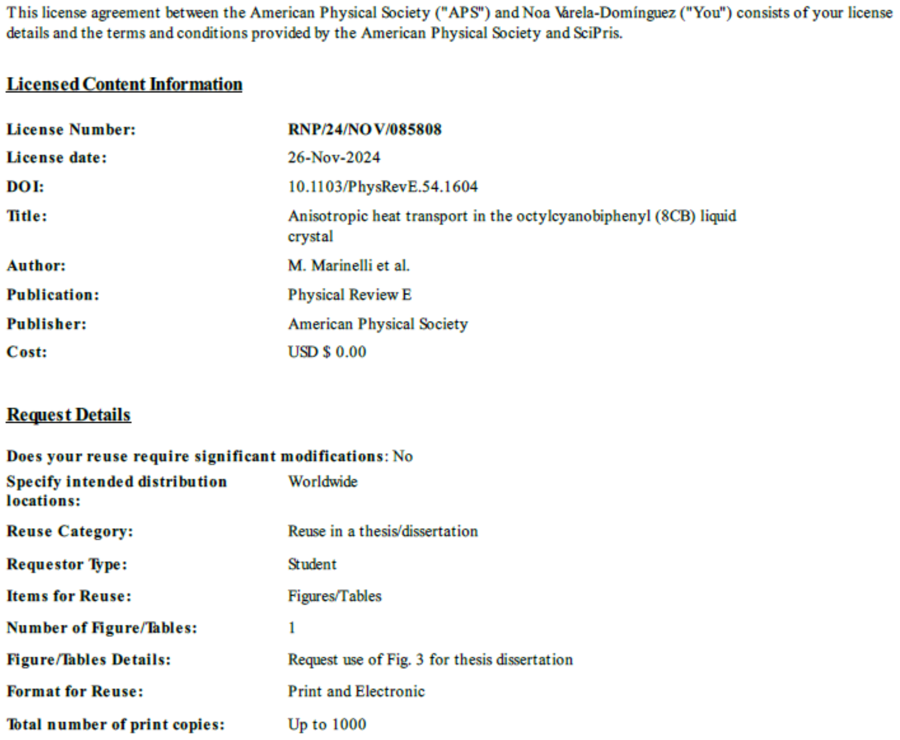

This license agreement between the American Physical Society ("APS") and Noa Varela-Domínguez ("You") consists of your license details and the terms and conditions provided by the American Physical Society and SciPris.

Licensed Content Information

License Number:	**RNP/24/NOV/085808**
License date:	26-Nov-2024
DOI:	10.1103/PhysRevE.54.1604
Title:	Anisotropic heat transport in the octylcyanobiphenyl (8CB) liquid crystal
Author:	M. Marinelli et al.
Publication:	Physical Review E
Publisher:	American Physical Society
Cost:	USD $ 0.00

Request Details

Does your reuse require significant modifications: No

Specify intended distribution locations:	Worldwide
Reuse Category:	Reuse in a thesis/dissertation
Requestor Type:	Student
Items for Reuse:	Figures/Tables
Number of Figure/Tables:	1
Figure/Tables Details:	Request use of Fig. 3 for thesis dissertation
Format for Reuse:	Print and Electronic
Total number of print copies:	Up to 1000

Figures 6.1a and 6.2

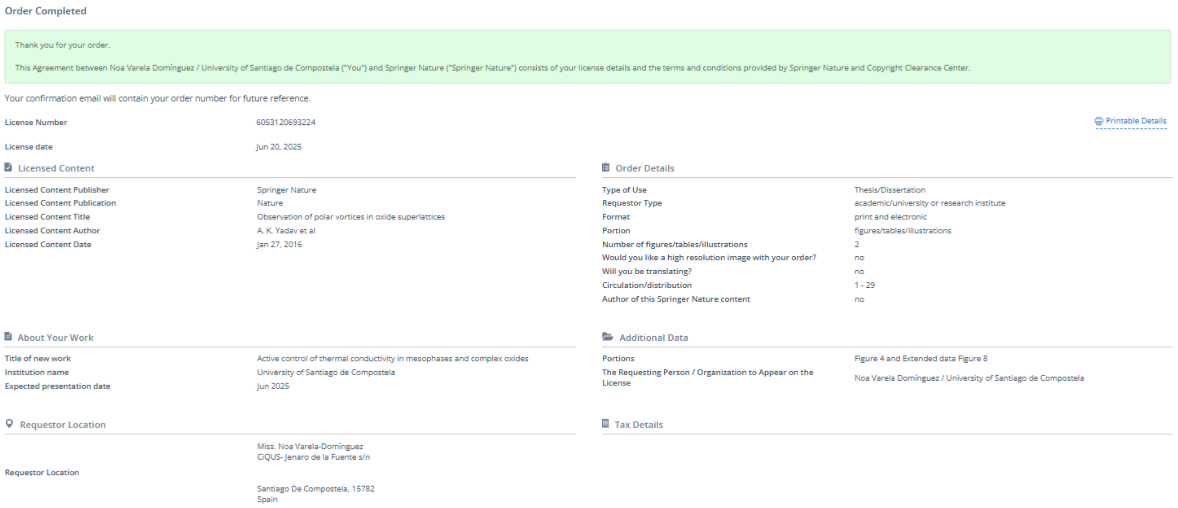

Order Completed

Thank you for your order.

This Agreement between Noa Varela Domínguez / University of Santiago de Compostela ("You") and Springer Nature ("Springer Nature") consists of your license details and the terms and conditions provided by Springer Nature and Copyright Clearance Center.

Your confirmation email will contain your order number for future reference.

License Number	6053120693224
License date	Jun 20, 2025

Licensed Content

Licensed Content Publisher	Springer Nature
Licensed Content Publication	Nature
Licensed Content Title	Observation of polar vortices in oxide superlattices
Licensed Content Author	A. K. Yadav et al
Licensed Content Date	Jan 27, 2016

Order Details

Type of Use	Thesis/Dissertation
Requestor Type	academic/university or research institute
Format	print and electronic
Portion	figures/tables/illustrations
Number of figures/tables/illustrations	2
Would you like a high resolution image with your order?	no
Will you be translating?	no
Circulation/distribution	1 - 29
Author of this Springer Nature content	no

About Your Work

Title of new work	Active control of thermal conductivity in mesophases and complex oxides
Institution name	University of Santiago de Compostela
Expected presentation date	Jun 2025

Additional Data

Portions	Figure 4 and Extended data Figure 8
The Requesting Person / Organization to Appear on the License	Noa Varela Domínguez / University of Santiago de Compostela

Requestor Location

Requestor Location	Miss. Noa Varela-Domínguez CiQUS- Jenaro de la Fuente s/n Santiago De Compostela, 15782 Spain

Tax Details

Figure 6.1b

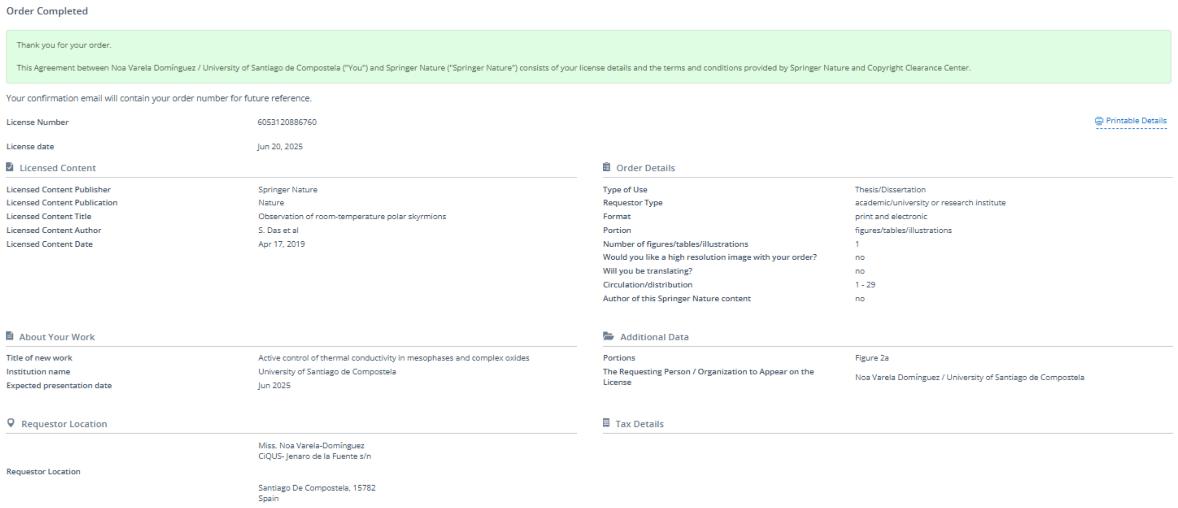

Order Completed

Thank you for your order.

This Agreement between Noa Varela Domínguez / University of Santiago de Compostela ("You") and Springer Nature ("Springer Nature") consists of your license details and the terms and conditions provided by Springer Nature and Copyright Clearance Center.

Your confirmation email will contain your order number for future reference.

License Number	6053120886760
License date	Jun 20, 2025

Licensed Content

Licensed Content Publisher	Springer Nature
Licensed Content Publication	Nature
Licensed Content Title	Observation of room-temperature polar skyrmions
Licensed Content Author	S. Das et al
Licensed Content Date	Apr 17, 2019

Order Details

Type of Use	Thesis/Dissertation
Requestor Type	academic/university or research institute
Format	print and electronic
Portion	figures/tables/illustrations
Number of figures/tables/illustrations	1
Would you like a high resolution image with your order?	no
Will you be translating?	no
Circulation/distribution	1 - 29
Author of this Springer Nature content	no

About Your Work

Title of new work	Active control of thermal conductivity in mesophases and complex oxides
Institution name	University of Santiago de Compostela
Expected presentation date	Jun 2025

Additional Data

Portions	Figure 2a
The Requesting Person / Organization to Appear on the License	Noa Varela Domínguez / University of Santiago de Compostela

Requestor Location

Requestor Location	Miss. Noa Varela-Domínguez CiQUS- Jenaro de la Fuente s/n Santiago De Compostela, 15782 Spain

Tax Details

Figure 6.1e

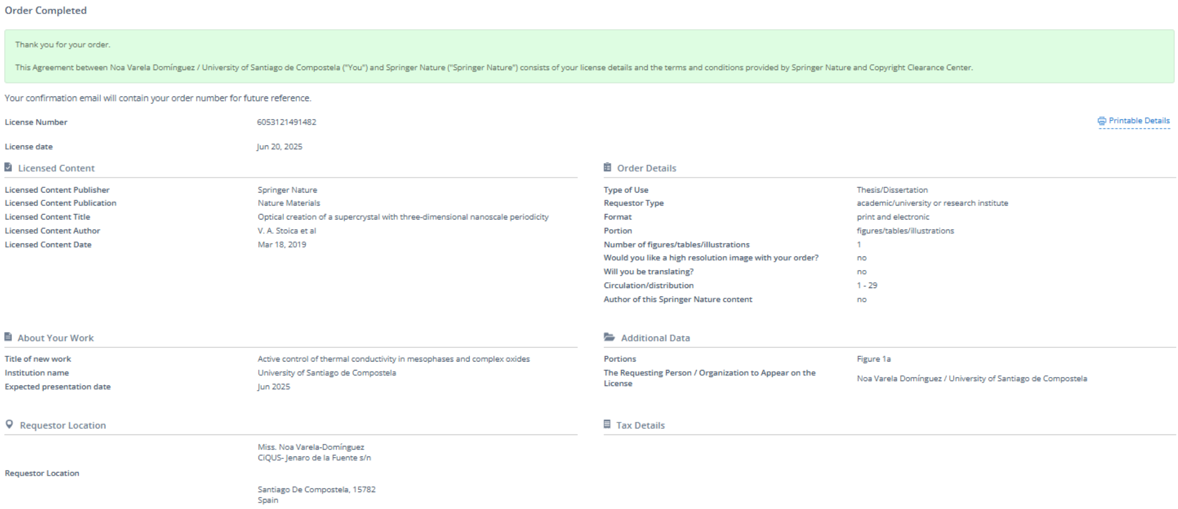

Order Completed

Thank you for your order.

This Agreement between Noa Varela Domínguez / University of Santiago de Compostela ("You") and Springer Nature ("Springer Nature") consists of your license details and the terms and conditions provided by Springer Nature and Copyright Clearance Center.

Your confirmation email will contain your order number for future reference.

License Number	6053121491482
License date	Jun 20, 2025

Licensed Content

Licensed Content Publisher	Springer Nature
Licensed Content Publication	Nature Materials
Licensed Content Title	Optical creation of a supercrystal with three-dimensional nanoscale periodicity
Licensed Content Author	V. A. Stoica et al
Licensed Content Date	Mar 18, 2019

Order Details

Type of Use	Thesis/Dissertation
Requestor Type	academic/university or research institute
Format	print and electronic
Portion	figures/tables/illustrations
Number of figures/tables/illustrations	1
Would you like a high resolution image with your order?	no
Will you be translating?	no
Circulation/distribution	1 - 29
Author of this Springer Nature content	no

About Your Work

Title of new work	Active control of thermal conductivity in mesophases and complex oxides
Institution name	University of Santiago de Compostela
Expected presentation date	Jun 2025

Additional Data

Portions	Figure 1a
The Requesting Person / Organization to Appear on the License	Noa Varela Domínguez / University of Santiago de Compostela

Requestor Location

Requestor Location	Miss. Noa Varela-Domínguez CiQUS- Jenaro de la Fuente s/n Santiago De Compostela, 15782 Spain

Tax Details

USC
UNIVERSIDADE
DE SANTIAGO
DE COMPOSTELA

CAMPUS VIDA
CAMPUS DE EXCELENCIA INTERNACIONAL

This PhD thesis explores the development of thermal switches: materials whose thermal conductivity can be precisely and reversibly controlled on demand by the application of an external stimulus. Four strategies have been investigated, based on a different physical mechanism and material platform: photoisomerization in azobenzene-based mesophases, topotactic redox transformations in (Ca,Sr)FeO_3 thin films, electric- field driven oxygen vacancy engineering in charge-transfer oxides, and polar topology manipulation in $PbTiO_3$/$SrTiO_3$ superlattices. The results establish heat transport as a functional, tunable property, opening pathways for programmable thermal materials in advanced technologies.